ABSTRACT

Title of Dissertation: SCALABLE MODELING APPROACHES IN SYSTEMS IMMUNOLOGY

Kyemyung Park
Doctor of Philosophy, 2020

Dissertation directed by: Dr. John S. Tsang
National Institutes of Health

Systems biology seeks to build quantitative predictive models of biological system behavior. Biological systems, such as the mammalian immune system, operate across multiple spatiotemporal scales with a myriad of molecular and cellular players. Thus, mechanistic, predictive models describing such systems need to address this multiscale nature. A general outstanding problem is to cope with the high-dimensional parameter space arising when building reasonably detailed models. Another challenge is to devise integrated frameworks incorporating behavioral characteristics manifested at various organizational levels seamlessly. In this dissertation, I present two research projects addressing problems in immunological, or biological systems in general, using quantitative mechanistic models and machine learning, touching on the aforementioned challenges in scalable modeling.

First, I aimed to understand how cell-to-cell heterogeneities are regulated through gene expression variations and their propagation at the single-cell level. To

better understand detailed gene regulatory circuit models with many parameters without analytical solutions, I developed a framework called MAchine learning of Parameter-Phenotype Analysis (MAPPA). MAPPA combines machine learning approaches and stochastic simulation methods to dissect the mapping between high-dimensional parameters and phenotypes. MAPPA elucidated regulatory features of stochastic gene-gene correlation phenotypes.

Next, I sought to quantitatively dissect immune homeostasis conferring tolerance to self-antigens and responsiveness to foreign antigens. Towards this goal, I built a series of models spanning from intracellular to organismal levels to describe the recurrent reciprocal relationships between self-reactive T cells and regulatory T cells in collaboration with an experimentalist. This effort elucidated critical immune parameters regulating the circuitry enabling the robust suppression of self-reactive T cells, followed by experimental validation. Moreover, by bridging these models across organizational scales, I derived a framework describing immune homeostasis as a dynamical equilibrium between self-activated T cells and regulatory T cells, typically operating well below thresholds that could result in clonal expansion and subsequent autoimmune diseases.

I start with an introduction with a perspective linking seemingly contradictory behaviors of the immune system at different scales: microscopic “noise” and macroscopic deterministic outcomes. By connecting these aspects in the adaptive immune system analogously with an ansatz from statistical physics, I introduced a view on how robust immune homeostasis ensues.

SCALABLE MODELING APPROACHES IN SYSTEMS IMMUNOLOGY

by

Kyemyung Park

Dissertation submitted to the Faculty of the Graduate School of the
University of Maryland, College Park, in partial fulfillment
of the requirements for the degree of
Doctor of Philosophy
2020

Advisory Committee:
  Professor Doron Levy, Chair
  Senior Investigator John S. Tsang
  Assistant Professor Philip Johnson
  Senior Investigator Ronald N. Germain
  Professor Sergei I. Sukharev, Dean's Representative

Dedication

To my beloved family, Woorim, Siyul, and Sionne.

To L. Boltzmann (1844 - 1906),

who kept inspiring me throughout hard transitions in my career path from physics, to medicine, to systems biology and immunology.

Acknowledgements

It has been a great pleasure being at the interface of physics, immunology, and computational biology, to name a few, together comprising systems biology/immunology. This would not have been possible without the academic freedom I have had throughout my PhD. My mentors have been indeed supportive throughout my journey. I would like to thank Dr. John Tsang for his continuous advice, support, patience, and encouragement throughout my stay in the Tsang lab. His endless curiosity and enthusiasm over science eventually shaped how I view nature and biology. The way he went through various fields in the past and finally arrived at immunology and the courage he showed in facing with new fields will always be the lessons I will keep for my future journey. I would like to thank Dr. Doron Levy for his continuous support and advice from choosing the lab all the way to completing the dissertation, even though I was away from the UMD campus. I would like to thank Dr. Sergei Sukharev for guiding me from the entry to the Biophysics program to the end of my PhD and especially for his kind understanding of my stay in NIH and my research interest not typical in biophysics. I would like to thank Dr. Philip Johnson for his generosity to serve in the dissertation committee and invaluable advice throughout my progress. Lastly, I would like to thank Dr. Ronald Germain for envisioning and creating the environment, LSB and now LISB, which I have dreamed of since I was a medical student, a refugee from physics, always nostalgic for where I am from. My naïve goal of finding connections between statistical physics and the immune system has transformed into more refined questions inspired by his earlier works and the collaboration with his group.

Also, I would like to thank other colleagues. I would like to thank Drs. Thorsten Prüstel, Manikadan Narayanan, Andrew Martins, and Yong Lu for guiding me over my initial projects. I would like to thank Dr. Harikesh Wong for the exciting collaboration during the later period of my PhD. I would like to thank Ms. Can Liu and Dr. John Kim for being together for another exciting project, although I could not contribute much due to my limited timeline. I would like to thank other lab members, Neha, Rachel, William, Candace, Dylan, Darius, Matt, Nick, Laura, Chris, Rohit, Richard, Yuri, Foo, and Pedro for active discussions and fun times. I will miss the teatime we had every Friday afternoon. I would like to thank Dr. Yong-Hee Kim in the Shevach lab. He has been my personal immunology teacher and role model pursuing basic science as an MD-PhD, which is a rare career path in Korea. I would like to thank Dr. Grégore Altan-Bonnet for pioneering a significant portion of the T cell model we built and providing us helpful advice and comments throughout the model development. I would like to thank Dr. Phil Hodgkin for inspirations and ideas smeared in this dissertation based on his earlier works and personal conversations with him at Cold Spring Harbor Laboratory and NIH.

Lastly, I would like to thank my family. I would like to thank my parents. They could not have higher education beyond elementary school due to the poverty caused by the devastating Korean war. Now, their son is having two doctoral degrees. I am deeply indebted to their sacrifice and grateful to them for opening the door for me to explore the world. I am now going back to stay with them. I would like to thank my grandmother-in-law and parents-in-law for their continued understanding and support over my pursuing PhD, even though their son-in-law has avoided the responsibility for their daughter. I will be a good son and husband once I go back. Lastly, I would like to thank my beloved wife, Woorim, who had to suffer all hardships on her own due to her husband’s lack of responsibility. I will not forget what you have gone through. I would like to thank my dear children, Siyul and Sionne, who always invigorate me. I apologize to my son, Siyul, for not being together on your 8th birthday this year, but I will be with you in the next year and forever.

Table of Contents

List of Tables

List of Figures

List of Abbreviations

Treg	regulatory T cell
MHC	Major Histocompatibility Complex
pMHC	peptide:MHC
SLO	Secondary Lymphoid Organ
DN	Double-Negative
DP	Double-Positive
TCR	T Cell Receptor
SP	Single-Positive
TdT	Terminal deoxynucleotidyl Transferase
CDR	Complementarity-Determining Region
TRA	Tissue-Restricted Antigen
mTEC	medullary Thymic Epithelial Cell
Aire	Autoimmune regulator protein
HEV	High Endothelial Venule
APC	Antigen Presenting Cell
OVA	ovalbumin
DAMP	Damage-Associated Molecular Pattern
Tconv	CD4$^+$ conventional T cells
cTregs	central Tregs
eTregs	effector Tregs
SOC	Self-Organized Criticality
GRN	Gene Regulatory Network
MAPPA	MAchine learning of Parameter-Phenotype Analysis
ML	Machine Learning
RF	Random Forests
PPM	Parameter-Phenotype Map
GVI	Global Variable Importance
LVI	Local Variable Importance
CME	Chemical Master Equation
PoV	Propagation of Variation
PPP	A *coherent* feedforward circuit motif
PNP	An *incoherent* feedforward circuit motif
FC	Fold-Change
QF	Quality Factor
PF	Peak Frequency
LC	Limit Cycle Oscillations
DO	Damped Oscillations
SS	Stable Steady States

Chapter 1: Introduction

Systems biology seeks to build quantitative predictive models of biological system behavior. Biological systems operate across multiple spatiotemporal scales: from molecules to the organismal level, and from milliseconds to days, and even to decades. A good example of such multiscale behavior is the immune system. A myriad of molecular and cellular players comprises the immune system. They operate throughout the body and interact with each other across space and time. Thus, building mechanistic, predictive models in the immune system needs to account for the multiscale nature of the system.

For my PhD dissertation, I have been addressing problems in immunology, or biological systems modeling in general, by building quantitative mechanistic models with a multiscale perspective. There are several challenges. A general problem in building models containing sufficiently realistic biological details is the large number of model parameters, which are often difficult to measure experimentally en mass. There is a tendency to oversimplify models in order to restrict the number of parameters, but useful models of biological systems often need higher levels of details and thus it can be challenging to reduce models to ones with a few parameters. How to cope with such high-dimensional parameter spaces effectively to build scalable yet detailed models has been an outstanding problem. Another issue in multiscale modeling is that different organizational levels may show different behavioral characteristics and putting them together seamlessly into a single modeling framework remained difficult. For example, dynamics of molecular species with low copy numbers at the subcellular level exhibit inevitable stochasticity due to thermodynamic noise while gross behaviors of physiological processes at the organismal level such as circadian rhythm is more subjected to deterministic regulations. Lastly, such modeling efforts have attracted skepticisms on how they can help to uncover meaningful or novel biology, which largely originated from successful reductionistic experimental molecular biology and biochemistry in the latter half of the 20th century. A successful approach to cope with this challenge has been finding recurrent regulatory/topological patterns out of complex biological interaction networks, often termed as "regulatory circuit motifs". Along similar lines, we may pursue recurrent behavioral patterns out of multiscale phenomena interlinked with feedback/feedforward interactions within/across scales in the immune system. We can first come up with a prototype model, the simplest giving rise to a particular behavioral pattern, followed by building context-dependent detailed models exhibiting such a behavior for specific cells or organs.

My dissertation consists of two major projects and one perspective chapter focusing on different scales of biological and immune systems that touch on the general challenges discussed above. First, I aimed to understand how single-cell heterogeneities are regulated through gene expression variations and their propagation at a single cell level. I used stochastic simulations in combination with machine learning approaches to better dissect high-dimensional parameter-phenotype mapping. I used this approach to analyze several recurrent network motifs with detailed models and found: 1) hysteretic gene-gene correlations induced by promoter switching, which was something that could not be explained by the existing analytical approximation scheme, 2) the wide tunability of gene-gene correlations enabled by the feedforward arm, and 3) oscillatory behaviors induced by a negative feedback loop operating in parameter regimes outside of those predicted by deterministic modeling.

The next major project was to quantitatively dissect immune homeostasis conferring tolerance to self-antigens and responsiveness to foreign antigens. I started with modeling of the early phase of T cell priming with the aim to quantitively dissect how the extent of T cell activation is determined through cellular interactions among conventional T cells, dendritic cells, and regulatory T cells, especially in the context of autoimmunity where the suppression of self-reactive T cells is important. Towards this goal, I used a multiscale modeling scheme to describe intracellular and intercellular dynamics using both ordinary differential equations and partial differential equations. In close collaboration with an experimentalist (Dr. Harikesh Wong), the model was tightly linked to lymph node imaging data and generated experimentally testable predictions. Next, I further incorporated additional regulatory layers of immune homeostasis: 1) quorum regulation of clonal expansion of self-activated T cells and 2) reciprocal regulatory relationships between self-activated T cells and regulatory T cells for determining their intranodal and organismal homeostatic population sizes. Combining models in different scales altogether, I derived an integrated quantitative framework assessing immune homeostasis as equilibrium between self-activated T cells and regulatory T cells, which is well below the threshold leading to clonal expansion that causes autoimmune diseases. Then, I explored several corollaries of this framework.

Finally, in the last, perspective chapter (that follows the current chapter), I argued how we can reconcile the contradicting behaviors of the immune system at different scales: microscopic randomness and macroscopic determinism. In particular, I illustrated how the adaptive immune system utilizes inevitable randomness at the molecular and cellular scales that give rise to predictable gross behaviors at the cell population and organismal levels. By borrowing an ansatz from statistical physics and contrasting with systems analyzed by statistical physics approaches, I proposed a framework to explain on how robust immune homeostasis can be achieved even though the immune systems can sometimes still go awry causing diseases. I concluded by suggesting future research directions.

Chapter 2: The immune system as a many-body system: linkage between microscopic randomness and macroscopic determinism

2.1 Background

A major challenge of the immune system is to cope with diversity and uncertainty of pathogen encounters (Murphy and Weaver, 2016). Since molecular and cellular immune machineries can also be dangerous to the host, they should remain quiescent in homeostasis, but react appropriately upon pathogen encounters (Germain, 2001). The immune response should be mounted timely, scale proportionally to the amount of threat burden, and contract quickly once the pathogenic threat has been cleared, followed by establishment of immune memory (Mayya and Dustin, 2016). The adaptive immune system is more specialized in mounting immune responses and establishing memory in an antigen-specific manner (Murphy and Weaver, 2016). Having antigen receptors specific to unique molecular patterns for each cell, adaptive immune cells such as T cells and B cells confer more sensitive and specific immune responses aided by clonal expansions and memory cell differentiations to efficiently deal with pathogen encounters.

This process possesses an inherent danger of responding to self, thereby potentially leading to autoimmune diseases (Theofilopoulos et al., 2017). The immune system has evolved myriad mechanisms of immune homeostasis, including the induction of self-tolerance, to mitigate such aberrant outcomes. In thymus, newly generated precursors of T cells undergo positive and negative selection, through which only thymocytes that recognize the self-peptide:major histocompatibility complex (self-pMHC) molecules above a certain affinity (positive selection), but not too strongly (negative selection) survive and move out to the periphery as naïve conventional T cells.[1] Those who recognize self-peptides too strongly are either removed or directed to become regulatory T cells (Tregs), which constitutes a key mechanism of "central tolerance". These Tregs play a crucial role through various modalities to ensure peripheral tolerance, suppressing the activation of naïve self-reactive T cells that escaped central tolerance in secondary lymphoid organs (SLOs) or effector functions of self-activated T cells in tissues.

An interesting aspect of adaptive immunity is that it seems to cast itself to and utilize randomness typical at the molecular and cellular levels to better deal with the uncertainty of pathogen encounters yet generates quite predictable gross behaviors in cell population and organismal levels. At first thought, this is rather counterintuitive in that reducing noise or randomness is beneficial for robust and predictable biological functions such as the kinetic proofreading mechanism in DNA replication processes (Hopfield, 1974) and refractory periods in action potential conductions in neurons or muscles (Purves et al., 2017). Indeed, there is already accumulated evidence that the adaptive immune system actually has evolved various mechanisms for filtering out noise to prevent aberrant immune responses (Wong and Germain, 2018). Another line of thought may take utilizing the randomness as a strategy. Since randomness can occur naturally in the microscopic world (molecular or cellular levels), reducing randomness

---

[1] TCRs recognize unique peptide sequences presented by the peptide-binding groove of MHCs on cell surfaces of other cells. There are mainly two classes MHCs, Class I MHC (MHC-I) and Class II MHC (MHC-II). MHC-I is expressed by all cell types and mainly presents endogenous self- or foreign antigens. MHC-II is expressed mainly by professional antigen-presenting cells (APCs) such dendritic cells, B cells, and macrophages and mainly presents self- or foreign antigens uptaken from the surrounding space or transferred by other APCs.

requires substantial resources that could have been otherwise utilized for biological functions if the organism can operate robustly in the presence of noise and could even exploit such randomness (Stoeger et al., 2016). In this chapter, we will argue, borrowing languages and concepts from statistical physics, that the latter is also likely the case for the adaptive immune system based on existing biological and immunological knowledge.

A rephrased fundamental question the adaptive immune system raises is how microscopic randomness gives rise to macroscopic determinism. More specifically, how does robust immune homeostasis, that is, being tolerant to self-antigens via central and peripheral tolerance while responsive to foreign antigens, emerge out of random processes of adaptive immunity at the time scale of decades? To consider this question in this chapter, first we will go through basic adaptive immunological processes conferring randomness. Then we will revisit a basic framework of statistical physics to consider how the connection between microscopic randomness and macroscopic determinism is possible and why it is robust. Finally, we will come back to the adaptive immune system and argue that the adaptive immune system indeed operates in a manner analogous to systems described by statistical physics to confer self/non-self discrimination, yet subject to fluctuations since it operates below the thermodynamic limit in terms of the numbers of constituent cells and molecules and the size of participating organs. Before we begin our main discussion from section 2.2, we will go over general notions related to the noise and size of biological systems at the microscopic scale in the following section (section 2.1.1).

2.1.1 Defining the parallel of the “thermodynamic limit” in biological systems

Biological systems consist of discrete entities such as macromolecules and cells. To realize biological functions, these entities interact, and their physical or biochemical states change over time. These processes inherently involve stochasticity, and the system is especially “noisy” at the microscopic scale, where low copy numbers of the constituent entities can render the random effects pronounced, e.g., in their abundances, states, or spatial movements. There are myriad examples in this regard. Stochastic gene expression at the single-cell level is one example: Elowitz and colleagues (Elowitz et al., 2002) utilized two reporter genes (cfp and yfp) regulated by identical promoters in E. coli. They showed that the expression variation of CFP and YFP across single cells was, in part, contributed by the inherent stochasticity of biochemical reactions of gene expression. Such stochasticity in gene expression was also observed in mammalian cells, particularly that arising from bursty transcription (Suter et al., 2011). Another example is bacterial chemotaxis involving directed movement guided by chemotactic molecules (Wadhams and Armitage, 2004). The challenge bacteria face is that their size is typically smaller than the average spacing of chemotactic molecules. To obtain maximal information on the concentration gradient of chemotactic molecules in the environment, bacteria evolved various strategies via their chemosensory signaling pathways. E. coli utilizes two modes of random motions (run and tumble) - they pick a direction for a run randomly, but biasedly based on the frequencies of their encounter with chemotactic molecules, thus leading to directional movements along with the concentration gradient of chemotactic molecules (Webre et al., 2003). The last example we consider here is the electrical noise in neurons (White et al., 2000). The variable electrical excitability of neurons can be attributed to random switching between open and close states of individual voltage-gated ion channels with the bias to either of these states based on the membrane potential. These examples illustrate noisy biological phenomena and a survival strategy to cope with noise at the microscopic scale.

However, these behaviors are somewhat different from what we experience in our daily lives. In systems with a large number of components, the microscopic noise tends to disappear due to the effect of averaging (in Statistics, this is called the "Law of Large Numbers"). In physics or chemistry, when the system reaches a sufficiently large size such that such fluctuations are averaged out, the system is termed as reaching the "thermodynamic limit". Mathematically, the concept of the thermodynamic limit is expressed as the limit when the system size (the numbers of constituent entities and the volume of the system) approaches infinity (or a macroscopic size) when the densities or concentrations of the constituent are fixed (Kampen, 2007; Pathria and Beale, 2011). In physics or chemistry, the Avogadro's number, 6.02×10^{23} is considered as a "practical" infinity, which is comparable in orders of magnitude to the numbers of molecules or atoms in typical objects we use daily such as a book. However, this notion is not directly applicable in biology involving living systems with intricate regulatory mechanisms operating under chemical non-equilibrium. Therefore, we need a more biological system-dependent definition of "how large is large."

Considering that biological systems at any scale can be modeled as a reaction system with multiple spatial compartments, the abundances of entities (molecules or cells) in the system can be described either by copy number (N; discrete number) or concentration (N/V; continuous number, V is the volume of a relevant compartment). A condition of size sufficiency is that adding/subtracting a single copy of a constituent species only affects the concentration negligibly. For example, let us consider two systems with the same concentration of a species, but with different sizes, to say, 3 particles in 1 cm^3 vs. 3000 in 1000 cm^3 with a concentration of 3 cm^{-3}. Adding a particle to both systems increase the concentrations by 33% for the former but by 0.03% for the latter. An additional condition is that the fluctuations of the abundances or fluxes out of discrete and probabilistic reaction events is negligible to the extent that they do not affect the phenotypic outcomes of the system. The estimation of fluctuations requires information on the average abundances of constituent species and rate parameters (or time scales) of relevant processes determining the abundances of the species. Biological negligibility depends on functions and needs to be evaluated in a context-dependent and, in some cases, qualitative manner. Throughout this chapter, if a system of interest does not meet the "largeness" conditions above, we will denote that the system is below (or less than) the "thermodynamic limit" following the terminology in physics and chemistry and provide quantitative and biological justifications if needed.

2.2 *Sources of randomness in the adaptive immune system*

2.2.1 Overview of T cell development with numbers

Lymphocytes originate from hematopoietic stem cells in the bone marrow. While B cells mature in the bone marrow, the progenitors of T cells migrate to the thymus. In the thymus, thymocytes (the precursors of T cells residing in the thymus) further expand and mature to become naïve T cells, finally exported to the periphery. Figure 2.1 illustrates the T cell development process with population sizes of different developmental stages and transition rates across stages in steady states (Krueger et al., 2017; Sawicka et al., 2014; Yates, 2014). The numbers introduced here are for young

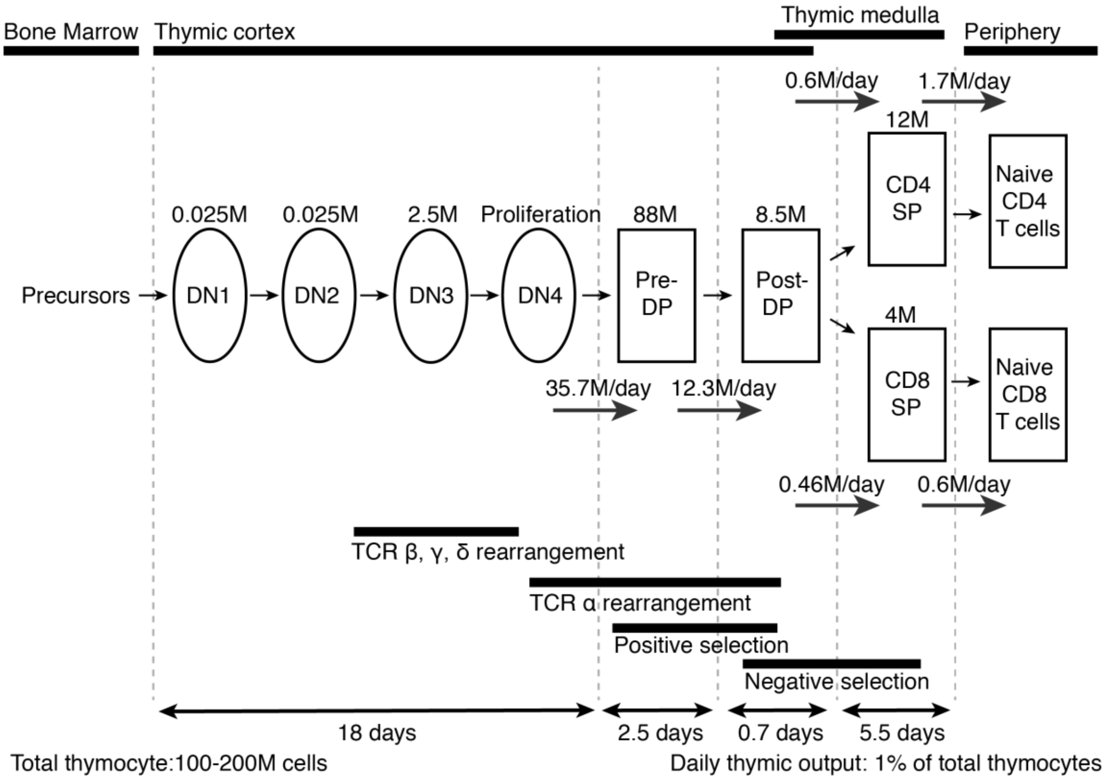

Figure 2.1 T cell development in the thymus with numbers in the young adult murine thymus. The numbers of cell populations are shown on the top of each population. The cell fluxes or transition rates are shown with arrows crossing developmental stages. DN: double-negative, DP: double-positive, SP: single-positive, M: 10^6 cells.

adult mice and median values of varying estimations across the literature. The thymocyte maturation processes are tightly linked to the spatial localization of thymocytes in the thymus. The thymus consists of the (outer) cortex and the (inner) medulla. The thymus-seeding progenitor cells enter the thymus through blood vessels in the corticomedullary junction. These progenitor cells receive Notch signal from thymic epithelial cells, resulting in the commitment to the T-cell lineage with the expression of CD2 and Thy-1.

The earliest stage of the T-cell lineage is the double negative (DN) population, which consists of DN1, DN2, DN3, and DN4 stages. The DN thymocytes lack cell-surface markers, including the CD3:T-cell receptor complex, CD4, and CD8 that define mature T cells. The name, 'double negative' came from the absence of both CD4 and CD8 in this population. The DN thymocytes reside in the cortex of the thymus, and their dwelling time at that stage is around 18 days. During this period, the number of the DN thymocytes expands from 25,000 (DN1) to 2,500,000 (DN3). The DN thymocytes initially express CD44, not CD25 (DN1) and begin to express CD25 as they mature (DN2). The thymocytes then downregulate CD44 (DN3). At the DN2 stage, rearrangement of the T cell receptor (TCR) β-chain (for the α:β thymocytes) or γ- and δ-chain (for the γ:δ thymocytes) loci begins, and it continues at the DN3 stage.[2] Once the functional TCR β-chain is formed and paired with a surrogate pre-T-cell receptor α-chain resulting in constitutive TCR signaling, thymocytes then reduce the expression of CD25 and move to the DN4 stage, where they proliferate and begin expressing both CD4 and CD8. Similarly, once the functional TCR γ- and δ-chain are

---

[2] The process of TCR gene rearrangements will be discussed in section 2.2.2.

formed, the resultant $\gamma{:}\delta$ thymocytes mature and migrate to the periphery as $\gamma{:}\delta$ T cells, residing in barrier tissues or lymphoid organs depending on the developmental stages of the host.

The resultant double-positive (DP; CD4$^+$CD8$^+$) (α:β) thymocytes do not further proliferate, arriving the population size of ~88,000,000 cells. They go through rearrangement of the TCR α-chain locus, finally producing α: β TCR for the duration of in average 2.5 days. Most of the cells with α: β TCR cannot signal in response to self-pMHCs, failing positive selection and thus being directed to apoptosis. The DP thymocytes that can recognize self-pMHCs with sufficient binding affinity to trigger pro-survival signaling pathways survive with a population size of ~8,500,000 cells and continue to mature for an additional 0.7 days. They start migrating to the thymic medulla and downregulate the expression of either CD8 or CD4, finally becoming single-positive (SP) thymocytes with the population sizes of 12,000,000 (CD4 SP) and 4,000,000 (CD8 SP) that together constitute only around 2% of the DP cells. This sharp reduction of the population size is due to negative selection. Thymocytes that survived positive selection undergo negative selection during or after the DP stage, in which only cells that cannot respond to self-pMHCs to trigger apoptotic signaling pathways survive. Finally, SP thymocytes mature to be naïve T cells for 5.5 days and emigrate to the periphery with the daily output of 1,000,000-2,000,000 naïve T cells, which is 1% of the total number of thymocytes.

Thus far, we briefly laid out the T cell development process with numbers for population sizes and cell fluxes (Figure 2.1). Note that the orders of magnitude of these numbers are likely less than the thermodynamic limit , suggesting that the T cell development process in terms of the population sizes of intermediate cell types and cell fluxes may suffer inevitable fluctuations out of random interactions among discrete entities (cells) in low abundance.[3] (Refs for the footnote: (Kampen, 2007; Pathria and Beale, 2011)). Not only for the gross cell population sizes, there are other sources of randomness shown in the following.

2.2.2 Generation of TCR repertoire

One of the remarkable features of adaptive immunity is the random generation of TCRs in individual T cells. This is a fundamental way for the immune system to address the uncertainty of pathogen encounters throughout the lifetime of individuals by casting itself to achieving the randomness.[4] Essentially, each T cell has a unique peptide sequence of TCR through random rearrangements of V, D (only in β-chain), and J gene segments of TCR gene loci together with random addition or deletion in junctions

---

[3] The thermodynamic limit is defined as the limit where the system size (the numbers of constituent entities and the volume of the system) goes to the infinity (or a macroscopic size) with fixed number densities of the constituent. Thermodynamic systems with the Avogadro's number of particles ($\sim 10^{23}$) and macroscopic volumes are considered as being in the thermodynamic limit, where the fluctuations of macroscopic quantities are negligible ($\sim 1/\sqrt{10^{23}} \approx 10^{-12}$) (Pathria and Beale, 2011). However, in reaction systems, the ratio between the flux and abundance of constituent entities determines the extent of fluctuations (Kampen, 2007). For example, the daily flux of the post-DP thymocytes that undergo negative selection is ~24.6M/day (Figure 2.1). The standard deviation of the daily fluctuation of the post-DP thymocyte population is roughly $\sqrt{24.6 \times 10^6} \approx 5000$. The relative fluctuation of the post-DP thymocyte abundance is 5000/8.5M = 0.0006, which may be considered as negligible. However, its effect on the downstream compartment can be significant. With the inferred rate of negative selection, 11.2/day (Figure 2.1), the daily fluctuation of negative selection is $5000 \times 11.2 \approx 55{,}000$/day. This comprises ~5% of the influx of the SP thymocyte population (~1.1M/day), indicating that the self-reactive repertoire size (4~10% of the peripheral TCR repertoire, section 2.4.1) is subject to significant fluctuations.

[4] There is a subtle issue regarding what "randomness" means. Sometimes, randomness is equated with a complete disorder or uniformity of chances over various possible outcomes. However, mathematically speaking, randomness involves associated probability distributions over possible outcomes, which are not necessarily uniform (or flat). Some outcomes may possess higher chances of realization, while other outcomes may possess negligible chances of realization, reducing the effective number of possible outcomes. Therefore, the outcome of each individual random event is unpredictable, yet the distribution of outcomes derived from multiple events can show predictable and conceivable patterns, such as overrepresentation of a particular outcome over other possible outcomes or the reduced number of realized outcomes compared to the theoretical possibility.

(Murphy and Weaver, 2016). This process enables each T cell to recognize potentially distinct pMHC molecules. For TCRs, three complementarity-determining regions (CDRs; CDR1, CDR2, and CDR3) mainly determine the affinity towards pMHCs. CDR1 and CDR2 are germline-encoded uniquely across the V segments of α- and β-chain and contact the MHC components of pMHCs. Most variations of TCRs come from CDR3 that is formed in junctions of V, (D,) and J segments and contact the unique antigenic peptide presented on the peptide-binding groove of MHCs. A current estimate of the (post-selection) TCR repertoire (the sum of all unique TCRs in the host) size is ~10^{10} for humans and ~10^7 for mice (Altan-Bonnet et al., 2019; Lythe et al., 2016).[5] (Refs for the footnote: Davis and Bjorkman, 1988; Quigley et al., 2010; Turner et al., 2006; Venturi et al., 2008)) This TCR diversity enables the immune system to react against almost limitless yet unknown pathogens.

2.2.3 Positive and negative selection

Having a randomly generated (pre-selection) TCR repertoire carries a burden of generating TCRs mostly not meeting the functional requirements of both adapting to the MHC alleles of the host and being non-functional against self-antigens. Thus, once

---

[5] The existence of the public repertoire shared by multiple individuals indicated convergent recombination of TCR loci that was confirmed experimentally. This biased recombination of V, (D,) and J gene segments reduces the diversity of TCRs from theoretical estimation (~10^{15}-10^{16} in mice). Moreover, the shared β-chains by multiple TCR clones due to massive proliferation of thymocytes at the DN4 stage after the β-chain recombination further reduce the TCR diversity. For neonates, the lack of terminal deoxynucleotidyl transferase (TdT) and the resultant lack of N additions lead to the utilization of only the germline-encoded V, (D,) and J segments, greatly reducing the TCR diversity (Davis and Bjorkman, 1988; Quigley et al., 2010; Turner et al., 2006; Venturi et al., 2008). However, such biasedness of TCR recombination and reduced diversity of TCRs do not contradict with the notion, randomness embedded in the processes of the TCR generation since we still cannot predict the outcome of TCR gene rearranements in each T cell. Such inherent mechanisms of reducing the TCR diversity leading to predictable TCR repertoires such as public repertoires is in line with our main argument in this chapter, which will be put forward in section 2.4. (Davis and Bjorkman, 1988; Quigley et al., 2010; Turner et al., 2006; Venturi et al., 2008).

DP thymocytes are generated after the rearrangement of TCR gene segments, they go through a two-step selection process: positive selection and negative selection. In positive selection, the T cells should recognize self-pMHC molecules presented by stromal cells of thymic cortex to the strength above a certain threshold to survive. Then, the survived T cells migrate to thymic medulla and go through negative selection invoking central tolerance, where only T cells that recognize self-peptide MHC molecules presented by stromal cells of thymic medulla not too strongly survive and eventually become mature single positive naïve T cells.[6] A small fraction of T cells that recognize self-pMHC strongly become regulatory T cells (Tregs) (comprising ~6% of the thymic out of naïve CD4 T cells) that play a major role in enforcing peripheral tolerance, but a majority of T cells that recognize self-peptide above a certain threshold go through apoptosis.

These processes have stochastic components. Presentation of self-peptides by stromal cells (thymic epithelial cells and thymic dendritic cells) and encounter of specific self-peptides by specific immature T cells for positive and negative selection can be "noisy" processes. For example, a T cell with TCR potentially binding a certain self-pMHC strong enough to survive positive selections may not be lucky enough to actually encounter such a self-pMHC molecule in the thymic cortex, thereby directed into apoptosis. Another scenario prone to more stochasticity with potential phenotypic outcomes is that a thymocyte that survived through positive selection but has a potential of strong self-recognition for a self-peptide may not actually encounter such a self-

---

[6] Negative selection against ubiquitous self-antigens (the types of self-antigens are more discussed below in this section) can begins when the DP thymocytes are still in the cortex after positive selection (Klein et al., 2019).

antigen in the thymic medulla, thereby surviving through negative selection and migrating to the periphery with high self-reactivity. This is due to the limited extent and abundance of self-antigen presentation at the individual stromal cell level in the thymus (Klein et al., 2019). Self-antigens presented in the thymus for negative selection can be divided into ubiquitous antigens and tissue-restricted antigens (TRAs). The former are expressed by all cell types including thymic stromal cells, and the latter are expressed in certain tissues and ectopically expressed in medullary thymic epithelial cells (mTECs) under control of a transcription factor, Autoimmune regulator protein (Aire) inducing promiscuous expression of TRAs. Although as a bulk, mTECs can express more than 85% of protein coding genes, the mRNA expression of a certain TRA is restricted to only 1-3% of mTECs, indicating stochastic nature of TRA expression in mTECs (Brennecke et al., 2015; Klein et al., 2019; Meredith et al., 2015).[7] Therefore, whereas thymocytes specific to ubiquitous self-antigens are almost certainly deleted, those specific to TRAs are subject to stochasticity of encountering stromal cells presenting cognate pMHCs, conferring an inevitable leakage of self-specific conventional T cells to the periphery (Hassler et al., 2019; Legoux et al., 2015; Malhotra et al., 2016; Zhang et al., 2020).[8] (Refs for the footnote: Le Borgne et al., 2009).

---

[7] (Brennecke et al., 2015; Meredith et al., 2015) reported that Aire-regulated TRA genes showed coordinated expression in each mTEC. The combinations of co-expressed genes seem to be encoded each mTEC. Single mTECs was clustered based on co-expression patterns. Authors suggested that this might be due to epigenetic "bookmarking" at the progenitor epithelial cell stage that is shared by the daughter cells. Therefore, the stochasticity seems to be embedded in the "bookmarking" process.

[8] This depends on how long a thymocyte stays in the medulla and how many stromal cells it encounters. (Le Borgne et al., 2019) estimated that a medullary thymocyte may interacts with at most around 500 stromal cells. If we assume that a thymocyte can scans 2% of self-antigens during each encounter (Klein et al., 2019), a simple *in silico* bootstrap experiment (data not shown) suggests that the numbers of encounters below 300 lead to sizeable frequencies (above 1%) of naïve T cells being self-reactive.

2.2.4 Trafficking through secondary lymphoid organs and encounter of cognate antigens

Once fully matured, naïve T cells migrate from thymus to the periphery. They transit through secondary lymphoid organs (SLOs) such as spleen and lymph nodes randomly. T cells enters lymph nodes through specialized blood vessels named high endothelial venules (HEVs) and are mainly located in the paracortical areas, also known as T-cell zones, where they search for and encounter antigen presenting cells (APCs), especially dendritic cells (DCs) bearing cognate antigens. DCs are abundant in barrier tissue sites such as the skin, intestine, and lung and also exist in solid organs. They actively uptake foreign- and self-origin antigens and migrate to the draining lymph nodes that are directly connected with the residing local tissue sites via the lymph vessels, and they preferentially reside in the paracortical areas as naïve T cells do. The encounter between rare precursor naïve T cells (0.1-10 per million naïve $CD4^+$ T cells in mice) and APCs with cognate antigens is in principle probabilistic (Hayes et al., 2019; Jenkins and Moon, 2012; Lee et al., 2012). Together, naïve T cells and APCs play hide-and-seek for opportunistic encounter between right pairs of TCRs and pMHC molecules.

2.2.5 Quorum regulation of initiation of clonal expansion

The fundamental paradigm of the adaptive immunity is based on clonal expansion of a small population of precursor T or B cells recognizing cognate antigens to generate a large population of effector cells to clear pathogens. For this, T cells require three signals, 1) TCR signal perceived via antigens, 2) CD28 stimulation via costimulatory ligands delivered by APCs, and 3) cytokine signals delivered in a para-/autocrine manner (e.g., IL-2 received by IL-2 receptors (IL-2Rs); CD25 (or IL-2 receptor a chain (IL2-Ra)) is a high affinity subunit of IL-2Rs, mainly determining the responsiveness of T cells towards IL-2.), which are integrated to determine, for example, the duration of proliferation and therefore should be sustained for around 5 days to allow > ~10 rounds of cell division corresponding to > ~1000 fold increase of the population size of cognate cells (Heinzel et al., 2017; Marchingo et al., 2014).[9] However, a complete picture of how such rare precursor lymphocytes primed by cognate antigens transition to clonal expansion still remained blurry. In vitro or in vivo experiments studying lymphocyte population growth upon activation usually use the unphysiological number of antigen-specific seeding cells. For example, to investigate how the response size is determined via the antigen amount (Fuhrmann et al., 2016), ~10^6 ovalbumin (OVA) specific naïve TCR-transgenic CD4$^+$ T cells were transferred per mouse to study their IL-2 secretion pattern after immune responses. This number corresponds to the frequency of 1 per 25 naïve CD4$^+$ T cells in a mouse, which is substantially above the physiologic frequency of naïve CD4$^+$ T cells specific to an antigen, which is typically in the range of 0.1-10 per million naïve CD4$^+$ T cells (Jenkins and Moon, 2012).

A multitude of experimental evidence suggest that initial priming of T cells by antigen presenting cells (APCs) sustain activating signals for around 48 hours (Bohineust et al., 2018) whereas a typical duration of clonal expansion of responding

---

[9] (Heinzel et al., 2017; Marchingo et al., 2014) suggested that each precursor T cell chooses different proliferation parameters such as the time to first division and the interval between subsequent divisions from their distributions. Thus, some clones may divide much faster than other clones. The distribution of the interval between subsequent divisions has a peak at around at 10 hours. With 10 hours per division, 5 days including the time to first division (~36 hours) are required to allow 10 rounds of divisions in average, yet subject to clone-to-clone variations.

T cells is around 5 days. This discrepancy of durations indicates that recently activated T cells require further activating signals from sources other than APCs to support the ongoing clonal expansion, and it is likely that those signals are mediated by IL-2 from neighboring activating and IL-2-secreting T cells to sustain proliferation and differentiation and suppress the apoptosis machinery (Butler et al., 2013; Marchingo et al., 2014). Therefore, the proximity between recently activated T cells and other activating T cells secreting IL-2 is subject to randomness in that it requires some luck for other activating T cells to happen to be located in the vicinity of activated T cells that need further boosting signals.

2.2.6 Ubiquitous intracellular and molecular heterogeneities

The most fundamental layer of randomness underlying the processes mentioned above are intracellular and molecular heterogeneities, which can be roughly divided into biochemical and physical layers. Regarding the biochemical layer, intracellular molecular species undergo biochemical reactions such as synthesizing and degrading mRNAs and proteins or signaling cascades triggered by receptor-ligand binding. Typically, the abundances of distinct mRNA and protein species do not exceed 10^5 and 10^8, respectively (Milo and Phillips, 2015; Schwanhäusser et al., 2011). Moreover, gene alleles exist in two copies. These numbers are below the thermodynamic limit, making fluctuations due to random motions and collisions for chemical reactions pronounced. Therefore, there exist inevitable variations in the abundances of molecular species and resultant various phenotypic aspects across cells at a snapshot or over a time course in single cells (Raj and van Oudenaarden, 2008). For example, variations in the expression levels of TCR and intermediate species of TCR signaling pathways may put each T cell in different states of responsiveness to antigen. One phenotype subject to these variations is differential IL-2 secretion dynamics due to differential TCR signals after antigen priming across each T cell even within a clonal population (Feinerman et al., 2008). This may impact the fate of thymocytes or effector T cells via differential IL-2 signaling (DiToro et al., 2018; Klein et al., 2019). The stochastic expression of TRAs by mTECs is another example in that it contributes to randomness of TCR:pMHC interactions between the SP thymocytes and mTECs in negative selection, explained above.

The physical layer of randomness can be exemplified with the physical interactions within/between molecules such as ligands and receptors or the conformational changes of macromolecules mediated by electric forces at the molecular/atomic level. The free energy related to molecular binding or conformations is directly translated into a probability as $\exp(-\frac{\Delta G}{k_B T})$, where ΔG is the difference in free energy, k_B is the Boltzmann constant, and T is temperature. This predicts the existence of inevitable fluctuations deviating from most probable states, such as nonspecific binding of TCRs and pMHC molecules, which has been linked to functional tonic TCR signals (Myers et al., 2017). If free energy is similar among different molecular states, the choice over plausible states can occur with comparable chances, which seems to be relevant to TCR repertoire generation via TCR gene loci rearrangements with biased pairing between segments.

2.2.7 Summary

Thus far, we have laid out briefly the sources of randomness in the adaptive immunity from the generation of TCR repertoire to the initiation of clonal expansions as well as the underlying intracellular and molecular heterogeneity. The underlying causes of randomness are three-fold: 1) thermal behavior at the molecular level - the temperature and energy gap between the states determine the extent of variation, 2) Poisson-type processes at the molecular, cellular, or higher levels - that are described with phenomenological rate constants not based on obvious physics, where the rate constants and the abundance of discrete entities together determine the extent of the variation, and 3) Cross-scale origin – the TCR repertoire is generated essentially at the molecular level via the rearrangement of TCR gene loci that can be described with thermodynamic consideration, yet manifests across cells and cell populations.[10] Such randomness may be regarded as being too overwhelming for the adaptive immune system to function robustly (i.e., being responsive to foreign antigens while being tolerant to self) even with regulation and control. Nevertheless, based on our experiences and existing data, it is evident that our immune system generally performs well at the time scale of decades, yet can be subjected to pathologic behaviors such as various autoimmune diseases. Therefore, understanding how such randomness at the molecular and cellular levels gives rise to the deterministic behaviors of robust immune response at the cell-population and organismal levels is crucial to address questions

---

[10] The cross-scale origin of randomness in the immune repertoire generation seems to be a unique feature of the immune system. This is the fundamental challenge the immune system has to deal with since the law of large numbers does not apply here in a manner that it does for Poisson-type processes (section 2.1.1). The main argument of this chapter (to put it another way from the main text) is to show that the law of large numbers applies at the repertoire level, thereby leading to deterministic immune parameters at the cell population level.

such as: 1) how is relatively robust self/non-self discrimination or immune homeostasis established out of such randomness?, 2) what is the probability that this breaks down to cause autoimmune diseases or cancer?, 3) how can we manipulate the system judiciously to reestablish or modulate immune homeostasis? Interweaving and transforming the catalogue of numerous parts involved in immune homeostasis into a multiscale integrated framework can be hinted from the establishment of statistical physics in the 19th century, the first moment of the linkage of microscopic randomness and macroscopic determinism.

2.3 Analogy from statistical physics

Physics of the 19th century prepared great leaps that would happen in the 20th century. Back then, the Newtonian mechanics had been established firmly and classical thermodynamics was being developed rapidly. While the majority of people in physical sciences were foreseeing completion of physics in the near future being satisfied with the contemporary physics, a few physicists were tackling a challenging problem: derivation macroscopic thermodynamics out of Newtonian mechanics on microscopic entities, atoms and molecules. (Note that even until the early 20th century, the existence of atoms and molecules was considered merely as a hypothetical and convenient concept to explain physical and chemical phenomena.) Ludwig Boltzmann was the main figure in this endeavor.

To understand how Boltzmann was able to establish the connection between microscopic and macroscopic worlds, let us consider an example (Figure 2.2A). Suppose there is a box filled with ideal and noninteracting gas. Macroscopically, we

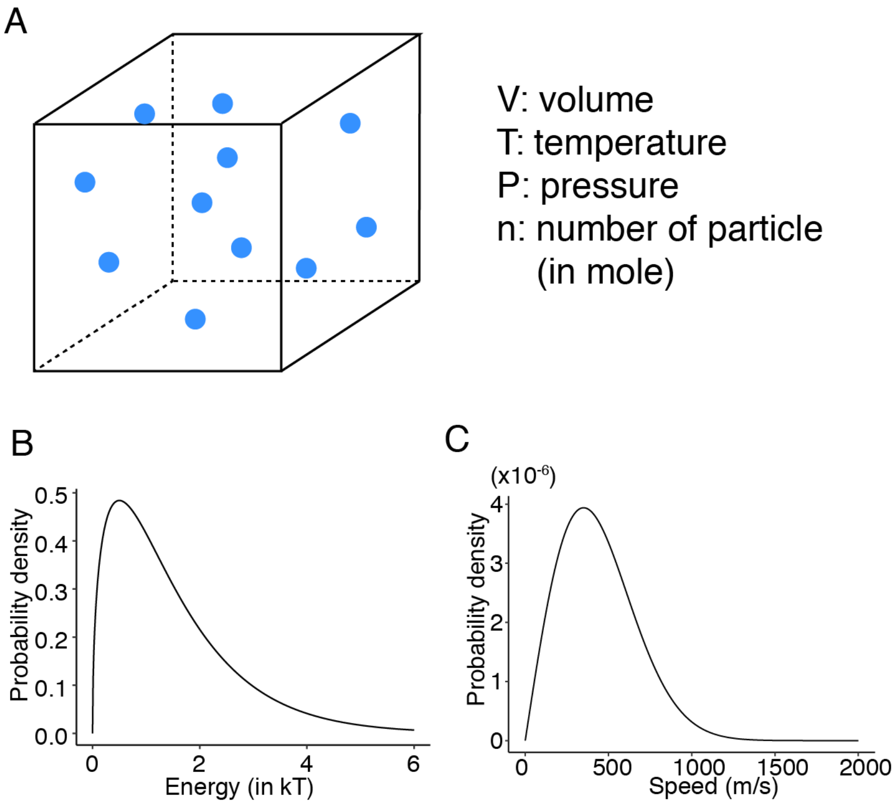

Figure 2.2 A system with ideal gas. (A) Introduction of relevant quantities. (B) Maxwell-Boltzmann distribution of kinetic energy of molecules. (C) Maxwell-Boltzmann distribution of speed of molecules with the mass of Neon and at the temperature, 278.15 K.

can measure quantities such as pressure (P), temperature (T), and volume (V). In thermodynamics, these quantities are related as so called the equation of states of ideal gas:

$$PV = nRT, \tag{2.1}$$

where n is the number of gas molecules in mole and R is the gas constant. Boltzmann wanted to derive this relationship out of microscopic random motions and collisions of molecules. However, one can realize that writing and solving equations of motion for about the order of 10^{23} particles with the specified initial positions and velocities of each molecule is essentially impossible (even with the modern computational power). Rather, he pursued a probabilistic or statistical approach. Let E be the total energy of the gas, the sum of kinetic energy of each individual molecule and N be the total number of molecules comprising the gas. Under the constraint of conservation of total energy and the number of molecules, we can count the number of ways (W) of distributing molecules to microstates with energy ϵ. Then, the maximization of W corresponding to the equilibrium or most probable macrostate of the gas gives rise to the probability distribution, $P(\epsilon)$ of molecules for being at microstates with energy ϵ (Figure 2.2B). Macroscopic (or thermodynamic) quantities and relationships among them were then derived from various statistical quantities of $P(\epsilon)$. Such quantities are not restricted to the mean or variation, but may include various aspects such as the tail of the distribution (Pathria and Beale, 2011).

The lesson we want to derive here is not the detailed mathematical treatments applied to a specific system (e.g., ideal gas) of statistical physics but the way the microscopic variables were linked to macroscopic variables. Although the individual molecules are subject to random dynamics in terms of collisions and resultant scattering angles of colliding molecules, the derived probability distribution, $P(\epsilon)$ itself is deterministic under the constraints of conservation of total energy and the total number of molecules. Thus, thermodynamic quantities as being statistical quantities derived from $P(\epsilon)$ are also deterministic. In other words, while we cannot predict the motion of individual molecules in terms of velocities or positions at a specific time point, we can predict the portion of molecules within a certain range of velocity or location (Figure 2.2C). Together, the individual level randomness transforms to the population level determinism provided with the (deterministic) population-level distributions shaped by constraints imposed on the system.

Note that the population level determinism is not necessarily through averaging and buffering the individual level fluctuations, but such randomness itself can contribute deterministic quantities at the population level.[11] For example, the shape of the energy distribution of gas molecules does not become narrower even though the systems size (V and N) increases. The macroscopic rate constants of chemical reactions are typically dependent on fractions of chemical species above certain energy thresholds (termed as activation energy) in the corresponding energy distributions (i.e., the tail of the distributions), and these fractions are deterministic quantities derived from the distributions. As we shall see below, the outliers in the distribution play a significant role for achieving immune homeostasis.

Thus far, we briefly surveyed how statistical physics was able to link the random microscopic world to the deterministic macroscopic world by changing the perspective from tracking random behaviors of all individual microscopic entities to deriving population level well-defined distributions of microscopic behaviors and statistical quantities out of such distributions that are eventually connected to macroscopic deterministic quantities. Additionally, constraints imposed on the system such as conservation laws in closed systems and entropy maximization in general including open systems enabled the derivation of well-defined distributions and determined the shapes of them.[12] (Refs for the footnote: (Dixit et al., 2018)) This is the ansatz that we borrow from statistical physics to better understand the adaptive

---

[11] More precisely, this is dependent on the source of randomness (section 2.2.7) and the macroscopic quantities of interest.

[12] Although our example is from an equilibrium system, non-equilibrium systems can be dealt with in a similar manner by deriving relevant probability distributions through maximization of "generalized" entropy with physical constraints (Dixit et al., 2018).

immunity, which deliberately exploits randomness to give rise to robust immune homeostasis, yet subject to fluctuations causing diseases since the size of the immune system (e.g., the number of cells and the sizes of the lymphoid organs) is below the thermodynamic limit.[13]

2.4 Back to the adaptive immune system: probabilistic molecules and cells giving rise to predictable behaviors

The quest of the adaptive immune system exploiting randomness for its robust self/non-self discrimination can be accomplished if such randomness of individual molecules and cells translates to well-defined probability distributions of relevant behavioral/phenotypic aspects. The delicate regulatory and controlling machineries on molecules and cells for immune homeostasis through intertwined interactions across multiple organizational levels play their roles in modulating the shape and location of probability distributions in the corresponding phenotypic space in a static and/or dynamical manner.[14] Our strategy here is to show that probability distributions derived throughout multiple processes eventually give rise to deterministic quantities, especially fractions in certain phenotypic intervals (e.g., tail portions) out of corresponding distributions such as the frequency of self-activated T cells and

---

[13] We will come back to this topic in more detail in section 2.4.4.

[14] Unlike physical constraints such as energy/mass conservation and entropy maximization in the ideal gas example in section 2.3, these biological regulations were shaped throughout the evolution under non-equilibrium conditions (the life). Moreover, whereas the physical constraints are imposed to the system externally, the biological regulations operate internally through interactions between the constituent entities of the system in non-equilibrium. Therefore, the practical implementation of the ansatz in describing the adaptive immune system requires different approaches from those of the ideal gas example in section 2.3 and may call for a new formalism that can encompass these aspects of the biological regulations.

pSTAT5$^+$ Tregs, which eventually participate in recurrent reciprocal regulations across scales to confer robust self-tolerance and foreign-directed responses in an almost all-or-none manner.[15] (Refs for the footnote: (Flajnik and Kasahara, 2010; Redmond et al., 2018))

2.4.1 From TCR repertoire generation to thymic selection

The (partially) deterministic TCR repertoire generated by biased random TCR rearrangements goes through thymic selection.[16] The net effects of thymic selection are to sort these unique TCRs in terms of their affinity (or avidity or functional reactivity (from the catch bond mechanism)) to self-pMHC molecules, which results in a probability distribution of unique TCRs over the affinity toward the self-pMHC molecules in thymus. Then, thymic selection trims the distribution to the shape we observe experimentally in the periphery (Figure 2.3). While individual encounters between TCRs and relevant self-pMHC molecules are stochastic and thus unpredictable, the probability distribution of the affinity the TCR repertoire exhibits upon random encounters of self-antigens can be deterministic and robust regardless of the detailed kinetic behaviors of relevant molecules and cells based on: 1) the central

---

[15] A related interesting question is how and when Tregs evolved. As we shall see in the following sections, the adaptive immune system allows the inevitable leakage of the self-reactive repertoire to the periphery, and Tregs counter it in the periphery. This suggests that Tregs should have evolved around the same time when the adaptive immunity evolved in jawed vertebrates around 500 million years ago (Flajnik and Kasahara, 2010; Redmond et al., 2018).

[16] As we discussed in detail in footnotes 4 and 5, the biased random molecular rearrangements of TCR gene loci give rise to (partially) deterministic TCR repertoires, which are shared in part among different individuals in the same species. The evolution might have optimized the process to ensure that the distribution of TCR specificities by biased random arrangements cover a wide range of possible antigens, but the distribution itself need to be deterministic enough for functional realization in each individual (~10^7 for mice) out of the enormous theoretical possibility (~10^{15} for mice). The preadaptation of germline-encoded CDR1 and CDR2 of TCRs to MHC alleles may play an important role in this regard as we will discuss further in footnotes 17 and 22.

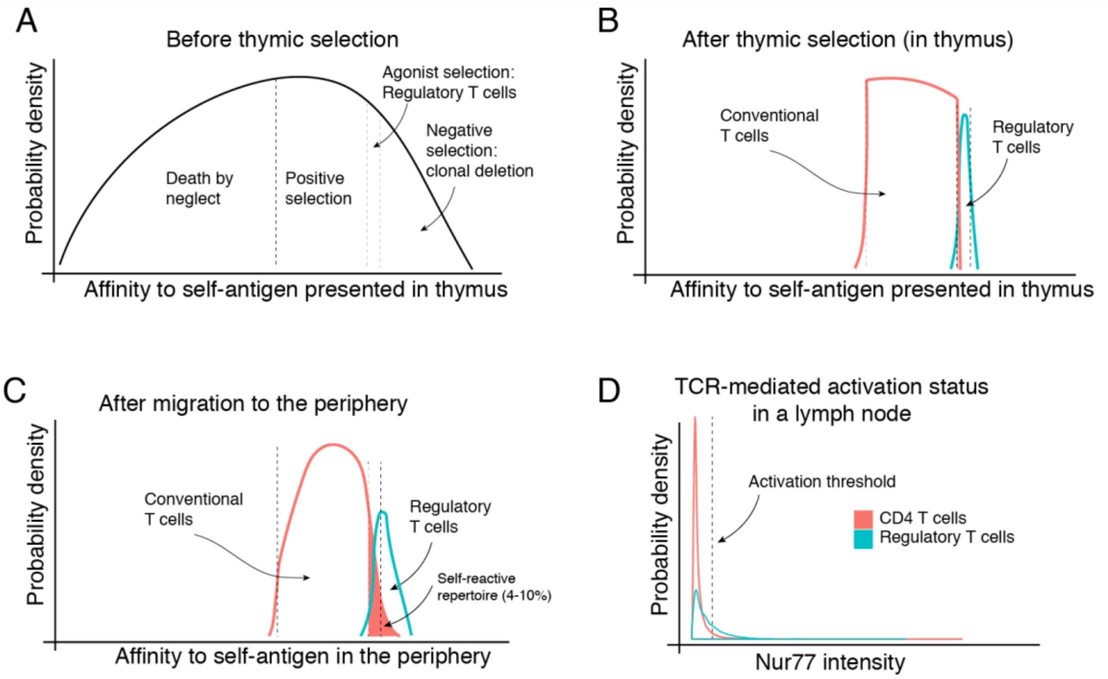

Figure 2.3 Schematic distributions of TCR affinity to self-antigen and TCR-mediated activation status. (A) Distribution of TCR affinity to self-antigen presented in thymus before selection. (B) Distribution of TCR affinity to self-antigen presented in thymus after selection. (C) Distribution of naïve TCR affinity to self-antigen in presented in the periphery. (D) Distribution of TCR-mediated activation status in a lymph node. An example of Nur77 intensity is shown (unpublished data from Dr. Harikesh Wong).

limit theorem in terms of the distribution of affinity a unique TCR potentially experiences for each self-pMHC molecule presented in the thymus and 2) the extreme value theory in terms of the strongest affinity a TCR experiences out of multiple encounters in thymus, based upon which positive and negative selection occur (Butler et al., 2013; Košmrlj et al., 2009) (Figure 2.3A).[17] (Refs for the footnote: Krovi et al., 2019). Eventually thymic selection removes T cells with TCR with affinity less than a threshold of positive selection or greater than a threshold of negative selection by deterministic fractions (75-80% of the DP thymocytes for the positive selection and 50-

---

[17] The shape of the probability density in Figure 2.3A is likely to be correct only if the preselection germline-encoded TCRs are inherently adapted to MHCs. If not, the majority of TCRs may reside in the region of death-by-neglect, showing an extremely right-skewed distribution. A recent study (Krovi et al. 2019) suggested that the former is likely the case, in that the preselection TCRs have biased affinity to pMHC.

80% of the positively selected population for the negative selection) (Altan-Bonnet et al., 2019; Krueger et al., 2017) (Figure 2.3B). Additionally, a small portion of CD4 T cells recognizing self-antigens strongly but not too strongly differentiate into Tregs comprising a deterministic fraction, about 6% of thymic output of Naïve CD4 T cells (Figure 2.3A-B). Together, despite the random nature of the TCR repertoire generation and thymic selection, the affinity distribution of the repertoire and the fraction of surviving cells and their fate choices are close to deterministic.

As we briefly mentioned in section 2.2.3**,** negative selection is not perfect in that it cannot remove all potential self-reactive T cells. The extent of the failure of negative selection is dependent on antigen presentation patterns distinct for ubiquitous antigens and TRAs in the thymus. The sporadic presentation of TRAs and the limited dwell time of thymocytes in the thymic medulla make each SP thymocyte tests only a fraction (1-10%) of the entire self-pMHC repertoire present in the periphery (Altan-Bonnet et al., 2019). This leads to the inevitable chance that a sizeable population of self-reactive T cells exists in the periphery, which has been revealed experimentally (Richards et al., 2015; Yu et al., 2015) (Figure 2.3C). Recent studies using knock-in or natural expression of ubiquitous and tissue-restricted self-antigens in the thymic medulla revealed that self-reactive SP thymocytes specific to a self-antigen choose their fates between clonal deletion, diversion to Tregs, and survival as naïve conventional T cells in distinct proportions based on expression patterns of their cognate self-antigens (whether ubiquitous or tissue-restricted, and whether under control of strong or weak promoter for TRAs) in the thymic epithelial cells (Hassler et al., 2019; Legoux et al., 2015; Malhotra et al., 2016; Zhang et al., 2020).[18] Depending on the abundance of self-antigens in thymic selection, two extreme outcomes are possible, which is either a complete clonal deletion or ignorance. In the former case, the abundant expression of ubiquitous self-antigens lead to deletion of the majority of antigen-specific thymocytes since the thymocytes can encounter such antigen even in the thymic cortex. In the latter, the near absence of antigen expression in the thymic medulla leads to near complete survival of self-reactive thymocytes. A subtlety comes in TRAs that are expressed in only a small fraction of mTECs at any given moment. In this condition, clonal deletion plays only a partial role, and a significant fraction of the SP thymocytes specific to the given TRA survive and emigrate to the periphery as naïve T cells. Of those who survived, another significant fraction is diverted to Tregs. Although quite variable, the numbers of Tregs and self-reactive conventional CD4$^+$ T cells specific to a TRA in SLOs seems to be comparable to each other in orders of magnitude while the number of Tregs were an order of magnitude smaller than that of CD4$^+$ T cells for antigens inducing complete deletion or ignorance (Hassler et al., 2019; Legoux et al., 2015; Malhotra et al., 2016; Zhang et al., 2020). Regarding this, the detailed processes of negative selection may ensue predictable fate decisions into deletion, diversion, and survival for the SP cells specific to a self-antigen despite the stochasticity involved. The IL-2 niche generated by self-activated SP cells in the thymic medulla is likely to play an important role in determining antigen-specific Treg pool sizes (Hemmers et al., 2019; Klein et al., 2019). Quantitative modeling approaches describing negative

---

[18] Note that the tetramer assay (the main experimental method in the cited studies) can detect TCRs that do not signal when bound to the corresponding pMHC molecules. Therefore, there may be a tendency to overestimate the frequency of T cell specific to a certain self-antigen using this assay.

selection may help link multiple parameters such as TCR affinity to self-antigens, precursor frequency of cognate cells, and expression patterns of self-antigen to the deterministic fate decision probability at the level of clones specific to an antigen. Finally, these individual clones of "escapee" self-reactive conventional T cells comprises 4-10% of the CD4 conventional T cell pool in the periphery (Figure 2.3C) (Amado et al., 2013; Kim et al., 2007; Richards et al., 2015). This cohort is 'invisible' in homoeostasis, remaining quiescent due to the Treg suppression, yet retaining capability of self-antigen recognition and becomes 'visible' with signs of activation upon rapid depletion of Tregs (Amado et al., 2013; Kim et al., 2007; Richards et al., 2015). Taken together, the affinity distribution of TCR repertoire relatively sharply demarcated after thymic selection becomes "leaky" in the periphery since the repertoire now tests against the entire set of self-peptides not exhaustively covered in negative selection (Figure 2.3A-C). Such leakiness in negative selection seems to be determined predictably at the antigen-specific population level and the entire repertoire level.

2.4.2 From the invisible distribution of affinity toward self in the periphery to the establishment of homeostasis

It has been revealed that self-reactive naïve T cells in the periphery eventually get activated in SLOs by cognate self-antigens, secrete IL-2, undergo brief proliferation, and get pruned out due to suppressive regulation by Tregs and intracellular apoptosis machineries (Liu et al., 2015; Wong et al., submitted). In the population level, around 1-2% of CD4$^+$ T cells show signs of ongoing activation by TCR signals such as IL-2 secretion and Nur77 expression in homeostasis under the existence of Tregs comprising 10-15% of CD4$^+$ T cells in SLOs (Amado et al., 2013; Liu et al., 2015; Richards et al., 2015; Wong et al., submitted). The fraction of activated CD4$^+$ T cells increases with rapid depletion of Treg population size or reduced Treg function up to 4-10% (as mentioned in the previous section), from which we can infer the original population size of invisible self-reactive T cells that survived thymic negative selection. Together, the affinity distribution of the peripheral TCR repertoire toward self-pMHC molecules including an invisible cohort (4-10% of T cells) of self-reactive cells is further molded by regulatory T cells and eventually manifest as a TCR-mediated activation distribution in SLOs with 1-2% of T cells in the tail portion of the distribution being activated yet constrained in homeostasis (Figure 2.3D).

As will be further discussed in Chapters 4, suppression of self-activated T cells by Tregs occur at two levels, the individual cell level and the cell population level. At the individual self-activated T cell level, suppression by Tregs mainly works to ensure that self-activated T cells are constrained in their activation status. For example, Treg-mediated suppression prevents the self-activated T cells from upregulating IL-2Rα (the high affinity IL-2 receptor subunit) high enough to get auto-/paracrine IL-2 signals. At the population level, Tregs reduce the number of self-activated (and IL-2 secreting) T cells in two possible ways: 1) preventing self-reactive T cells from ever responding by suppressing dendritic cells and 2) decreasing the duration of priming of self-activated T cells (to be further discussed in Chapter 4). The extent to which each mode contribute is not clear yet due to the lack of experimental data, but we derived a general mathematical formula to describe this in Chapter 4. The latter can be understood as: if self-reactive T cells are being activated generally for a shorter duration (e.g., secreting IL-2 for a shorter duration), then there is less chance for asynchronously activated T cells to be overlapped in time, resulting in a less frequency of self-activated T cells at any given moment.

Additional layer of ensuring the homeostatic frequency of self-activated T cells is dependence of Tregs in SLOs on IL-2 for their population pool size maintenance through proliferation and survival (Owen et al., 2018; Smigiel et al., 2014; Stolley and Campbell, 2016). The main IL-2 producers in SLOs for Treg maintenance in homeostasis are likely self-activated CD4$^+$ T cells (Liu et al., 2015; Setoguchi et al., 2005; Stolley and Campbell, 2016; Yi et al., 2018), and this can be justified using mathematical arguments by showing that homeostatic frequencies of self-activated and IL-2 secreting T cells (1-2%) and pSTAT5$^+$ Tregs (10-15%) form stable equilibrium out of reciprocal interactions between self-activated and IL-2 secreting T cells and Tregs, which is the main topic of Chapter 4.

Finally, under homeostasis it can be shown that the probability that self-activated T cells undergo clonal expansion through continuous paracrine IL-2 signals by other self-activated T cells is extremely low (~0) (Chapter 4). The crucial parameters

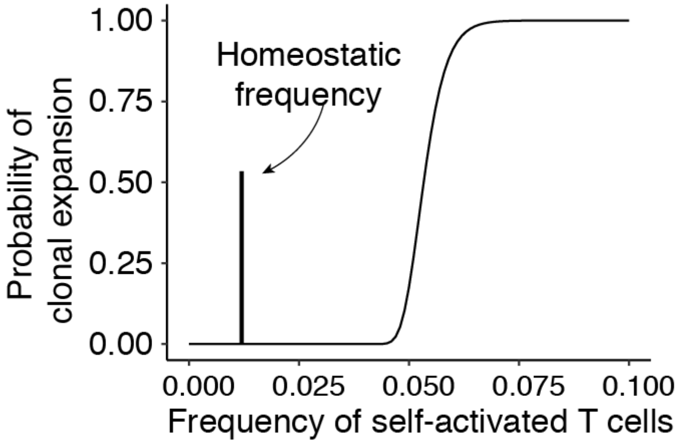

Figure 2.4 Schematic of immune homeostasis. The vertical line indicates the frequency of self-activated CD4 T cells secreting IL-2 in homeostasis. This is far from the sharp transition point of the probability of clonal expansion. The detailed derivation of the curve is shown in Chapter 4.

are the frequency (or more precisely the number density) of self-activated and IL-2 secreting T cells and the activation status (especially the IL-2Rα level) of self-activated T cells at the end of priming when responding T cells disengage from APCs. These together shape a sharp transition point of the probability of clonal expansion from extremely low (~0) to almost certain (~1) at around 5-6%, the frequency of self-reactive T cells (Figure 2.4). This transition point agrees with the experimentally inferred size of invisible cohort of self-reactive T cells, which go through massive proliferation upon Treg depletion (Kim et al., 2007; Richards et al., 2015).

In summary, robust immune homeostasis (self-tolerance) is possible through the recurrent reciprocal regulations between self-activated T cells and regulatory T cells across scales with their (well-regulated) homeostatic frequencies in dynamical equilibrium. These frequencies are resulted from the tail portions of deterministic distributions of relevant phenotypes that emerge from underlying molecular and cellular random processes. The immune homeostasis ensures that the sharp transition of the probability of clonal expansion from (near) 0 to (near) 1 occurs at the frequency of self-activated (IL-2 secreting) T cells substantially above the equilibrium frequency. These arise naturally from random processes and regulatory/controlling constraints of constituent molecules and cells.

2.4.3 Colocalization of right partners, symmetry breaking between self and non-self, and robust foreign-specific responses

Another important question is then how the immune system mounts a robust immune response against pathogens while maintaining self-tolerance at the same time. The question can be subdivided into two: 1) how do rare antigen-specific precursor T cells randomly surveying SLOs quickly locate cognate antigens? 2) how are T cells encountering foreign antigens instructed to undergo full-blown clonal expansion while self-reactive T cells remain suppressed in this process? The nature of these questions is again closely related with the recurring theme, random processes giving rise to deterministic probability distributions that are shaped and controlled by regulatory constraints of constituent molecules and cells and structural organizations of SLOs.

The quest for rare antigen-specific precursor T cells (1-100 out of 10^6 cells) to locate the right draining lymph nodes and antigen presenting cells bearing the right antigen within a few days is accomplished by 1) strategic surveillance patterns of naïve T cells within and across SLOs and 2) strategic positioning of dendritic cells and chemotactic interactions between T cells and dendritic cells leading to a finer and further compartmentalization of the T cell zone, at the same time taking advantage of spatial structures of SLOs (Baptista et al., 2019; Fricke et al., 2016; Hayes et al., 2019; Lee et al., 2012; Mandl et al., 2012; Textor et al., 2014). These factors greatly reduce the search space of T cells and maximize thoroughness and coverage of T cell surveillance over the T cell zone and across SLOs.[19] (Refs for the footnote: Cahalan and Parker, 2005). Additionally, inflammation greatly increases the blood flow in the inflamed tissue and local draining lymph nodes leading to increased amount of free antigen drained and T cell migration to the lymph nodes, respectively (Soderberg et al.,

---

[19] For example, DCs and T cells in SLOs are concentrated on and move along the fibrous networks formed by fibroblastic reticular cells, effectively reducing the search space in size and dimensionality (Wong and Germain, 2017). Another example is preferential colocalization of $CD4^+$ and $CD8^+$ T cells with their relevant DCs in distinct compartments of the paracortex in lymph nodes (Baptista et al., 2019). A simple estimation based on 2-photon experimental observations of stochastic encounters between naïve T cells and DCs in the paracortex suggested that with > 95% probability, any T cells can find relevant antigens presented by around 100 DCs in a lymph node within 6 hours (Cahalan and Parker, 2005).

2005). This further contribute to the increased chance of the cognate encounter between T cells and antigens. Therefore, while individual encounters occur randomly, the dynamical and structural constraints ensure the distribution of duration between antigenic challenge and the antigen encounter forms a narrow shape and thus T cells' locating cognate antigens under inflammatory condition certainly happen within around 72 hours (Heijst et al., 2009). Interestingly, this time scale coincides with the kinetics of dendritic cell migrations from infection sites to draining SLOs, maximizing antigen accessibility over the distribution of duration until the relevant encounters (Hayes et al., 2019).

Having been recruited to the relevant SLOs with cognate antigens, how such foreign specific T cells transition to a phase of clonal expansion without invoking the response of self-reactive T cells is still unclear. Each individual naïve T cell do not know whether the antigen its TCR recognizes is from self or foreign. Therefore, the homeostatic condition where self-tolerance is guaranteed also applies to foreign specific T cells (Figure 2.4). A possible way to allow clonal expansion of foreign-

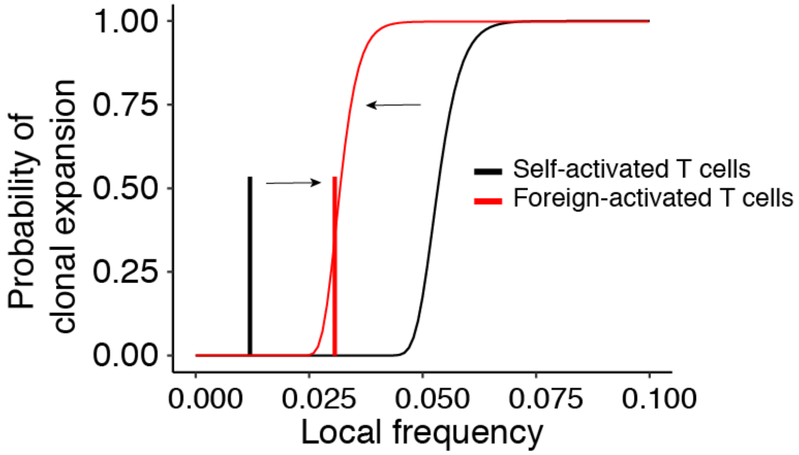

Figure 2.5 Schematic of symmetry breaking between self and non-self. The net effect is the increase of local density of foreign-activated T cells and the lowering of the transition point of the probability of clonal expansion due to higher activation status of foreign-activated T cells.

specific T cells is to increase the local density of activated foreign-specific T cells and the activation status (or IL-2Rα level) of those to create a local milieu that resides above the sharp transition point of the probability of clonal expansion, while the self-reactive T cells remain less affected (Figure 2.5). Several known molecular or cellular mechanisms seem to work to make this possible. The inflamed dendritic cells due to infections upregulate costimulatory ligands (CD80 and CD86) and pMHC molecules in their surfaces and other machineries for cell adhesion. Therefore, T cells engaged with the inflamed dendritic cells overcome the suppression by Tregs and activate further to lower the transition point of the probability of clonal expansion (Figure 2.5). Since the inflamed dendritic cells also present self-antigens, there is a danger that self-reactive T cells also get highly activated due to upregulated costimulation that Tregs cannot fully suppress (further discussed in Chapter 4). Here, we propose several mechanisms of the symmetry breaking between self and non-self. The first mechanism involves relatively weak TCR signals received by self-activated Tconvs due deletion of Tconvs with high self-reactivity (Hassler et al., 2019) and the preferential localization of Tregs in SLOs where their cognate self-antigens are prevalent (Lathrop et al., 2008; Wheeler et al., 2009). If Treg's TCR-mediated depletion of self-antigens from inflamed DCs together with weak TCR signals play a major role in suppression of the priming of self-reactive T cells as a main rate-limiting process (Akkaya et al., 2019), then it seems plausible that self-activated T cells remain constrained with a low IL-2Rα level through weak and early declining TCR signals even with upregulated costimulation from inflamed DCs. This allows self-activated T cells to maintain the probability of clonal expansion low while conferring full-blown activation signals to foreign-specific T cells. Additional asymmetry between self and non-self may come from differential migration patterns of newly activated T cells based upon their activation status (Krummel et al., 2016). More highly activated T cells are more sensitive to chemotactic cues from other inflamed DCs or responding T cells. Activated T cells also can recruit DCs. Therefore, the higher activation status of foreign-specific T cells increases the probability of colocalization with successive foreign-specific responding T cells via less random and more directional migration, thereby increasing the local density of those cells to form an IL-2-sharing microenvironment that enables full-blown clonal expansion. Self-reactive T cells are likely to be sterically excluded in this milieu since these are in more random and less directional migration with less sensitivty to chemotactic cues, thus maintaining their homeostatic density.

Together, robust foreign-specific response is possible through 1) the narrow probability distribution of the duration spent by rare foreign-antigen specific T cells until cognate antigen encounter and the matching distribution of the duration for which DCs migrate to draining SLOs and present antigens and 2) symmetry breaking between self and non-self enabling rare foreign-antigen specific T cells to engage with DCs with cognate antigens over an extended duration and colocalize with other activated T cells ensuring continuous exposure to IL-2 in the local milieus, but suppressing self-reactive T cells excluded from such milieus. The probability of clonal expansion of foreign specific T cells is almost certain while that of self-reactive T cells for clonal expansion still remains low. The symmetry breaking mechanisms proposed here are worth further experimental and quantitative investigations.

2.4.4 When does the robust immune homeostasis go awry: being below thermodynamic limit

One of the fundamental differences between typical thermodynamic systems and the immune system is that the immune system is not in the thermodynamic limit. In other words, as we have seen above, the number of constituent molecules and cells in their relevant spatial compartments are at most in the order of 10^8, which is below the thermodynamic limit.[20] Moreover, the local nature of cellular and molecular interactions shrinks the effective size of the spatial compartments and thus the effective numbers for constituent entities in each local milieu.[21] The time scale of intercellular or intracellular process (minutes to hours to days) is much longer than that (nanosecond to millisecond) of typical thermodynamic systems. As a result, the probability distributions of phenotypes themselves we have discussed so far are prone to fluctuations even with robust regulatory/controlling constraints shaping the distributions. To exacerbate the situation further, while the constraints shaping probability distributions in statistical physics are typically based on fundamental laws of physics such as laws of energy or mass conservation or the second law of thermodynamics (entropy maximization), those in the immune system are not from

---

[20] This number, 10^8 is for mice. It is interesting to consider other species such as humans, elephants, and whales. Blue whales typically weigh ~100 ton, whereas mice weigh ~10 g (a difference of seven orders of magnitude). If we assume that the size differences of the relevant organs (the thymus or lymph nodes) between mice and whales are the same as those of body sizes, a typical lymphoid organ of whales may encompass ~10^{15} cells, which is a substantial increase compared to that of mice. As we further discuss below, the effective size of local cellular interaction milieus and typical time scales of relevant processes may remain the same across the species as underlying physical or chemical principles remain the same. Therefore, even for whales, it is not likely that the immune system satisfies the conditions of the thermodynamic limit.

[21] For example, a typical length scale of local interactions between cells in lymphoid organs is around ~100 μm. With an average dimension of each lymphocyte, ~10 μm, a typical local milieu encompasses only ~1000 cells. With a typical concentration of IL-2 in lymph nodes, 10 pM, a local milieu with ~100 μm dimensions includes only 602 molecules.

such first principle laws but arising from constituent molecules and cells performing regulatory/controlling mechanisms out of the interweaved interaction topology among themselves, which again reside below the thermodynamic limit and under continuous influences of environmental and genetic factors. Therefore, the picture we have suggested so far should be modified a bit in reality (Figure 2.6).

The most relevant are the small tail portions of the distributions (self-reactive and IL-2 secreting T cells) in Figure 2.3 C-D that are crucial in establishing immune homeostasis. The low frequencies of these populations (4-10% and 1-2%, respectively) are especially prone to fluctuations, which may drive the system to reside near the transition point of the probability of clonal expansion (Figure 2.6). The evolution has worked out to ameliorate this danger by having various immune checkpoint mechanisms via suppressive feedback regulations operating across scales to enable robust immune homeostasis at least over the time scale of the reproduction age (Wong and Germain, 2018). However, genetic susceptibility and/or environmental stimuli drive the system towards particularly dangerous situations by influencing TCR

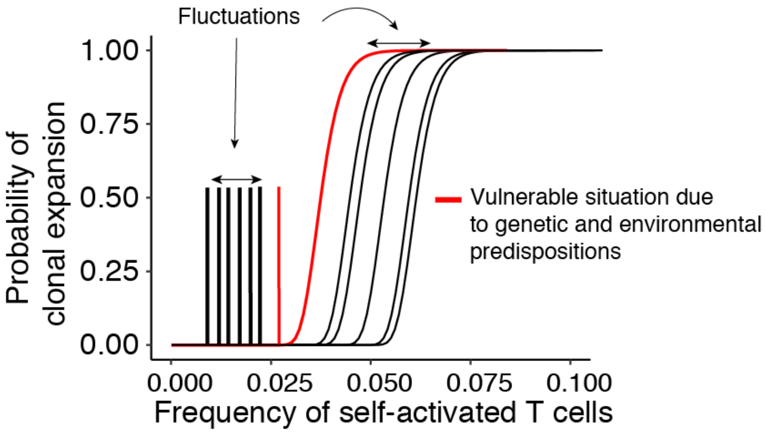

Figure 2.6 Schematic of immune homeostasis under continuous fluctuations. Being far from the thermodynamic limit and varying environmental and genetic factors contribute to these fluctuations.

rearrangement, thymic selection, intrinsic responsiveness and checkpoints of self-reactive T cells, Treg maintenance and function, innate inflammatory signaling, and/or antigen presentation, potentially resulting in autoimmune diseases (Figure 2.6, red) (Rosenblum et al., 2015; Theofilopoulos et al., 2017). Once a spontaneous initiation of self-specific response in this regime results in a sizeable expansion (if not a full-blown clonal expansion) with differentiation to effector cell types enough to damage the corresponding tissue sites, self-perpetuating and aggravating inflammation and tissue damages ensue via enhanced self-antigen presentation in quantity and variety with inflammation due to damage-associated molecular patterns (DAMPs) out of damaged cells.

Worldwide, around 5-10% of human population suffer from various autoimmune diseases (Theofilopoulos et al., 2017). This indicates that assuming the average age of the onset of diseases to be around 30 years, immune homeostasis of each human eventually fails roughly at the time scale of 300 years, which is robust enough given the average lifespan of the human being, ~80 years. While autoimmune diseases seem thermodynamically inevitable, better understanding the nature of immune homeostasis would allow us opportunities to come up with more precise therapeutic modalities that can overcome inevitable fluctuations and reestablish immune homeostasis.

2.5 Outlook

Thus far, we have gone through how we can reconcile between microscopic randomness and macroscopic determinism that seems to be manifested in the maintenance of immune homeostasis in the adaptive immune system. While some discussions in this chapter sound speculative, nevertheless transforming this argument into a concrete mathematical/computational framework is a timely task as evidenced by 1) the success of statistical physics that had overcome skepticisms and proved itself to be a fundamental way of connecting microscopic and macroscopic worlds consisting of many constituent entities and 2) the nature of the immune system made up of various cell types and molecules operating together to ensure robust immune functions that are now being uncovered collectively in the era of 'systems immunology'. We propose this as an overarching framework of understanding and assessing immune homeostasis. Through this endeavor, the list of numerous molecular and cellular parts involved in adaptive immune processes can really be interweaved and transformed to become a quantitative predictive multiscale model of immune homeostasis, which is one of the ultimate goals of immune systems biology and may guide more fine-tuned therapeutic strategies for autoimmune diseases and cancer. To achieve this, quantitative modeling, quantitative experiments, and molecular biological approaches should go in parallel since still there are unknowns we cannot even estimate in molecular and cellular processes and new discoveries will be better appreciated under quantitative frameworks and continuously update the model (Germain, 2018).

An immediate staring point to make the argument more concrete is to derive the consistently observed numbers from detailed molecular and cellular processes. One related question is why the frequencies of 'invisible' self-reactive T cells and Tregs in thymic output (4-10% and 6-10%, respectively) are similar. Is this agreement merely a coincidence? Can known cellular and molecular processes in thymic selection explain this agreement? Are yet to be known processes required to derive this? What are the consequences of this in immune homeostasis? Answering these questions may shed light on underlying processes in thymic selection and devising better therapeutic manipulations for modulating immune homeostasis.

Zooming out a little bit, an interesting and conceptual question is what the central and peripheral tolerance try to optimize. A prevailing notion has been to remove self-reactive cells and thus prevent autoimmunity; Central tolerance occurring via negative selection is not perfect for removing self-reactive cells, and peripheral tolerance with regulatory cell types such as Tregs further ensures the suppression of self-reactive T cells in the periphery. However, recent data suggest that self-reactive T cells are not kept from ever being activated, but continuously get activated. Intriguingly, the peripheral maintenance of Tregs appears to rely on IL-2 secreted by such self-activated T cells. Self-reactive T cells are required to be activated to suppress themselves to prevent autoimmunity. This may lead us to rethink about the fundamental purpose of the machineries of tolerance solved out through the evolution. We propose that immune homeostasis tries to maximize the utility of maintaining self-specific repertoires in the periphery to the extent to which the self-reactivity is not dangerous to cause autoimmunity past the reproduction age. This is from an assumption that if the immune system can tolerate sizable peripheral self-specific repertoires, the evolution of which might occurred to promote maximal utilization of self-specific repertoires. The implication of this can involve various aspects. First, this can allow positive selection to shape the repertoire to be more self-reactive in general to confer more effective responses against pathogens at the expanse of the potential leakage of self-reactive T cells to the periphery (Mandl et al., 2013). Second, this can increase the total size of the repertoire, and the cross-reactivity of the self-specific repertoire against foreign antigen can be beneficial for fighting against pathogens (Yu et al., 2015). Third, this can be beneficial fighting against altered-self arising from cancer or increased self-antigen arising from benign yet physiologically detrimental hypertrophy of tissues (Kohanim et al., 2019; Menares et al., 2019). Lastly, related to the first and second points, we may speculate that removing self-reactivity too stringently from the repertoire may allow pathogens to coevolve to resemble peptides of the host over the evolutionary time scale.[22] If this happens, the adaptive immune system cannot function to clear such pathogens anymore. Therefore, maintaining self-reactivity may enable the host to cope with "camouflaged" pathogens. Endogenous retroviral elements in our genome may suggest some hints for this possibility. Self-reactivity may play a role to keep these "immigrant" self under check.

---

[22] (Mandl et al., 2013) suggests that the germline encoded CDR1 and CDR2 mainly determine the reactivity of TCRs towards pMHCs, and CDR3 contributes in a minor portion, yet most decisively. In this scenario, it may be hard to classify peripheral T cells into solely the self-reactive or the foreign-reactive. All T cells are somewhat both self-reactive and foreign-reactive with different weights on either of these. Therefore, it may be inevitable to harbor self-reactive repertoires to maintain enough foreign-reactive repertoires in the periphery. Stringent reduction of self-reactive repertoires may lead to an insufficient size of foreign-reactive repertoires.

Chapter 3: Machine learning of stochastic gene network phenotypes

3.1 Introduction

A major goal of systems biology is to develop quantitative models to predict the behavior of biological systems (Germain et al., 2011; Gunawardena, 2014). However, most realistic molecular and cellular models have a large number of parameters (e.g., reaction rates, cellular proliferation rates, extent of physical interactions among cells or molecules), whose values remain unknown and are often challenging to measure or infer quantitatively (Babtie and Stumpf, 2017; Gutenkunst et al., 2007). While some biological phenotypes are robust to parameter variations (Li et al., 2004), most are "tunable" by parameters (Bialek, 2018). Moreover, parameter variations in biological systems typically span multiple orders of magnitude in physiologic and/or pathologic conditions, and their effects on phenotypic variations may differ in distinct local regions of the plausible parameter space due to typical nonlinearity in interactions among components. Therefore, analyzing the behavior of a system over the *entire* plausible space of parameters is needed to study the phenotypic range of a biological system and its parameter-phenotype relationships (Baum et al., 2016; Koeppl et al., 2013; Lim et al., 2013).

Ideally, the quest of parameter-phenotype relationships can be readily achieved with analytical solutions of the given model. However, realistic biological models are often the case intractable analytically, thereby dealt with by computational simulations, which alone do not yield intuitive understanding. Sensitivity and uncertainty analyses have been invaluable ways to delineate parameters' contributions in variation or uncertainty of model outcomes obtained by simulations in various fields, not restricted to biological modeling (Saltelli et al., 2012). Various methods of obtaining global or local sensitivity measures are available yet require sophisticated parameter sampling design. Additionally, a comprehensive tool (called Simmune) capable of building and simulating detailed models easily using graphical rules and dissecting parameters leading to experimentally testable outcomes was developed and utilized to solve various biological problems (Angermann et al., 2012; Meier-Schellersheim et al., 2019). However, these methods often require extensive computational resources to analyze the high-dimensional parameter space, given the large uncertainty in parameter values and the complex correlation structure among parameters. To cope with the computational cost for conducting a lot of simulations, metamodeling/emulation utilizing various regression techniques has been applied to sensitivity/uncertainty analyses. However, the capacity of sensitivity/uncertainty analyses is still far from what can be expected from analytical solutions: 1) fast evaluation of model phenotypes for new parameter values, 2) intuitive and immediate delineation of parameters' role for shaping model phenotypes in both local and global levels in a scalable manner, 3) flexible and incremental improvements of coverage and/or resolution of the plausible parameter space as needed.

Here, we combine computational simulation of full-feature dynamical models and machine learning (ML) to develop a framework, called MAchine learning of Parameter-Phenotype Analysis (MAPPA), for constructing, exploring, and analyzing the mapping between parameters and quantitative phenotypes of dynamical systems.

In contrast to the limited usages of ML in metamodeling/emulation merely as tools for some other functionalities such as sensitivity measures, feature selections, or model calibration and optimization, it is now our primary goal to generate computationally efficient, reliable, and interpretable ML models mapping between parameters and quantitative phenotypes of dynamical systems. This is enabled by taking advantage of the large amounts of data that can be generated from bottom-up, mechanistic computational simulation of dynamical systems and the full functionalities of modern machine learning approaches to "compress" such data. The ML models capture the nonlinear mapping between parameter and phenotypic spaces (parameter-phenotype maps) and therefore, can be viewed as "phenomenological" solutions of the given dynamical model in analogy to analytical solutions in ideal situations. As corollaries of having such phenomenological solutions, ML models can predict the system's quantitative behavior from parameter combinations, thus bypassing computationally expensive simulations. They also can delineate which and how parameters and parameter combinations shape phenotypes, both globally throughout the parameter space and locally in the neighborhoods of individual parameter configurations efficiently without further computational costs. Furthermore, unlike existing sensitivity analysis methods requiring delicate designs of parameter sampling and thus rendering the schemes not flexible for further improvements later on, ML models can be easily improved with additional training data in coverage and resolution of the plausible parameter space. Finally, we introduce visualizations to enable interactive exploration of the parameter-phenotype map, including a web application for interrogations of analysis below (https://phasespace-explorer.niaid.nih.gov).

We applied MAPPA to a contemporary problem in single cell biology: Despite the increasing availability of single-cell gene expression data enabled by rapid technological advances (Tanay and Regev, 2017), an important unanswered question is how cell-to-cell expression variation and gene-gene correlation among single cells are regulated by the underlying gene regulatory network (GRN), within which different signals, including those arising from environmental variations or biochemical fluctuations, are transmitted (Elowitz et al., 2002; Martins et al., 2017; Raj and van Oudenaarden, 2008). Chemical master equations (CMEs) (see section A.1) can be used to model, analyze, and predict single-cell heterogeneity and gene-gene correlation behaviors based on GRNs. However, existing analytical schemes of solving CMEs are only available in simple models involving gene products from one gene or describing mRNAs and proteins as an aggregated gene product when involving two genes (Cao and Grima, 2018). To make CMEs analytically tractable, simplifying assumptions are needed with the risk of ignoring important features such as “bursty” transcription (Elf and Ehrenberg, 2003; Kampen, 2007). Together, these are far from realistic descriptions of GRNs we want to achieve (Cao and Grima, 2018). Here, we used MAPPA together with Gillespie’s Stochastic Simulation Algorithm (SSA) (Gillespie, 2007)) and were able to generate predictive ML models mapping between a multitude of kinetic parameters and behaviors of propagation of gene expression variations for full-feature stochastic models of gene circuit motifs. We first explored information transmission behaviors in a simple two-gene network and illustrated a proof-of-concept of MAPPA and advantage over existing analytical methods. Then, we further applied MAPPA for more complex gene networks such as three gene feedforward networks and a two-gene negative feedback networks and illustrated additional layer of PoV regulations and oscillatory behaviors arising due to stochastic fluctuations.

3.2 Results

3.2.1 Learning the parameter-phenotype map of stochastic network dynamics

Given a well specified stochastic gene network model and associated kinetic parameters, we seek to understand how the phenotypes of the system behave and change across the parameter space. Here, phenotypes can be any quantitative measures assessing certain aspects of the dynamical behavior of the given model (Figure A.1). While the quantitative relationship between parameters and phenotypes in a given system can be mathematically complex, we hypothesize that the mapping can be captured quantitatively by interpretable ML models such as Random Forests (RF) in

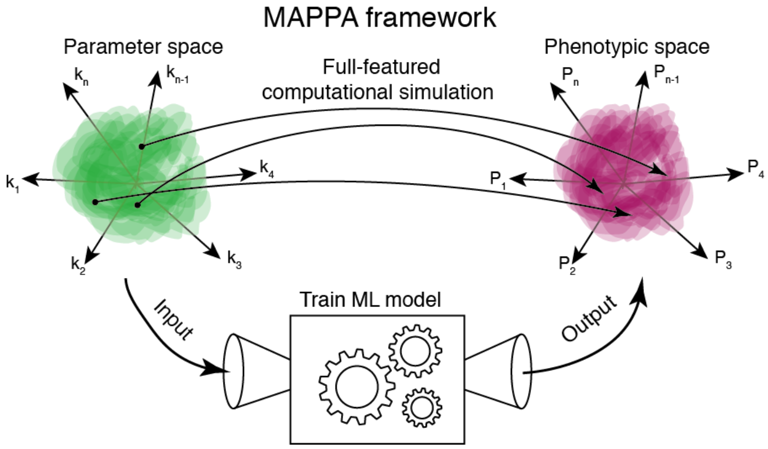

Figure 3.1 MAPPA framework. MAPPA utilizes massive simulation data and machine learning to construct models that can accurately and efficiently predict quantitative phenotypes given high-dimensional parameter combinations without using resource intensive dynamical simulations. The resulting machine learning models also serve as interpretable parameter-phenotype maps.

which the contribution of individual parameters to achieve accurate mapping can be delineated (Breiman, 2001) (Figure 3.1). For example, the gene expression dynamics of a network of genes and proteins in cells can be modeled by CMEs. However, analytical solutions of non-linear CMEs (e.g., those with ON-OFF promoter dynamics) are generally intractable and evaluating how parameters affect a phenotype of interest, e.g., the correlation between two genes over time (Figure A.1), rely on conducting computational simulations over a large number of parameter combinations. Here we sought to use ML models to learn the PPM.

MAPPA comprises three steps (Figure 3.2). In step 1, we model a system as a network of interacting entities (e.g., proteins, mRNAs, cells), whose states/levels are governed by stochastic birth-death processes (e.g., transcript production and degradation). While still poorly measured, particularly *in vivo*, plausible ranges of some parameters can be obtained from the literature or approximated based on physical and/or biological constraints. Next, in step 2, using methods designed for uniform sampling of high-dimensional parameter spaces (section A.3), we obtain parameter combinations from the plausible parameter space and conduct stochastic, dynamical simulations of the system using each one of the parameter combination samples. We then compute quantitative phenotypes of interest (here we focus on correlation of expression between genes in single cells, but the MAPPA approach is applicable to any phenotypes/modeling combinations) to obtain an *in-silico* dataset that links parameter values to phenotypes. In the final and critical step (step 3), we train a ML model that quantitatively maps parameters to phenotypes, and we evaluate the predictive performance of the model by using parameter combinations not used in the training set. Using this approach, we can obtain arbitrarily large training and testing sets with size limited only by computational capacity. Any good ML approach generating

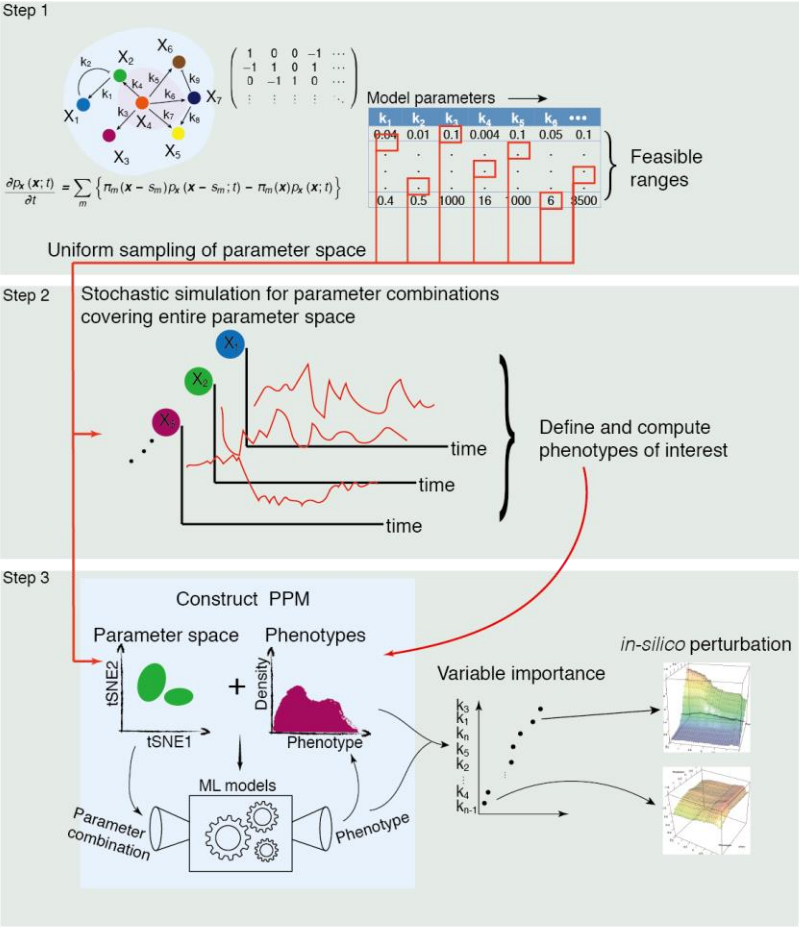

Figure 3.2 Three steps in MAPPA framework. **Step 1:** Model the system as a network of interacting molecular species; their interactions are governed by kinetic parameters; **Step 2:** Uniformly sample parameter combinations from the plausible parameter space and conduct mechanistic/stochastic simulation on each of the combinations and compute the quantitative phenotype(s) of interest from the simulation results; **Step 3:** Construct Parameter-Phenotype Maps (PPMs) by training ML models using the simulated dataset generated in the previous step; PPMs map parameters to phenotypes. The trained ML models can be tested using additional simulated data from parameter combinations distinct from those used to generate the training set. This process can be repeated to improve the PPM, for example, by increasing the representation of parameter combinations that lead to rare phenotypic values. The resultant ML models can be used to explore, in a computationally efficient manner, how parameter perturbations may change the phenotype and delineate which parameters contribute to controlling the phenotype, both globally throughout the parameter space or locally at specific neighborhoods of the parameter space.

interpretable nonlinear models can in principle be used, here we use RF based on 1) ease of use without tuning hyperparameters as opposed to support vector machines and neural networks, 2) good performance and scalability comparable to support vector machines and neural networks for up to around 10^5 input data points, 3) faster training than support vector machines, neural networks, and gaussian process, and 4) (most importantly) delineation of contributions of individual parameters to phenotypic variations through global and local variable importance measures (across parameter space and at specific locations in parameter space, respectively) computed during the training process (not available for other nonlinear ML methods) (Breiman, 2001; Villa-Vialaneix et al., 2012).

Once we have a predictive ML model, we can use it as a “phenomenological” solution of the CME to efficiently predict phenotypes from parameters without using computationally intensive simulations (Figure 3.1). Guided by dimensionally-reduced visualizations and information on which parameters contributed to prediction, we can further evaluate the system and test our understanding by *in-silico* perturbation analysis, e.g., by assessing how well we can predict phenotypic changes as the parameter values are altered (Figure 3.2). These interactive, exploratory assessments are efficiently enabled by the ML model without full stochastic simulations; they can further help reveal the design principles of the systems and suggest parameter optimization strategies to attain specific phenotypes in synthetic gene circuits (Mohammadi et al., 2017). To illustrate these use cases, we have developed an interactive website to allow the exploration of PPMs we analyzed below (https://phasespace-explorer.niaid.nih.gov).

3.2.2 Information transfer (propagation of variation (Pov)) in a two-gene network

To assess MAPPA, we first applied it to study how information (as encoded by the changes in gene expression over time) is transmitted from one gene to another (i.e., the propagation of variation (PoV)) in a prototypical, two-gene network model in single cells (Figure 3.3A, see section A.2.3) (Martins et al., 2017). While existing analytically tractable models for this circuit require simplifying assumptions (Elf and Ehrenberg, 2003; Kampen, 2007), here we analyzed a full-feature model with mRNAs and proteins as distinct species, and promoters that can be switched stochastically between transcriptionally active (on) and inactive (off) states known as the random telegraph process (Peccoud and Ycart, 1995). As a measure of information propagation between

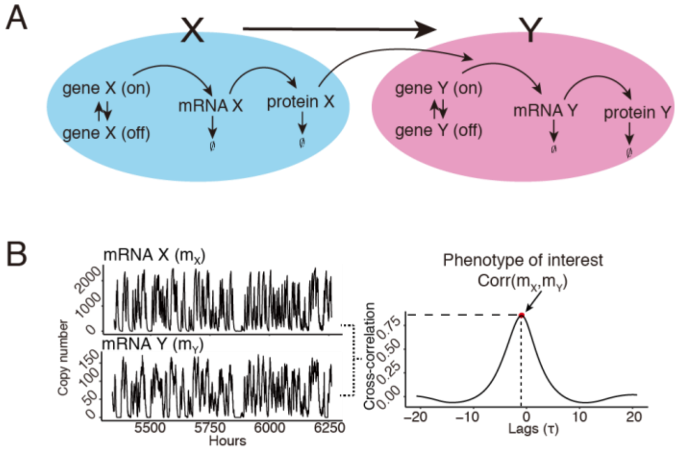

Figure 3.3 Two-gene network model and the phenotype of interest. **(A)** The two-gene network model in which the protein product of gene X regulates the transcription rate of gene Y. The promoter of both X and Y undergoes stochastic on-off state switching. Both the mRNAs and proteins undergo first order degradation. See A.2 for additional details. **(B)** Definition of the phenotype of interest: quantifying the propagation of gene expression variability (or information) from gene X to gene Y. The time trajectories of mRNA X and Y generated by stochastic simulation from a specific parameter configuration is shown here for illustration. Here the metric of information transmission/propagation used, $Corr(m_X, m_Y)$, was defined as the maximum of the cross-correlation between $m_X(t)$ (level of the mRNA X) and $m_Y(t-\tau)$ (level of the mRNA Y) across a pre-defined range of time lags τ (here the red dot indicates the maximum across τ's). We only consider correlations with $\tau < 0$ in this network to capture the causal relationship between X and Y (X → Y).

genes X and Y, we defined the maximum time-lagged correlation (denoted as $Corr(m_X, m_Y)$) between mRNAs X and Y as the maximum cross-correlation between $m_X(t)$ and $m_Y(t-\tau)$, where $m_X(t)$ and $m_Y(t)$ are copy numbers of mRNAs X and Y at time t, respectively, and τ is the time lag (Figure 3.3B). The same metric can be applied to proteins, here we chose to focus on mRNAs since they are the dominant measurement modality in single cell studies.

Simulation on a large number (76,532) of randomly sampled (through the uniform grid scheme), biologically plausible parameter combinations (see section A.3) revealed that very few had high correlations (e.g., only 315 had a correlation of greater than 0.7) (Figure 3.4A) (Martins et al., 2017). Dimension reduction visualization using tSNE (Figure 3.4C) indicated that the parameters with high $Corr(m_X, m_Y)$ formed clusters. Moreover, additional parameter combinations sampled from these regions also had high correlations. Thus, biased sampling guided by the phenotype of the neighbors can be used to increase the representation of rare parameter combinations (Figure 3.4B and D). Using this approach, we trained random forest (RF) regression models for $Corr(m_X, m_Y)$ and assessed their predictive capacity using independently simulated data (Figure 3.5A). Both the model trained using the initial, uniformly sampled parameter combinations (r=0.93; Figure A.2A) and the one trained by incorporating additional samples from the high-correlation regions showed excellent prediction performance (r = 0.98; Figure 3.5B); the latter had better performance in the high-correlation regions (Figure A.2E). A two-class (high versus low correlations),

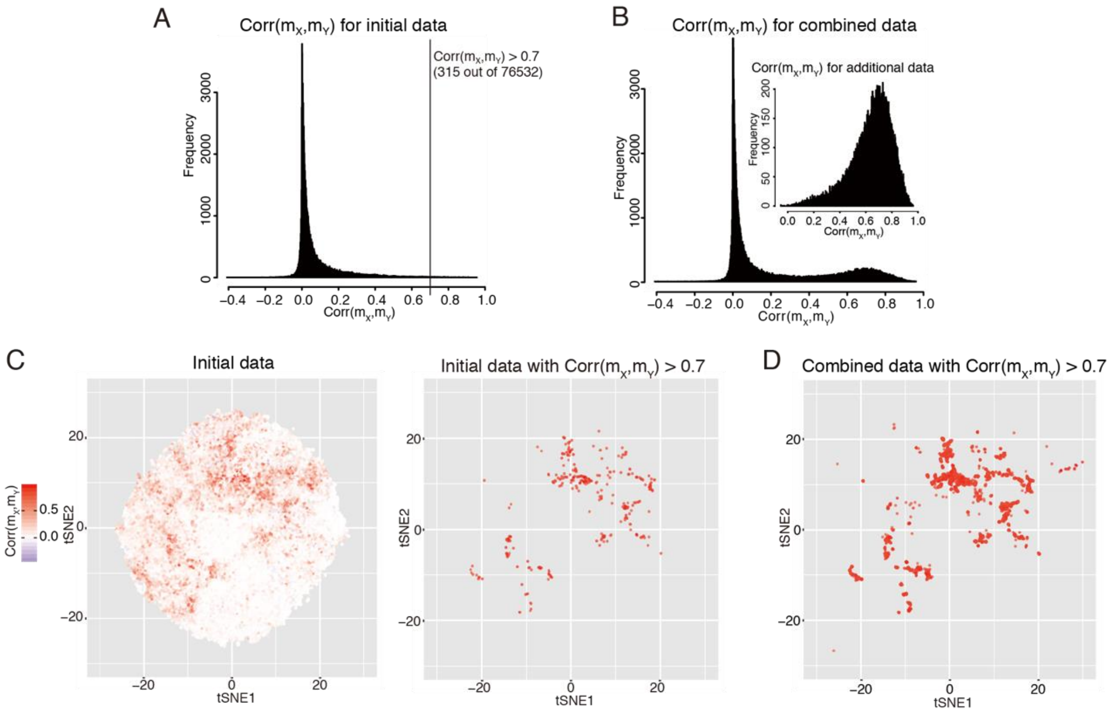

Figure 3.4 Simulation results of the two-gene network. **(A)** Distribution of $Corr(m_X, m_Y)$ from the simulations using the first, initial set of sampled parameter combinations (see Figure 1D left panel). Among the 76,532 parameter combinations simulated, only 315 had $Corr(m_X, m_Y) > 0.7$ with most exhibiting very low correlations. **(B)** Additional simulations were performed on parameter combinations sampled near those shown in (A) with high correlations. Here the distribution of $Corr(m_X, m_Y)$ from both the initial and additional parameter combinations is shown; the inset shows that of the additional parameter combinations only. **(D and E)** Visualization of the parameter space and the phenotype using two-dimensional (2d) t-distributed Stochastic Neighbor Embedding (tSNE) computed from the sampled parameter combinations. (D) tSNE plot for (left) the initial simulated data and its subset (right) with $Corr(m_X, m_Y) > 0.7$. (E) Additional parameter combinations nearby those with $Corr(m_X, m_Y) > 0.7$ were sampled (referred herein as "additionally sampled") and simulated to increase the representation of high-correlation parameter combinations; here the tSNE plot for the combined data (initial samples plus additionally sampled) with $Corr(m_X, m_Y) > 0.7$ is shown. The color scale denotes $Corr(m_X, m_Y)$.

categorical RF model performed similarly well (AUC = 0.98; Figure A.2C; see section A.7).

RF ML models provide "variable importance" to quantify the extent of influence a parameter can exert on the phenotype, both globally (GVI, Figure 3.5C and

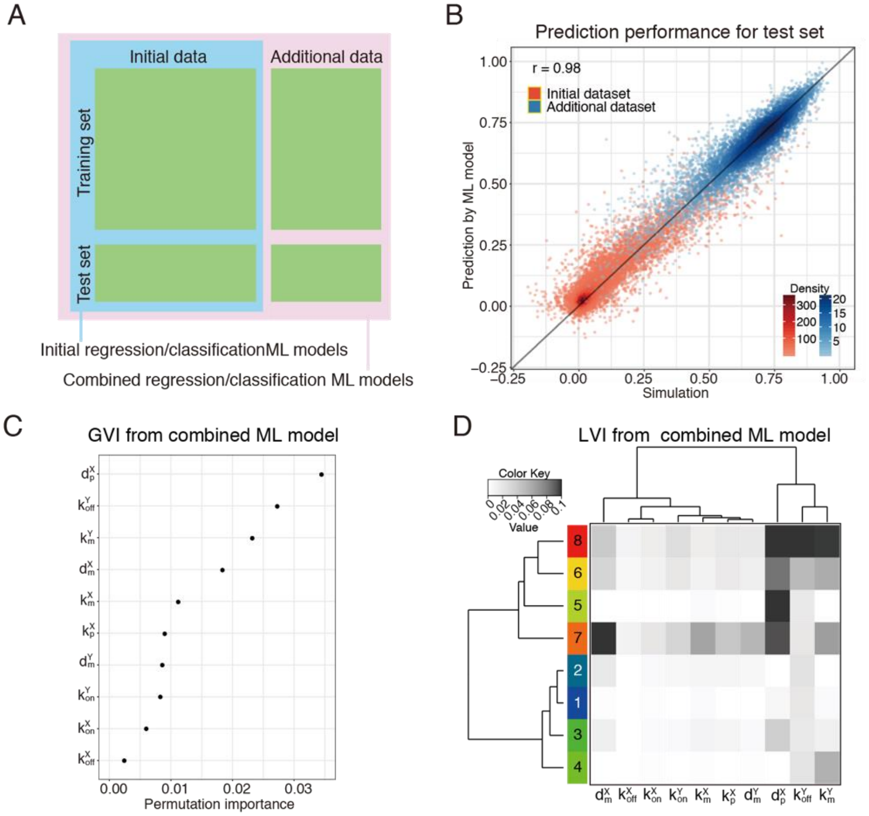

Figure 3.5 ML model training, performance, and variable importance. **(A)** The ML model training-testing scheme involving the initial (within the blue box) and additionally sampled (pink box; outside the blue box) data. Each of the two data sets were divided into independent, non-overlapping training and testing sets. We trained 4 ML models ($Corr(m_X, m_Y)$ ~ kinetic parameters (R notation)): two of which were RF regression models, one using the initial (blue box) and the other using the combined (pink box) training set; similarly, two RF classification models for categorical outcomes (high vs. low $Corr(m_X, m_Y)$) were trained (see A.7). Categorical labels for the classification models: 'high' if $Corr(m_X, m_Y) > 0.7$ or 'low' if $Corr(m_X, m_Y) \leq 0.7$. **(B)** Scatter plot showing the concordance between the independently simulated $Corr(m_X, m_Y)$ (x axis – not used in ML model training) vs. those predicted by the RF regression model using the model parameter values alone (y axis) (r = 0.98); note that the RF model was trained using the combined training data; each point corresponds to a parameter combination. The red points are those from the independent test set of the initially sampled parameter combinations; the blue dots correspond to the independent test set of the additionally sampled parameter combinations nearby the initial combinations with high (>0.7) $Corr(m_X, m_Y)$. **(C)** Global Variable Importance (GVI) (x axis) of the model parameters (y axis) fitted by the RF regression model. The permutation GVI is shown, which reflects the increase in prediction errors in out-of-bag data after permuting the indicated variable. Another type of GVI (impurity GVI) is shown together with the permutation GVI in Figure A.3 B. **(D)** A summary heatmap depicting the Local Variable Importance (LVI) of the RF regression model. Each row corresponds to a cluster of parameter combinations that exhibit similar LVI profiles across the indicated parameters (columns); the values

shown in the heatmap are the average across all parameter combinations within each cluster. Eight clusters are shown as indicated by the cluster number/color bar on the left; the number of clusters were chosen qualitatively by considering: 1) ease of visualization in the limited space, 2) the qualitative diversity of LVIs that the clusters can illustrate (section A.8). The LVI values shown in the heatmap are the average increases in the squared out-of-bag residuals provided by the *randomForest* package in R (see section A.8).

Figure A.3 A-B) for the entire parameter space and locally (LVI, Figure 3.5D and A.3C) at a particular point in that space (see A.8). For example, GVI from the combined ML model revealed that the degradation rate of protein X (d_p^X), the off-rate of the promoter of gene Y (k_{off}^Y), and the transcription rate of mRNA Y (k_m^Y) are the most important for determining $Corr(m_X, m_Y)$, while the promoter switching rates of gene X (k_{off}^X and k_{on}^X) are less important (Figure 3.5C and A.3B). The additional data from the high $Corr(m_X, m_Y)$ regions made the rank of k_{off}^Y higher, suggesting its role is pronounced in those regions and GVI of ML models can adapt flexibly to augmented data (Figure 3.5C and A.3A-B). Based on the LVI profiles, parameter combinations can be clustered into qualitatively distinct groups (Figure 3.5D and A.3C). For example, the degradation rate of mRNA X is more important in cluster 7 than in other clusters (Figure 3.5D). Thus, individual parameters can exert local, “neighborhood”-dependent influences on the phenotype, consistent with the notion that gene networks may employ distinct strategies for PoV regulation depending on the cellular and environmental conditions (Martins et al., 2017).

The LVI can be used to guide fast, high-resolution *in silico* explorations of how parameter perturbations of different extents may affect phenotypes, which can be computationally slow and resource intensive when full-blown simulations are used. For example, the LVI of a parameter configuration with high $Corr(m_X, m_Y)$ (= 0.83) predicted that the degradation rate of protein X (d_p^X) and the transcription rate of gene X (k_m^X—regulating the "burst" size) were the most important determinants of $Corr(m_X, m_Y)$, while the on-rate of promoters X and Y (k_{on}^X and k_{on}^Y) were the least important (Figure 3.6A). Indeed, as confirmed by actual simulations, tuning d_p^X and k_m^X locally affected $Corr(m_X, m_Y)$ substantially, while changing k_{on}^X and k_{on}^Y did not (Figure 3.6B-C). Together, our results illustrate that predictive ML models linking parameter and phenotypic spaces can be built successfully and are useful as computationally efficient and phenomenological solutions of the associated CMEs.

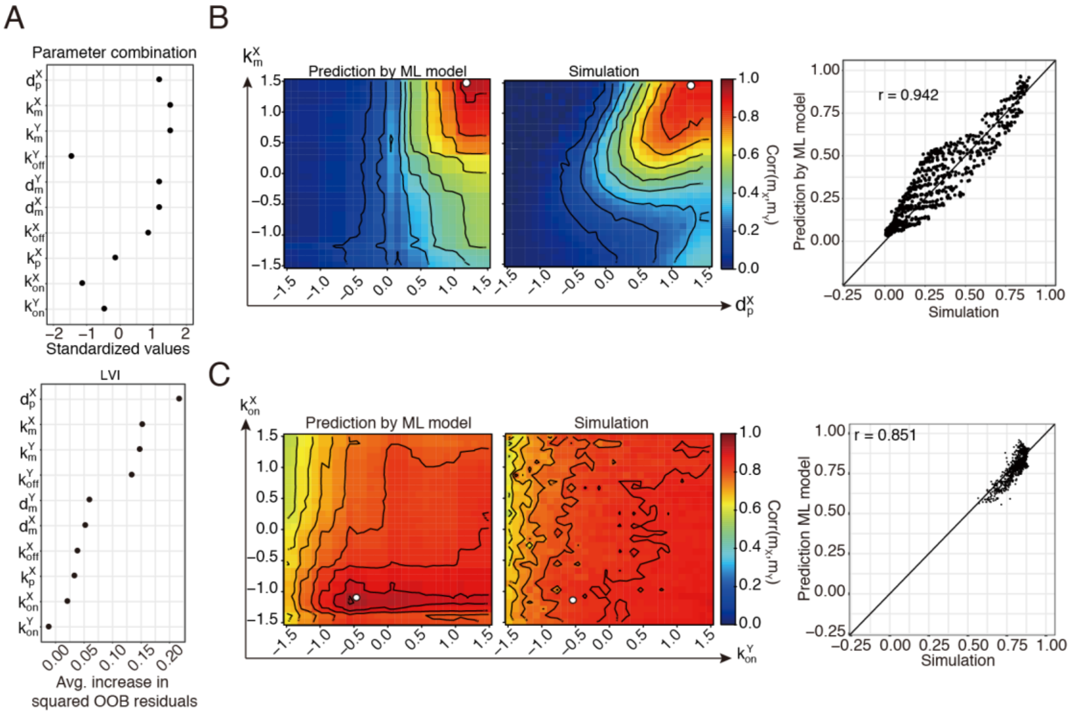

Figure 3.6 *in-silico* perturbation analysis using ML model. **(A)** The specific parameter combination (the "starting point") (parameter key: 042015_AAACEZGP) selected for *in-silico* perturbation experiments and its corresponding LVI. Avg. - average; OOB - out-of-bag. **(B)** Contour maps depicting the predicted (top) and simulated (bottom) phenotypic values ($Corr(m_X, m_Y)$) as parameters d_p^X(x axis) and k_m^X (y axis) were perturbed starting from the selected parameter combination shown in (I) (denoted by white dots); A scatter plot of the predicted vs. the simulated data points from these maps is shown at the bottom. **(C)** Similar to (B) but for perturbing k_{on}^X and k_{on}^Y (parameters with lowest LVI) starting from the parameter combination (denoted by white dots) shown in (A).

3.2.3 Assessing the robustness of the MAPPA analysis of PoV exploration in a two-gene network

Next, we sought to test the robustness of the results above. First, we questioned whether having a different measure of PoV such as mutual information still produces consistent results as above. Mutual information computed from the same simulation results showed a good concordance with $Corr(m_X, m_Y)$ (Figure 3.7A). Based on this phenotype, we could train an ML model with good prediction performance (Figure A.4A). GVI of this ML model showed a good agreement with that of the ML model predicting $Corr(m_X, m_Y)$ in terms of highly ranked parameters, k_m^Y, d_p^X, k_{off}^Y, and d_m^Y (Figure 3.5A, A.3, 3.7B, and A.4B), suggesting that PoV behaviors captured by ML models were not affected by specific definitions. This analysis also illustrated the flexibility of the MAPPA framework in that ML models for different phenotypes can be easily constructed in contrast with the potential difficulty of analytically deriving functional forms for different phenotypes dependent on model parameters.

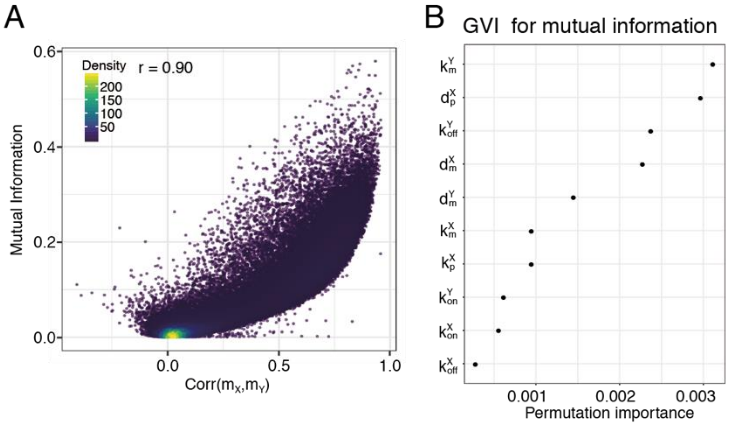

Figure 3.7 MAPPA analysis on mutual information. **(A)** Scatter plot showing mutual information vs. $Corr(m_X, m_Y)$. **(B)** GVI of the RF regression model for mutual information. Permutation GVIs are shown. See Figure A.4B for both permutation and impurity GVIs.

Next, we sought to examine the effects of the size of training data and sampling schemes on ML model performance and GVIs. For this, we generated parameter combinations using the Sobol' sampling scheme and conducted simulation using these combinations (section A.3). The performance of ML models increased with the increased sizes of training data and plateaued above the size of 20000 data points, suggesting that the size of the initial data (76532 data points) was already enough to cover the plausible parameter space for training reliable ML models (Figure 3.8A-B). GVI was also better resolved with increasing the size of training data (Figure 3.8C-D). Interestingly, both sampling schemes, uniform grid and Sobol', showed comparable ML model performance and GVIs (Figure 3.8A-B), suggesting that the uniform grid

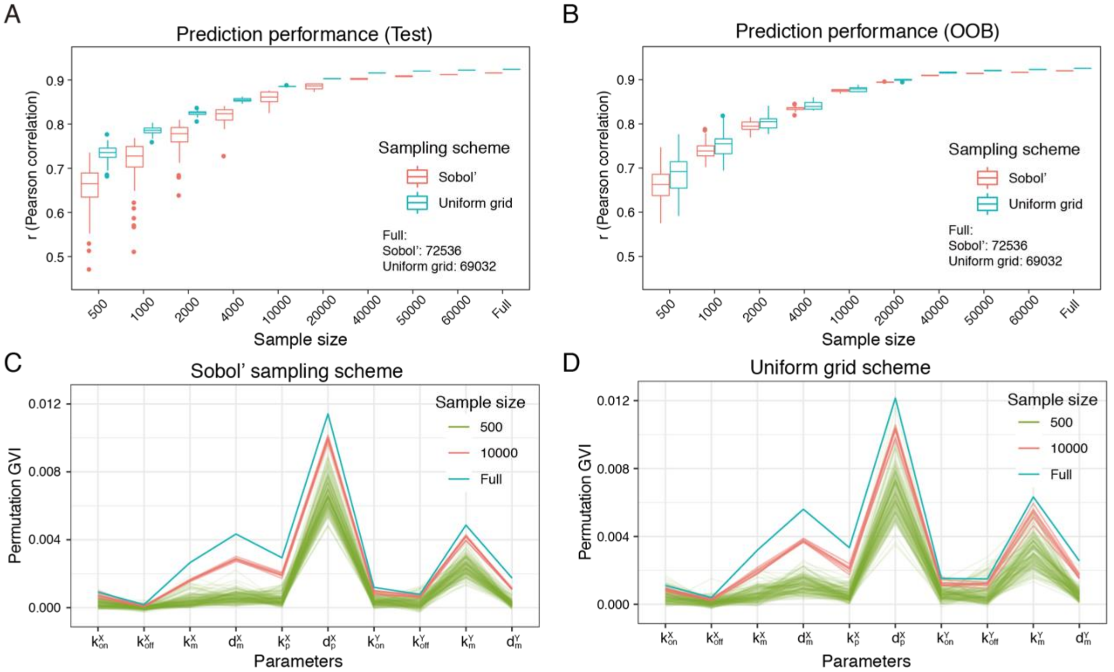

Figure 3.8 ML model performance over different data sample sizes and sampling schemes. **(A)-(B)** Comparison of prediction performance on (A) a test data set and (B) out-of-bag (OOB) data set for different training sample sizes between the uniform grid and Sobol' sampling schemes. The test data set was prepared by pooling 7500 parameter combinations from both uniform grid and Sobol' schemes and not used for ML model training. **(C)-(D)** Comparison of permutation GVI over different training sample sizes for (C) the Sobol' sampling scheme and (D) the uniform grid scheme.

scheme has the similar space-filling capacity to that of the Sobol' scheme, a low-discrepancy quasi-random sampling scheme.

Next, we examined the reliability of GVI and LVI generated by ML models by comparing these with independently computed global and local sensitivity measures. We first computed Sobol's variance-based global sensitivity indices (first order indices and total indices) by conducting simulations on a parameter sample designed for Sobol's indices (Figure 3.9) (Saltelli et al., 2012) (see section A.10 for the method detail). GVI and global sensitivity indices showed good concordance in terms of high-ranked parameters (Figure A.3A and 3.9). Moreover, total sensitivity indices showed better concordance with GVI among other mid- or low-ranked parameters. Therefore, GVI is a reliable global sensitivity measure comparable to variance-based sensitivity indices. Moreover, considering the results of additional sampling on focused regions and different training sample sizes above, GVI is more flexible in further improvements of coverage and resolution over the plausible parameter space enabled by quick training of ML models augmented with additional data.

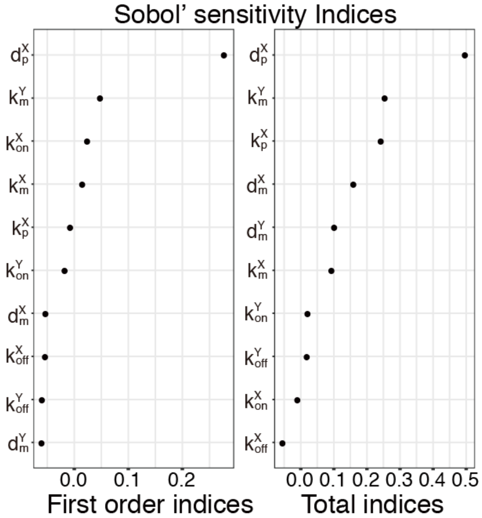

Figure 3.9 Sobol' variance-based sensitivity indices. First order indices (left) and total indices (right) are shown. See section A.10 for the method detail.

To compare LVI with local sensitivity measures, we randomly selected 500 parameter combinations (300 from those with $Corr(m_X, m_Y) > 0.4$ and 200 from those with $Corr(m_X, m_Y) \leq 0.4$) and conducted simulations and obtained $Corr(m_X, m_Y)$ on perturbed parameter combinations (section A.10). We prepared perturbed parameter combinations by changing a parameter at a time to other grid points over the full plausible range. Thus, the additional expense of local sensitivity analysis was 90 more simulations for each parameter combination. Among several types of local sensitivity measures we tried (section A.10), the mean squared deviation turned out to be the most concordant with LVI from RF (Figure 3.10A), which can be understood given that LVI is estimated by the increase of mean squared errors in prediction after permuting each parameter values across all training data in RF (section A.8 and A.10). Interestingly, LVI itself tells whether it can be trusted or not through its maximum value for each parameter combination depending on the relative magnitude in the distribution of LVI across all parameter combinations in the training set (Figure

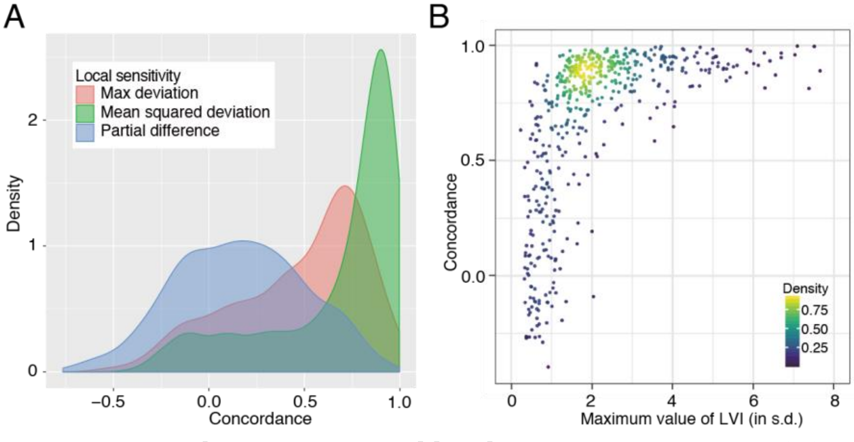

Figure 3.10 Comparison between LVI and local sensitivity measures. **(A)** Distribution of concordance between LVI and three different local sensitivity measures over 500 parameter combinations. See section A.10 for the definition of local sensitivity measures. **(B)** Scatter plot showing maximum values of LVI (in the unit of standard deviation) vs. concordance between LVI and mean squared deviation (local sensitivity measure). s.d.-standard deviation. (see section A.10).

3.10B). The high concordance also coincided with the large effect size on the phenotype of perturbations, and low values of LVI is prone to estimation noise due to the small effect size on the phenotype (data not shown). In turn, the relative magnitude of LVI indicates the potential effect size on the phenotypes upon parameter variations. Together, LVI can be considered as reliable local sensitivity measures as well as indicators of the effect size upon parameter perturbations, which are generated automatically in the training process of RF models, significantly reducing computational cost compared to existing local sensitivity analysis schemes.

To assess MAPPA further, we examined analytical approximation schemes such as linear noise approximation (LNA) (lowest order system-size expansion) and inverse omega square approximation (IOS) (higher order system-size expansion) to derive $Corr(m_X, m_Y)$ analytically (Elf and Ehrenberg, 2003; Grima et al., 2011; Paulsson, 2004). These methods employ simplifying assumptions to attain tractability (e.g., the promoter on/off switching is averaged; see section A.12). In overall, LNA already gave reasonable estimations of $Corr(m_X, m_Y)$ (r = 0.95), and IOS slightly improved the estimations over LNA (r = 0.96) except some parameter combinations giving worse predictions than those from LNA or unrealistic values (e.g., values higher than 1 or complex numbers) (Figure 3.11A and A5). However, some estimations by LNA or IOS turned out to be significantly lower than corresponding simulation outcomes, showing worse prediction performance than the ML model (Figure 3.11A-B). The LNA model showed that $\frac{d_m^Y}{d_m^Y + d_m^X}$ is one of the main factors determining $Corr(m_X, m_Y)$ (see section A.12), which is consistent with the GVI that d_m^X is important. This explains the lower estimations of $Corr(m_X, m_Y)$ by analytical

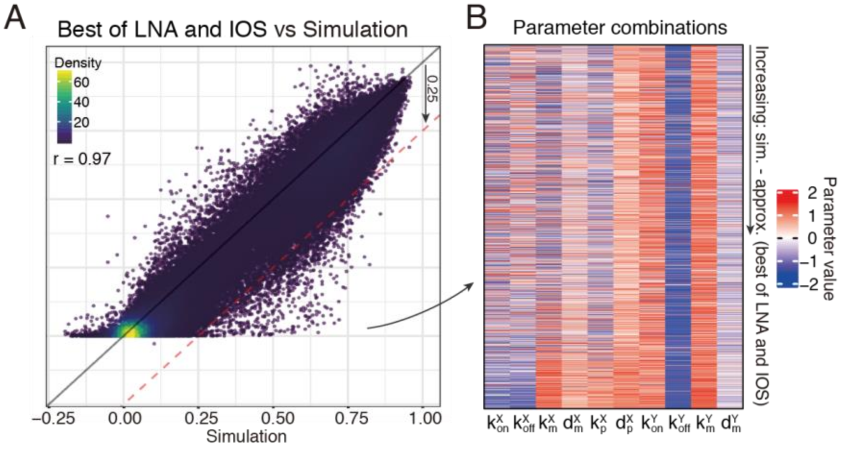

Figure 3.11 Comparison between MAPPA and analytical approximation schemes over the entire parameter combination. **(A)** Scatter plot of $Corr(m_X, m_Y)$ computed from analytical approximation (y axis) versus that from the stochastic simulation in the entire dataset (both "initial" and "additional" – see Figure 3.5A). Best estimations of LNA and IOS for each parameter combination are plotted. The results from each approximation scheme are shown in Figure A.5. **(B)** Heatmap of parameter combinations (rows) for which the analytical approximation deviates significantly from the simulation results (i.e., with the differences > 0.25 in $Corr(m_X, m_Y)$) The rows are sorted in increasing order of the difference of $Corr(m_X, m_Y)$ between simulation and analytical approximation.

approximation schemes since those parameter combinations in general showed $d_m^X > d_m^Y$ (Figure 3.11B).

To further understand why then actual simulations yielded higher $Corr(m_X, m_Y)$ for those, we focused on LVI clusters 7 and 8 with differential importance of d_m^X on $Corr(m_X, m_Y)$ shown above (Figure 3.5D). Notably, it is important in LVI cluster 7 but less so in cluster 8. In both clusters (more pronounced in cluster 8), the ML model again performed better than the analytical models (Figure 3.12). The parameter combinations with incorrect analytical estimation were more prevalent in cluster 8 having $d_m^X > d_m^Y$ (Figure 3.12B). Closer examination revealed that these parameter configurations had a hierarchical relationship of parameter values as k_m^X, $d_m^X > d_m^Y > k_{on}^X$, k_{off}^X (Figure 3.12B). Thus, the promotor switching dynamics of gene X was the main driver of the fluctuations of mRNA X: a burst of transcripts was made in the on-state and transcripts were then degraded rapidly in the off-state. This gave rise to non-Poissonian mRNA fluctuations (Raj et al., 2006). mRNA Y captured such promoter-induced fluctuations of mRNA X (by $d_m^Y > k_{on}^X, k_{off}^X$) while buffering out mRNA X-intrinsic fluctuations (by $k_m^X, d_m^X > d_m^Y$) and showed transient hysteretic and memory behaviors after gene X switched to the off-state, which both analytical schemes (LNA and IOS) could not delineate (Thomas et al., 2014). Together, our analyses provided insights on PoV regulation that go beyond those from analytically tractable approaches.

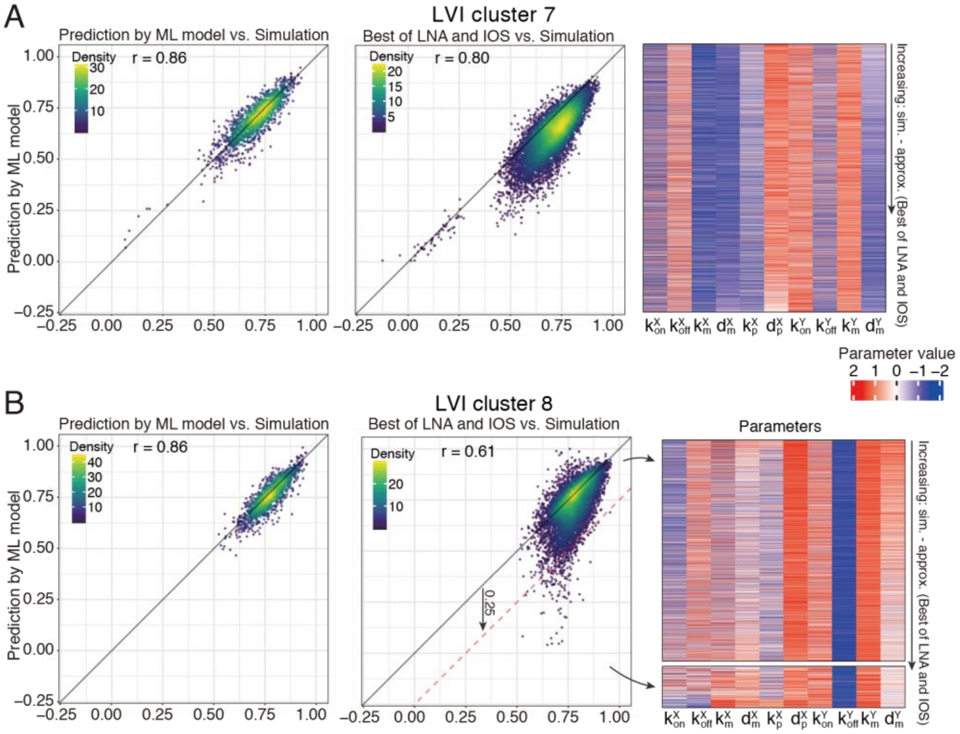

Figure 3.12 Comparison between MAPPA and analytical approximation schemes over LVI clusters 7 and 8. **(A)-(B)** Scatter plots showing $Corr(m_X, m_Y)$ of ML model prediction vs. simulation (left) and best analytical approximation out of LNA and IOS vs. simulation (center) and heatmap of parameter combinations (rows) (right) in LVI clusters (A) 7 and (B) 8. The parameter combinations in the heatmap ranked in increasing order by the "error" made by the analytical model compared to actual simulations, i.e., by the difference of $Corr(m_X, m_Y)$ between simulation and the analytical model; for LVI cluster 8 (in B), the parameter sets were split into those with differences ≤ 0.25 (top) or >0.25 (bottom). See Figure A.6 for comparisons between each of LNA and IOS and simulation.

3.2.4 Information transfer in three-gene feedforward network motifs

Gene networks containing feedforward interactions are found across phylogeny and biological processes (Milo et al., 2002; Neph et al., 2012) (Figure 3.13). To assess the ability of MAPPA to analyze more complex networks, we applied it to study two types of feedforward circuits: 1) the coherent type (PPP), in which X positively regulates Y and Z, and Y also positively regulates Z, 2) the incoherent type (PNP), in which X activates both Y and Z, while Y represses Z (Mangan and Alon, 2003) (see section A.2 for detailed model descriptions). The PPPs can function as delayed activators to filter out transient fluctuations in upstream signals, while the PNPs can serve as accelerated activators or detectors of changes in the input signal over time (Goentoro et al., 2009; Mangan and Alon, 2003). However, although these circuits have been studied for the aforementioned functions quite substantially, the function of these circuits, especially that of the Y arm, in shaping gene-gene correlations is not well understood for gene regulatory (transcription factor) networks described realistically with mRNAs and

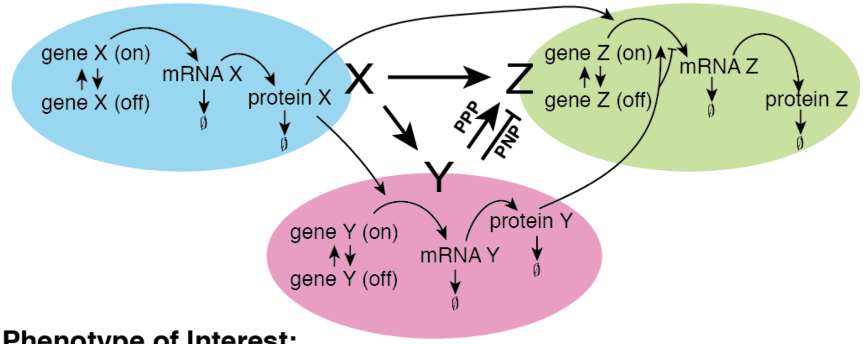

Phenotype of Interest:

Fold-change of Corr(m_X,m_Z) (FC) = $\dfrac{\text{Corr}(m_X,m_Z)\text{ with Y}}{\text{Corr}(m_X,m_Z)\text{ without Y}}$

Figure 3.13 Three-gene feedforward network models and the phenotype of interest. The PPP (coherent) and PNP (incoherent) network types are considered. The quantitative phenotype of interest is the ratio of $Corr(m_X, m_Z)$ (or fold-change (FC)) between the network with and without the Y-mediated feedforward; the goal of the analysis is to assess the function/effect of the Y feedforward arm.

proteins being modeled as separate entities and discrete promoter switching dynamics when stochasticity is present—e.g., how is information transmission from gene X to gene Z ($Corr(m_X, m_Z)$) regulated by gene Y and what specific processes (e.g., degradation or translation of mRNA Y) in gene Y are most relevant? We thus defined the phenotype of interest as the ratio (or "fold change" (FC)) between the $Corr(m_X, m_Z)$ of the network with and that without the Y feedforward arm when all the other parameter values remained fixed (Figure 3.13; see section A.2).

Stochastic simulation revealed a notable difference in FC between the two types of feedforward circuits (Figure 3.14A-B left panels and A.7A-B). In PPP, the Y-mediated loop can either increase (FC>1) or decrease (FC<1) $Corr(m_X, m_Z)$, but the correlation was reduced (FC<1) in PNP for most parameter combinations, even down to negative values in some cases (i.e., the direction of correlation flipped); these were more apparent when the correlation was lower (e.g., less than 0.4) when Y is absent (Figure 3.14A-B left panels). Moreover, PPP and PNP also differ in the time lag needed to maximize the correlation ($Corr(m_X, m_Z)$): the Y-mediated arm tends to lengthen or shorten the delay between X and Z in the PPP or PNP, respectively (Figure A.7C-D), which are consistent with the aforementioned functions of PPP and PNP as delayed and accelerated activators, respectively. Together, simulations revealed distinct functions of the Y arm in regulating information propagation in the PPP and PNP circuits: in a "co-activating" circuit (PPP), the Y arm can increase the correlation extended over longer timescales, while the negative regulating Y arm in the PNP can reduce the transmission of variation from X to Z, thereby maintaining Z homeostasis and reducing Z's "memory" on X fluctuations.

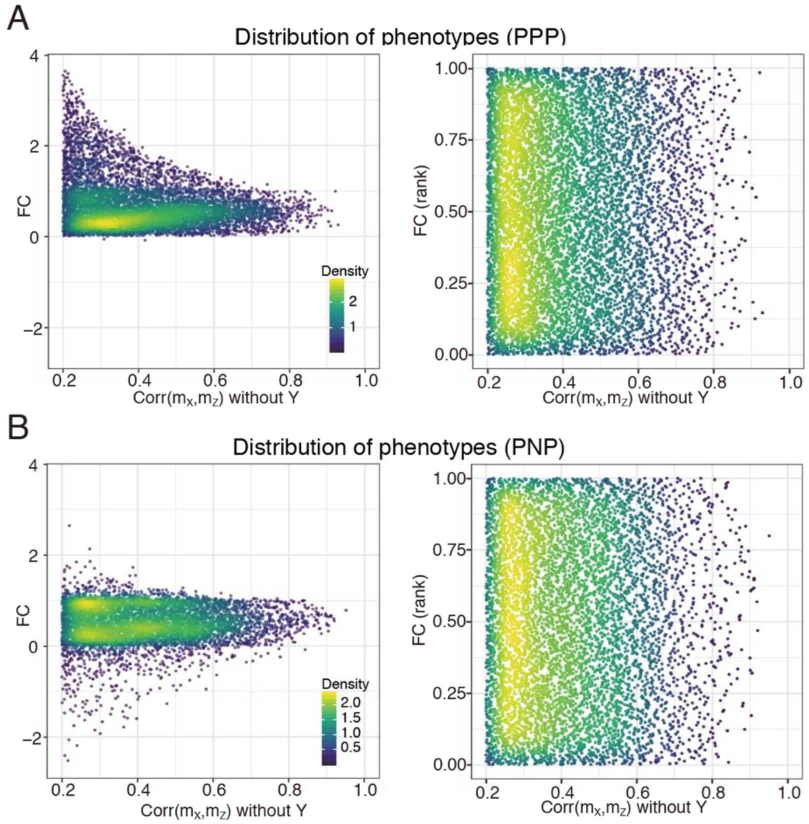

Figure 3.14 Distribution of the phenotypes, FC and FC (rank). **(A)-(B)** Scatter plot of phenotypes, FC (left) and FC (rank) (right) versus $Corr(m_X, m_Z)$ without Y for (A) PPP and (B) PNP; each dot corresponds to a single parameter combination sampled. Note that only parameter combinations with $Corr(m_X, m_Z) > 0.2$ without Y are considered since FC is less robust and would diverge when $Corr(m_X, m_Z)$ without Y is near 0. FC (rank) was defined to eliminate the effect of $Corr(m_X, m_Z)$ without Y from FC by taking ranks of FC in each intervals of width 0.05 of $Corr(m_X, m_Z)$ without Y.

What specific processes in Y regulate FC is less clear. We therefore trained RF ML models that maps parameters to FC (section A.7). To account for FC's dependence on $Corr(m_X, m_Z)$ without Y, we also defined a rank-based FC (FC (rank)) by taking percentiles of FC values in each interval of width 0.05 of $Corr(m_X, m_Z)$ without Y followed by ML model training for this phenotype as well (section A.7) (Figure 3.14A-B right panels). These models showed excellent prediction performance (PPP; r = 0.93 (FC), 0.92 (FC (rank)) and PNP; r = 0.91 (FC), 0.92 (FC (rank))) (Figure A.8A-B). Interestingly, despite their phenotypic differences, the most important parameters for determining FC and FC (rank) were similar between the two circuit types (Figure 3.15 and A.9). These parameters fall into three categories regulating the transmission of the fluctuations from: 1) X to Y (K_{XY} and k_m^Y), 2) Y to Z (d_p^Y and K_{YZ}), and 3) X to Z (K_{XZ}). As we intended by removing the dependence of FC (rank) on $Corr(m_X, m_Z)$ without Y, GVI of FC (rank) showed only the former two categories (X to Y and Y to Z) as high-ranked. Most notably, tuning the K parameters (Eq. A.29, A.35, and A.36 in section A.2.3) can shift the transfer function in and out of the range of variation of the upstream regulator: when operating out of range (at the saturating regime of the transfer function), variation in the activity level of the upstream factor are buffered and thus cannot be transmitted to the downstream gene (Figure 3.16A). Posttranslational modification of the upstream regulator and epigenetic modification of the promoters/enhancers of the target gene are capable of regulating K in this manner (Filtz et al., 2014). Thus, given permitted transmission of variation directly from X to Z,

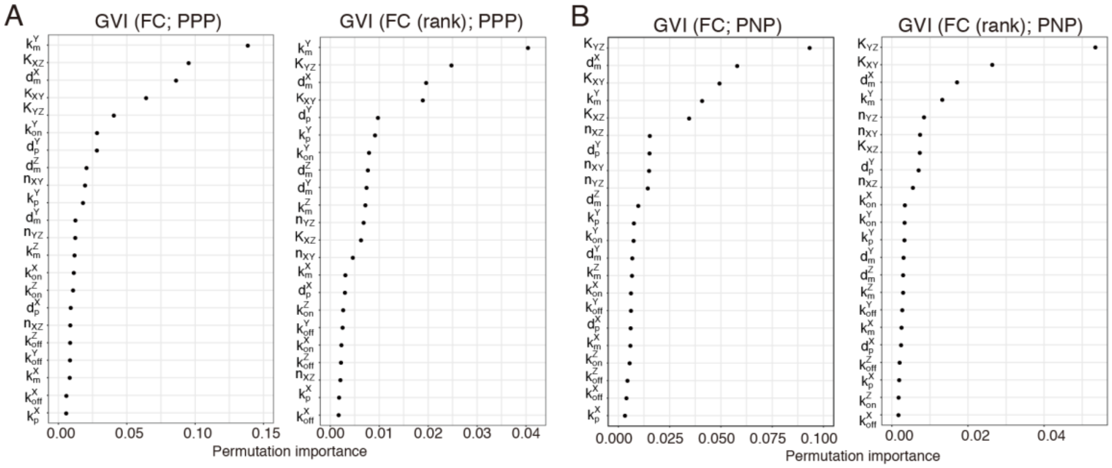

Figure 3.15 Global variable importance of ML models in three-gene networks. **(A)-(B)** GVI generated by ML models of FC (left) and FC (rank) (right) for (A) PPP and (B) PNP. Permutation GVIs are shown. See Figure A.9 for both permutation and impurity GVIs and a comparison between the two.

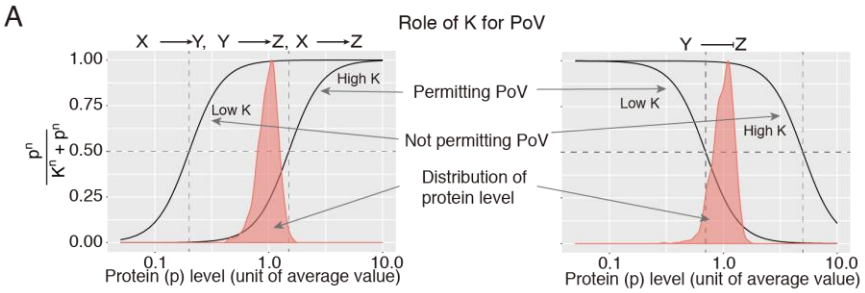

B

Role of Y in relaying PoV

Transmissibility of X to Y	Transmissibility of Y to Z	Effect on FC
Yes	Yes	Tuned by parameters as discussed in the text.
No	Yes	FC between 0 and 1 due to additional, independent fluctuations from Y.
Yes/No	No	FC ≈ 1; Y arm has minimal effect.

Figure 3.16 Role of the feedforward arm for regulating PoV. **(A)** Illustrating the role of K (K_{XY}, K_{YZ}, and K_{XZ}), the level of upstream input needed to attain half maximal activation of the downstream gene, plays in tuning the propagation of variability/information. The input (upstream protein level) is illustrated as a distribution to depict variability over time within a single cell (or cell-to-cell variation at a given time-point.) (red), this together with the relative value of K determine whether upstream variations are buffered or transmitted to effect downstream transcription. Left and right panels illustrate a positive and negative regulatory relationship, respectively, between the upstream gene and its downstream target gene. **(B)** Illustrating the main qualitative scenarios of variability propagation in the Y arm and the corresponding effect on the FC phenotype.

MAPPA pointed to several means for Y to influence the correlation between X and Z (and thus the FC) (Figure 3.16B).

Similar to the example above (Figure 3.5D), the LVI map revealed that the contribution of individual parameters to FC and FC (rank) depends on the parameter configuration (Figure A.10; see section A.8). For example, the Hill coefficients (e.g., n_{YZ}), which govern the "steepness" of the transfer functions, are generally not important (Figure A.10). However, LVI showed that n_{YZ} is important at a particular parameter configuration in the PPP circuit (Figure 3.17A). With this configuration information can be transmitted from X to Z and from Y to Z, but that between X and

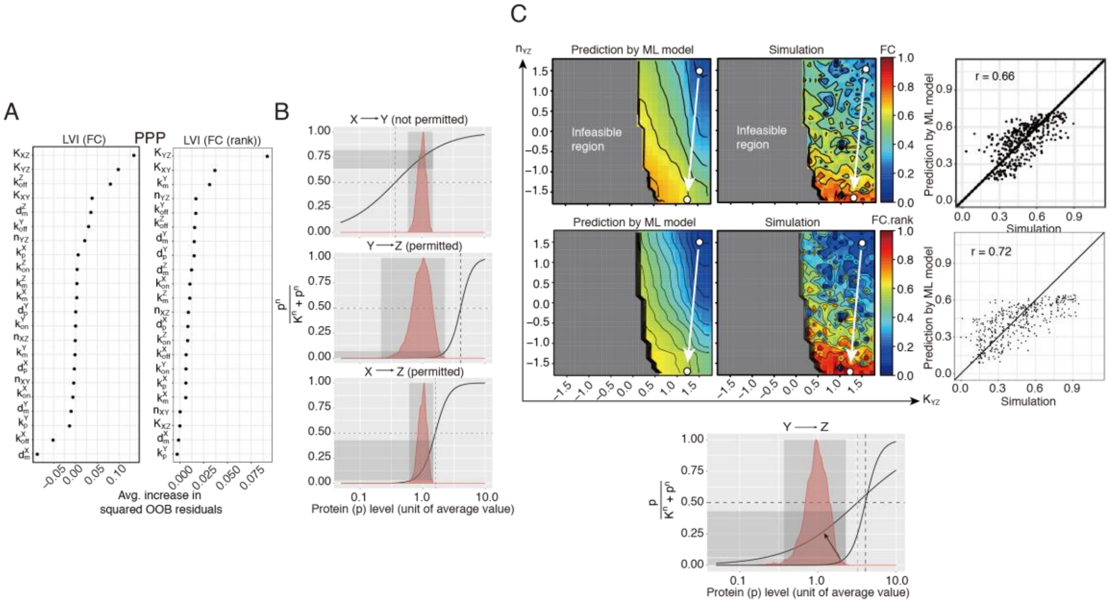

Figure 3.17 *in-silico* perturbation analysis using ML model. **(A)** LVI of FC (left) and FC (rank) (right) for the specific parameter combination from PPP selected for local perturbation analysis. Avg. - average; OOB - out-of-bag. **(B)** Distributions of protein levels (p_X, p_Y, and p_Z) (red) and the transfer functions (black curve – see Figure 3.16A) between the indicated upstream protein and downstream gene at the selected parameter combination. The shaded areas indicate the effective regulation regimes between the input (upstream protein) and output (transcription rate). **(C)** Prediction (by RF ML model) and validation (based on stochastic simulations) for the perturbation on the two indicated parameters (x and y axes) starting from the selected parameter combination shown in (B). (Top and middle) Prediction and simulation of phenotypic values (the two contour maps on the left), and a scatter plot comparing prediction and simulation for the given perturbations (right panel) for FC (top) and FC (rank) (middle). The grey regions in the contour maps represent parameter combinations deemed biologically infeasible (section A.6). The starting point (white dot) of the arrow is the parameter combination, and the arrow indicates the shift in the transfer function (especially in the Hill coefficient) arriving at the second parameter combination (the end point of the arrow) as a result of the parameter perturbation; the bottom plot (similar to (B)) shows the changes in the transfer function between these two parameter combinations (indicated by the arrow) and how the second parameter combination allows higher transmission of variation (higher FC and FC (rank)).

Y was minimal because K_{XY} and k_m^Y were low and FC and FC (rank) was therefore low due to the added noise transmitted from Y to Z (Figure 3.17A-B). Actual simulation confirmed that decreasing n_{YZ} leads to decreased noise transmission from Y to Z (Figure 3.16B) and thus an increase in FC (Figure 3.17C). These data illustrate that by employing even simple feedforward architectures, cells can attain additional flexibility in tuning the co-variation between circuit components (X and Z). For example, having separate "modulatory" Y feedforward arms can be useful when X is a master regulator of many genes: each Y can independently tune information transfer between X and a specific set of downstream genes.

3.2.5 Information transfer in a two-gene negative feedback circuit: oscillations and frequency domain analysis

Negative feedback circuit motifs are ubiquitous in biology; their functions include maintaining homeostasis, buffering fluctuations, and driving oscillatory behaviors (Alon, 2007; Brandman and Meyer, 2008; Germain, 2012). While either autoregulatory feedbacks or positive and negative coupled feedbacks have been analyzed in the context of noise suppression or generation of oscillations (Becskei and Serrano, 2000;

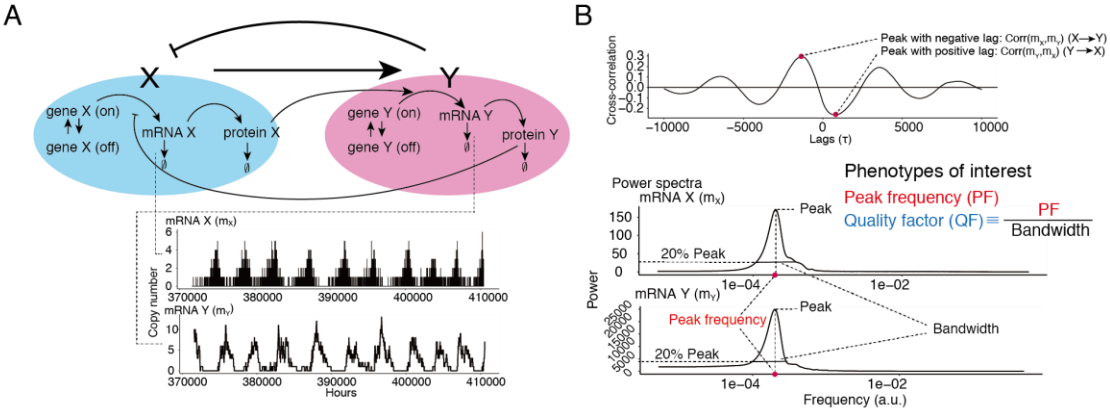

Figure 3.18 Two-gene negative feedback network model and the phenotypes of interest. **(A)** Description of a two-gene negative feedback network model. **(B)** Definition of the phenotypes of interest. Due to the bidirectional regulation between X and Y, peak cross-correlation can be considered with both positive and negative time lags (see Figure S6A). The phenotypes of interest for analyzing oscillatory behaviors include the quality factor (QF) and the peak frequency (PF) of the power spectra in the frequency domain of gene expression dynamics. Example trajectories of mRNAs X and Y are shown for a parameter combination exhibiting oscillations.

Brandman and Meyer, 2008), the two-gene negative feedback circuit (Figure 3.18 and secrtion A.2), an extension of the simple two gene circuit we analyzed earlier (Figure 3.3), has received less attention despite its simple topology and intriguing, implicated roles in generating oscillatory behaviors such as circadian rhythm (Pett et al., 2018). We performed deterministic modeling and bifurcation analysis, which confirmed that this circuit is capable of oscillations (limit cycle oscillations or damped oscillations) (Figure 3.19A and section A.13) (Strogatz, 2015; Woller et al., 2014). Stochastic simulations of this circuit revealed parameters showing comparable absolute magnitudes of $Corr(m_X, m_Y)$ and $Corr(m_Y, m_X)$ (maximum correlations between mRNA X and Y for negative and positive lags, respectively), indicative of oscillatory behavior (Figure 3.18B and 3.19B). When stochasticity is considered, oscillations (due

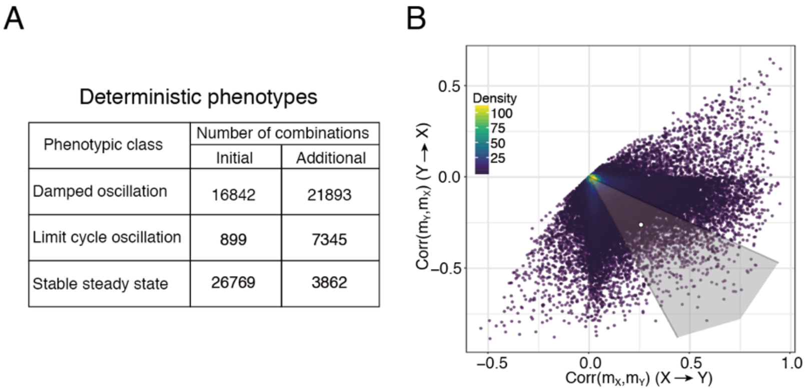

Deterministic phenotypes

Phenotypic class	Number of combinations	
	Initial	Additional
Damped oscillation	16842	21893
Limit cycle oscillation	899	7345
Stable steady state	26769	3862

Figure 3.19 Deterministic and stochastic oscillatory behaviors **(A)** Number of parameter combinations for each type of oscillatory behavior predicted by deterministic modeling; damped oscillations (DO), limit cycle oscillations (LC), and stable steady states (SS) for both initial and additional parameter sets. **(B)** Simulation results showing peak cross-correlations between m_X and m_Y with negative time lag (x axis – $Corr(m_X, m_Y)$; information flows from X to Y) vs. positive time lag (y axis – $Corr(m_Y, m_X)$; information flows from Y to X) for the sampled parameter combinations. Shown in the shaded region are those parameter combinations with comparable magnitudes of $Corr(m_X, m_Y)$ and $Corr(m_Y, m_X)$ (defined as within two-folds between the positive- and negative-lagged correlations), which potentially exhibiting oscillations. The example oscillatory trajectories shown in Figure 3.18 was generated from the parameter combination denoted by the white dot.

to “stochastic resonance”) can occur even under parameter regimes that are predicted to not oscillate according to deterministic models (Forger and Peskin, 2005; Li et al., 2005; McKane et al., 2007), thereby suggesting that in this circuit, stochasticity together with the appropriate coupling (i.e., governing the PoV) between genes X and Y can give rise to oscillations beyond classic “limit cycle” mechanisms.

We thus applied MAPPA to explore how the PoV between X and Y can regulate oscillatory behaviors when stochasticity in gene expression is present. To quantify oscillatory phenotypes, time-varying gene expression levels were transformed to the frequency domain via power spectra analysis. Since a dominant and narrow peak at a specific frequency is expected if the system is oscillating with a relatively constant period and amplitude (Figures Figure 3.18B, section A.14), we focused on two quantitative phenotypes: 1) the quality factor of oscillation (QF), quantifying how tall and narrow the dominant peak is, and 2) the peak frequency (PF), where the peak is located in the power spectrum (Figure 3.18B and A.11; section A.14) (Guisoni et al., 2016).

Predictive ML models for both QF (r = 0.87; Figure A.12A) and PF (r = 0.97; Figure A.12B) could be built (section A.7) after adding data sampled and simlulated from high QF (QF > 0.4) regions to mitigate the tendency of the initial ML model to underestimate QF when QF is large (Figure A.12A left). We also confirmed that the different sampling scheme did not show difference in ML model performance and the size of data is enough to cover the parameter space (Figure A.12C). Based on GVI, K_{YX} (the TF activity needed to achieve half maximal transcription rate of the target gene) and n_{YX} (the Hill coefficient) governing modulatory range and nonlinearity of protein

Y's suppression of mRNA X synthesis were among the most important for predicting QF (Figure 3.20A). Degradation rates (d_m^X, d_p^X, d_m^Y, and d_p^Y) were among the most important for predicting both QF and PF (Figure 3.20). We further examined parameter combinations and associated averaged LVI with higher QF (QF>0.4) (Figure 3.21). For these parameter combinations, protein degradation rates for X and Y (d_p^X and d_p^Y) tended to be similar to each other, yet matching mRNA degradation rates (d_m^X and d_m^Y)

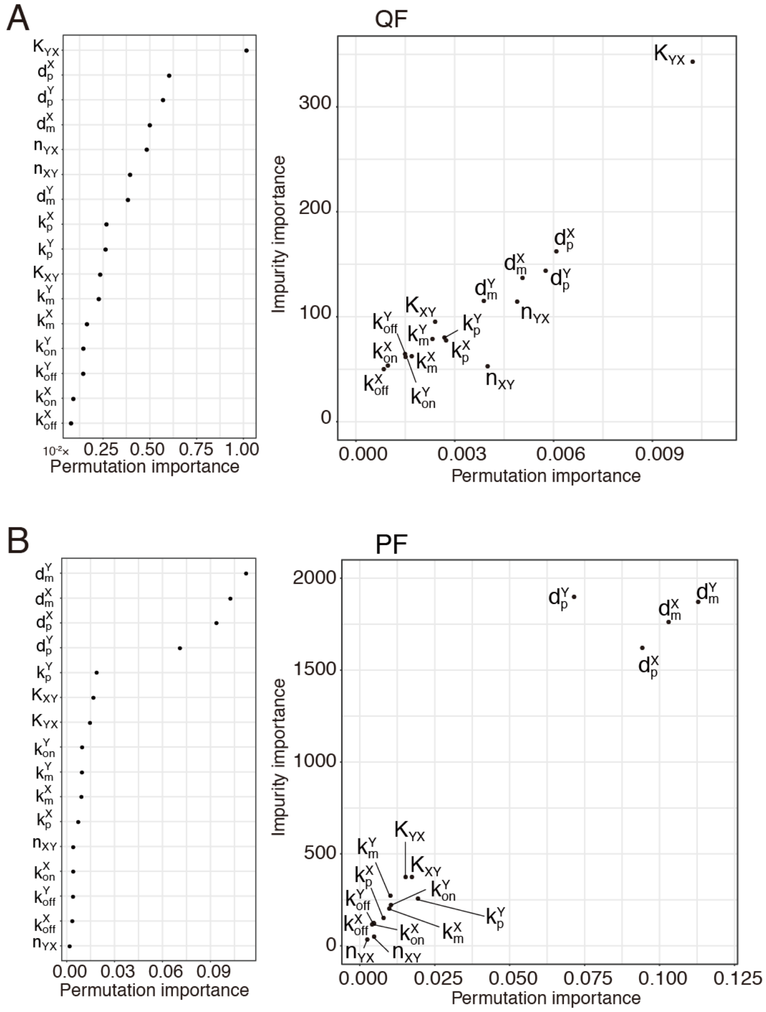

Figure 3.20 Global variable importance generated by ML models for oscillation phenotypes.**(A)-(B)** GVI of the RF regression model for (A) QF and (B) PF. (Left) Permutation GVIs are shown. (Right) Both permutation and impurity GVIs are shown.

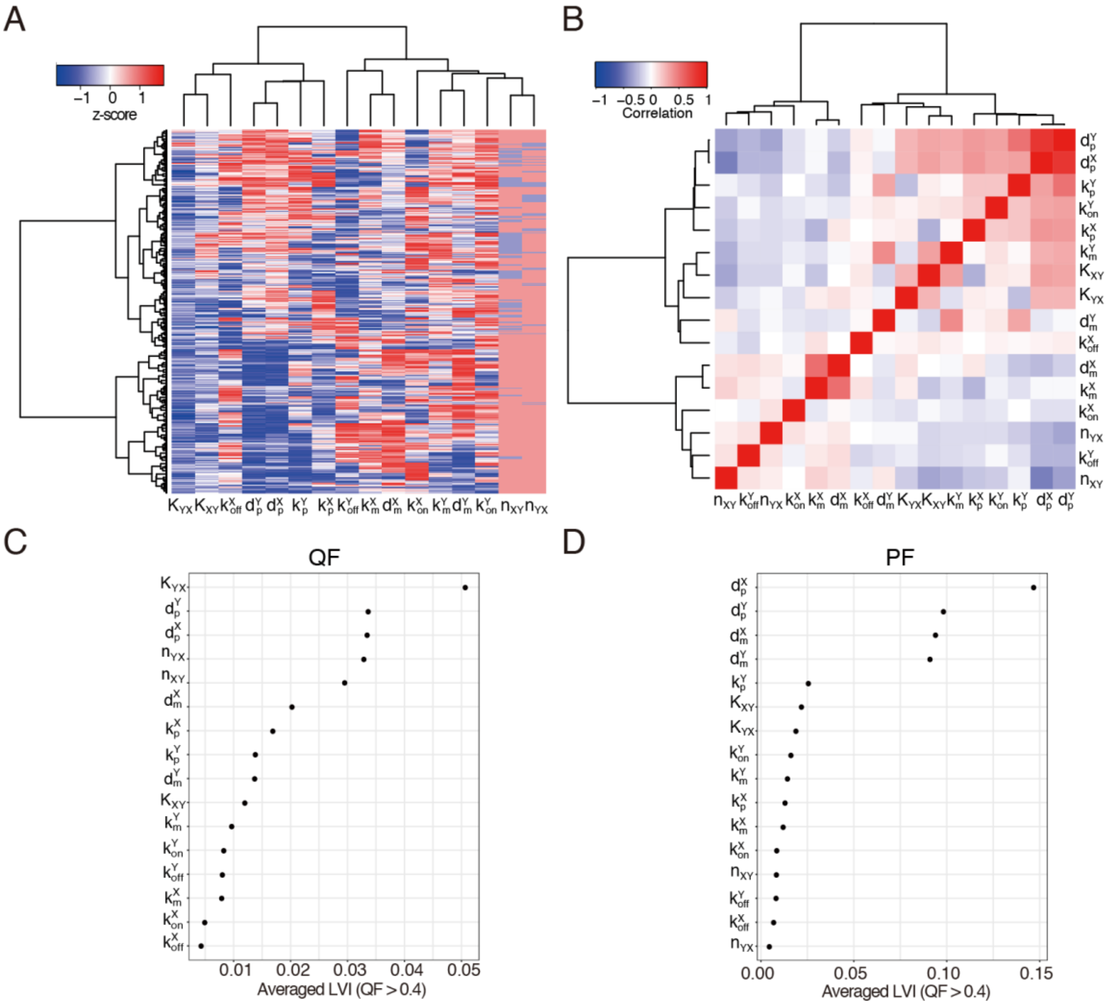

Figure 3.21 Closer examination on the high QF region. **(A)** Hierarchical clustered heatmap of combined parameter combinations (rows) with QF > 0.4. The color scale denotes the relative (z-score scaled) magnitude of the parameter value. **(B)** Correlation heatmap of combined parameter combinations with QF > 0.4. The color scale denotes Pearson correlation between parameters. **(C)-(D)** Averaged LVI for parameter combinations with QF > 0.4 for (C) QF and (D) PF.

was not necessary (Figure 3.21A-B). K_{YX} also needs to be low, and n_{YX} tends to be high so that even low levels of the Y protein can have a sizable suppressive effect on the transcription rate of gene X (Figure 3.21A). Averaged LVI for these parameter combinations revealed increased importance of d_p^X and d_p^Y for determining PF and decreased importance of d_m^X and d_m^Y for determining QF compared to corresponding GVI (Figure 3.22 and 3.21C-D), consistent with characteristic patterns revealed in parameter combinations (Figure 3.21A-B). Together, the appropriate nonlinearity and modulatory range of suppressive regulation and matching combination of relaxation time scales of proteins are required for robust oscillations and for setting the period. Deterministic modeling similarly suggested that nonlinearity due to a high Hill coefficient is required for oscillations (Gonze and Abou-Jaoudé, 2013), suggesting that, in general, parameters like n_{YX} may regulate both the "average" (as revealed by deterministic models) and fluctuation induced oscillatory phenotypes.

We next asked how stochasticity and PoV shape oscillatory phenotypes beyond the behavior predicted by deterministic models. Deterministic modeling predicted three non-overlapping classes of parameter configurations with distinct behaviors: 1) limit cycle oscillations (LC), 2) damped oscillations (DO), or 3) stable steady states (SS). We assessed the QF for each of the parameter combinations that fell within these individual phenotypic classes (Figure 3.22). This analysis revealed that even the non-

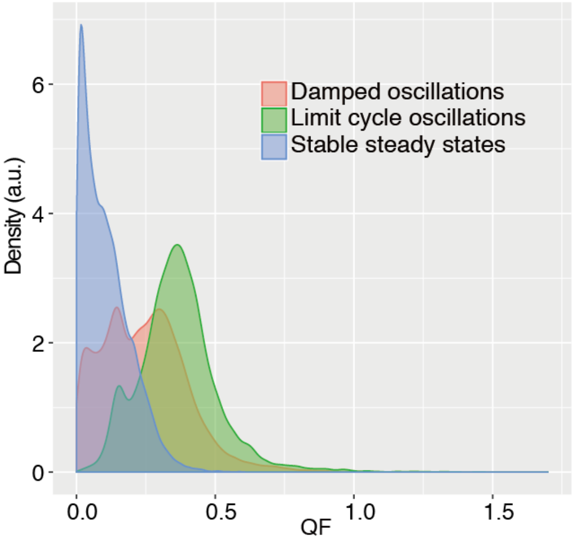

Figure 3.22 Distributions of QF shown by deterministic behavioral classes. QF is obtained by stochastic simulation over combined parameter combinations and plotted for each type of circuit behaviors classified by deterministic ordinary differential equation modeling; DO: damped oscillations, LC: limit cycle oscillations, and SS: stable steady states.

oscillatory parameter regimes (based on deterministic modeling) can have non-zero, sizable QF once the effect of stochasticity is considered, and each class has distinct but overlapping distributions of QF. As expected, LC had the largest fraction of its parameter combinations with high QF while SS had the least. More surprisingly, each of the three distributions span wide ranges and even some of the SS parameter combinations can have QF approaching the median of the LC distribution. These results suggest that stochasticity and PoV between X and Y may together be exploited by cells to attain and finetune oscillatory behavior beyond that predicted by deterministic considerations alone (Figure 3.22).

To assess the regulatory effects of the key parameters predicted by our ML model, we chose a parameter combination with high QF and varied both K_{YX} and n_{YX}, as suggested by their high LVI for QF at this particular point in parameter space (which belongs to the LC class exhibiting relaxation-type oscillations due to the strong feedback (low K_{YX} and high n_{YX}) based on deterministic modeling) (Figure 3.23A) (Gonze and Abou-Jaoudé, 2013). Our ML model predicted that increasing K_{YX} or decreasing n_{YX} can lower QF, which was confirmed using data from actual stochastic simulation (Figure 3.23B and 3.24A). While deterministic modeling suggested a qualitatively similar requirement of low K_{YX} for limit cycle oscillation (green area in Figure 3.24B), here with stochasticity considered a higher QF (e.g., QF>0.4) can be attained even when n_{YX} is lower (grey area in Figure 3.24B), especially when compensated by a lower K_{YX} (i.e., higher sensitivity to X suppression) (Figure 3.24). Our analyses thus revealed interesting insights on the regulation of noise induced oscillation in this feedback circuit. By utilizing naturally arising stochasticity and PoV,

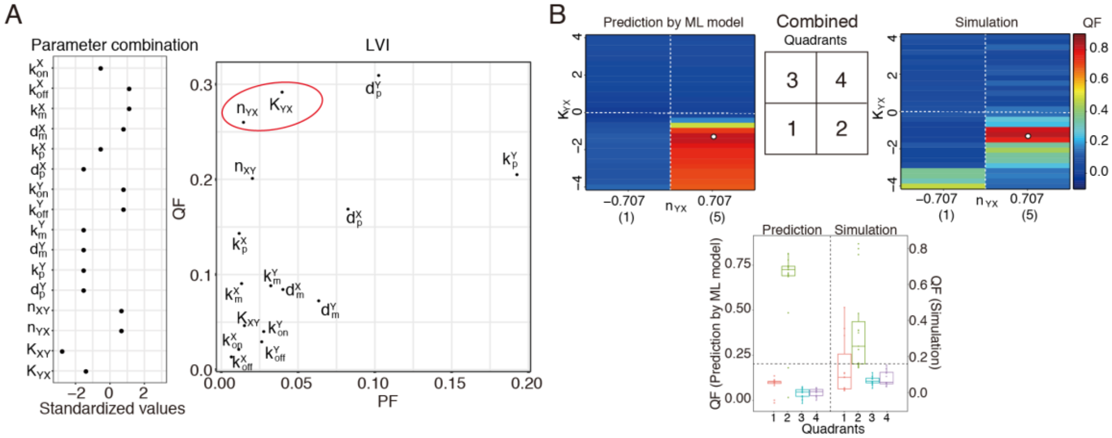

Figure 3.23 in-silico perturbation analysis using ML model. **(A)** A selected parameter combination for local, in silico perturbation analysis (left) and its LVI for QF and PF (right; shown as a scatter plot). The two parameters being perturbed are circled in red. **(B)** Comparison between ML prediction and stochastic simulation of QF as n_{YX} and K_{YX} were perturbed starting from the selected parameter combination (denoted by white dots). We compared the discrete/qualitative behavior by dividing the space into four quadrants with high/low values for n_{YX} and K_{YX} (shown in the middle) since the ML model was trained based on only two possible values of n_{YX}, -0.707 (on the relative scale; the original Hill coefficient value is 1) and 0.707 (the original Hill coefficient value is 5) (see section A.3). The QF predicted by the ML model is shown on the left of the quadrant map and the actual simulation is shown on the right. The change in QF across the quadrants is qualitatively consistent between the simulation and the prediction (bottom plot). The full simulation result, as the two parameters were perturbed along the continuous range, is shown in Figure 3.24A.

this circuit could generate oscillation even when n_{YX} is low and thus far from the DO-LC bifurcation point (where the system transitions from DO to LC; the boundary between green and pink areas in Figure 3.24B). Operating at a lower n_{YX} may be biologically more desirable as achieving high n_{YX} requires additional energy expenditure and thus allowing low n_{YX} can potentially improve operational robustness (e.g., under changing environments) (Estrada et al., 2016; Gonze and Abou-Jaoudé, 2013; Weiss, 1997). These results further illustrate how MAPPA can complement and provide information beyond analytically tractable models in a computationally efficient manner.

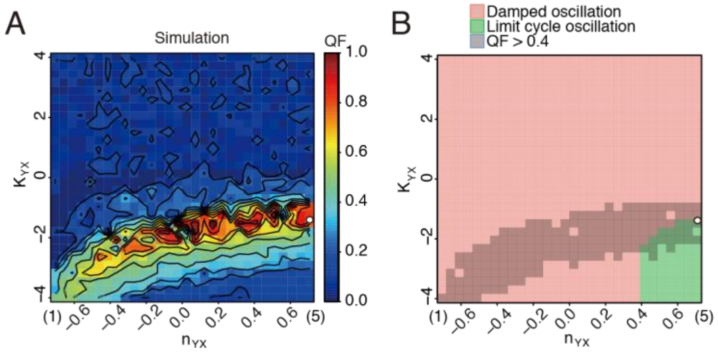

Figure 3.24 Bifurcation behavior of stochastic oscillations. **(A)** Stochastic simulation result of QF as n_{YX} and K_{YX} are perturbed starting from the parameter combination (denoted by a white dot) shown in (F). Here n_{YX} is varied continuously between the scaled/standardized values of -0.707 (corresponding to an original Hill coefficient of 1) and 0.707 (original Hill coefficient of 5). The color scale denotes QF. **(B)** The oscillatory behaviors predicted by deterministic modeling in the same parameter space shown in (A) (see section A.13). Damped oscillation regions are depicted in pink and limit cycle oscillation regions are in green. The "oscillatory" region (defined as those with QF>0.4) predicted by stochastic modeling is shown in grey.

3.2.6 Discussion

MAPPA generates and utilizes massive data from mechanistic simulation of biological models and builds ML models to map parameters to phenotypes. The resulting ML models can enable computationally efficient exploration of large parameter spaces and reveal which and how parameters affect a system's behavior at both the global and local (parameter dependent) levels. MAPPA can guide which parameters to measure, dissect the robustness and "optimality" of the system, suggest evolutionary trajectories, and empower synthetic biology (Arpino et al., 2013; Babtie and Stumpf, 2017; Shoval et al., 2012). Moreover, MAPPA can potentially be paired with approximate Bayesian computation methods for posterior estimation of model parameters based on real world data (Jagiella et al., 2017; Raynal et al., 2017).

MAPPA can in principle be applied to study systems comprising hundreds and thousands of parameters. Given the enormous parameter space, however, it may be computationally intractable to sample sufficient representative parameter combinations for training generalizable ML models. One strategy worth further testing, as we had explored above, would be to start with sparse random sampling and then increase the sampling depth incrementally but biasedly. For example, we can iterate between ML model evaluation (i.e., prediction performance) and targeted sampling from parameter regions associated with desired phenotypes but poor prediction performance. This scheme may converge towards informative models relatively quickly even when the number of parameters is large. For example, Loyola et al. (Loyola R et al., 2016) suggested an iterative sampling strategy that theoretically does not depend on the dimensionality of the input space, thus effectively avoiding the curse of dimensionality. As future work, incorporating such approaches to MAPPA can potentially enable efficient analysis of networks with orders of magnitude more parameters.

With the rapid expansion of high-throughput single-cell measurement technologies, we came to better appreciate the extensive cell-to-cell heterogeneity in diverse cell populations, present even in those that were thought to be relatively homogeneous (Tanay and Regev, 2017). As suggested by the complex correlation among genes across single cells or within individual cells over time (Eldar and Elowitz, 2010; Filipczyk et al., 2015; Martins et al., 2017), an essential source of cellular heterogeneity is the propagation of gene expression variations across the underlying regulatory network. Thus, a better understanding of this mechanism requires realistic stochastic modeling of gene regulatory networks across multiple genes describing gene products (mRNA and protein) as separate entities and keeping discreteness and nonlinearity of the system. Although CMEs can be an ideal treatment and there have been substantial developments in analytical theories of CMEs, those are still limited to simple models involving only one gene or one aggregate gene product (not separately modeling mRNA and proteins) if involving more than one gene. Even the simple two-gene circuit (Figure 3.3) is not tractable analytically yet even in a linear form to the best of our knowledge (Cao and Grima, 2018; Schnoerr et al., 2017). Various approximation schemes such as Fokker-Planck equations, linear-noise approximation and its variant with higher order terms, and moment-closure methods are available and successfully applied. However, these are relying on assumptions such as relatively large copy numbers of species, linearity, and unimodality of the system, which are not always the case for modeling gene regulatory networks. Therefore, the application of MAPPA on the gene circuit models we dealt with in this study represents good use cases, and the results we have shown suggest that MAPPA can complement the existing methods when these are unreliable.

Although we tried to keep details in modeling gene regulatory circuits compared to those analytically tractable, these still contained approximations of the actual gene expression dynamical processes (Rodriguez et al., 2019). Some underlying assumptions are worth mentioning. Promoter switching between active and inactive states is independent of the expression level of the upstream TF and decoupled from TF binding status of promoters, and the binding and unbinding interactions between TFs and promotors are fast enough to be approximated as the Hill-type functions. A recent work (Holehouse and Grima, 2019) illustrated that deterministically derived propensity functions in the form of the Hill-type functions are only accurate in the regime of fast promoter switching dynamics compared to other processes in the model under the assumption that TF binding is coupled with promoter switching. Although assumptions in (Holehouse and Grima, 2019) are not the same as those of our study, this suggests that our choice of the Hill-type functions for describing the regulation of TFs on the transcription of downstream genes may not always hold. However, in addition to the cooperative binding of molecules, several other molecular mechanisms were proposed in generating the Hill-type functions: such as energy expenditure-driven binding or multisite phosphorylation of TFs (Estrada et al., 2016; Gonze and Abou-Jaoudé, 2013; Weiss, 1997). Therefore, in this study, we did not specify molecular mechanisms of the Hill-type functions, which were instead considered phenomenological descriptions of quantitative relationships between the level of TFs and the effective transcription rates of downstream genes.

Taken together, utilizing the large amounts of data generated from bottom-up, mechanistic computational simulation of dynamical systems and the ability of modern machine learning approaches to “compress” such data to generate computationally efficient and interpretable models is a promising direction for dissecting complex dynamical systems.

Chapter 4: Quantitative dissection of immune homeostasis using multiscale modeling approaches

4.1 Introduction

The adaptive immune system mounts immune responses in an antigen-specific manner. To enable this efficiently for vastly diverse pathogens, lymphocytes such as T cells and B cells express unique receptors generated through the random combination of relevant genetic loci for each cell to recognize unique molecular patterns from pathogens. Once these cells recognize cognate foreign antigens under proper costimulatory signals provided by antigen-presenting cells (APCs), they undergo clonal expansions accompanying differentiation to effector cell types. However, this process possesses an inherent danger of recognizing self, thereby potentially leading to autoimmune diseases. The immune system has evolved several mechanisms of self-tolerance to mitigate such aberrant outcomes. In the thymus, newly generated precursors of T cells undergo positive and negative selection, through which only thymocytes that recognize the self-peptide- histocompatibility complex (self-pMHC) molecules above a particular affinity (positive selection), but not too strongly (negative selection) survive and move out to the periphery as naïve conventional T cells. Most of those who recognize self too strongly are either removed or directed to become regulatory T cells (Tregs). These Tregs play a crucial role in the peripheral self-tolerance through various modalities to suppress the activation of naïve self-reactive T cells in secondary lymphoid organs (SLOs) or effector functions of self-activated T cells in tissues.

Recently, experimental evidence suggested that self-reactive T cells are remarkably prevalent in the periphery due to incomplete thymic deletion (Moon et al., 2011; Yu et al., 2015). The frequencies of self-specific T cells were shown to be comparable to those of foreign-specific T cells (Moon et al., 2011; Yu et al., 2015). Moreover, such self-reactive T cells get activated secreting IL-2, undergo several rounds of proliferation, and eventually get pruned out through apoptosis (Liu et al., 2015; Wong et al., submitted). This whole process is possible due to suppression through localized spatiotemporal and functional regulations of regulatory T cells, mainly dependent on IL-2 secreted by self-activated T cells (Liu et al., 2015; Wong et al., submitted). Intriguingly, separate lines of studies illustrated that the peripheral maintenance of the Treg population pool is dependent on IL-2 (Amado et al., 2013; O’Gorman et al., 2009; Smigiel et al., 2014). Blocking or knock-out of endogenous IL-2 showed a decrease in the pool size of peripheral Tregs resulting in autoimmunity while external IL-2 injection showed the opposite, thereby showing promising outcomes for treating various autoimmune diseases (Amado et al., 2013; Rosenzwajg et al., 2019; Stolley and Campbell, 2016). Moreover, primary IL-2 producers responsible for homeostatic Treg maintenance were shown to be CD4$^+$ T cells, and in homeostatic SLOs, 1-2% of CD4$^+$ T cells are secreting IL-2 at any given moment (Amado et al., 2013; Liu et al., 2015; Owen et al., 2018). In the spleen, such T cells were self-reactive (Stolley and Campbell, 2016). Together, these studies illustrate that the maintenance of immune homeostasis involves dynamical and multilayered regulatory mechanisms between self-activated CD4$^+$ T cells and Tregs. Whereas individual self-activated CD4$^+$ T cells are dynamically constrained by nearby Tregs, the peripheral maintenance of a physiologic Treg population size requires IL-2, and primary producers of IL-2 are likely self-activated CD4$^+$ T cells in SLOs. This suggests that immune homeostasis is established as dynamical equilibrium between self-activated CD4$^+$ T cells and Tregs at the cellular and cell population levels.

Although a list of numerous parts regarding immune homeostasis has been accumulated, the integrated quantitative framework has remained to be developed 1) to comprehensively dissect critical immune parameters governing robust self/non-self discrimination, 2) to intuitively understand at what level and how the sharp transition between tolerance and full-blown response occurs, and 3) to guide therapeutic manipulations of immune homeostasis to treat cancer and autoimmune diseases. To achieve this goal, we employed multiscale modeling approaches to quantitatively describe reciprocal relationships between self-reactive CD4$^+$ T cells and Tregs occurring across scales from the intracellular level to the organismal level. First, we developed a multiscale dynamical model describing T cell activation out of cellular interactions among CD4$^+$ conventional T cells (Tconvs), dendritic cells (DCs), Tregs with their evolving internal states (Wong et al., submitted). We found that the activation status of activated Tconvs such as the duration of IL-2 secretion and the responsiveness to IL-2 is regulated mainly by the Treg density in homeostasis and by the costimulatory ligand level of DCs in inflammation. Some of these results were experimentally validated. Then, we built probabilistic models of clonal expansion of self-activated Tconvs occurring through paracrine IL-2 signals. We showed that the activation status of recently self-activated Tconvs and the frequency of self-activated, IL-2 secreting Tconvs in SLOs shape a sharp transition between tolerance and full-blown responses, conferring an extremely low probability of clonal expansion in homeostasis. Finally, we built cell population models of peripheral maintenance of Treg pool size at the intranodal and organismal levels. We showed that the homeostatic IL-2 niche size provided by the homeostatic pool size of self-activated, IL-2 secreting Tconvs is indeed sufficient to maintain the homeostatic Treg pool size. Based on these modeling results, we derived an integrated quantitative framework illustrating immune homeostasis as dynamical equilibrium between self-activated, IL-2 secreting T convs and Tregs, which is away from thresholds of clonal expansion causing autoimmune diseases. Then, we explored several corollaries of this framework.

4.2 Results

4.2.1 Multiscale T cell activation model recapitulates the two-phase response

T cells require TCR, CD28, and cytokine-mediated signals such as IL-2 to be activated and undergo proliferation and differentiation to effector cell types. Myc was shown to be an integrator of these signals and translates into the proliferation capacity (Heinzel et al., 2017; Marchingo et al., 2014). However, *in vivo* acquisition of these signals by a T cell undergoing activation engaged with DCs while subject to Treg-mediated suppression is a highly dynamical process with interlinked interactions occurring at the intra- and intercellular levels (Figure 4.1A-C). Therefore, it is challenging to intuit the full dynamical picture of this process, although detailed knowledge of important molecular and cellular components has been accumulated. To better delineate the

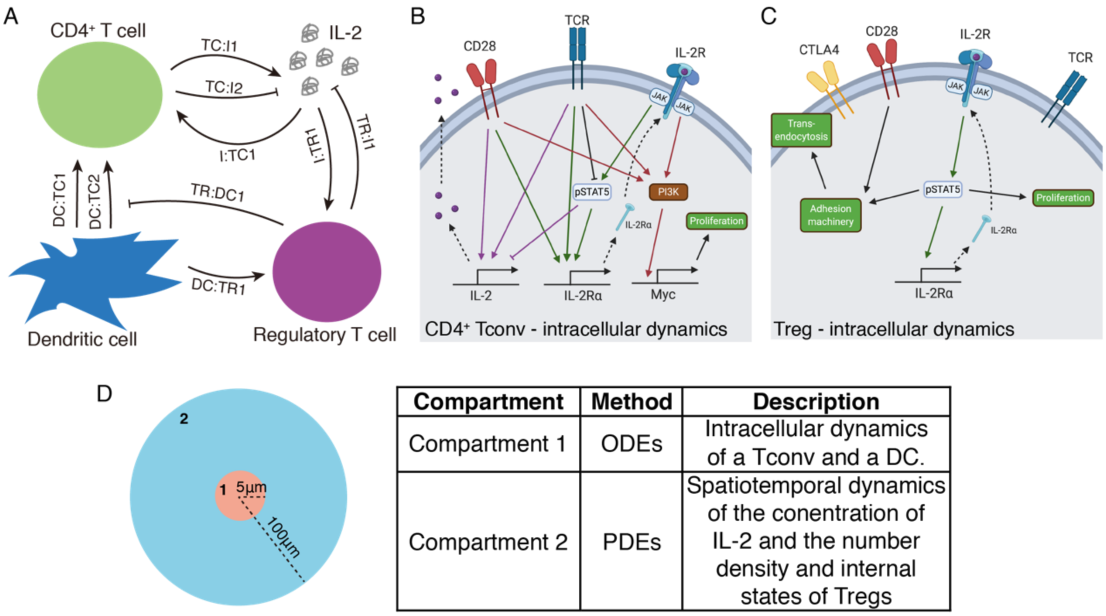

Compartment	Method	Description
Compartment 1	ODEs	Intracellular dynamics of a Tconv and a DC.
Compartment 2	PDEs	Spatiotemporal dynamics of the conentration of IL-2 and the number density and internal states of Tregs

Figure 4.1 Model schematics of the T cell activation model. **(A)** Model schematic of cellular interactions. Participating cells are a conventional CD4$^+$ T cell (Tconv), a dendritic cell (DC), and surrounding regulatory T cells (Tregs). IL-2 also mediates cellular interactions. **(B)** Model schematic of intracellular signaling pathways of the Tconv. **(C)** Model schematic of intracellular signaling pathways of the Treg. **(D)** Model schematic of the spatial compartments. Spatial compartments are divided into two regions. In Compartment 1, intracellular dynamics of the Tconv and DC are described using ordinary differential equations. In Compartment 2, the spatial movements and internal state evolutions of Tregs and diffusions of IL-2 are described using partial differential equations. See Methods for detailed model descriptions. ODE-ordinary differential equation; PDE-partial differential equation.

quantitative contribution of key immunological parameters on the extent of activation and proliferation of a responding T cell in SLOs, we developed a multiscale, dynamical model of T cell activation occurring through intra- and intercellular processes of a priming Tconv, DC, surrounding Tregs, and secreted IL-2 (Figure 4.1; section B.1) (Wong et al., submitted).

Our strategy of model development was to integrate existing models of each component from the literature into a single framework (See section B.1 for detailed descriptions of the model). We described intracellular dynamics of molecular species in the Tconv and DC with ordinary differential equations (ODEs) and spatial dynamics of the concentration of IL-2 and the number density and internal states of Tregs with partial differential equations (PDEs) (Figure 4.1D). These descriptions in two different compartments are connected using boundary conditions at $r = 5\ \mu m$. We employed several key assumptions and added new features based on these in building the model (section B.1). The variables and parameters of the model are shown in Table B.2 with corresponding references.

Next, we generated dynamical trajectories of the model in various conditions (Figure 4.2). The baseline condition from a randomly selected model parameter combination represents homeostatic regulation of a self-activated Tconv, where the rapid loss of CD80/86 and thus costimulation through trans-endocytosis by Tregs plays a role as a rate-limiting process (Qureshi et al., 2011). The resultant early cease of IL-2 secretion did not allow IL-2Ra level to increase high enough for autocrine IL-2 signaling and thus led to a low level of pSTAT5. The Myc level, representing proliferation capacity (Heinzel et al., 2017), increased indicative of a few rounds of

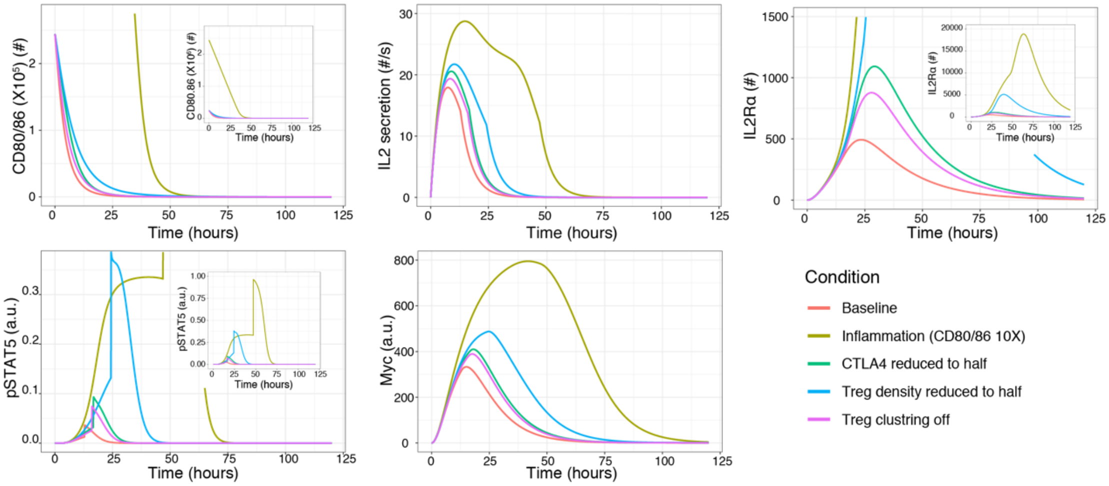

Figure 4.2 Dynamical trajectories of key molecular species during T cell activation. The simulation was conducted for various conditions. The baseline condition represents the situation of the successful suppression of self-activated T cells by Tregs simulated on a randomly sampled parameter combination. Other conditions represent conditions where indicated parameters are perturbed.

proliferation but decreased early before reaching significant accumulation due to early stopping of TCR and costimulation and the lack of IL-2 signal. In contrast, other conditions showed delayed loss of costimulation, the resultant prolonged IL-2 secretion, higher accumulation of IL-2Ra owing to longer duration of autocrine IL-2 signaling. Finally, prolonged and higher Myc accumulation occurred, suggesting increased proliferation capacity. The most distinguished condition was inflammation, where the costimulatory ligand level in DCs increased by 10-fold from the homeostatic value. The next influential condition was half reduction of the initial Treg density. The rest conditions, reducing the level of CTLA4 of Tregs to half and turning off Treg clustering, showed similar differences from the baseline condition with a modest increase of T cell activation/proliferation status. These simulation results quantitatively recapitulate experimental findings such as inflammation as additional information on the invasion of non-self and autoimmunity occurring due to dysregulation of the peripheral Treg population pool size. In turn, in the inflammatory condition, the current modeling assumptions are not sufficient to prevent self-reactive T cells from escaping Treg's suppression, thereby warranting additional mechanisms such as trogocytosis by Tregs for stealing cognate antigens from APCs (Akkaya et al., 2019).

These simulation results illustrated how TCR, CD28, and IL-2 signals are dynamically regulated in *in vivo* settings. We can summarize the dynamics of these signals into two phases (Figure 4.3) (Waysbort et al., 2013). Initially, Tconvs undergo activation based on TCR and CD28 signals from DCs, but lack IL-2 signaling due to the low level of IL-2Ra (Phase 1). Once the priming Tconvs disengage from APCs, the only signal they further obtain is through autocrine and/or paracrine IL-2 signaling

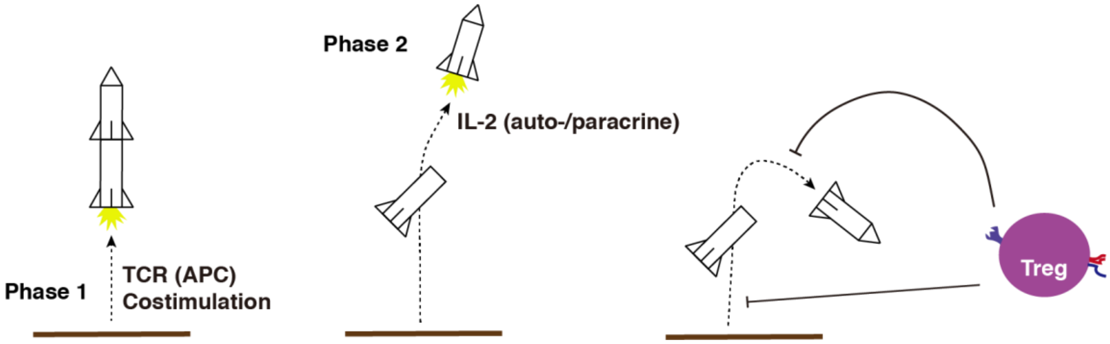

Figure 4.3 The two-phase response of Tconvs. The temporal dynamics of Tconv activation can be decomposed into two phases.

(Phase 2). Suppression by Tregs makes self-reactive T cells in homeostasis, although they do activate through phase 1, rarely achieve the capacity to proceed to phase 2 by lowering autocrine IL-2 availability and IL-2 sensing capacity (low IL-2Ra).

4.2.2 MAPPA analysis revealed generalizable quantitative roles of immune parameters for T cell activation status

Simulation results above, however, could hold only for the particular parameter combinations we chose due to the nonlinear feature of the model. Therefore, we applied the MAPPA (MAchine learning of Parameter-Phenotype Analysis) framework we developed (Park et al., 2019) (Chapter 3) to assess the robustness vs. turnability of various phenotypes throughout the plausible parameter space by quantifying relative contributions of immune parameters (Figure 3.1 and 3.2). MAPPA utilizes unbiased sampling of parameter combinations from the plausible parameter space, variations of quantitative phenotypes in the parameter space, and machine learning (ML) models trained by Random Forests (RF) mapping the parameter space to phenotypes. We defined biologically plausible ranges of parameters from phenomenological descriptions such as signaling transductions described by the Hill functions or those

Name	Definition	MATLAB notation	min	max
$\boldsymbol{\nu}$	pMHC-TCR on-rate	nu	0.2	0.4
$\boldsymbol{K_{TCR \rightarrow IL2R\alpha}}$	Half saturation level (EC50) of TCR activation for IL2Rα production	K_TCR_IL2R_alpha	0.1	1
$\boldsymbol{K_{costim \rightarrow IL2R\alpha}}$	Half saturation level (EC50) of costimulation for IL2Rα production	K_costim_IL2R_alpha	10	100
$\boldsymbol{K_{JAK \rightarrow pSTAT5}}$	Half saturation level (EC50) of JAK activation for IL2Rα production	K_JAK_pSTAT5	0.01	0.1
$\boldsymbol{K_{TCR \rightarrow IL2}}$	Half saturation level (EC50) of TCR activation for IL2 production	K_TCR_IL2	0.1	1
$\boldsymbol{K_{costim \rightarrow IL2}}$	Half saturation level (EC50) of costimulation for IL2 production	K_costim_IL2	10	100
$\boldsymbol{K_{pSTAT5 \rightarrow IL2}}$	Half saturation level (EC50) of costimulation for IL2 production	K_pSTAT5_IL2	0.1	1
$\boldsymbol{K_{TCR \rightarrow PI3K}}$	Half saturation level (EC50) of TCR activation for PI3K activation	K_TCR_PI3K	0.1	1
$\boldsymbol{K_{costim \rightarrow PI3K}}$	Half saturation level (EC50) of costimulation for PI3K activation	K_costim_PI3K	10	100
$\boldsymbol{K_{JAK \rightarrow PI3K}}$	Half saturation level (EC50) of JAK activation for PI3K production	K_JAK_PI3K	0.01	0.1
$\boldsymbol{D_{IL2}}$	Diffusion constant of IL2	D_IL2	10	100
$\boldsymbol{n_{tr0}}$	Initial number density of Tregs	n_tr0	0.0001	0.001
$\boldsymbol{f_{cont\_low}}$	Basline contact efficiency between Tregs and DCs	f_contact_low	0.1	0.4
$\boldsymbol{f_{cont\_high}}$	Stimulated contact efficiency between Tregs and DCs	f_contact_high	1	2.5
$\boldsymbol{L_{antigen}}$	Number of peptide-MHC per cell	L_antigen	100	1,000
$\boldsymbol{L_{CD80 \mid CD86\_i}}$	Initial number of CD80/86 molecules per cell	L_CD80_86_i	(homeo) 100,000 (inflam) 300,000	(homeo) 1,000,000 (inflam) 3,000,000

Table 4.1 Ranges of parameter values used for the MAPPA framework. The ranges span an order of magnitude for each cell. The MATLAB notations were used to denote parameters in the main text and figures. homeo-homeostasis; inflam-inflammation.

varying dynamically or across cells such as the number density of Tregs, or those without consensus values such as the diffusion coefficient of IL-2 within their plausible ranges. We fixed the rest of the parameters obtained from biophysical or biochemical experimental measurements (Table 4.1). We sampled 20,000 random parameter combinations within the aforementioned plausible ranges of parameters and conducted simulations on them. We tested two different ranges of the initial costimulatory ligand level (CD80/86), 100,000-1,000,000 for the homeostatic condition and 300,000-3,000,000 for the inflammatory condition, given that the mature and inflammatory dendritic cells tend to upregulate CD80/86.

From the simulation results, we focused on various aspects of T cell activation status. (Figure 4.4). We categorized the phenotypes into the receiver, sender, and signal integrator (Figure 4.4A). For the receiver, we defined a phenotype, the maximum level of IL-2Ra (IL-2Ra.max) in the time course, which reflects the capacity of a priming T cell to "receive" auto-/paracrine IL-2 signals to proceed to the Phase 2 response. For

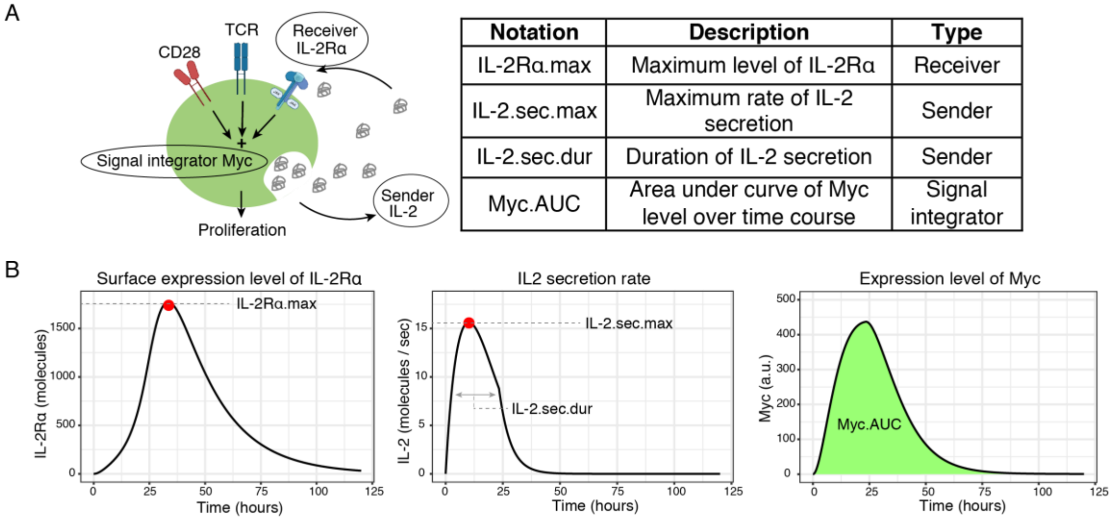

Notation	Description	Type
IL-2Rα.max	Maximum level of IL-2Rα	Receiver
IL-2.sec.max	Maximum rate of IL-2 secretion	Sender
IL-2.sec.dur	Duration of IL-2 secretion	Sender
Myc.AUC	Area under curve of Myc level over time course	Signal integrator

Figure 4.4 Definition of activation phenotypes. **(A)** (Left) The activation phenotypes can be divided into the receiver (associated with IL-2Ra), the sender (associated with IL-2), and the signal integrator (associated with Myc) phenotypes. (Right) Based on this categorization, we defined phenotypes, the maximum level of IL-2Ra (IL-2Ra.max), the maximum rate of IL-2 secretion (IL-2.sec.max), the duration of IL-2 secretion (IL-2.sec.dur), and the area under curve of Myc time course (Myc.AUC). **(B)** Detailed definitions of the phenotypes based on dynamical trajectories of IL-2Ra, IL-2, and Myc are shown.

the sender, we defined two phenotypes, the maximum IL-2 secretion rate (IL-2.sec) and the effective duration of IL-2 secretion (IL-2.dur), which reflect the capacity of a priming T cell to “send” auto-/paracrine IL-2 signals to itself or nearby conventional/regulatory T cells by creating an IL-2 niche. For the signal integrator, we defined a phenotype, the area under the curve of the time course of Myc (Myc.AUC), which reflects the “integration” of all activation signals through TCR, CD28, and IL-2, interpreted as proliferation capacity according to the Hodgkin’s model (Heinzel et al., 2017).

Simulations on 20,000 parameter combinations in homeostatic and inflammatory conditions revealed the distributions of phenotypes across the parameter space (Figure 4.5). The distributions of IL-2Ra.max showed that the majority of parameter combinations exhibited low IL-2Ra.max in both homeostatic and inflammatory conditions, which is consistent with our earlier report that responding T cells rarely achieve high pSTAT5 level indicative of IL-2 signaling in homeostasis (Liu et al., 2015; Wong et al., submitted). The difference between these two conditions was better delineated in the log scale, revealing the increased mode and heavier right tail of the distribution in the inflammatory condition. Myc.AUC and IL-2.sec.dur showed very distinct distributions with inverted skewness between the homeostatic and inflammatory conditions while IL-2.sec.max did not. These results suggest that inflammation exerts differential regulatory effects on different phenotypes of T cell activation.

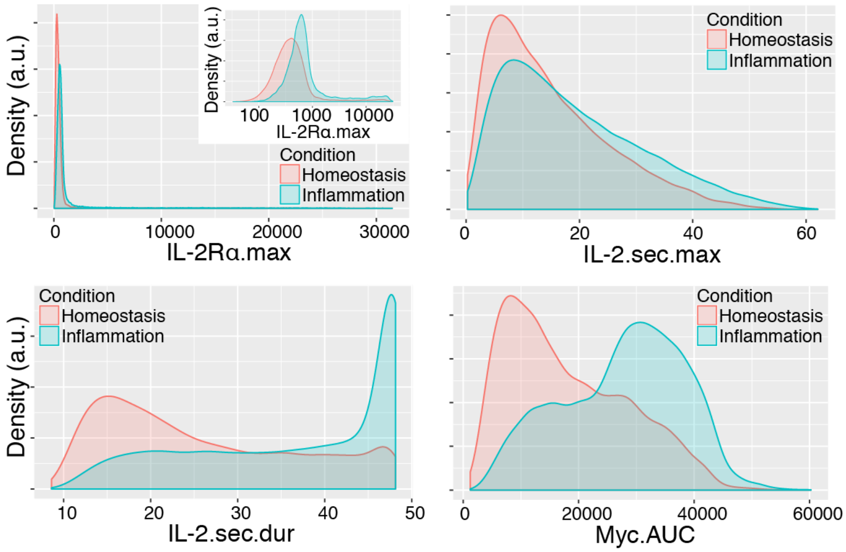

Figure 4.5 Distributions of activation phenotypes generated by simulations. The simulation was conducted on 20,000 randomly sampled parameter combinations for two different conditions, homeostasis and inflammation. For the definitions of phenotypes, see Figure 4.4.

For quantitative delineation of such phenotypic variations contributed by parameter variations, we trained predictive RF ML models for each phenotype, which map parameter combinations to phenotypes with quantification of each parameter’s importance (Figure 4.6 and B.1). Indeed, the phenotypes, IL-2Ra.max, IL-2.sec.dur, and Myc.AUC exhibited distinct regulatory contributions of parameters between homeostasis and inflammation (Figure 4.6A, C, and D) as alluded by their different distributions between conditions (Figure 4.5). The initial Treg density (n_tr0) was the most influential for these phenotypes in homeostasis, whereas the initial costimulatory ligand level (L_CD80_86_i) was so in inflammation. Interestingly, in both conditions, the TCR off-rate (nu) of the responding T cell was lowly ranked for these phenotypes. In contrast, the phenotype, IL-2.sec.max was affected mostly by the TCR off rate (nu) in both conditions (Figure 4.6B), which was consistent with the similar phenotypic distributions in both conditions (Figure 4.5). Together, these results suggest a

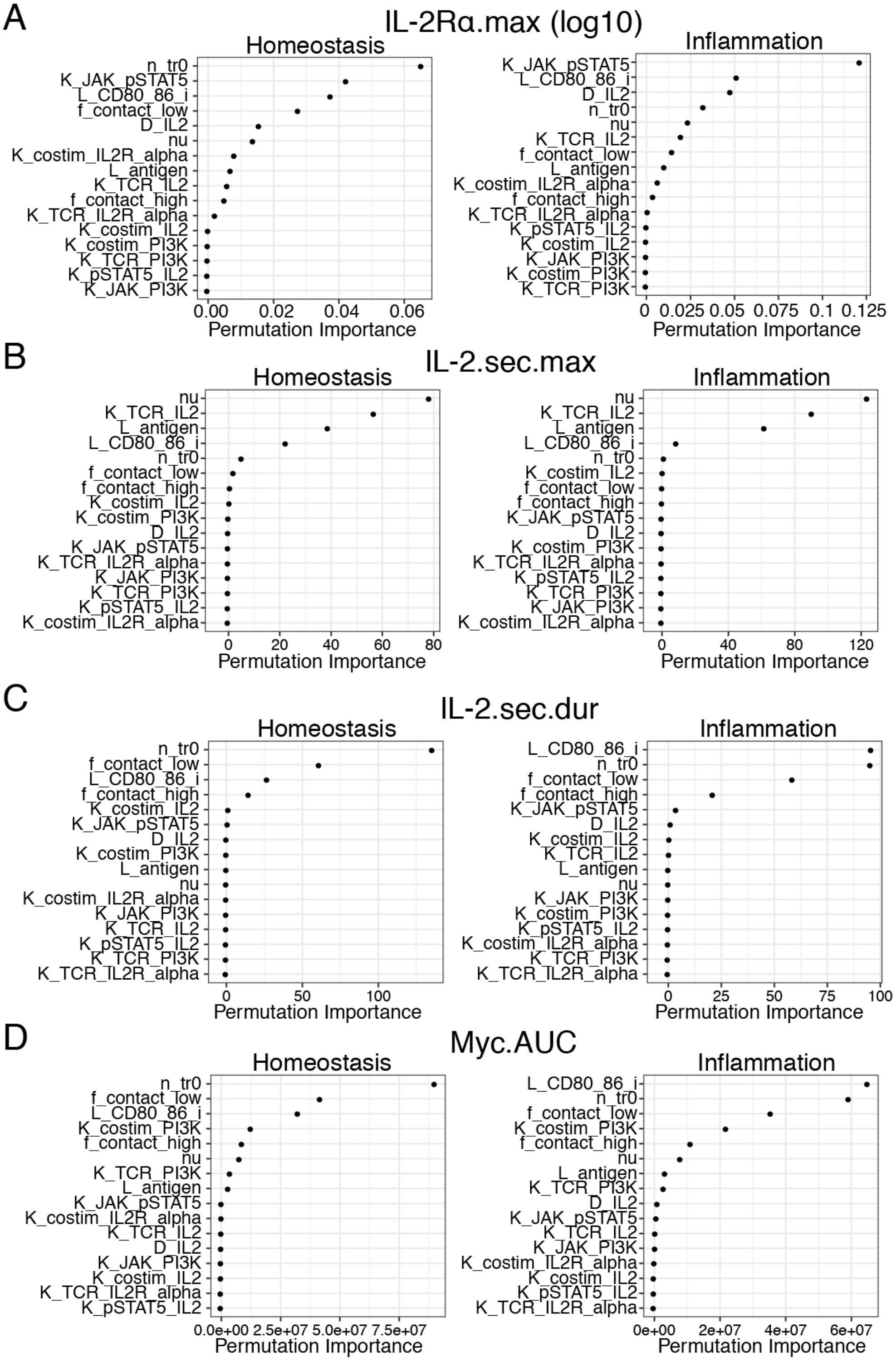

Figure 4.6 Global variable importance determining the activation phenotypes. **(A)** for IL-2Ra.max (log10) after taking log10 of IL-2Ra.max, **(B)** for IL-2.sec.max, **(C)** for IL-2.sec.dur, and **(D)** for Myc.AUC. Permutation importance is generated as decrease of prediction performance after permuting each parameter across parameter combinations. (Left) homeostasis and (right) inflammation.

quantitative insight on the relative importance of immune parameters for regulating different activation phenotypes in deferent contexts (homeostasis and inflammation). The predisposed Treg density is the primary regulator of IL-2Ra.max, IL-2.sec.dur), and Myc.AUC in homeostasis. However, the upregulated costimulatory ligand level inflammation overrides the regulatory effect of the Treg density, enabling the responding T cells to be more receptive to IL-2 signal (higher IL-2Ra.max), secreting IL-2 over a longer duration (higher IL-2.sec.dur), and more proliferative (higher Myc.AUC) (Yi et al., 2018; Wong et al., submitted).

4.2.3 Modest reductions in micro-domain size or molecular functionality enable self-activated T cells to respond to IL-2

Next, we sought to explore an experimentally accessible phenotype. We focused the maximum pSTAT5 signal within the Tconv (pSTAT5.max; categorized as the escapee phenotype) at any time point following activation (up to 120h) in homeostasis since this phenotype reflected the extent of escape from Treg control in our experimental studies (Figure 4.7) (Wong et al., submitted). As shown in Figure 4.9, the majority of

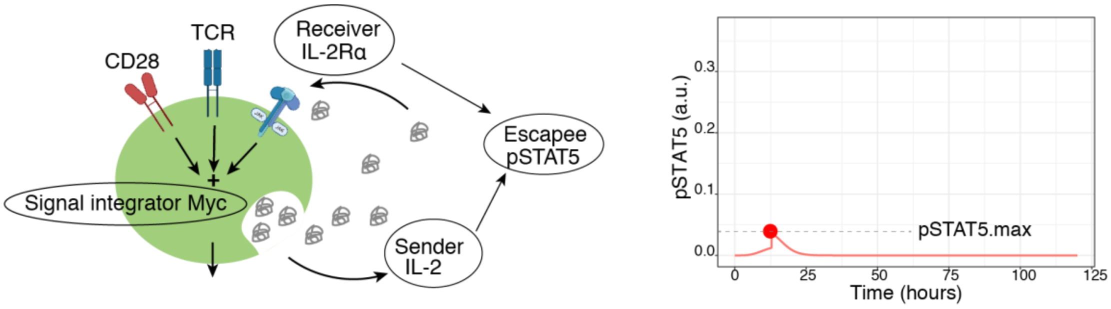

Figure 4.7 Definition of the escapee phenotype. The maximum level of pSTAT5 (pSTAT5.max) signal can be seen as the extent of escape. A high level of pSTAT5 signal indicates that the responding Tconv can accumulate a high level of IL-2Rα and secrete IL-2 for a long duration, resulting in autocrine IL-2 signal.

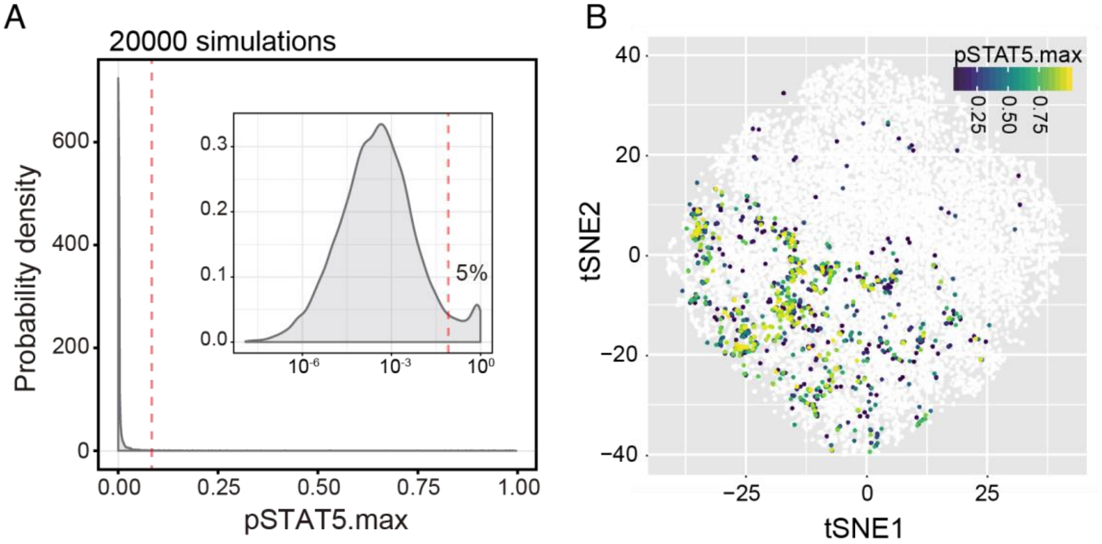

Figure 4.9 Distribution of pSTAT5.max generated by simulation. **(A)** Distribution of pSTAT5.max values from 20000 dynamic simulations. Inset: distribution of pSTAT5.max values plotted on a log10 scale for visual clarity. Dashed red line represents a discrete threshold for parameter configurations within the top 5% of the distribution **(B)** Two-dimensional visualization of sampled parameter space using t-distributed stochastic neighbor embedding (t-SNE). Each dot represents a parameter configuration. Colored dots represent configurations with pSTAT5.max values within the top 5% of the distribution while white dots represent those outside.

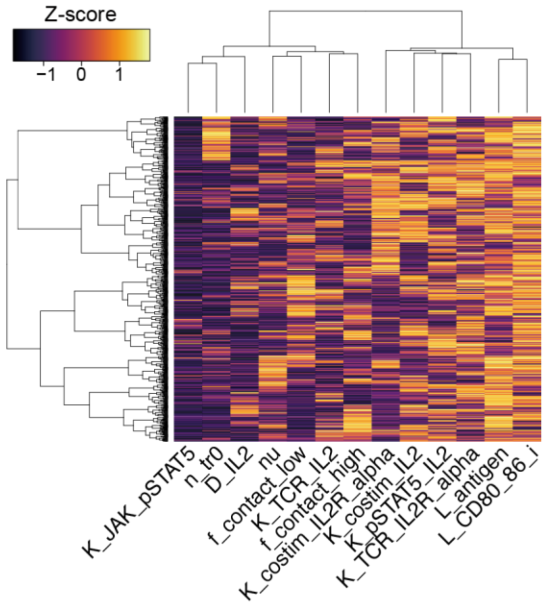

Figure 4.8 Closer examination of parameter configurations with high pSTAT5.max. Heatmap illustrating individual parameters (columns) and their standard scores (Z-score) within each configuration (rows) from the top 5% of the pSTAT5.max distribution.

parameter configurations generated a low pSTAT5.max. This result was consistent with the nearly negligible frequency of pSTAT5^{+} CD4^{+} T cells in LNs of healthy animals (Wong et al., submitted) and suggested that the three-cell circuit was largely robust against parameter variation. However, examination of the few configurations that did produce a large pSTAT5.max — referred to as "active" configurations — revealed characteristic features, such as a high level of costimulatory ligand on the surface of DCs (L_CD80_86_i) and a low initial Treg density (n_tr0) (Figure 4.8, Table 4.1).

We generated a predictive RF ML regression model to determine the influence of individual parameters on the pSTAT5.max quantitatively (prediction accuracy: r = 0.95) (Figure B.2). The ML model revealed that the Treg density (n_tr0) ranked second highest in terms of "variable importance" both globally, across all parameter configurations, and locally, for a specific configuration associated with large

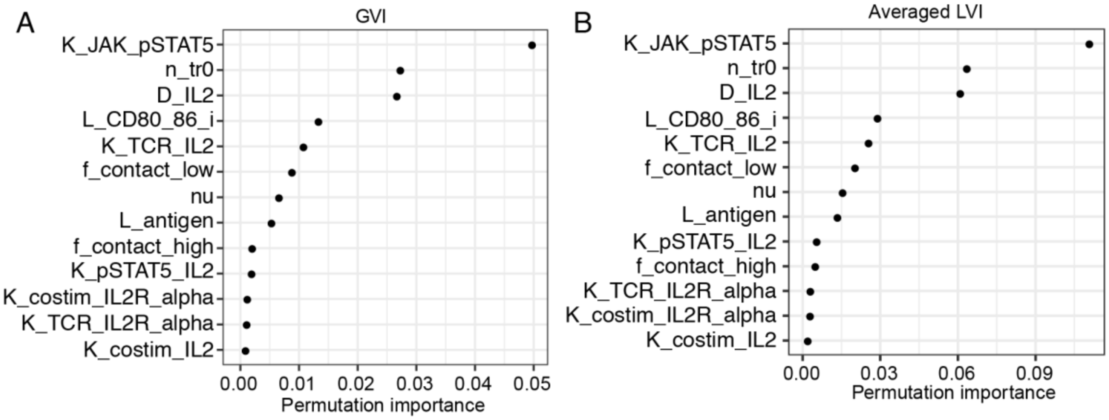

Figure 4.10 Variable importance generated by ML model for pSTAT5.max. **(A)** Global variable importance (GVI) of the dynamical model parameters (y-axis) fitted by the RFML regression model using "combined data" (see Figure B.2B). "Permutation importance" (x-axis) represents the increase in prediction errors using out-of-bag (OOB) data after permuting the indicated parameters. **(B)** Averaged local variable importance (LVI) of the parameter configurations above the cut-off for the pSTAT5.max shown in Figure 4.9A. The LVI was calculated using the combined data model described above. "Permutation importance" (x-axis) represents the increase in prediction errors for the OOB data after permuting the indicated variables.

pSTAT5.max values. (Figure 4.10). Both the costimulatory ligand level (L_CD80_86_i) and the TCR-pMHC off-rate (nu) were also important, although to a lesser extent. As expected, the EC50 for pSTAT5 (K_JAK_pSTAT5) was the highest ranked parameter (Figure 4.10).

Thus, during homeostasis, MAPPA revealed that the density of Tregs within a micro-domain largely dictated whether a self-activated T cell responded to IL-2. To further study this prediction, we ran new sets of simulations to assess the impact of increasing or decreasing the Treg density by two-fold on the number of active configurations. These simulations revealed that increasing the Treg density decreased the number of active configurations by ~2.5-fold, while decreasing this parameter resulted in a ~2-fold increase, findings that were consistent with the predictions from the RF model described above (Figure 4.11 and 4.11).

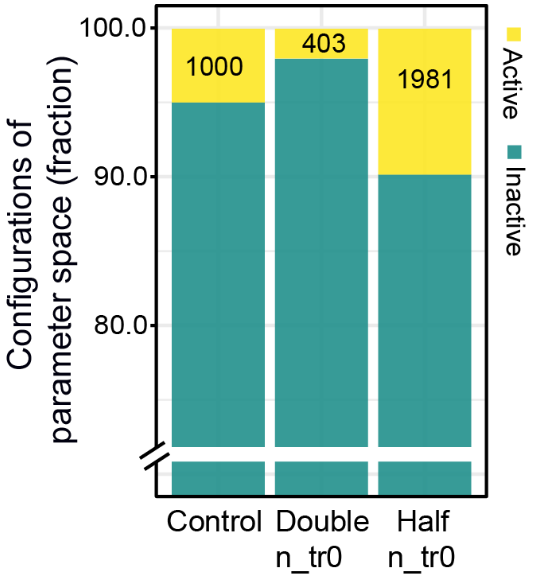

Figure 4.11 Effect of the perturbation of the Treg density. Stacked bar graphs depict the percentage of active and inactive configurations in parameter space when the Treg density is increased or decreased by two-fold. The control represents the results from the original 20000 dynamic simulations, while each perturbation represents the results from a set of 20000 new dynamic simulations

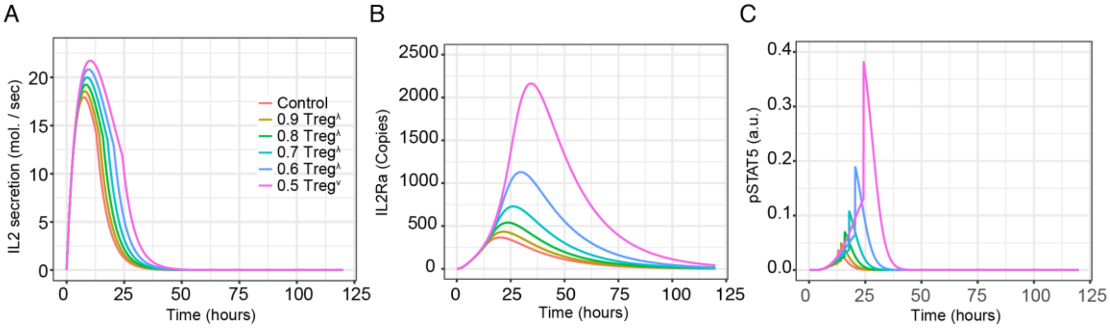

Figure 4.12 Dynamical trajectories of the model with different Treg densities. **(A)-(C)** Dynamical trajectories of (A) IL-2 secretion, (B) IL-2Rα protein copy number, and (C) pSTAT5 signal in a CD4$^+$ T cell as the Treg density is varied. The control condition represents an inactive configuration that was picked at random from parameter space.

To understand why the Treg density had such a substantial impact on the number of active configurations, we examined the dynamic trajectories of IL-2 secretion, IL-2Rα expression, and pSTAT5 signaling in CD4$^+$ T cells as the Treg density was lowered linearly down to 50% (Figure 4.12). This analysis revealed that as the local density of Tregs decreased, IL-2 secretion increased linearly (Figure 4.12A). By contrast, IL-2Rα expression and pSTAT5 signaling exhibited a degree of nonlinearity: we observed sharp increases in both parameter values after a 40% reduction in the local density of Tregs (Figure 4.12B-C). Collectively, these data indicated that quantitatively modest reductions in the size of micro-domains were sufficient to shift certain configurations from inactive to active and suggested that the system exhibited a sharp decision boundary enforced by Tregs.

The model implied that within micro-domains, elevated Treg densities could compensate for reduced Treg molecular functionality, thereby preventing self-activated CD4$^+$ T cells from responding to IL-2 (Figure 4.11 and 4.11). To explore the limitations of this compensation, we simulated disrupting Treg functions by setting certain parameters outside of their normal, homeostatic range, including Treg’s ability to strip costimulatory ligands (trans-endocytosis) or consume IL-2. Such perturbations could arise naturally due to genetic or environmental variation. The former was particularly relevant given the range of quantitative gene expression variants associated with autoimmune disorders. For instance, human patients with heterozygote mutations in either CTLA4 or IL-2Rβ reduce the respective cell-surface protein concentrations by ~50%. Interestingly, some CTLA4 heterozygotes develop multi-organ autoimmune disease, largely attributed to defective Treg function, while IL-2Rβ heterozygotes appear stable(Kuehn et al., 2014; Schubert et al., 2014; Zhang et al., 2019). To test the impact of these perturbations on the control of self-activated T cells, we ran 20,000 new simulations, but this time, the concentrations of either of these two proteins were reduced by 50%. These perturbations were selectively restricted to Tregs only for

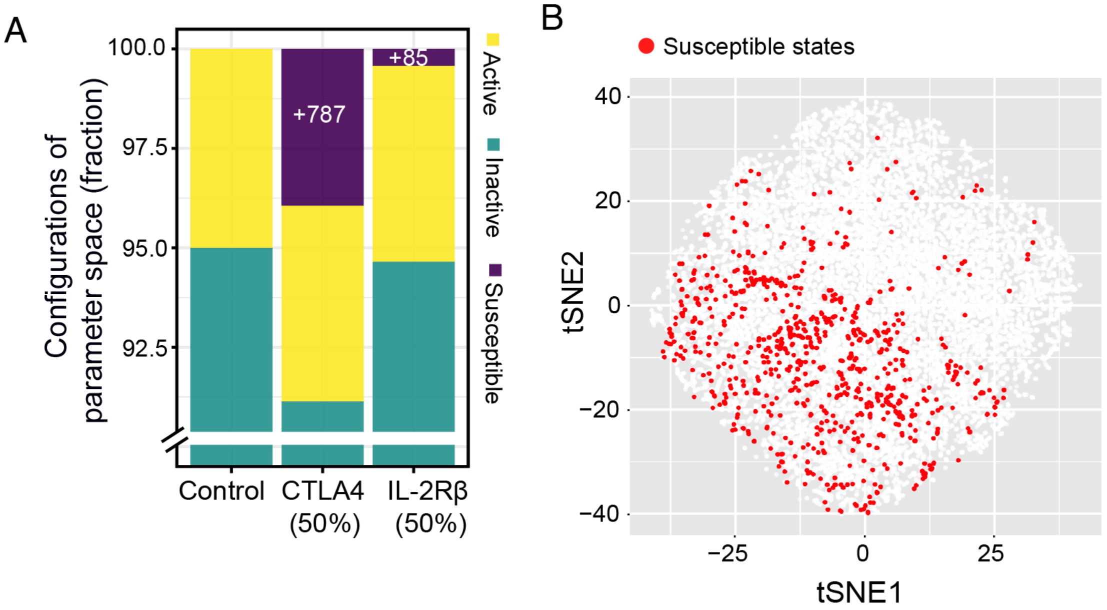

Figure 4.13 Functional perturbations on Tregs revealing susceptible configurations. **(A)** Stacked bar graphs depicting the percentage of active, inactive, and susceptible configurations. For each perturbation (i.e., a 50% reduction in the concentration of CTLA4 or IL-2Rβ in Tregs), 20000 new dynamic simulations were performed. **(B)** Susceptible configurations were pooled from each perturbation in A and visualized within parameter space (red dots).

simplicity. As shown in Figure 4.13A, reducing CTLA4 or IL-2Rβ by 50% resulted in 783 (3.9%) or 85 (0.4%) new configurations with a large pSTAT5.max, respectively (Figure 4.13A). We refer to these configurations as "susceptible", which shift to exhibit high pSTAT5.max (i.e., become more active) only upon perturbing local Treg functionality (Figure 4.13).

Within the parameter space, susceptible configurations resided near those that were active (Figure 4.8B and 4.13B), suggesting that the former were on the verge, but fell just short of breaking down during homeostasis. We therefore used MAPPA to quantitatively compare susceptible versus active configurations. This analysis revealed that the Treg density was by far the most important parameter separating these two groups, with susceptible configurations generally exhibiting ~2-fold higher density (Figure 4.14 and B.3). Thus, elevated Treg densities in susceptible configurations were often sufficient to constrain self-activated T cells as long as the other parameter values fell within homeostatic ranges. However, modest "secondary hits" that affected Treg

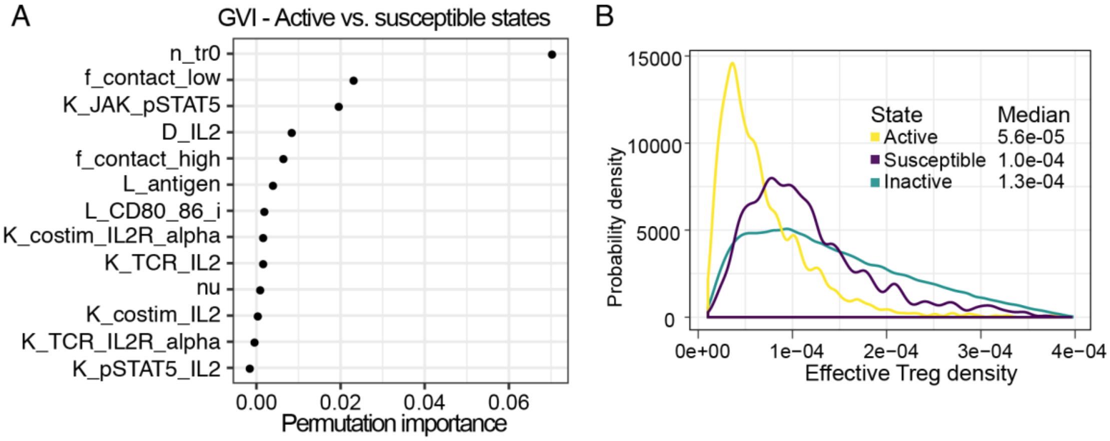

Figure 4.14 Delineation of susceptible configurations. **(A)** GVI of the RF ML classification model comparing susceptible and active configurations. **(B)** Distributions of values for the effective Treg density (n_tr0 * f_contact_low; derived from the top two parameters in A. Distributions are shown for active, inactive, and susceptible configurations. See Figure B.3.

functionality (e.g., reduction in CTLA4 expression) made these regions active, enabling self-activated T cells to escape control.

The modeling results presented in this section regarding the escapee phenotype, pSTAT5.max, were tested experimentally and shown to be consistent with the experimental results (Wong et al., submitted).

4.2.4 Existing experimental evidence together with modeling results above informs conditions required to establish immune homeostasis

Although the results presented so far demonstrated regulatory constraints on activation of self-reactive T cells shaped by the local intra- and intercellular regulatory topology, how these can relate to a sharp demarcation between tolerance and full-blown response is less clear. In homeostatic conditions, multiple lines of experimental studies consistently reported that around 1-2% of Tconvs in SLOs secrete IL-2 (Amado et al., 2013; Liu et al., 2015) and 2-4% of Tconvs show signs of activation (Richards et al., 2015; Wong et al., submitted). This striking abundance of (seemingly) self-activated Tconvs raises a concern. Although individual self-activated T cells are well constrained by Tregs in their initial priming by APCs, there is a danger that they continuously obtain paracrine IL-2 signal from other IL-2 secreting T cells leading to clonal expansion and subsequent autoimmunity. Separate lines of studies showed that the homeostatic maintenance of the peripheral Treg pool size in SLOs relies on IL-2 secreted by Tconvs, with 10-15% of Tregs being pSTAT5$^+$ (Almeida et al., 2006; Owen et al., 2018; Smigiel et al., 2014). Such IL-2 producing Tconv are likely to have been activated by self-antigens presented by MHC class II (MHC-II) of DCs (Liu et al., 2015; Stolley and Campbell, 2016; Yi et al., 2018). In contrast, the Treg pool size inversely regulates the size of the IL-2 secreting and activated CD4^{+} T cell population (Amado et al., 2013; Kim et al., 2007; Richards et al., 2015). These studies together with modeling results above suggested sufficient and necessary conditions enabling the establishment of immune homeostasis:

Condition 1: 1-2% of conventional CD4^{+} T cells that are self-activated and secreting IL-2 determined by homeostatic Treg density are not dangerous to cause full-blown autoimmunity and well constrained in an isolated manner.

Condition 2: The homeostatic Treg population size in SLOs can be maintained by self-activated, IL-2 secreting T cells (1-2% of CD4 T cells) and pSTAT5^{+} Tregs (10-15% of Tregs) in SLOs.

In the following sections, we sought to quantitatively justify that these conditions are indeed met in homeostasis by building various models, which were then extrapolated towards the breakdown of self-tolerance to readily see where a sharp decision boundary between tolerance and full-blown response exists.

4.2.5 Treg suppression of self-activated T cells guarantees the seemingly abundant frequency of IL-2 secreting T cells in homeostasis is safe, not causing full-blown self-specific responses

To show Condition 1 is indeed the case, we defined a model T cell zone with relevant quantities (Figure 3A). We previously measured that the median Treg density in the paracortex of a popliteal lymph node is around $0.0004\ \mu m^{-3}$ (data not shown; Wong et al., submitted). In SLOs, the fraction of Tregs of total CD4^{+} T cells is 10-15%, and around 10-15% of Tregs are pSTAT5^{+} (Liu et al., 2015; Smigiel et al., 2014; Stolley

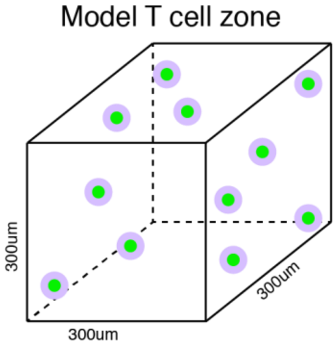

Notation	Description	Value
V_{tot}	Volume of (model) T cell zone	$2.7 \times 10^7 \mu m^3$
f_{IL2+}	Frequency of IL-2 secreting CD4+ T cells	0.01
$f_{pSTAT5+}$	Frequency of pSTAT5+ Tregs	0.1
n_{tr}	Number density of Tregs	$0.0004 \mu m^{-3}$
N_{tr}	Number of Tregs	10800 cells
n_{tconv}	Number density of CD4+ conventional T cells	$0.00293 \mu m^{-3}$
N_{tconv}	Number of CD4+ conventional T cells	79200 cells

Figure 4.15 Definition of the model T cell zone with related quantities. These quantities were back-calculated to fit the size of the model T cell zone based on experimental data.

and Campbell, 2016). With IL-2-GFP reporter mice, the homeostatic frequency of IL-2 secreting CD4 Tconvs was measured as roughly 1-2% (Amado et al., 2013; Liu et al., 2015). To make the argument more specific, we assumed the T cell zone to be a cube with 300 μm for each dimension (Figure 4.15). From the Treg density, $n_{tr} = 0.0004\, \mu m^{-3}$, the total number of Tregs in the T cell zone is $N_{tr} = 10800$ cells. With the assumption that 12% of total CD4$^+$ T cells are Tregs, the number of Tconvs in the zone is $N_{tconv} = 79200$ cells. With the frequency of IL-2 secreting CD4$^+$ T cells, $f_{IL2+} = 0.01$, the number of IL-2 secreting CD4$^+$ Tconv in the T cell zone is $N_{IL2+} = 792$ cells. Assuming that 10% of Tregs are pSTAT5$^+$ ($f_{pSTAT5+} = 0.1$), the effective IL-2 niche accessible to Tregs can be estimated as 10% of the total volume of the T cell zone. With these quantities, we then estimated the effective size of IL-2 niche for each IL-2 secreting T cell as $l_D = 9.79 \mu m$ (Figure 4.17) (See section B.3 for detailed calculation). In fact, l_D varies dynamically depending on the Treg density, the capacity of IL-2 reabsorption through IL-2Rα of Tregs, and the IL-2 diffusion coefficient (Oyler-Yaniv et al., 2017).

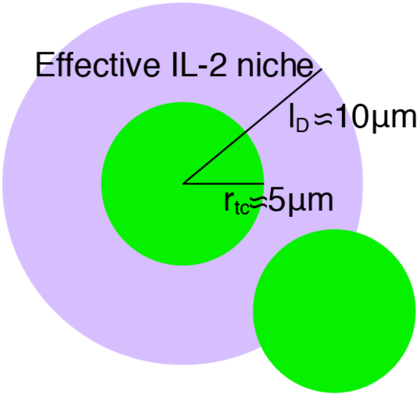

Figure 4.17 Estimated effective IL-2 niche size generated by a self-activated IL-2 secreting Tconv. See section B.3 for details. The green circle is a Tconv secreting IL-2. The purple region is the effective IL-2 niche, where IL-2 concentration is high enough to provide IL-2 signals to Tregs. r_{tc}: the radius of Tconvs, l_D: the effective size of the IL-2 niche created by an IL-2 secreting Tconv.

We then sought to build probabilistic models of self-activated T cells undergoing clonal expansion with assumed and estimated quantities shown above (Figure 4.15). According to the results in previous sections and experimental evidence from (Bohineust et al., 2018; Marchingo et al., 2014), once a self-reactive Tconv gets activated and disengages from a DC, the full-blown response through clonal expansion is possible only if the self-activated Tconv continuously obtains IL-2 signals provided by neighboring IL-2 secreting T cells for around five days. We may think of two possibilities. First, the self-activated T cell sequentially encounters other IL-2 secreting T cells within their IL-2 niches through random movements for five days (Figure 4.16).

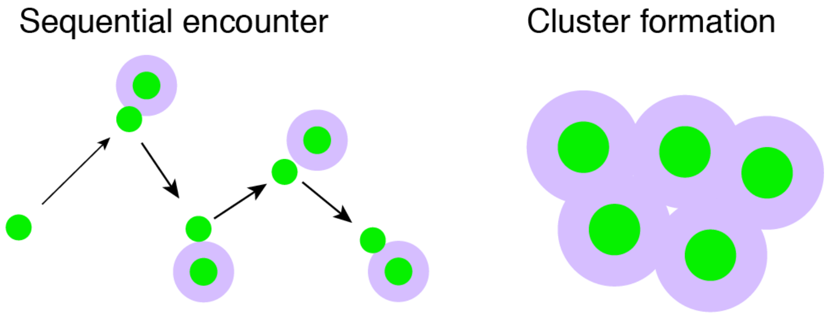

Figure 4.16 Schematics of potential mechanisms of self-activated T cell to undergo clonal expansion.

The other possibility is the self- activated, IL-2 secreting T cells form a cluster, where the cells mutually maintain and provide the TCR or costimulation signals to each other to maintain IL-2 secretion in that milieu for five days although solid *in vivo* experimental evidence in a physiological setting is still not available (Figure 4.16) (Sabatos et al., 2008; Zenke et al., 2020).

In the sequential encounter model, once disengaging from a DC, a self-activated T cell randomly moves in the T cell zone with its average speed, $v_{rand} = 5\ \mu m/min$, and its cross-section of the IL-2 niche size and the diameter of the cell (Figure 4.18A). Then, the volume swept by this cross-section per unit time together with the frequency

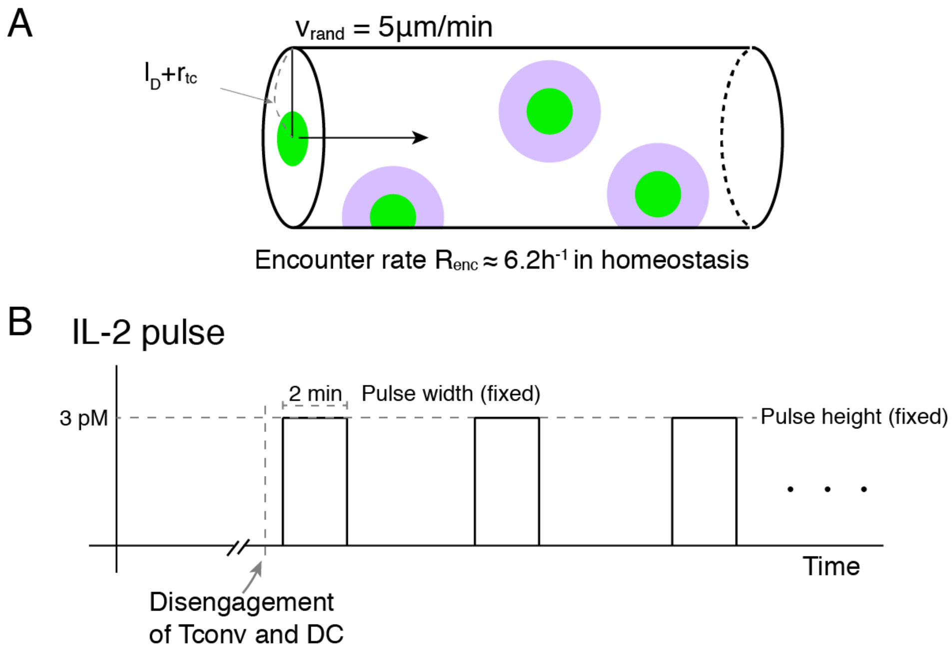

Figure 4.18 Sequential encounter model. **(A)** Formal estimation of average encounter rate in the homeostatic condition. R_{enc}: the average encounter rate, v_{rand}: the average speed of self-activated Tconvs. See section B.4.1 for details. **(B)** Schematic of IL-2 pulses introduced in the T cell activation models. Based on the simulation result of the IL-2 diffusion dynamics in the baseline condition in Figure 4.2, the average IL-2 concentration was estimated to be 3 pM. The average width of each pulse was estimated to be 2 min based on the effective IL-2 niche size per cell and the average speed of self-activated T cells. The rate of pulses was equated with the encounter rate that is adjusted by the frequency of IL-2 secreting Tconvs.

of IL-2 secreting T cells in the T cell zone determines the average rate of IL-2 niche encounter per hour as $R_{enc} = 6.2\ h^{-1}$ (See section B.4.1 for detailed computation). Each encounter lasts for, on average, $\frac{l_D}{v_{rand}} \approx \frac{10}{5} = 2\ min$. Thus, hourly the self-activated T cell is subject to IL-2 niches for, on average, 12 minutes.

To examine how the encounter rate of the IL-2 niches affects the proliferation capacity (the dynamics of Myc) of the self-activated T cells, we modified the multiscale

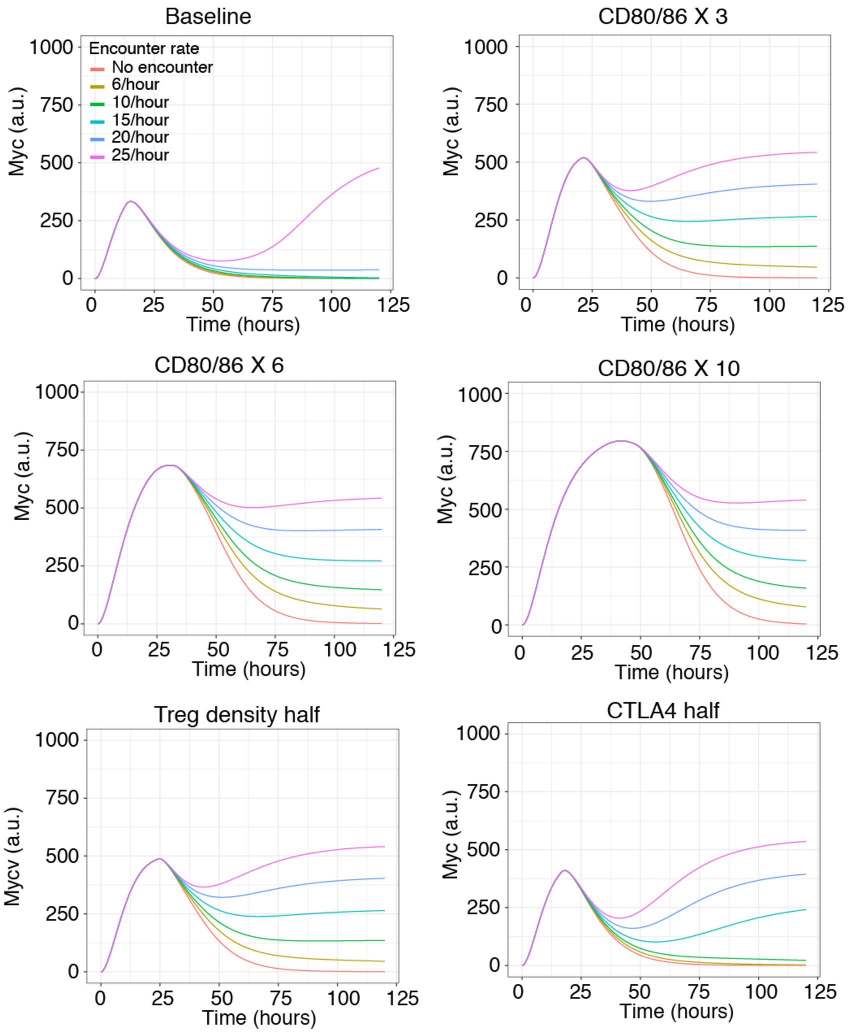

Figure 4.19 Dynamical trajectories of Myc under different IL-2 pulse rates for various conditions. The parameter combination for the baseline condition is the same as one used in Figure 4.2. The costimulatory ligand (CD80/86) level, the Treg density, and the level of CTLA4 in Tregs were perturbed.

T cell activation model (Figure 4.1) by adding IL-2 pulses after the disengagement between the priming T cells and DC (Figure 4.18B). Using the same parameter combination that illustrated homeostatic suppression of the self-activated Tconv by Tregs in Figure 4.2, we conducted simulations with different rates of IL-2 niche encounter and altered activation statuses after initial priming by a DC (Figure 4.19). The baseline condition showed that up to the encounter rate of 20/hour, the self-activated T cells eventually lost Myc expression indicative of aborted proliferation. A sharp transition of Myc dynamics exists between 20/hour and 25/hour, and with the latter, the Myc level kept upregulated, suggesting continued proliferation in the time scale of 5 days and thus clonal expansion (Figure 4.19). In contrast, other conditions with either increased CD80/86 or reduced CTLA4/Treg density showed upregulated Myc in later time points even with low pulse rates (around 10-15/hour) (Figure 4.19). Since the IL-2 signal is the only input signal upregulating Myc after the disengagement, the receiver phenotype, IL-2Rα.max, determines the threshold number of encounters, $N_{enc.trhesh}$.

Based on these results, we finally derived a probabilistic model describing the probability of achieving encounter rates equal to or greater than a threshold rate given the frequency of IL-2 secreting Tconvs determining the average encounter rate, R_{enc} (Figure 4.20) (See section B.4.1 for the detailed derivation). The probability of achieving the threshold encounter rate $\geq$ 20/hour for continued proliferation for five days (clonal expansion) in the baseline condition (Figure 4.19) is extremely low over the time scale beyond the lifespan of mice and humans under the homeostatic frequency of IL-2 secreting Tconvs (Figure 4.20). The probability sharply increases at around the

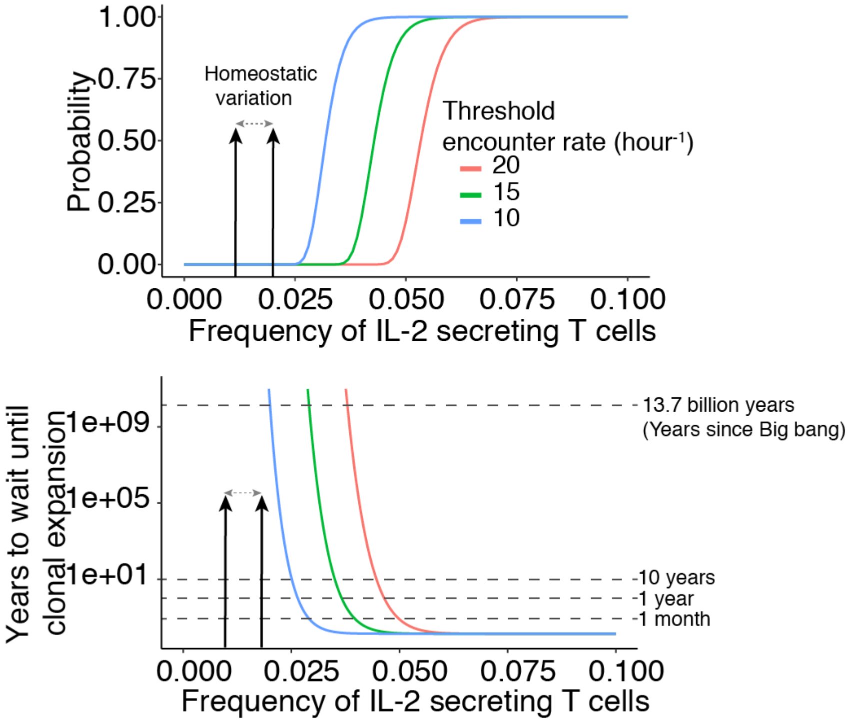

Figure 4.20 Probability of self-activated Tconvs for undergoing clonal expansion tuned by the frequency of IL-2 secreting Tconvs for different threshold encounter rates over the time window of 120 hours. (Top) Probability regulated by the frequency of IL-2 secreting T cells for different threshold encounter rates over the time window of 120 hours. (Bottom) The time scales until the occurrence of a single event of clonal expansion in the model T cell zone. The arrows indicate the homeostatic variation of the frequency of IL-2 secreting Tconvs.

frequency of 0.05 (5%), which is only possible when a substantial fraction of Tregs are depleted (Amado et al., 2013). When we imposed lower threshold encounter rates, 10-15/hour for clonal expansion as in the conditions with an increased CD80/86 and reduced CTLA4/Treg density (Figure 4.19), the probability of achieving such encounter rates were still extremely low with the homeostatic frequencies of IL-2 secreting Tconvs (Figure 4.20). However, the sharp increase of the probability of clonal expansion happened at the frequency of 0.03-0.04 (3-4%), which are lower than that for the baseline threshold encounter rate, 20/hour, and slightly higher than the upper limit of the homeostatic range of the frequency, suggesting an increased risk of clonal expansion of self-activated Tconvs and resultant autoimmunity if additional perturbations as infections occur. Taken together, based on the sequential encounter model in conjunction with the T cell activation model, the homeostatic frequency of IL-2 secreting T cells in SLOs are safe enough under the regulatory constraints of Tregs for each self-activated T cell, and perturbed conditions impose a higher risk of clonal expansion of self-activated T cells.

Alternatively, we also derived a probabilistic model of cluster formation, enabling clonal expansion of self-activated Tconvs (Figure 4.21) (See section B.4.2 for the detailed derivation). The requirement of the threshold size of the precursor frequency of cognate T cells (in other words, quorum regulation) for clonal expansion and a full-blown response has been suggested both theoretically and experimentally (Bosch et al., 2017; Butler et al., 2013), yet no quantitative mechanistic description is available so far. Based on the homeostatic quantities defined above, the quorum size threshold of full-blown responses (minimum five cells) measured in (Bosch et al., 2017), and the kinetic parameters of T cell-T cell spatial interactions inferred from (Fricke et al., 2016; Matheu et al., 2015), we derived the probability of cluster formation and maintenance of self-activated, IL-2 secreting Tconvs with the size $\geq$ five cells at least for 10 hours. This time window is a typical time scale of T cell division (Heinzel et al., 2017), and we assumed that after this time window the cluster is self-sustained with the mutual provision of relevant signals to keep adhesion between cells and IL-2 secretion of participating cells (Zenke et al., 2020). As for the sequential encounter model, the cluster formation model also exhibited a drastic transition in the probability of clonal expansion from 0 to 1 with increasing frequencies of IL-2

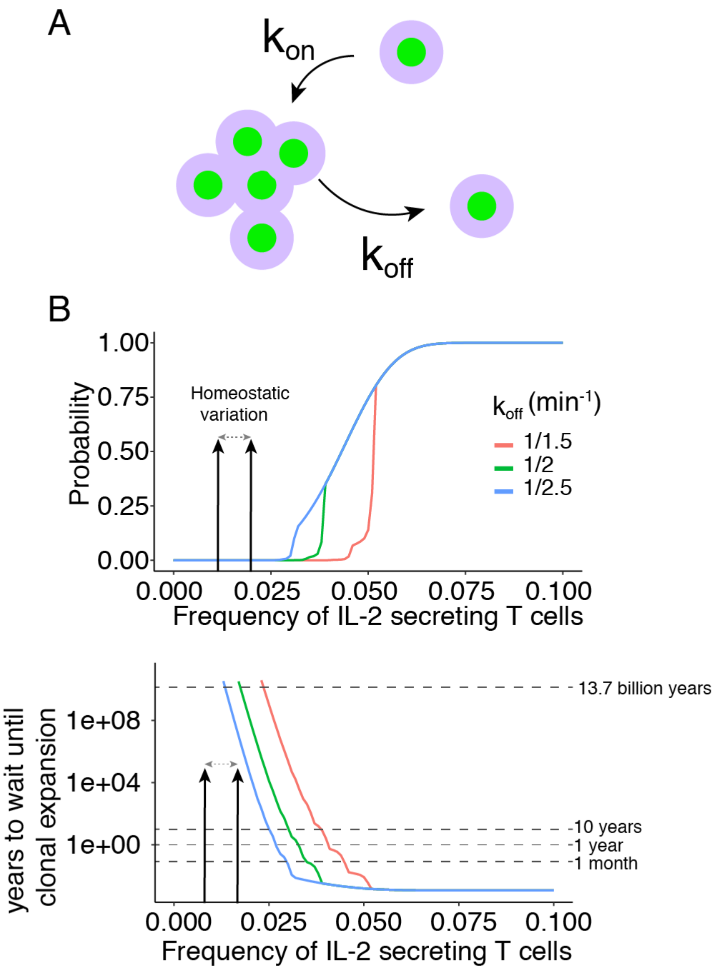

Figure 4.21 Cluster formation model. **(A)** Formal derivation of the probability of cluster formation requires parameters related to T cell-T cell interaction kinetics that can be estimated through intravital imaging experiments. **(B)** Probability of self-activated Tconvs for undergoing clonal expansion by forming a cluster sustained at least for 10 hours tuned by the frequency of IL-2 secreting Tconvs for different adhesion coefficients (Top) Probability regulated by the frequency of IL-2 secreting Tconvs for different adhesion coefficients. (Bottom) The time scales until the occurrence of a single event of clonal expansion in the model T cell zone. The arrows indicate the homeostatic variation of the frequency of IL-2 secreting Tconvs.

secreting Tconvs (Figure 4.21B). With the homeostatic value of the adhesion coefficient, $k_{off} = \frac{1}{1.5}\ min^{-1}$, the homeostatic frequency of IL-2 secreting Tconvs again showed an extremely low probability of cluster formation that sharply transitions to 1 at the frequency around 0.05 (5%) that is unlikely in homeostasis (Amado et al., 2013; Liu et al., 2015). In contrast, the increased adhesion coefficient due to more activated status of the self-activated T cell after initial priming led to the sharp transition of the probability occurring at the decreased frequencies of IL-2 secreting T cells at around 0.03-0.04 (3-4%), again showing an increased risk of clonal expansion under additional activating perturbations. Together, the cluster formation model also showed that the homeostatic frequency of self-activated, IL-2 secreting Tconvs are safe, not likely causing autoimmunity, yet more activated status of self-activated Tconvs after initial priming has a higher risk of full-blown responses.

4.2.6 The homeostatic frequencies of IL-2 secreting T cells and Tregs in SLOs guarantee the dynamical equilibrium between self-activated, IL-2 secreting Tconvs and Tregs

We next turned to Condition 2. We first asked whether the homeostatic IL-2 niche provided by self-activated Tconvs is sufficient to maintain the peripheral homeostatic Treg pool size (section B.5). We focused on the relevant experimental studies that reported the effects of IL-2 blocking on Tregs (Owen et al., 2018; Smigiel et al., 2014; Tong et al., 2019). Our strategy was to show that 10% of the total volume of SLOs covered by the IL-2 niche indicated by $f_{pSTAT5+} = 0.1$ is sufficient to maintain Treg pool at the intranodal (Figure 4.22A) and whole lymphatic system (Figure 4.22B) levels within a reasonable range of the proliferation rate. Of note, two subtypes of Tregs, central Tregs (cTregs) and effector Tregs (eTregs), were considered in the studies considered. cTregs comprising about half of the peripheral Treg pool in SLOs were shown to entirely rely on IL-2 while eTregs are differentiated from cTregs and rely on ICOS for their survival and proliferation (Smigiel et al., 2014). Therefore, we only

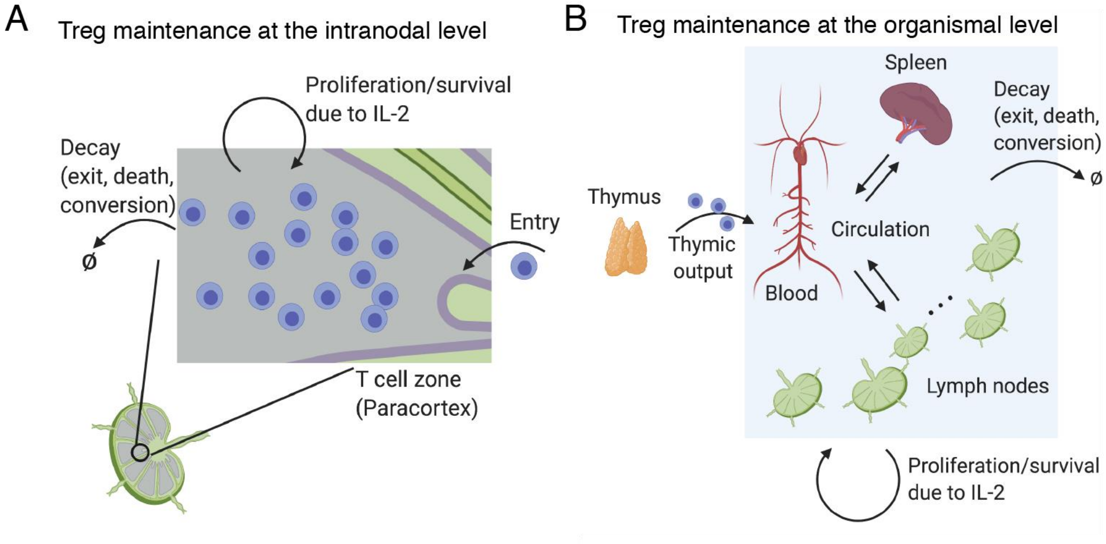

Figure 4.22 Schematic of the cell population model describing the peripheral Treg maintenance supported by the IL-2 niches at **(A)** the intranodal level (Eq 4.1) and **(B)** the organismal level (Eq 4.2).

considered cTregs, and the maintenance of eTregs was regarded as a corollary of that of cTregs.

At the intranodal level (Figure 4.22A), the governing equation of the cTreg pool size is

$$\frac{dn_{ctr}}{dt} = k_{entry} + k_{prolif} \cdot f_{pSTAT5+} \cdot n_{ctr} - k_{decay} \cdot \left(1 - f_{pSTAT5+}\right) \cdot n_{ctr}, \qquad (4.1)$$

where n_{ctr}: the number density of cTregs, $f_{pSTAT5+}$: the frequency of pSTAT5^{+} cTregs in an SLO, k_{entry}: the rate of Treg entry, k_{prolif}: the rate of Treg proliferation with IL-2 signal, and k_{decay}: the rate of Treg disappearance due to death/exit/conversion. The goal is to show that the steady state of this equation ($\frac{dn_{ctr}}{dt} = 0$) is guaranteed with experimentally measured and inferred parameter values of k_{entry}, $f_{pSTAT5+}$, and k_{decay} and reasonable values of k_{prolif}. We again applied the model system with the defined quantities in Figure 4.15. From data in (Smigiel et al., 2014; Tong et al., 2019), which presented results of the mean dwelling time of cTregs in SLOs and cTreg decay upon administration of IL-2 blocking antibodies in SLOs, respectively, we inferred the values of k_{entry} and k_{decay} (See section B.5.1 for details). Considering these values and the steady state assumption, we estimated the rate of Treg proliferation to be $k_{prolif} = 0.07\ h^{-1}$ (doubling time: around 10 hours) (See section B.5.1 for details). This value is consistent with the time for each T cell division estimated in (Heinzel et al., 2017). Together, this quantitative analysis strongly suggests that the IL-2 niche created by the homeostatic frequency of self-activated, IL-2 secreting Tconvs is sufficient to maintain the homeostatic Treg pool size with biologically reasonable kinetic parameter values, especially k_{prolif}, at the intranodal level.

At the organismal level considering the whole lymphatic system (Figure 4.22B), the governing equation of the Treg pool size is

$$\begin{aligned}\frac{d(N_{cTr})}{dt} &= k_{thy,Tr} + k_{prolif} \cdot f_{pSTAT5+,tot} \cdot N_{cTr} \\ &-k_{decay,tot} \cdot \left(1 - f_{pSTAT5+,tot}\right) \cdot N_{cTr}, \end{aligned} \tag{4.2}$$

where N_{cTr}: the total number of cTregs, $k_{thy,tr}$: the rate of thymic output of cTregs, $k_{decay,tot}$: the rate of cTreg decay due to death/conversion/exit, and $f_{pSTAT5+,tot}$: the fraction of cTreg within the IL-2 niches in all SLOs. The goal is to show that the estimated fraction of cTreg within the IL-2 niche, $f_{pSTAT5+,tot}$, in the steady state is comparable or less than that of cTreg experimentally measured in SLOs. (den Braber et al., 2012; Milanez-Almeida et al., 2015) provided data for estimating the numbers of T cell subtypes at the organismal level. The steady state assumption and the estimated k_{prolif} led us to estimate that $f_{pSTAT5+,tot}$ = 0.025, which is lower than typical frequencies of pSTAT5$^+$ Tregs (0.05-0.2) in SLOs (See section B.5.2 for detail). We then pursued a more stringent estimation of $f_{pSTAT5+,tot}$ assuming an extreme situation where the number of cTregs in peripheral blood, not accessible to the IL-2 niche, is the same as that in SLOs, which led to an estimation that $f_{pSTAT5+,tot} = 0.06$, which is still comparable or lower than typical frequencies of pSTAT5$^+$ Tregs (0.05-0.2) in SLOs (section B.5.2). Together, these results strongly suggest that the IL-2 niche in SLOs provided by the homeostatic number of self-activated T cells is sufficient to maintain the homeostatic pool size of Tregs at the organismal level.

We next derived the relationship between the IL-2 niche size and the Treg pool size in SLOs by extrapolating the governing equation at the intranodal level (Eq 4.1) from the steady state condition. To prevent n_{ctr} from diverging, we modified the equation by introducing the carrying capacity factor as

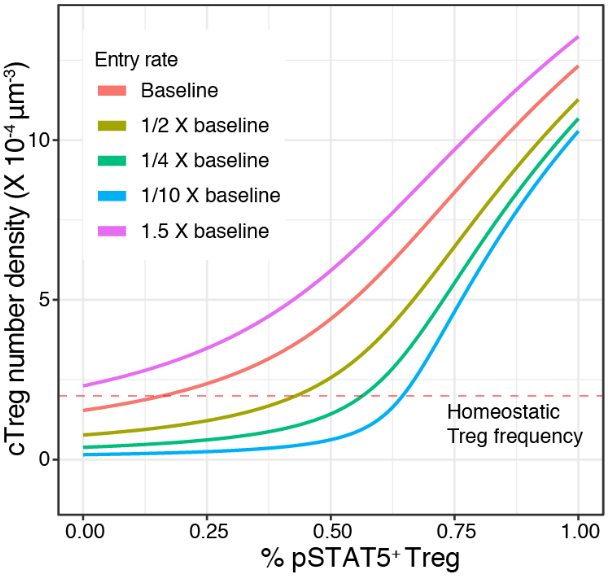

Figure 4.23 Model extrapolation of the intranodal Treg population size deviating from the homeostatic value by tuning the IL-2 niche size and the entry rate reflecting the thymic output of Tregs. Central Tregs (cTregs) were considered.

$$0 = k_{entry} + k_{prolif} \cdot f_{pSTAT5+} \cdot n_{ctr} \cdot \left(1 - \frac{n_{ctr}}{K_{cc}}\right)$$
$$-k_{decay} \cdot \left(1 - f_{psTAT5+}\right) \cdot n_{ctr}, \tag{4.3}$$

where the carrying capacity: $K_{cc} = 0.001/\mu m^3$. The resultant quantitative relationships between n_{ctr} and $f_{psTAT5+}$ for different k_{entry} revealed that a sizable entry rate is required to maintain the homeostatic Treg population size under the homeostatic IL-2 niche size (or the homeostatic frequency of IL-2 secreting Tconvs) (Figure 4.23).

We next sought to quantitatively derive Treg's negative regulation of the frequency of self-activated, IL-2 secreting Tconvs, which has been shown experimentally in (Amado et al., 2013) (Figure 4.24A). The schematic relationship between the frequencies of Tregs and IL-2 secreting Tconvs based on the experimental data showed two distinct linear trends joining near the homeostatic frequency of Tregs (Figure 4.24B). We derived a mathematical relationship that may explain this feature as

$$N_{IL2+}(n_{tr}) = N_{tconv} \cdot f_{self} \cdot f_{act}(n_{tr}) \cdot \frac{P_{LN}(n_{tr})}{P_{tot}} \cdot \frac{\tau_{sec.dur}(n_{tr})}{\tau_{dwell}}, \tag{4.4}$$

where f_{self}: the predisposed number of potentially self-reactive CD4$^+$ T cells, P_{tot}: the total number of distinct self-peptide sequences presented through MHC-II, P_{LN}: the number of distinct peptide sequences presented in a particular lymph node, f_{act}: the probability of the lymph node-specific self-reactive T cells being activated upon encounter with cognate antigen-bearing DCs, τ_{dwell}: the average lymph node dwelling time of CD4$^+$ T cells, and $\tau_{sec.dur}$: the duration of IL-2 secretion (See section B.5.3 for the detailed derivation). N_{IL2+}'s dependence on the Treg density is mediated by the

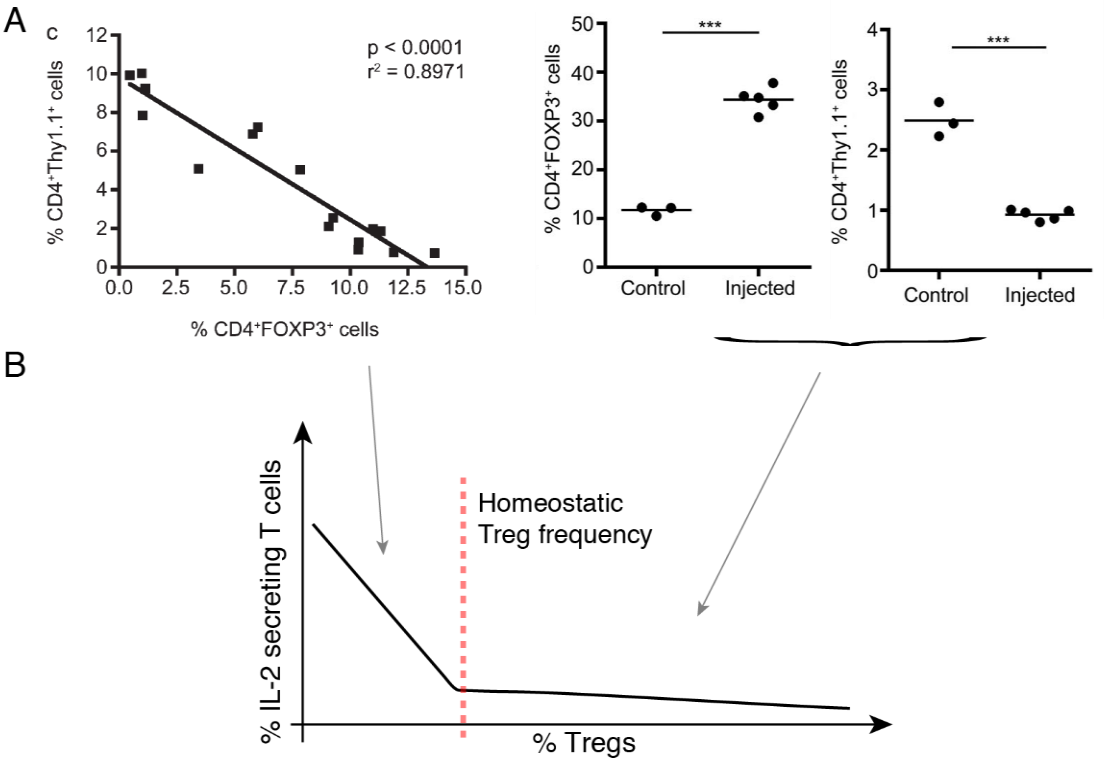

Figure 4.25 Treg regulation of the frequency of IL-2 secreting T cells. **(A)** Experimental data illustrating Treg regulation of the frequency of IL-2 secreting T cells. Adopted from (Amado et al., 2013). Tregs deviate from the homeostatic frequency (~ 12%) through either depletion (left) or expansion (right) **(B)** Schematic summary of experimental data shown in (A).

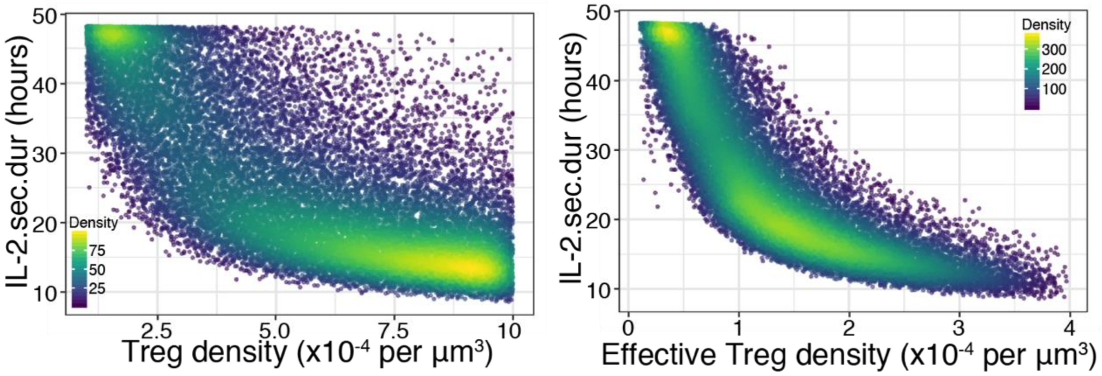

Figure 4.25 Relationship between the Treg density and the duration of IL2 secretion. Scatter plots depicts IL-2.sec.dur vs. (left) Treg density and (right) effective Treg density. These are from the MAPPA results in homeostasis shown in Figure 4.6C.

quantities, f_{act}, P_{LN}, and $\tau_{sec.dur}$. Determining the detailed dependence of f_{act} and P_{LN} on the Treg density requires further experimental data on Treg-mediated regulations of antigen presentation and migration patterns of Tconvs, which is out of the scope of this study. However, we were able to extract $\tau_{sec.dur}$'s dependence on the Treg density from the MAPPA results (Figure 4.6C), which revealed that their detailed relationship from the simulation (Figure 4.25) likely explains the discrete transition of slope in Figure 4.24B. These results illustrate that the individual cell level phenotype, the duration of IL-2 secretion, contributes to the cell population size regulation.

4.2.7 The integrated quantitative framework bridging models across scales enables intuitive assessment of immune homeostasis

Bridging quantitative models we developed so far altogether, we derived an integrated quantitative framework assessing immune homeostasis (Figure 4.26). Curve 1 illustrates the regulation of the Treg population size by the IL-2 niche size determined by the number of self-activated, IL-2 secreting Tconvs or reflected by the frequency of pSTAT5^{+} Tregs (Figure 4.22 and 4.23). Curve 2 illustrates Treg's negative regulation of the number of self-activated IL-2 secreting Tconvs (Figure 4.24 and 4.25). The shaded area indicates the region where autoimmune propensity is high enough within a lifespan of the host (Figure 4.22 and 4.21). Immune homeostasis is achieved as dynamical equilibrium between self-activated IL-2 secreting Tconvs and regulatory T cells (the intersection of Curves 1 and 2), which is formed well below thresholds of clonal expansion and subsequent autoimmune diseases. The system fluctuates around this equilibrium point, being subject to strong restoring forces directing back towards the equilibrium point, which ensures the system does not go across the autoimmune

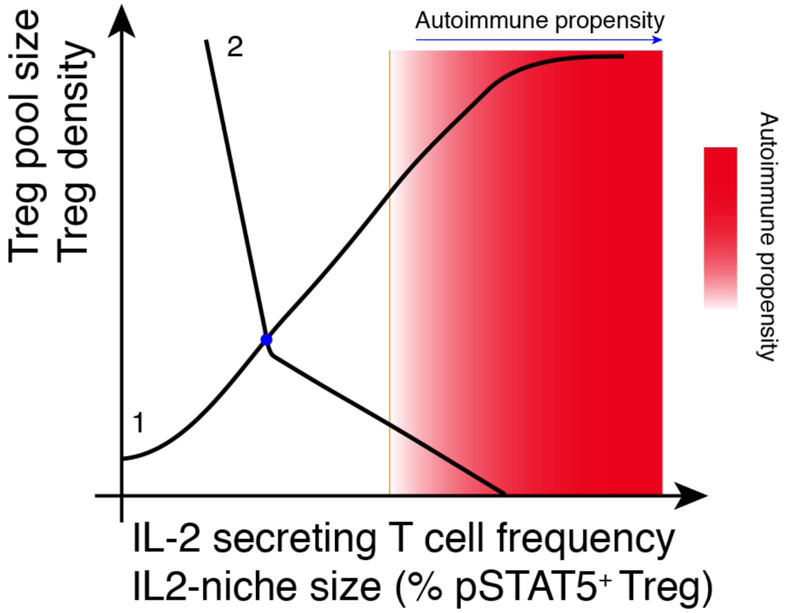

Figure 4.26 Phase portrait proposed as an integrated quantitative framework sewing all models explored in this study together.

region (Figure 4.26). Using this framework, we can reinterpret the role of thymic negative selection (Figure 4.27A). It does not have to remove all self-reactive T cells. Instead, it needs to prune them to ensure that the equilibrium point resulting from the reciprocal interplay between peripheral Tregs and self-activated T cells falls far below the autoimmune region. Therefore, even with the seemingly high prevalence of peripheral self-reactive T cells (Richards et al., 2015), immune homeostasis far from the autoimmune propensity is assured. In this manner, the peripheral TCR repertoire can harbor a 4-10% larger TCR repertoire beneficial to fight against foreign pathogens or altered self such as cancer. In contrast, thymic involution due to aging hinders negative selection, resulting in high autoimmune propensity (Coder et al., 2015).

We explored several scenarios of deviation of immune homeostasis using this framework. With defects in Treg proliferation, the equilibrium point may fall within the dangerous region due to the altered curve 1 (Figure 4.27B). If intracellular checkpoints are flawed due to some genetic factors, the decision boundary of

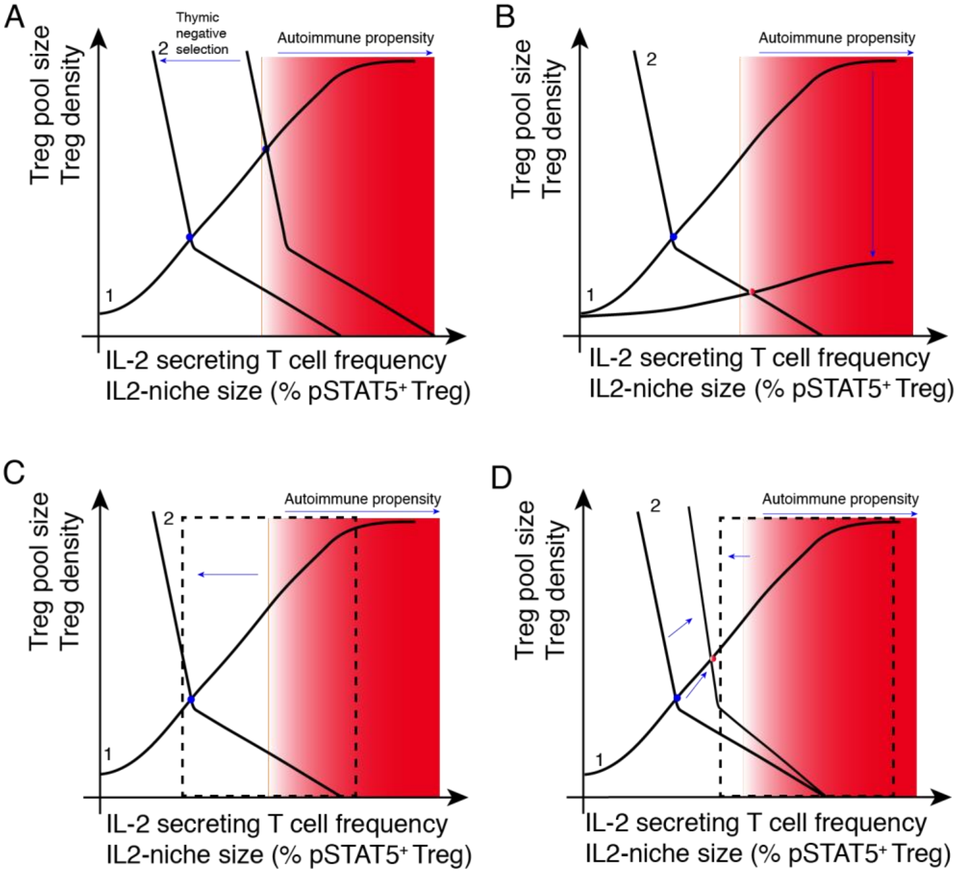

Figure 4.27 Schematic depiction of several scenarios of modulating immune homeostasis using the integrated framework. **(A)** Thymic negative selection. **(B)** Treg-intrinsic defects in proliferation and/or survival. **(C)** Defects in intracellular checkpoints for Tconv activation. **(D)** Anti-CTLA4 antibody treatment. The blue arrows indicates the evolution of the system towards a new equilibrium point.

autoimmunity shifts towards left, and thus the equilibrium now may reside within the autoimmune region (Figure 4.27C). The anti-CTLA4 immune therapy mainly perturbs Curve 1 and the decision threshold of clonal expansion together (Figure 4.27D), which makes the system reside near the threshold. Therefore, a significant portion of patients treated with this therapy experience immune-related adverse events (Trinh and Hagen, 2013).

We next sought to assess immune homeostasis of SFZ70 mice, which are TCR transgenic mice generated by knocking in Tcra and Tcrb genes from a self-reactive

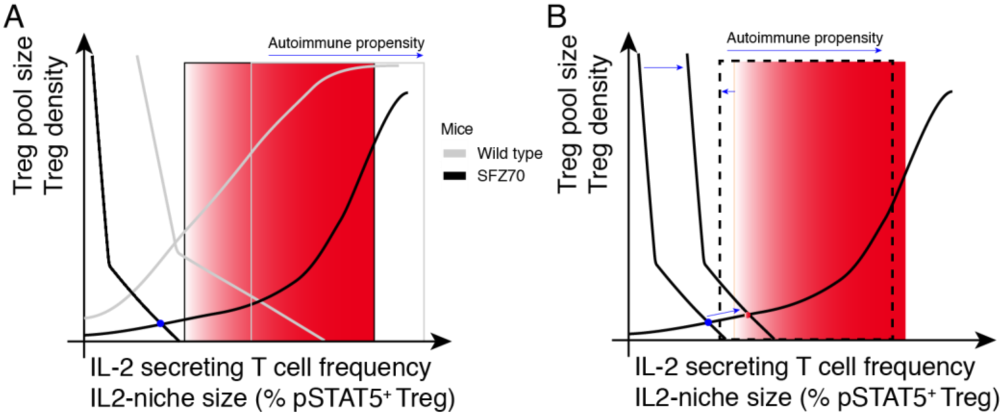

Figure 4.28 Assessment of immune homeostasis of SFZ270 mice. **(A)** Altered immune homeostasis of SF270 mice (black) compared to the wild type mice (gray). **(B)** Modulation of immune homeostasis of SFZ70 by DC activation.

Tconv specific to an antigen drained from the skin from a scurfy mouse (Killebrew et al., 2011). SFZ70 mice generate both TCR-transgenic Tconvs and Tregs and do not develop autoimmunity in homeostasis. The absolute counts of Tconvs and Tregs in skin draining lymph nodes in these mice were 1/100 and 1/30 of the counts of those cells in wild type mice, respectively. Unlike in wild type mice, Tconvs in SFZ70 mice are all self-reactive, and therefore the size of the IL-2 niche in SFZ70 mice is comparable in the order of magnitude to that of wild type mice although the absolute counts differ by two orders of magnitude. This enabled the maintenance of the Treg population size that is sufficient to ensure the equilibrium point formed in the safe region (Figure 4.28A). The activation of DCs by agonistic anti-CD40 antibodies and the resultant upregulation of costimulatory signals resulted in autoimmune manifestation in SFZ70 mice (Killebrew et al., 2011), which can be recapitulated in our framework in that the increased frequency of IL-2 secreting Tconvs and the lowered threshold of clonal expansion drive the system to the autoimmune region.[23] Together, our integrated

---

[23] Although this observation may suggest a heightened autoimmune propensity under inflammatory conditions, in general, wild type mice or healthy humans do not develop overt autoimmune diseases after infections due to the symmetry breaking between self and non-self ensuring the system to remain in the

framework readily provided an intuitive understanding of the establishment of immune homeostasis and demonstrated the assessments of the deviation from immune homeostasis, potentially guiding efficient treatment modalities reverting the system to homeostasis.

4.3 Discussion

In this study, we illustrated that immune homeostasis is established as dynamical equilibrium between self-activated, IL-2 secreting Tconvs and Tregs, which is formed well below thresholds that could result in clonal expansion of self-activated T cells and subsequent autoimmune diseases. To arrive at this, we employed various modeling approaches describing crucial processes occurring at different organizational levels. We began with multiscale modeling of T cell activation occurring via three cell-type interactions describing both intracellular and intercellular dynamics of constituent cells and molecules. This model recapitulated the two-phase response of T cells, and Treg suppression ensures a temporal mismatch between IL-2 secretion and autocrine IL-2 sensing through the early cease of IL-2 secretion and the aborted upregulation of IL-2Rα (Figure 4.2 and 4.3). The application of the MAPPA approach to unbiasedly explore the plausible parameter space revealed that the number density of Tregs is the most crucial parameter constraining activation phenotypes of self-activated T cells in homeostasis, yet the suppression is overridden mostly by the increased costimulatory ligand (CD80/86) level in inflammation. Through the probabilistic models of paracrine

---

safe region (possible mechanisms are proposed in section 2.4.3). On the other hand, in SFZ70 mice, the low count of Tregs (1/30 of that of wild type mice) in lymph nodes leads to the failure of the symmetry breaking for overcoming increased costimulation.

IL-2-mediated T cell clonal expansion, we showed that Treg suppression on individual self-activated T cells in homeostasis ensures self-activated T cells do not go through clonal expansion under the homeostatic frequency of self-activated, IL-2 secreting Tconvs (1-2% of Tconvs). The sharp transition in the probability of clonal expansion existed for higher frequencies (> 5%). Lastly, the cell population models revealed that such homeostatic frequencies of Tregs and self-activated, IL-2 secreting Tconvs ensuring tolerance are determined as equilibrium of opposing regulations between these cell populations. Combining and extrapolating all models together, we derived an integrated quantitative framework for the intuitive assessment of immune homeostasis and demonstrated its potential usage in guiding therapeutic manipulation of immune homeostasis.

The most crucial component among processes ensuring immune homeostasis is the negative feedback interaction between self-activated, IL-2 secreting Tconvs and Tregs that operates at both cellular and population levels, illustrating the fractal nature of this recurrent regulatory motif (Germain, 2012). The net effect of the negative feedback arm of this motif across layers is to constrain the activation status of each asynchronously self-activated Tconv, the population size of IL-2 secreting Tconvs, and the diffusion range of secreted IL-2. These constraints together warrant that self-activated Tconvs do not undergo clonal expansion even with the paracrine IL-2 niche provided by surrounding IL-2 secreting Tconvs. The frequency/number density of Tregs is the most influential parameter ensuring this in homeostasis. Intriguingly, the positive forward arm via the IL-2 niche provided by self-activated Tconvs enables the homeostatic maintenance of the Treg population size in SLOs. Therefore, the design principle of immune homeostasis as a multilayered feedback motif suggests a fresh insight over self-activated Tconvs; the prevalent self-reactive Tconvs and their overt activation against self-antigens are not an imperfection but an integral part of immune homeostasis, driving the system towards dynamical equilibrium.

Such prevalence of self-activated T cells raised a question; where does a sharp decision boundary between tolerance and full-blown clonal expansion of T cells exist? The individual Tconvs are ignorant of whether they are seeing self or not. Previous theoretical and experimental studies suggested a quorum-regulated mechanism for determining full-blown activation and clonal expansion of T cells, but they lacked mechanistic explanations on quorum regulation and the consideration of ongoing self-activations of Tconvs (Bosch et al., 2017; Butler et al., 2013). In this study, we quantitatively and mechanistically demonstrated that both the activation status (especially the receiver phenotype, IL-2Rα.max) of individual self-activated Tconvs at the end of initial priming by DCs and the IL-2 niche size provided by self-activated, IL-2 secreting Tconvs together determine the probability of going through clonal expansion for self-activated Tconvs (section 4.2.5). In homeostasis, the probability showed a sharp transition from near 0 to near 1 at a frequency of IL-2 secreting T cells substantially above the homeostatic frequency, guaranteeing the dynamical equilibrium between Tregs and IL-2 secreting Tconvs is formed within safe regions. Together, our results suggested more refined models of a quorum-regulated decision of clonal expansion dependent on both cellular and cell population-level parameters.

Our illustration of immune homeostasis leads us to rethink what the tolerance mechanisms optimize. The sizeable peripheral self-reactive repertoire with less danger of autoimmunity suggests that the adaptive immune system may have evolved to preserve and even maximize the utility of self-reactivity in the periphery to the extent of not causing autoimmunity over the reproductive period of hosts. It has been shown that higher self-avidity within the peripheral TCR repertoire shaped by positive selection can provide better foreign-specific responses and this may happen at the expense of the leakage of overtly self-reactive T cells to the periphery (Mandl et al., 2013). It has been also suggested that efficient deletion of self-reactive T cells may create holes in the TCR repertoire, through which pathogens breach the host (Yu et al., 2015). Retaining the self-reactive repertoire may also be beneficial for clearing neoplasms that may become malignant or physiologically detrimental for the host (Kohanim et al., 2019; Menares et al., 2019).

Our proposed framework suggests a potential benefit in clinical settings. Recently, the modulation of immune homeostasis has become a major therapeutic modality in treating autoimmunity and cancer. The low-dose IL-2 administration on autoimmune patients showed promising therapeutic outcomes relieving symptoms of various autoimmune diseases (Rosenzwajg et al., 2019). However, the double-edged nature of the IL-2 signals affecting both Tconvs and Tregs requires a more optimized determination of IL-2 dosages. Likewise, despite the excellent outcomes and increasing indications of immune checkpoint inhibition therapies for treating cancer, a significant fraction of patients treated with this modality develop immune-related adverse events that sometimes require the cease of the therapy (Esfahani et al., 2020). Even worse, the genetic variations in relevant loci related to crucial molecular and cellular components in immune homeostasis across patients add additional complexities for preventing and treating autoimmunity and cancer (Farh et al., 2015). In this regard, our framework may be able to quantitatively assess the effects of various therapeutic scenarios and subtle genetic variations on the modulation of immune homeostasis and guide personalized therapeutic plans. Our framework, currently describing the most basic axes, is already able to assess the effect of IL-2 administration and CTLA4 reduction. A systematic framework to quantitatively link model parameters to patient-specific immune status, genetic variations, and therapeutic regimens remained to be developed to move forward in this direction. Adding additional components in the models and determining uncertain parameters through additional experimental data are also required to make our framework more practical.

As we showcased in this study, different mathematical/computational modeling modalities are used for describing different biological organizational layers. The entities described in each layer are also distinct. Therefore, an intuitive and comprehensive understanding of a multiscale biological system requires sewing distinct models seamlessly all together, and this remained challenging. In this regard, we suggested a way of bridging different models together by introducing a phase portrait depicting all regulatory relationships across scales (Figure 4.26). The integration was enabled by identifying quantities that are linked across models. For example, we equated the frequency of IL-2 secreting Tconvs with the frequency of pSTAT5$^+$ Tregs and collectively considered them as the IL-2 niche size. The IL-2 niche size provided by a single self-activated Tconv is spatially limited (Oyler-Yaniv et al., 2017). Therefore, the volume of the space covered with the IL-2 niche is proportional to the frequency of IL-2 secreting Tconvs and reflected with the frequency of pSTAT5$^+$

Tregs obtaining IL-2 signaling. Each of these quantities was related to the probability of clonal expansion of self-activated Tconvs (Figure 4.22 and 4.21) and the Treg density (Figure 4.23 and Curve 1 of Figure 4.26), respectively, and these relationships were plotted along the same horizontal axis (Figure 4.26). Likewise, we derived the relationship between the frequency of IL-2 secreting Tconvs and the duration of IL-2 secretion (IL-2.sec.dur or $\tau_{sec.dur}$) (section B.5.3), and the latter was related to the Treg density/frequency from the T cell activation model (Figure 4.6C and 4.25). In this way, the empirical relationship between the population sizes of IL-2 secreting Tconvs and Tregs in Figure 4.24Figure 4.25 was recapitulated quantitatively, forming Curve 2 (Figure 4.26).

Lastly, a theoretical consideration points to the intriguing feature of immune homeostasis in that the system drives itself by allowing self-reactive Tconvs to respond to self-antigens and eventually arrives at dynamical equilibrium between self-activated, IL-2 secreting T cells and regulatory T cells. This equilibrium point is itself fluctuating yet allows full-blown clonal expansions rarely in homeostasis. Occasional relevant signals readily allow the system to go across the transition point to let clonal expansion almost certainly happen (discussed in Chapter 2). After the triggering signals are gone, then the system goes back to the equilibrium due to various negative feedback mechanisms across scales that are not covered in this study. This behavior is reminiscent of self-organized criticality (SOC), a class of phenomena described in statistical physics, where the system is self-driven to the near-critical regime in terms of the control parameter. The control parameter of the system occasionally goes across the critical point and exhibits a phase transition. The order parameter defining the distinct phases are intimately coupled to the control parameter and brings the control parameter back to the self-driven near-critical regime. The homeostatic condition and clonal expansion can be considered as different phases of the adaptive immunity. The local density/frequency of self-activated, IL-2 secreting Tconvs and their activation status after initial priming can be considered as the control parameters. The exact mapping between the adaptive immune system and SOC has not been pursued yet. We hypothesize that the cluster formation model (Figure 4.21) in the context of nucleation theory may provide a solid connection (Ginot et al., 2018), which may reveal the underlying cause of the power-law distribution of clonal sizes in the peripheral TCR repertoire (Desponds et al., 2017).

Chapter 5: Final discussion and outlook

The overarching goal of this dissertation was to explore scalable approaches of dynamical modeling in biology and immunology in search of novel biology by interweaving a catalog of numerous parts. This touches on both methodological and biological challenges, which arise from the inherent complexities of biological systems such as many types of constituent molecules and cells in various spatial compartments and complicated interaction among them often occurring across scales in space and time.

Traditional modeling tools from physical/mathematical sciences aimed at problems confined in scales often face limits dealing with such complexities despite those are invaluable ingredients we can start with. As mentioned in earlier chapters, the explosion of the number of model parameters in reasonably detailed models is a major hurdle. Additionally, it remained challenging to seamlessly bridge different modeling modalities describing different aspects of biological behaviors at different scales and thus to readily build multiscale dynamical models.

To address the explosion of parameters in realistic biological models, we introduced a framework, MAPPA to better dissect high-dimensional parameter-phenotype maps aided by machine learning (ML) regression models trained by Random Forests (RF) (Chapter 3). RF ML models readily provide information on tunability vs. robustness for model phenotypes at both global and local levels in the parameter space. Such ML models are considered as “phenomenological solutions” in analogous to analytical solutions in mathematical approaches. However, in MAPPA, phenotypes are flexibly defined out of simulation data, thereby bypassing complicated mathematical manipulation of deriving analytical formula linking parameters and phenotypes. We applied MAPPA to several problems, such as dissecting gene-gene correlation behaviors in single cells and assessing the robustness of Treg suppression of self-activated T cells.

In the biological aspect, high-throughput quantitative experimental methods are becoming more available even at the subcellular level, and the overarching themes such as precision or personalized medicine is now thriving. In this regard, there are unmet needs to better understand the complexity of biological system behavior for better therapeutic intervention in hope for desired outcomes to prevent and cure diseases. The problem is that such behaviors are sometimes beyond mere static and linear input-output relationships, the maximum that humans may mentally intuit. In earlier chapters, we have seen that even a simple model such as a two-gene network generated PoV behaviors that were hard to intuit without the quantitative modeling even though fairly accumulated knowledge on gene expression processes. The immune homeostasis is another example that the delicate balance between self-activated T cells and Tregs kept away from autoimmune propensity is formed through the multilayered negative feedback circuit occurring at the intracellular, cellular, and cell population levels. Therefore, merely tuning one knob, such as the anti-CTLA4 administration, would result in both the desired outcomes and an increased risk of the autoimmune side effects. These examples illustrate a potentially major role of quantitative modeling in this “precision” era in designing and guiding therapeutic interventions tailored to individual patients.

Apart from dealing with many parameters, realistic biological models capable of solving real-world problems should incorporate another dimension of biological details, which are different modeling modalities describing different behavioral aspects at different organizational levels. In dissecting immune homeostasis (Chapter 4), we employed different ways of model integrations. In the T cell activation models, we used ODEs for describing the evolution of intracellular entities and PDEs for describing diffusion, migration, and the internal states of the entities in the surrounding space. We were able to integrate these under the assumption of the spherical symmetry of the model and the time separation between ODEs and PDEs (Figure 4.1). Although this is still a simple situation given the typical complexity in biology, computational tools for flexibly designing and executing these modalities together under more generalized situations without the symmetries or time separations do not seem to exist. Another approach we employed for bridging dissimilar modeling modalities was to link quantities at different scales and merge them to derive a simple phase portrait that quantitatively depicts the whole. This approach revealed the nature of immune homeostasis (Figure 4.26). However, this approach may not apply for other situations since identifying a family of quantities linked together requires biological insights that are problem-specific. Together, the integration across modeling modalities needs further investigation, yet problem-specific biological insights can also fill the gaps.

Immune homeostasis revealed by our integrated framework suggests an interesting direction that may immediately help cancer patients. The aforementioned autoimmune side effect of the anti-CTLA4 therapy is due to its blind action on both tumor neoantigens and other normal tissue-derived self-antigens. As we proposed a potential symmetry breaking mechanism between self and non-self in section 2.4.3, introducing new intervention arms such as the low dose IL-2 administration in modulating immune homeostasis may enhance asymmetry between tumor neoantigens and normal tissue-derived self-antigens and may reduce side effects of immune checkpoint inhibition therapies while maintaining the efficacy against cancer antigens. Our framework can readily test this possibility *in silico.*

Lastly, as mentioned in Introduction, how can we address the skepticisms towards the modeling efforts? Indeed, reductionist biology has created a playground where scalable modeling approaches may prove themselves invaluable in biology. However, scalable modeling is still in an early stage, and this also requires previous modeling efforts describing smaller components. Therefore, it may not always be possible to keep up with cutting-edge biology. Overcoming this may require friendly and nurturing environments for enough maturity of the modeling field. On the other hand, the active engagement between modelers and biologists with a common language may help identify immediate biological problems the current stage models can solve. Indeed, the work presented in this dissertation was enabled by active interactions with experimental biologists. Continuous endeavors in this manner may pave a way to firmly establish scalable modeling as an essential approach in biology.

Appendix A: Supporting information for Chapter 3

A.1 *Glossary*

MAPPA: MAchine learning of Parameter-Phenotype Analysis - the name of our framework.

Parameter space: Multidimensional space in which each dimension is defined by the biologically plausible range of each parameter.

Phenotypes: The quantities reflecting specific aspects of dynamical or stationary behaviors of the model/system, which are defined and can be computed using dynamical/stochastic simulation results for each parameter combination.

Phenotypic space: Multidimensional space defined by plausible ranges of each phenotype.

PPM - Parameter-Phenotype Map: Quantitative relationship between parameter values and phenotypes of interest. In our work PPMs are fitted as ML (Machine Learning) models.

GVI - Global Variable Importance: The relative contribution of a parameter for predicting phenotypes averaged over parameter combinations in the training set.

LVI - Local Variable Importance: The relative contributions of a parameter for predicting phenotypes at a particular point in parameter space (i.e., at a specific parameter combination).

CME - Stochastic or Chemical Master Equation: Equations describing the dynamic evolution of probability distribution of system states in chemical reaction networks.

SSA - Stochastic Simulation Algorithm: A simulation algorithm that generates dynamic trajectories of system states (e.g. the abundance of chemical species) in a chemical reaction network. The timing and type of reactions are determined probabilistically based on the current system state and kinetic parameters. Ensemble of time trajectories constitute time evolution of probabilities of states described by CMEs.

PoV (Propagation of variation), information transfer, information propagation, transmission of information, transmission of variation: These terms were used interchangeably; they refer to the phenomenon that variation in gene expression across single cells (or dynamic fluctuations over time within single cells) can be propagated from gene to gene in gene regulatory networks. This can be captured by gene-gene correlations across single cells in a cell population (e.g., via singe cell transcriptomic data).

PPP (see Figure 3.13): A *coherent* feedforward circuit motif. X positively regulates Y (P). Y positively regulates Z (P). X positively regulates Z (P).

PNP (see Figure 3.13): An *incoherent* feedforward circuit motif– “incoherent” because Z is regulated by X and Y in opposite directions. X positively regulates Y (P). Y negatively regulates Z (N). X positively regulates Z (P).

FC: Fold-change of $Corr(m_X, m_Y)$ between PPP or PNP circuits with and without the Y feedforward arm.

Transfer function: a mathematical (e.g., Hill) function describing how the activity of upstream transcription factors affects that of the downstream promotor/enhancer.

QF - Quality Factor: A quantity measuring the extent of oscillation in a system.

PF - Peak Frequency: The dominant frequency of oscillation in a system identified as the most dominant peak in the power spectra (frequency domain analysis) obtained from dynamic trajectories.

LC - Limit Cycle Oscillations: Persistent oscillations with a well-defined frequency/period.

DO - Damped Oscillations: Transient oscillations followed by settling down to stable fixed states.

SS - Stable Steady States: Evolution to fixed stable states without any transient oscillations.

A.2 Model descriptions

Here we describe variables, parameters, and reactions constituting our models in Figure 3.3, 3.13, and 3.18.

A.2.1 Model variables

The chemical species (or variables) used in this study are as follows (Figure 3.3, 3.13, and 3.18):

g_a^X: Gene X with an “active” promoter (on-state)

g_i^X: Gene X with an “inactive” promoter (off-state)

m_X: mRNA transcribed from gene X

p_X: Protein translated from mRNA X

g_a^Y: Gene Y with an “active” promoter (on-state)

g_i^Y: Gene Y with an “inactive” promoter (off-state)

m_Y: mRNA transcribed from gene Y

p_Y: Protein translated from mRNA Y

g_a^Z: Gene Z with an “active” promoter (on-state)

g_i^Z: Gene Z with an “inactive” promoter (off-state)

m_Z: mRNA transcribed from gene Z

p_Z: Protein translated from mRNA Z

A.2.2 Kinetic parameters

The range of the kinetic parameters (Table A.1) was obtained from the experimental literature (Dolken et al., 2008; Jovanovic et al., 2015; Li et al., 2014; Mariani et al., 2010; Rabani et al., 2011; Raj et al., 2006; Schwanhäusser et al., 2011), similar to what we did in our previous work (Martins et al., 2017). We summarized the prior experimental findings into biologically feasible ranges for each parameter (Table A.1). Based on the reported range of copy numbers of transcription factors (TFs) and correlations between protein copy numbers and other quantities such as translation rate constants (Milo and Phillips, 2015; Schwanhäusser et al., 2011), we obtained modified ranges of the transcription and translation rate constants, which were applied to upstream genes acting as TFs in the models (Table A.1).

Over the course of the model development across different network motifs, we tested different ways to specify K (which can be interpreted as the level of the upstream TF needed to achieve the half maximum rate of transcription) when sampling parameter combinations. For the two-gene network (Figure 3.3), K was fixed to a single value as in our previous work (Table A.2) (Martins et al., 2017), while for other circuit motifs (Figure 3.13 and 3.18), K was not fixed. For the two-gene negative feedback network

Parameter	Description (unit)	Range
$\boldsymbol{k_{on}}$	The rate of switching of the promoter state from off- to on-state (event/hour)	0.04-0.4
$\boldsymbol{k_{off}}$	The rate of switching of the promoter state from on- to off-state (event/hour)	0.01-0.5
$\boldsymbol{k_m}$	The maximum rate of mRNA production (events/hour)	0.1-3500 (0.1-1000)*
$\boldsymbol{d_m}$	The rate of mRNA degradation (events/molecule/hour)	0.004-16
$\boldsymbol{k_p}$	The rate of protein production (events/molecule/hour)	0.1-20000 (0.1-1000)*
$\boldsymbol{d_p}$	The rate of protein degradation (events/molecule/hour)	0.0005-6
$\boldsymbol{n}$	Cooperativity for Hill functions of proteins (Hill coefficient) regulating the promoters/enhancers of downstream genes	1 1-5 1, 5
$\boldsymbol{K}$	The level (copy number or ratio to mean protein copy number) of the protein needed to achieve half maximum transcriptional rate for the downstream gene	133.33 (copy number) for two-gene** 30-3000 (copy number) for two-gene negative feedback*** 0.2-5 for (ratio) for three-gene feedforward

Table A.1 Kinetic parameters with biologically plausible ranges from the literature. (Related to Figure 3.3, 3.13, and 3.18) Superscripts are used to denote the gene (for example, k_{off}^{X}) and subscripts are used to denote parameters involved in the interaction between genes, for example, K_{XZ} and n_{XZ} for interaction between protein X and the promoter/enhancer of gene Y). *For genes encoding transcription factors. **The value was fixed as our previous work (Martins et al., 2017). ***In our analyses, these parameters were rescaled and expressed as a ratio to the estimated mean copy number of the protein.

(Figure 3.18), the unit of K was the copy number, which is the same as that for proteins (Table A.4). For the three-gene feedforward networks (Figure 3.13), we tested specifying K as a relative quantity, namely as a ratio to the mean copy number of the upstream TF estimated from the corresponding deterministic model at steady state (Table A.3). For downstream analyses including ML model training and visualizations, we decided to make the unit of K consistent across models as the relative ratio, and thus we converted the unit of K in the two-gene negative feedback network copy number to the relative ratio. Observing that the resultant values of K span several orders of magnitude ($10^{-4} \sim 10^{4}$), we applied the base-10 logarithm transformation, resulting in K spanning the range -4 to 4.

A.2.3 Chemical reactions and the deterministic dynamics for each system

The following biochemical reactions are modeled in the two-gene network (Figure 3.3).

Reaction	Description	Propensity	
$\boldsymbol{g_i^X \longrightarrow g_a^X}$	Promoter activation of gene X	$k_{on}^X \cdot g_i^X$	$(\mathrm{A}.1)$
$\boldsymbol{g_a^X \longrightarrow g_i^X}$	Promoter deactivation of gene X	$k_{off}^X \cdot g_a^X$	$(\mathrm{A}.2)$
$\boldsymbol{g_a^X \longrightarrow g_a^X + m_X}$	mRNA X production: Transcription of gene X	$k_m^X \cdot g_a^X$	$(\mathrm{A}.3)$
$\boldsymbol{m_X \longrightarrow m_X + p_X}$	Protein X production: Translation of mRNA X	$k_m^X \cdot m_X$	$(\mathrm{A}.4)$
$\boldsymbol{m_X \longrightarrow \emptyset}$	Degradation of mRNA X	$d_m^X \cdot m_X$	$(\mathrm{A}.5)$
$\boldsymbol{p_X \longrightarrow \emptyset}$	Degradation of protein X	$d_p^X \cdot p_X$	$(\mathrm{A}.6)$
$\boldsymbol{g_i^Y \longrightarrow g_a^Y}$	Promoter activation of gene Y	$k_{on}^Y \cdot g_i^Y$	$(\mathrm{A}.7)$
$\boldsymbol{g_a^Y \longrightarrow g_i^Y}$	Promoter deactivation of gene Y	$k_{off}^Y \cdot g_a^Y$	$(\mathrm{A}.8)$
$\boldsymbol{g_a^Y + p_X \longrightarrow g_a^Y + p_X + m_Y}$	mRNA Y production: Transcription of gene Y	$g_a^Y \cdot k_m^Y \cdot \frac{{p_X}^{n_{XY}}}{{K_{XY}}^{n_{XY}} + {p_X}^{n_{XY}}}$	$(\mathrm{A}.9)$
$\boldsymbol{m_Y \longrightarrow m_Y + p_Y}$	Protein Y production: Translation of mRNA Y	$k_m^P \cdot m_Y$	$(\mathrm{A}.10)$
$\boldsymbol{m_Y \longrightarrow \emptyset}$	Degradation of mRNA Y	$d_m^Y \cdot m_Y$	$(\mathrm{A}.11)$
$\boldsymbol{p_Y \longrightarrow \emptyset}$	Degradation of protein Y	$d_p^Y \cdot p_Y$	$(\mathrm{A}.12)$

The following equations are deterministic descriptions of the reactions above using ordinary differential equations:

$$\frac{dm_X}{dt} = \frac{k_{on}^X}{k_{on}^X + k_{off}^X} \cdot k_m^X - d_m^X \cdot m_X \tag{A.13}$$

$$\frac{dp_X}{dt} = k_p^X \cdot m_X - d_p^X \cdot p_X \tag{A.14}$$

$$\frac{dm_Y}{dt} = \frac{k_{on}^Y}{k_{on}^Y + k_{off}^Y} \cdot \frac{{p_X}^{n_{XY}}}{{K_{XY}}^{n_{XY}} + {p_X}^{n_{XY}}} \cdot k_m^Y - d_m^Y \cdot m_Y \tag{A.15}$$

$$\frac{dp_X}{dt} = k_p^Y \cdot m_Y - d_p^Y \cdot p_Y. \qquad (A.16)$$

Stationary states can be estimated by setting derivatives in the left-hand side of equations above equal to zero, resulting in the following expressions:

$$\overline{m_X} = \frac{k_{on}^X}{k_{on}^X + k_{off}^X} \cdot \frac{k_m^X}{d_m^X}, \qquad (A.17)$$

$$\overline{p_X} = \frac{k_p^X}{d_p^X} \cdot \overline{m_X}, \qquad (A.18)$$

$$\overline{m_Y} = \frac{k_{on}^Y}{k_{on}^Y + k_{off}^Y} \cdot \frac{\overline{p_X}^{n_{XY}}}{{K_{XY}}^{n_{XY}} + \overline{p_X}^{n_{XY}}} \cdot \frac{k_m^Y}{d_m^Y}, \qquad (A.19)$$

$$\overline{p_Y} = \frac{k_p^Y}{d_p^Y} \cdot \overline{m_Y}. \qquad (A.20)$$

The following reactions describe the elements of the three-gene feedforward networks (PPP and PNP) (Figure 3.13).

Reaction	Description	Propensity	
$\boldsymbol{g_i^X} \longrightarrow \boldsymbol{g_a^X}$	Promoter activation of gene X	$k_{on}^X \cdot g_i^X$	(A.21)
$\boldsymbol{g_a^X} \longrightarrow \boldsymbol{g_i^X}$	Promoter deactivation of gene X	$k_{off}^X \cdot g_a^X$	(A.22)
$\boldsymbol{g_a^X} \longrightarrow \boldsymbol{g_a^X} + \boldsymbol{m_X}$	mRNA X production: Transcription of gene X	$k_m^X \cdot g_a^X$	(A.23)
$\boldsymbol{m_X} \longrightarrow \boldsymbol{m_X} + \boldsymbol{p_X}$	Protein X production: Translation of mRNA X	$k_m^X \cdot m_X$	(A.24)
$\boldsymbol{m_X} \longrightarrow \emptyset$	Degradation of mRNA X	$d_m^X \cdot m_X$	(A.25)
$\boldsymbol{p_X} \longrightarrow \emptyset$	Degradation of protein X	$d_p^X \cdot p_X$	(A.26)
$\boldsymbol{g_i^Y} \longrightarrow \boldsymbol{g_a^Y}$	Promoter activation of gene Y	$k_{on}^Y \cdot g_i^Y$	(A.27)
$\boldsymbol{g_a^Y} \longrightarrow \boldsymbol{g_i^Y}$	Promoter deactivation of gene Y	$k_{off}^Y \cdot g_a^Y$	(A.28)

$\boldsymbol{g_a^Y + p_X \longrightarrow g_a^Y + p_X + m_Y}$	mRNA Y production: Transcription of gene Y	$g_a^Y \cdot k_m^Y \cdot \frac{{p_X}^{n_{XY}}}{{K_{XY}}^{n_{XY}} + {P_X}^{n_{XY}}}$	(A. 29)
$\boldsymbol{m_Y \longrightarrow m_Y + p_Y}$	Protein Y production: Translation of mRNA Y	$k_m^P \cdot m_Y$	(A. 30)
$\boldsymbol{m_Y} \longrightarrow \emptyset$	Degradation of mRNA Y	$d_m^Y \cdot m_Y$	(A. 31)
$\boldsymbol{p_Y} \longrightarrow \emptyset$	Degradation of protein Y	$d_p^Y \cdot p_Y$	(A. 32)
$\boldsymbol{g_i^Z \longrightarrow g_a^Z}$	Promoter activation of gene Z	$k_{on}^Z \cdot g_i^Z$	(A. 33)
$\boldsymbol{g_a^Z \longrightarrow g_i^Z}$	Promoter deactivation of gene Z	$k_{off}^Z \cdot g_a^Z$	(A. 34)
$\boldsymbol{g_a^Z + p_X + p_Y \longrightarrow g_a^Z + p_X + p_Y + m_Z}$	mRNA Z production: Transcription of gene Z	$g_a^Z \cdot k_m^Z \cdot \frac{{p_X}^{n_{XZ}}}{{K_{XZ}}^{n_{XZ}} + {p_X}^{n_{XZ}}} \cdot \frac{{p_Y}^{n_{YZ}}}{{K_{YZ}}^{n_{YZ}} + {P_Y}^{n_{YZ}}}$; PPP $g_a^Z \cdot k_m^Z \cdot \frac{{p_X}^{n_{XZ}}}{{K_{XZ}}^{n_{XZ}} + {p_x}^{n_{XZ}}} \cdot \frac{{K_{YZ}}^{n_{YZ}}}{{K_{YZ}}^{n_{YZ}} + {p_Y}^{n_{YZ}}}$; PNP	(A. 35) (A. 36)
$\boldsymbol{m_Z \longrightarrow m_Z + p_Z}$	Protein Z production: Translation of mRNA Z	$k_m^Z \cdot m_Z$	(A. 37)
$\boldsymbol{m_Z} \longrightarrow \emptyset$	Degradation of mRNA Z	$d_m^Z \cdot m_Z$	(A. 38)
$\boldsymbol{p_Z} \longrightarrow \emptyset$	Degradation of protein Z	$d_p^Z \cdot p_Z$	(A. 39)

The deterministic descriptions are:

$$\frac{dm_X}{dt} = \frac{k_{on}^X}{k_{on}^X + k_{off}^X} \cdot k_m^X - d_m^X \cdot m_X, \tag{A. 40}$$

$$\frac{dp_X}{dt} = k_p^X \cdot m_X - d_p^X \cdot p_X, \tag{A. 41}$$

$$\frac{dm_Y}{dt} = \frac{k_{on}^Y}{k_{on}^Y + k_{off}^Y} \cdot \frac{{p_X}^{n_{XY}}}{{K_{XY}}^{n_{XY}} + {p_X}^{n_{XY}}} \cdot k_m^Y - d_m^Y \cdot m_Y, \tag{A. 42}$$

$$\frac{dp_Y}{dt} = k_p^Y \cdot m_Y - d_p^Y \cdot p_Y, \tag{A. 43}$$

$$\frac{dm_Z}{dt} = \begin{cases} \frac{k_{on}^Z}{k_{on}^Z + k_{off}^Z} \cdot \frac{{p_X}^{n_{XZ}}}{{K_{XZ}}^{n_{XZ}} + {p_X}^{n_{XZ}}} \cdot \frac{{p_Y}^{n_{YZ}}}{{K_{YZ}}^{n_{YZ}} + {p_Y}^{n_{YZ}}} \cdot k_m^Z - d_m^Z \cdot m_Z; \text{PPP} \\ \frac{k_{on}^Z}{k_{on}^Z + k_{off}^Z} \cdot \frac{{p_X}^{n_{XZ}}}{{K_{XZ}}^{n_{XZ}} + {p_X}^{n_{XZ}}} \cdot \frac{{K_{YZ}}^{n_{YZ}}}{{K_{YZ}}^{n_{YZ}} + {p_Y}^{n_{YZ}}} \cdot k_m^Z - d_m^Z \cdot m_Z; \text{PNP} \end{cases}, \tag{A. 44}$$

$$\frac{dp_Z}{dt} = k_p^Z \cdot m_Z - d_p^Z \cdot p_Z. \tag{A.45}$$

Stationary states were obtained as follows:

$$\overline{m_X} = \frac{k_{on}^X}{k_{on}^X + k_{off}^X} \cdot \frac{k_m^X}{d_m^X}, \tag{A.46}$$

$$\overline{p_X} = \frac{k_p^X}{d_p^X} \cdot \overline{m_X}, \tag{A.47}$$

$$\overline{m_Y} = \frac{k_{on}^Y}{k_{on}^Y + k_{off}^Y} \cdot \frac{\overline{p_X}^{n_{XY}}}{{K_{XY}}^{n_{XY}} + \overline{p_X}^{n_{XY}}} \cdot \frac{k_m^Y}{d_m^Y}, \tag{A.48}$$

$$\overline{p_Y} = \frac{k_p^Y}{d_p^Y} \cdot \overline{m_Y}, \tag{A.49}$$

$$\overline{m_Z} = \begin{cases} \dfrac{k_{on}^Z}{k_{on}^Z + k_{off}^Z} \cdot \dfrac{{K_{XZ}}^{n_{XZ}}}{{K_{XZ}}^{n_{XZ}} + {p_X}^{n_{XZ}}} \cdot \dfrac{\overline{p_Y}^{n_{YZ}}}{{K_{YZ}}^{n_{YZ}} + \overline{p_Y}^{n_{YZ}}} \cdot \dfrac{k_m^Z}{d_m^Z}; \text{PPP} \\ \dfrac{k_{on}^Z}{k_{on}^Z + k_{off}^Z} \cdot \dfrac{\overline{p_X}^{n_{XZ}}}{{K_{XZ}}^{n_{XZ}} + \overline{p_X}^{n_{XZ}}} \cdot \dfrac{{K_{YZ}}^{n_{YZ}}}{{K_{YZ}}^{n_{YZ}} + \overline{p_Y}^{n_{YZ}}} \cdot \dfrac{k_m^Z}{d_m^Z}; \text{PNP} \end{cases}, \tag{A.50}$$

$$\overline{p_Z} = \frac{k_p^Z}{d_p^Z} \cdot \overline{m_Z}. \tag{A.51}$$

The following reactions describe the elements of the two-gene negative feedback network (Figure 3.18).

Reaction	Description	Propensity
$\boldsymbol{g_i^X \longrightarrow g_a^X}$	Promoter activation of gene X	$k_{on}^X \cdot g_i^X$ (A.52)
$\boldsymbol{g_a^X \longrightarrow g_i^X}$	Promoter deactivation of gene X	$k_{off}^X \cdot g_a^X$ (A.53)
$\boldsymbol{g_a^X + p^Y \longrightarrow g_a^X + p^Y + m^X}$	mRNA X production: Transcription of gene X	$g_a^X \cdot k_m^X \cdot \frac{{K_{YX}}^{n_{YX}}}{{K_{YX}}^{n_{YX}} + {p_Y}^{n_{YX}}}$ (A.54)
$\boldsymbol{m_X \longrightarrow m_X + p_X}$	Protein X production: Translation of mRNA X	$k_m^X \cdot m_X$ (A.55)
$\boldsymbol{m_X \longrightarrow \emptyset}$	Degradation of mRNA X	$d_m^X \cdot m_X$ (A.56)
$\boldsymbol{p_X \longrightarrow \emptyset}$	Degradation of protein X	$d_p^X \cdot \mathrm{p}_X$ (A.57)
$\boldsymbol{g_i^Y \longrightarrow g_a^Y}$	Promoter activation of gene Y	$k_{on}^Y \cdot g_i^Y$ (A.58)
$\boldsymbol{g_a^Y \longrightarrow g_i^Y}$	Promoter deactivation of gene Y	$k_{off}^Y \cdot g_a^X$ (A.59)
$\boldsymbol{g_a^Y + p_X \longrightarrow g_a^Y + p_X + m_Y}$	mRNA Y production: Transcription of gene Y	$g_a^Y \cdot k_m^Y \cdot \frac{{p_X}^{n_{XY}}}{{K_{XY}}^{n_{XY}} + {p_X}^{n_{XY}}}$ (A.60)
$\boldsymbol{m_Y \longrightarrow m_Y + p_Y}$	Protein Y production:	$k_m^P \cdot m_Y$ (A.61)

	Translation of mRNA Y		
$\boldsymbol{m_Y} \longrightarrow \emptyset$	Degradation of mRNA Y	$d_m^Y \cdot m_Y$	$(\mathrm{A}.62)$
$\boldsymbol{p_Y} \longrightarrow \emptyset$	Degradation of protein Y	$d_p^Y \cdot p_Y$	$(\mathrm{A}.63)$

Corresponding deterministic descriptions of reactions are:

$$\frac{dm_X}{dt} = \frac{k_{on}^X}{k_{on}^X + k_{off}^X} \cdot \frac{{K_{YX}}^{n_{YX}}}{{K_{YX}}^{n_{YX}} + {p_Y}^{n_{YX}}} \cdot k_m^X - d_m^X \cdot m_X, \tag{A.64}$$

$$\frac{dp_X}{dt} = k_p^X \cdot m_X - d_p^X \cdot p_X, \tag{A.65}$$

$$\frac{dm_Y}{dt} = \frac{k_{on}^Y}{k_{on}^Y + k_{off}^Y} \cdot \frac{{p_X}^{n_{XY}}}{{K_{XY}}^{n_{XY}} + {p_X}^{n_{XY}}} \cdot k_m^Y - d_m^Y \cdot m_Y, \tag{A.66}$$

$$\frac{dp_Y}{dt} = k_p^Y \cdot m_Y - d_p^Y \cdot p_Y. \tag{A.67}$$

The corresponding stationary states are:

$$\overline{m_X} = \frac{k_{on}^X}{k_{on}^X + k_{off}^X} \cdot \frac{{K_{YX}}^{n_{YX}}}{{K_{YX}}^{n_{YX}} + \overline{p_Y}^{n_{YX}}} \cdot \frac{k_m^X}{d_m^X}, \tag{A.68}$$

$$\overline{p_X} = \frac{k_p^X}{d_p^X} \cdot \overline{m_X}, \tag{A.69}$$

$$\overline{m_Y} = \frac{k_{on}^Y}{k_{on}^Y + k_{off}^Y} \cdot \frac{\overline{p_X}^{n_{XY}}}{{K_{XY}}^{n_{XY}} + \overline{p_X}^{n_{XY}}} \cdot \frac{k_m^Y}{d_m^Y}, \tag{A.70}$$

$$\overline{p_Y} = \frac{k_p^Y}{d_p^Y} \cdot \overline{m_Y}. \tag{A.71}$$

A.3 Sampling of parameter combinations

To obtain the system's phenotypic behavior throughout the biologically plausible parameter space, our strategy was to sample parameter combinations unbiasedly (but sparsely to keep computational cost reasonable).

We first used a simple 'uniform grid scheme' for the two-gene network and the two-gene negative feedback network. The range of each parameter was divided into discrete points uniformly in the original or logarithmic scales based on the range of each parameter determined by the distribution reported in the literature (Jovanovic et al., 2015; Schwanhäusser et al., 2011). Then, we sampled parameter combinations by randomly selecting a value out of the grid points for each parameter. For the two-gene network, for example, it has 10^{10} possible parameter combinations since each of the 10 parameters was divided into 10 grid points; there a total of 10^5 parameter combinations were sampled (Table A.2). For the two-gene negative feedback network having 12 parameters total, 8, 2, and 2 were divided into 10, 5, and 2 grid points, respectively, resulting in a total of 10^{14} possible parameter combinations (Table A.4).

Second, we used the ‘Sobol’ sampling scheme’ for the three-gene feedforward networks due to the larger number of parameters. The Sobol’ sequence is a low-discrepancy and quasi-random sequence, which fills the unit interval (0,1) more evenly than a pseudorandom sequence (Sobol’, 1967), thus is appropriate for our goal of sampling parameter combinations as uniformly as possible in the high-dimensional parameter space. Using a Sobol’ sequence generator implemented in the *randtoolbox* package in R, a 16-dimensional Sobol’ sequence of 10^5 points filling a $(0,1)^{16}$ hypercube was generated. Then, this sequence was rescaled linearly in the original or logarithmic scales to fit the parameter ranges previously specified for the three-gene feedforward networks (Table A.3). To further specify the network type (out of the 8 possible types (Mangan and Alon, 2003)) for each of parameter combinations, we added a sign (positive and negative) to the Hill coefficients and randomly assigned either a + or – to n_{XY}, n_{YZ}, and n_{XZ}, respectively, where the +/- signs represent positive and negative regulation/influence on downstream promoters, respectively. Thus, either activating or repressive Hill functions were used based on the sign of the Hill coefficients during simulations. In the main text/analysis, we only considered two of the most prevalent types (PPP and PNP; Figure 3.13).

We also note that Latin hypercube sampling is another possible scheme, although we did not use in our current work (Mckay et al., 2000). In the context of global sensitivity analysis, it has been reported that both the Sobol' sequence and the Latin hypercube work better than pseudorandom sequence, but the relative performance between Sobol and Latin hypercube is less clear (Homma and Saltelli, 1996; Mckay et al., 2000; Saltelli et al., 2012).

We further tested the Sobol' sampling scheme for the simple two-gene and two-gene negative feedback networks and compared ML model performance from this scheme to that from the uniform grid scheme for different training sample sizes. The ranges of parameters for the Sobol' sampling scheme were the same as those for the uniform grid sampling scheme.

A.4 Parameter key

Each of the sampled parameter combination was assigned a unique key to make it easily identifiable. The basic syntax for parameter keys is [date of sampling]_[letter combinations] (e.g., 111315_AAAAENMF).

A.5 Additional sampling around specific parameter neighborhoods

Once simulations for the uniformly sampled parameter combinations were conducted for the two-gene, three-gene feedforward, two-gene negative feedback networks (Figure 3.3, 3.13, and 3.18) and phenotypes of interest were computed, we sought to obtain a more detailed picture around the regions of the parameter space that exhibit interesting but rare phenotypic states (e.g., high correlations between the genes in the two-gene network). We thus sampled additional parameter combinations around those regions, conducted simulations for these combinations, and augmented this additional data for training new ML models (see Figure 3.5A).

The detailed method we implemented is as follows. First, parameter combinations exhibiting phenotypic states of interest were selected. Second, for each parameter combination of interest, the sub-range of detailed sampling for each parameter was created (with 1/10 the width of the original parameter range and centered at its value in the parameter combination). Third, additional parameter combinations were sampled on these sub-ranges using the uniform grid sampling scheme or the Sobol' sampling scheme as described above. Finally, we conducted stochastic simulations for these new parameter combinations and computed the phenotypes of interest based on the simulation results. Note that for the three-gene feedforward circuit motifs, the parameter combinations for additional sampling were chosen based on a hard cutoff: we selected those whose $Corr(m_X, m_Y)$ in the circuit with Y differ from that without Y by least 0.2 (Figure A.7A-B). This was chosen qualitatively through visual inspection of the left panels of Figure A.7A-B to enrich for parameter combinations in the off-diagonal regions.

A.6 Stochastic simulation scheme

As mentioned in the main text, we used Gillespie's Stochastic Simulation Algorithm (SSA) to generate dynamic trajectories for each of the parameter combinations (Gillespie, 2007). To save space for data storage, we stored the simulation data once every 5 minutes. To ensure that the copy numbers of mRNAs and proteins stay within biologically feasible ranges, we applied a filtering step before starting simulations, such that only parameter combinations for which the estimated mean (steady-state) copy numbers of mRNAs and proteins of genes do not exceed 1,000 and 2,000,000 copies, respectively, can proceed to simulation (Milo and Phillips, 2015; Schwanhäusser et al., 2011).

We used the following procedure to obtain stationary time trajectories. First, we estimated the time scale under which the system would fluctuate around the mean copy number of chemical species based on deterministic differential equations. Each chemical species fluctuates differently in accordance with the "firing" rates of the chemical species and the slowest reactions determine the overall timescale of fluctuation. For proteins and mRNAs, the contributors to the firing rate are degradation and synthesis rates. The mean firing rate can be estimated as:

$$fr = k + d \cdot \bar{A} \approx 2 \cdot d \cdot \bar{A}, \tag{A.72}$$

where *fr*: the firing rate, *k*: the synthesis rate, *d*: the degradation rate, $\bar{A}$: the mean copy number of the species; '$\approx$' indicates the stationary state where $k = d \cdot \bar{A}$. Therefore, we have an expression that depends only on the degradation rate and the mean copy number. Assuming this firing occurs as a Poisson process, the variance of the number of firing events per unit time is also the firing rate itself. We can define a time scale, τ_f as:

$$\tau_f \equiv \frac{\bar{A}}{fr} = \frac{1}{2 \cdot d}. \tag{A.73}$$

This as a mean time interval during which the variance of the number of firing events is the same as the mean copy number of the chemical species, which can be interpreted as the time it takes to randomize the system such that the “information/memory” about the copy number is lost after this time interval. A related interpretation is that the waiting time of the Poisson process is exponentially distributed with mean waiting time for a single firing event being the inverse of the firing rate $(1/(2 \cdot d \cdot \bar{A}))$, thus it would take on average τ_f units of time for $\bar{A}$ firing events to occur. For promoters, for example, τ_f can be estimated as $1/k_{off}$ or $1/k_{on}$. The maximum of τ_f among all chemical species, $\tau_{f,max}$, can be considered as a good approximation of the time scale of fluctuation for the system. To obtain a stationary time trajectory of the system, a simulation needs to span multiple intervals of $\tau_{f,max}$ to allow the system to explore distinct regions of the state space. This argument is supported by theoretical studies, for example, see (Elf and Ehrenberg, 2003; Gillespie, 2000).

Having defined the time scale of fluctuation, $\tau_{f,max}$, given system with a particular parameter combination, we divided the simulation into two phases: 1) a burn-in phase with a duration of $4 \cdot \tau_{f,max}$ and 2) the main phase with duration of multiples of $20 \cdot \tau_{f,max}$ (see below). The simulation begins with the burn-in phase with the initial condition of zero copies for mRNAs and proteins and inactivated states for promoters, which allows the copy numbers of each species to build up to or near the stationary values; the data from the burn-in phase is discarded in later analyses. Then, the main phase begins and generates time trajectories of each molecular species until the stationary test is passed (see below) or a time limit, t_{max}, is reached. Only the trajectories that passed the stationary test were used for downstream analyses.

The stationary test was conducted after every $20 \cdot \tau_{f,max}$ and the test was performed using only the last 2/3 of the data/trajectories (partly to mitigate the risk that the copy number did not yet reach near the steady-state values) and consisted of two steps. In the first step, the mean values of two halves of the data (latter 2/3) were compared. If the difference between the two values is less than a cut-off (expressed as a percentage of the mean value of the first half of the data), then the second step is applied. If not, the simulation would continue for another $20 \cdot \tau_{f,max}$. In the second step, we used the KPSS test (Kwiatkowski et al., 1992) to evaluate stationarity for higher order moments since the phenotypes of interest involved cross-correlations and power spectra involving second moments. We stopped the simulation if the generated trajectory passed the test or continued for another $20 \cdot \tau_{f,max}$ if it failed the test.

A.7 Machine learning scheme

We used Random Forests (RF) (Breiman, 2001) to build machine learning (ML) models that learn the nonlinear relationships between parameters and phenotypes. We combined each parameter combination with its phenotype computed from the simulations (e.g., correlations between mRNAs X and Y) to form a data table; we then partitioned the data into training and test sets with the ratio of ~4:1 and only the training set was used in fitting the model. The function *randomForest* in the R package *randomForest* was applied to the training set to construct an ensemble of 500 decision trees (Breiman, 2001). Once trained, we tested the ML model using the unseen test set. The prediction performance of the ML model was shown as Receiver Operator Characteristic (ROC) and recall-precision curves for classification ML models (the area under these curves (AUC) was used as the quantitative metric), and the Pearson correlation coefficient between the predicted and simulated values was used for the RF regression based ML models (for predicting continuous values such as gene-gene correlation). For GVI, LVI, and *in-silico* parameter perturbation analyses, we trained ML models by using the entire data set for maximal performance since our goal is to predict the effect of unseen perturbations followed by evaluation by additional stimulations.

For the two-gene (Figure 3.3), three-gene feedforward (Figure 3.13), and two-gene feedback (Figure 3.18) networks, to evaluate whether the use of additional samples drawn nearby the parameter combinations exhibiting desirable phenotypes (see above) can lead to improved prediction accuracy, we first trained ML models using only the "initial" data (without additional samples) and used the "combined" data (with additional samples) to train another model (Figure 3.5A). We saw that the performance of the combined ML models was indeed better (or at least comparable to) than that of the initial ML models (Figure A.2B-C and A.12A-B, data not shown for the three-gene feedforward networks). We thus used combined ML models for the rest of analyses, including the determination of GVIs and LVIs and in the *in-silico* perturbation experiments.

We used RF regression models for continuous value phenotypes. To address the inherent bias of RF regression (Breiman, 1996; Zhang and Lu, 2012), we applied a bias correction method for all ML regression models we trained in this study (Zhang and Lu, 2012). Briefly, we trained additional models for the "error" or the residuals $y - \hat{y}$, where y is the phenotypic value from the training set and $\hat{y}$ is the value predicted by the uncorrected, original RF regression model. The bias-corrected predictions were obtained by adding the predicted corrections from the residual ML model.

A.8 Variable importance

The *randomForest* package in R generates variable importance both at the global level (global variable importance (GVI), which can be thought as average over all data points in training sets) and in the local level (local variable importance (LVI)) for each individual data point in the training sets with the 'importance' and 'localImp' options turned on, respectively (Breiman, 2001; Liaw and Wiener, 2002). Two types of global variable importance were computed: permutation and impurity GVIs. The permutation GVI is generated based on the increase in the out-of-bag prediction errors (using the training set only) after randomly permuting each input variable. The impurity GVI is generated by measuring the total decrease in the node "impurity" (which quantifies the heterogeneity/entropy of the outcomes underneath each tree node; Gini index is used for categorical outcome variables and the residual sum of squares for continuous outcome variables) conferred by each variable in the training set. LVI is the increase in the out-of-bag prediction error on a specific data point of the training set (thus a particular point in the parameter space) after permuting each of the input variables. The permutation GVI was generated by averaging the LVIs from all data points. Although GVI gives a general overview, the variable importance can differ across parameter space as captured by the LVI. We grouped the individual LVIs (at each point in the parameter space) by hierarchical clustering and visualized the resulting clusters using tSNE plots and used them to guide *in-silico* perturbation experiments.

For the hierarchical clustering heatmaps (Figure 3.5D and A.11), we showed the average values of LVIs for each cluster rather than showing all LVIs for individual parameter combinations. The number of clusters were chosen based on visual inspection of the original heatmaps to allow visualization of major patterns capturing the full qualitative diversity of the LVIs. Detailed heatmaps showing all LVIs can be generated on our website (https://phasespace-explorer.niaid.nih.gov).

A.9 Nonlinear dimension reduction visualization end embedding of additional samples

We used t-distributed stochastic neighbor embedding (tSNE), a technique for dimensionality reduction, to visualize high-dimensional parameter spaces. We first generated a reference tSNE plot in 2D space using the original sampled parameter combinations. Since the tSNE algorithm does not provide a general parameterized transformation from higher to lower dimensional spaces, adding additionally sampled parameter combinations (see above) to an existing visualization requires a new tSNE plot. Thus, we implemented a customized algorithm for embedding additional points in an existing tSNE plot by following Appendix D of Berman et al. (Berman et al., 2014) and applied it for generating Figure 3.4D. The procedure is briefly summarized below.

Starting with a lower dimensional tSNE embedding, Y, of the original high dimensional data, X, where X and Y are matrices, and the rows in them, x_i and y_i, correspond to individual data points with $i = 1, 2, \ldots, N$, with N being the number of data points. Then, for an additional high-dimensional point (with the same dimension as X), z, we want to obtain lower dimensional embedding, w (with the same dimension as Y), on the reference embedding, Y. To accomplish this, as in the tSNE algorithm, we first defined transition probabilities as

$$p_{x_i|z} = \frac{\exp\left(-\frac{\|x_i - z\|^2}{2\sigma^2}\right)}{\sum_k \exp\left(-\frac{\|x_k - z\|^2}{2\sigma^2}\right)}, \tag{A.74}$$

$$q_{y_i|w} = \frac{(1 + \|y_i - w\|^2)^{-1}}{\sum_k (1 + \|y_k - w\|^2)^{-1}}, \tag{A.75}$$

where $\|\cdots\|$ denotes the Euclidian norm of a vector inside, and σ is related to the perplexity, P, a parameter used in the tSNE algorithm, roughly equivalent to the number of nearest points that z can perceive as specified by the following relation,

$$-\sum_j p_{x_j|z} \log_2 p_{x_j|z} = \log_2 P\,. \tag{A.76}$$

These transition probabilities reflect the similarity between the existing data points and the additional point we would like to embed. Next, the lower dimensional coordinates, w, was obtained by minimizing the Kullback-Leibler divergence between $p_{x_i|z}$ and $q_{y_i|z}$, $KL(p||q)$ by tuning each component of w as:

$$w^* = \underset{w}{\operatorname{argmin}}\, KL(p||q) = \underset{w}{\operatorname{argmin}} \sum_i p_{x_i|z} \log\left(\frac{p_{x_i|z}}{q_{y_i|w}}\right). \tag{A.77}$$

We note that UMAP (Uniform Manifold Approximation and Projection) is also a good method for nonlinear dimension reduction and known to better preserve the global distance relationship in dimension-reduced space than tSNE (McInnes et al., 2018). Moreover, UMAP has its own built-in function for embedding additional data on the top of an existing embedding with fast performance.

A.10 Global and local sensitivity analysis

We computed Sobol's variance-based sensitivity indices to compare with GVI from RF models for the simple two gene network (Figure 3.9) (Saltelli et al., 2008). Given a model in the form of $Y = f(X_1, X_2, \dots, X_k)$, with Y a scalar model output and X_i model inputs, two types of sensitivity indices were computed: first-order indices S_i and total indices S_{T_i} defined as

$$S_i = \frac{V_{X_i}\left(E_{X_{\sim i}}(Y|X_i)\right)}{V(Y)}, \tag{A.78}$$

$$S_{T_i} = \frac{E_{X_{\sim i}}\left(V_{X_i}(Y|X_{\sim i})\right)}{V(Y)} = 1 - \frac{V_{X_{\sim i}}\left(E_{X_i}(Y|X_{\sim i})\right)}{V(Y)}, \tag{A.79}$$

where $X_{\sim i}$ denotes all input variables except X_i. The first-order indices (S_i) can be understood as the fraction of the total variance of Y contributed by X_i as a first-order effect while the total indices (S_{T_i}) include the first-order effect and higher-order interaction effects of X_i. We used Salteli's implementation in the *sensitivity* package in R to compute the indices. This required preparing two independent parameter sets with the same size using preferentially the Sobol' sequence: to say, A and B, where rows are parameter combination vectors. Then the simulation experiment scheme was designed by replacing each column of B with the corresponding column of A denoted as C_i. If we start from A and B with N rows with p parameters, then we end up having $N \cdot (p + 2)$ parameter combinations to be simulated. For our case with $N = 1000$ and $p = 10$, we simulated 12000 parameter combinations. Once we obtained the outcome Y after simulations, we empirically computed S_i and S_{T_i} as

$$S_i = \frac{\frac{1}{N} \cdot \left(Y(A) \cdot Y(C_i)\right) - f_0^2}{\frac{1}{N} \cdot \left(Y(A) \cdot Y(A)\right) - f_0^2}, \tag{A.80}$$

$$S_{T_i} = 1 - \frac{\frac{1}{N} \cdot \left(Y(B) \cdot Y(C_i)\right) - f_0^2}{\frac{1}{N} \cdot \left(Y(A) \cdot Y(A)\right) - f_0^2}, \tag{A.81}$$

where $Y(\ldots) \cdot Y(\ldots)$ denotes the inner product of two output vectors and $f_0 = \frac{1}{N} \cdot \sum_{j=1}^{N} Y(A^j)$ with A^j being the jth row of A.

For local sensitivity analysis for comparison with LVI from ML models, we randomly selected 500 parameter combinations (300 from those with $Corr(m_X, m_Y) > 0.4$ and 200 from those with $Corr(m_X, m_Y) \leq 0.4$) and conducted simulations on perturbed parameter combinations. We prepared perturbed parameter combinations by changing a parameter at a time to other grid points over the full plausible range. Thus, additional expanses of local sensitivity analysis were 90 more simulations for each parameter combination. Then, we defined three different local sensitivity measures out of simulation results: 1) maximum deviation, the full ranges of the phenotypic variations upon perturbing a parameter in the full range: 2) mean squared deviation of the phenotype from the original values upon perturbing a parameter to different values within the full range, and 3) partial difference defined as a change of the phenotype if the value of a parameter was changed to an adjacent grid point, analogous to a partial derivative. The concordance between LVI and a local sensitivity measure for a particular parameter combination was defined as Pearson correlation coefficient between them.

A.11 Mutual information

From simulation outcomes of the simple two-gene network, we computed entropies $H(m_X)$ for mRNA X and $H(m_Y)$ for mRNA Y, and a joint entropy

$H(m_X, m_Y)$ for mRNA X and mRNA Y. We used the *entropy* package in R. We applied the discretize (for two univariate entropy) or discretize2d (for bivariate entropy) functions to obtain discretized probability distributions, followed by the entropy function applied on such estimated distributions. The mutual information was obtained as

$$I(m_X, m_Y) = H(m_X) + H(m_Y) - H(m_X, m_Y). \tag{A.82}$$

We further normalized this as

$$I'(m_X, m_Y) = \frac{I(m_X, m_Y)}{\sqrt{H(m_X) \cdot H(m_Y)}}, \tag{A.83}$$

which was finally used as a phenotype of interest in the Results.

A.12 <u>Analytical linear noise approximation and inverse omega square approximation</u>

We derived the linear noise approximation of $Corr(m_X, m_y)$ by following the approach of Elf and Ehrenberg (Elf and Ehrenberg, 2003) and Paulsson (Paulsson, 2004). With stationary assumption and linearization of the CMEs describing the system, the following relationship (a Lyapunov matrix equation) can be derived,

$$J \cdot C + C \cdot J^T + B = 0, \tag{A.84}$$

where J: the Jacobian of the deterministic equations, C: the covariance matrix, and B: the diffusion matrix. J and B at the stationary state were obtained as:

$$\mathrm{J}=\begin{pmatrix} -\left(k_{on}^X + k_{off}^X\right) & 0 & 0 & 0 & 0 \\ k_m^X & -d_m^X & 0 & 0 & 0 \\ 0 & k_p^X & -d_p^X & 0 & 0 \\ 0 & 0 & 0 & -\left(k_{on}^Y + k_{off}^Y\right) & 0 \\ 0 & 0 & \alpha k_m^Y \overline{g_a^Y} & \beta k_m^Y & -d_m^Y \end{pmatrix}, \tag{A.85}$$

$$B = \begin{pmatrix} 2k_{off}^{X}\overline{g_a^X} & 0 & 0 & 0 & 0 \\ 0 & 2d_m^X\overline{m_X} & 0 & 0 & 0 \\ 0 & 0 & 2d_p^X\overline{p_X} & 0 & 0 \\ 0 & 0 & 0 & 2k_{off}^{Y}\overline{g_a^Y} & 0 \\ 0 & 0 & 0 & 0 & 2d_m^Y\overline{m_Y} \end{pmatrix}, \qquad (\mathrm{A}.86)$$

where $\alpha = \frac{n_{XY}K_{XY}{}^{n_{XY}}\overline{p_X}^{n_{XY}-1}}{\left(K_{XY}{}^{n_{XY}}+\overline{p_X}^{n_{XY}}\right)^2}$, $\beta = \frac{\overline{p_X}^{n_{XY}}}{K_{XY}{}^{n_{XY}}+\overline{p_X}^{n_{XY}}}$, and $\overline{g_a^X}$, $\overline{m_X}$, $\overline{p_X}$, $\overline{g_a^Y}$, and $\overline{m_Y}$ were obtained by solving stationary equations in the **Model Description** above. Then, the covariance matrix, C, was obtained by solving the matrix equation (Eq. 84) with elements C_{ij} with indices i and j (1, 2, 3, 4, and 5 corresponding to the variables, g_a^X, m_X, p_X, g_a^Y, and m_Y):

$$C_{11} = \left(1-\overline{g_a^X}\right)\cdot\overline{g_a^X}, \qquad (\mathrm{A}.87)$$

$$C_{12} = C_{11}\cdot\frac{\overline{m_X}}{\overline{g_a^X}}\cdot\frac{d_m^X}{k_{on}^X+k_{off}^X+d_m^X}, \qquad (\mathrm{A}.88)$$

$$C_{22} = \overline{m_X} + C_{11}\cdot\frac{\overline{m_X}^2}{\overline{g_a^X}^2}\cdot\frac{d_m^X}{k_{on}^X+k_{off}^X+d_m^X}, \qquad (\mathrm{A}.89)$$

$$C_{13} = C_{12}\cdot\frac{\overline{p_X}}{\overline{m_X}}\cdot\frac{d_p^X}{k_{on}^X+k_{off}^X+d_p^X}, \qquad (\mathrm{A}.90)$$

$$C_{23} = C_{13}\cdot\frac{\overline{m_X}}{\overline{g_a^X}}\cdot\frac{d_m^X}{d_m^X+d_p^X} + C_{22}\cdot\frac{\overline{p_X}}{\overline{m_X}}\cdot\frac{d_p^X}{d_m^X+d_P^X}, \qquad (\mathrm{A}.91)$$

$$C_{33} = \overline{p_X} + C_{13}\cdot\frac{\overline{p_X}}{\overline{g_a^X}}\cdot\frac{d_m^X}{d_m^X+d_p^X} + C_{22}\cdot\frac{\overline{p_X}^2}{\overline{m_X}^2}\cdot\frac{d_p^X}{d_m^X+d_p^X}, \qquad (\mathrm{A}.92)$$

$$C_{14} = C_{24} = C_{34} = 0, \qquad (\mathrm{A}.93)$$

$$C_{44} = \left(1-\overline{g_a^Y}\right)\cdot\overline{g_a^Y}, \qquad (\mathrm{A}.94)$$

$$C_{15} = C_{13}\cdot(1-\beta)\cdot n_{XY}\cdot\frac{\overline{m_Y}}{\overline{p_X}}\cdot\frac{d_m^Y}{k_{on}^X+k_{off}^X+d_m^Y}, \qquad (\mathrm{A}.95)$$

$$C_{25} = C_{15} \cdot \frac{\overline{m_X}}{\overline{g_{on}^X}} \cdot \frac{d_m^X}{d_m^X + d_m^Y} + C_{23} \cdot (1-\beta) \cdot n_{XY} \cdot \frac{\overline{m_Y}}{\overline{p_X}} \cdot \frac{d_m^Y}{d_m^X + d_m^Y}, \tag{A.96}$$

$$C_{35} = C_{25} \cdot \frac{\overline{p_X}}{\overline{m_X}} \cdot \frac{d_p^X}{d_p^X + d_m^Y} + C_{33} \cdot (1-\beta) \cdot n_{XY} \cdot \frac{\overline{m_Y}}{\overline{p_X}} \cdot \frac{d_m^Y}{d_p^X + d_m^Y}, \tag{A.97}$$

$$C_{45} = C_{44} \cdot \frac{\overline{m_Y}}{\overline{g_a^Y}} \cdot \frac{d_m^Y}{k_{on}^Y + k_{off}^Y + d_m^Y}, \tag{A.98}$$

$$C_{55} = \overline{m_Y} + C_{35} \cdot (1-\beta) \cdot n_{XY} \cdot \frac{\overline{m_Y}}{\overline{p_X}} + C_{45} \cdot \frac{\overline{m_Y}}{\overline{g_a^Y}}, \tag{A.99}$$

Finally, the analytical approximation of $Corr(m_X, m_Y)$ was obtained as:

$$Corr(m_X, m_Y) = \frac{C_{25}}{\sqrt{C_{22} \cdot C_{55}}}, \tag{A.100}$$

where C_{22} and C_{55} are the variances of mRNA X and mRNA Y, respectively. Further expansion of the covariance between mRNAs X and Y, C_{25}, revealed:

$$\begin{aligned} C_{25} = {} & \delta \cdot \frac{d_m^X}{d_m^X + d_m^Y} \cdot \frac{d_m^X}{k_{on}^X + k_{off}^X + d_m^X} \cdot \frac{d_p^X}{k_{on}^X + k_{off}^X + d_p^X} \cdot \frac{d_m^Y}{k_{on}^X + k_{off}^X + d_m^Y} \\ & + \delta \cdot \frac{d_m^X}{k_{on}^X + k_{off}^X + d_m^X} \cdot \frac{d_m^Y}{d_m^X + d_m^Y} \cdot \frac{d_m^X}{d_m^X + d_p^X} \cdot \frac{d_p^X}{k_{on}^X + k_{off}^X + d_p^X} \\ & + \delta \cdot \frac{\overline{g_a^X} \cdot \overline{m_X}}{1 - \overline{g_a^X}} \cdot \frac{d_m^Y}{d_m^X + d_m^Y} \cdot \frac{d_p^X}{d_m^X + d_p^X} \\ & + \delta \cdot \frac{d_m^Y}{d_m^X + d_m^Y} \cdot \frac{d_m^X}{k_{on}^X + k_{off}^X + d_m^X} \cdot \frac{d_p^X}{d_m^X + d_p^X}, \end{aligned} \tag{A.101}$$

where $\delta = \frac{\left(1-\overline{g_a^X}\right)}{\overline{g_a^X}} \cdot \overline{m_X} \cdot \overline{m_Y} \cdot (1-\beta) \cdot n_{XY}$, showing $\frac{d_m^Y}{d_m^X + d_m^Y}$ as one of the main contributors to $Corr(m_X, m_Y)$ according to this analytical treatment.

For the inverse omega square approximation (IOS) (Grima et al., 2011), we used the package, *CERENA* (ChEmical REaction Network Analyzer) written in Matlab

(Kazeroonian et al., 2016). Note that although IOS is in principle analytically solvable, the simple two-gene model is already in the complexity beyond hand calculation of IOS, rendering symbolic computational tools such as *CERENA* only feasible ways of applying IOS in a practical sense.

A.13 Deterministic modeling of the two-gene negative feedback circuit: bifurcation analysis at a fixed point

We explored the phase space and bifurcation behaviors of the two-gene negative feedback circuit (Figure 3.18) (Strogatz, 2015). Our goal is to delineate, using deterministic modeling only based on the **Model Descriptions (section A.2)** above, whether a given parameter combination would result in damped oscillation, limit cycle oscillation, or stable steady state. First, the fixed points (i.e., $\overline{m_X}$, $\overline{p_X}$, $\overline{m_Y}$, and $\overline{p_Y}$) were obtained for each of parameter combinations by solving the stationary equations numerically shown in the **Model Descriptions (section A.2)** above. Then, the Jacobian J at the fixed point was obtained as:

$$J = \begin{pmatrix} -d_m^X & 0 & 0 & -\alpha \\ k_p^X & -d_p^X & 0 & 0 \\ 0 & \beta & -d_m^Y & 0 \\ 0 & 0 & k_p^Y & -d_p^Y \end{pmatrix}, \tag{A.102}$$

whereA.103

$$\alpha = \frac{k_{on}^X k_m^X}{k_{on}^X + k_{off}^X} \cdot \frac{n_{YX} {K_{YX}}^{n_{YX}} \overline{p_Y}^{n_{YX}-1}}{\left({K_{YX}}^{n_{YX}} + \overline{p_Y}^{n_{YX}}\right)^2}, \tag{A.104}$$

$$\beta = \frac{k_{on}^Y k_m^Y}{k_{on}^Y + k_{off}^Y} \cdot \frac{n_{XY} {K_{XY}}^{n_{XY}} \overline{p_X}^{n_{XY}-1}}{\left({K_{XY}}^{n_{XY}} + \overline{p_X}^{n_{XY}}\right)^2}. \tag{A.105}$$

The eigenvalues λ of the Jacobian J at the fixed point were obtained by solving the characteristic equation of J:

$$(\lambda + d_m^X)(\lambda + d_p^X)(\lambda + d_m^Y)(\lambda + d_p^Y) + \alpha\beta k_p^X k_p^Y = 0. \qquad (A.106)$$

Depending on the parameter combination, this equation can have: 1) four real negative roots, 2) two real negative and two complex roots, or 3) four complex roots. Since the analytical approach for solving fourth degree polynomial equations is complex, we numerically solved this equation for each of the parameter combinations. More thorough treatment of four-dimensional Hopf bifurcation can be found in Asada and Yoshida (Asada and Yoshida, 2003).

The nature of the eigenvalues obtained for each parameter combination determine the behaviors of the circuit (Kuznetsov, 2004; Strogatz, 2015). First, if the eigenvalues are all real and negative, then the system evolves to and settles at the stable fixed point ($\overline{m_X}$, $\overline{p_X}$, $\overline{m_Y}$, and $\overline{p_Y}$). Second, if the eigenvalues include a pair or two pairs of complex values with negative real part, then, the system exhibits damped oscillation, eventually settling down to the stable fixed point. Lastly, if the eigenvalues include a pair of complex conjugates with positive real part and other two with negative real parts, then the system exhibits limit cycle oscillations. Here we provide a brief proof of limit cycle oscillations. The trajectory in eigen bases corresponding to eigenvalues with negative real parts eventually decays to the stable fixed point. Therefore, the trajectory is confined to the 2-dimensional center manifold defined by eigen bases of eigenvalues with positive real parts and exhibits radially growing oscillations from the neighborhood of the fixed point in that manifold (Kuznetsov, 2004). Due to the degradation terms and nonlinearity in the model, any trajectory after a sufficiently long time is confined within a hypercube defined by

$$m_X;\ \left(0, \frac{k_{on}^X}{k_{on}^X + k_{off}^X} \cdot \frac{k_m^X}{d_m^X}\right),$$

$$p_X;\ \left(0, \frac{k_{on}^X}{k_{on}^X + k_{off}^X} \cdot \frac{k_m^X}{d_m^X} \cdot \frac{k_p^X}{d_p^X}\right),$$

$$m_Y; \left(0, \frac{k_{on}^Y}{k_{on}^Y + k_{off}^Y} \cdot \frac{k_m^Y}{d_m^Y}\right),$$

$$p_Y; \left(0, \frac{k_{on}^Y}{k_{on}^Y + k_{off}^Y} \cdot \frac{k_m^Y}{d_m^Y} \cdot \frac{k_p^Y}{d_p^Y}\right),$$

given that the vector field, $(\frac{dm_X}{dt}, \frac{dp_X}{dt}, \frac{dm_Y}{dt}, \frac{dp_Y}{dt})$ points always inward on the boundary of the hypercube. Therefore, by Poincaré-Bendixson theorem any trajectory in the center manifold eventually evolves to a closed orbit or a limit cycle (Strogatz, 2015) (Figure 3.19A and 3.22). Note that it is impossible that all eigenvalues have positive real parts since the sum of all eigenvalues should be negative based on the relationship: $\sum \lambda_i = -\left(d_m^X + d_p^X + d_m^Y + d_p^Y\right) < 0$.

A.14 *Power spectral analysis*

The oscillatory behavior in the two-gene negative feedback network can be described in the frequency domain using power spectra analysis of the time trajectories. Power spectra were obtained by Fourier transformation of the auto-correlation functions or cross-correlation functions as proven by the Wiener-Khinchin theorem (Kampen, 2007). Ideally, we need a large number of realizations of the time trajectories to obtain the power spectra. However, here (and often in practice) we only have a single time trajectory and thus noise can be an issue. There are several methods to reduce such noise, including the averaging of multiple estimates from segments of the original trajectories and applying window functions for Fourier transformations (Percival and Walden, 1993). We employed both strategies together. We divided single time trajectories into multiple segments, applied Welch's methods implemented in the *sapa* package in R to each of those segments, and averaged over multiple estimates. Based on the resolution needed and computation time, we set a limit on the length of the segment to not exceed 10^5 time-points, which corresponds to ~8333 hours ($10^5 \times 5$ minutes) in the system's time. Thus, this approach would miss anything that occurs in longer timescales or shorter than 5 minutes (the data acquisition time interval), which were not captured in the current power spectral analysis.

The unit of frequency in power spectra analysis is $1\ unit\ = \frac{1}{5}\min^{-1} = 3.33 \times 10^{-3} Hz$ since the unit time interval is 5 min. The frequency range spanned several orders of magnitude. Thus, we applied the logarithm (with base 10) to define peak frequency (PF). PF spanned values ranging from -5 to -1, and the corresponding values of these in Hz spanned from $3.33 \times 10^{-8} Hz$ to $3.33 \times 10^{-4} Hz$ using the general conversion formula; $10^{\mathrm{PF}} \times 3.33 \times 10^{-3} Hz$. Intuitively, for example, if a periodic event occurs once every hour, the frequency is $\frac{1}{3600}\sec^{-1} = 2.78 \times 10^{-4} Hz = 8.35 \times 10^{-2}\ unit,$ and after taking logarithm with base 10, $\mathrm{PF} = -1.08$.

A.15 Supplementary Figures

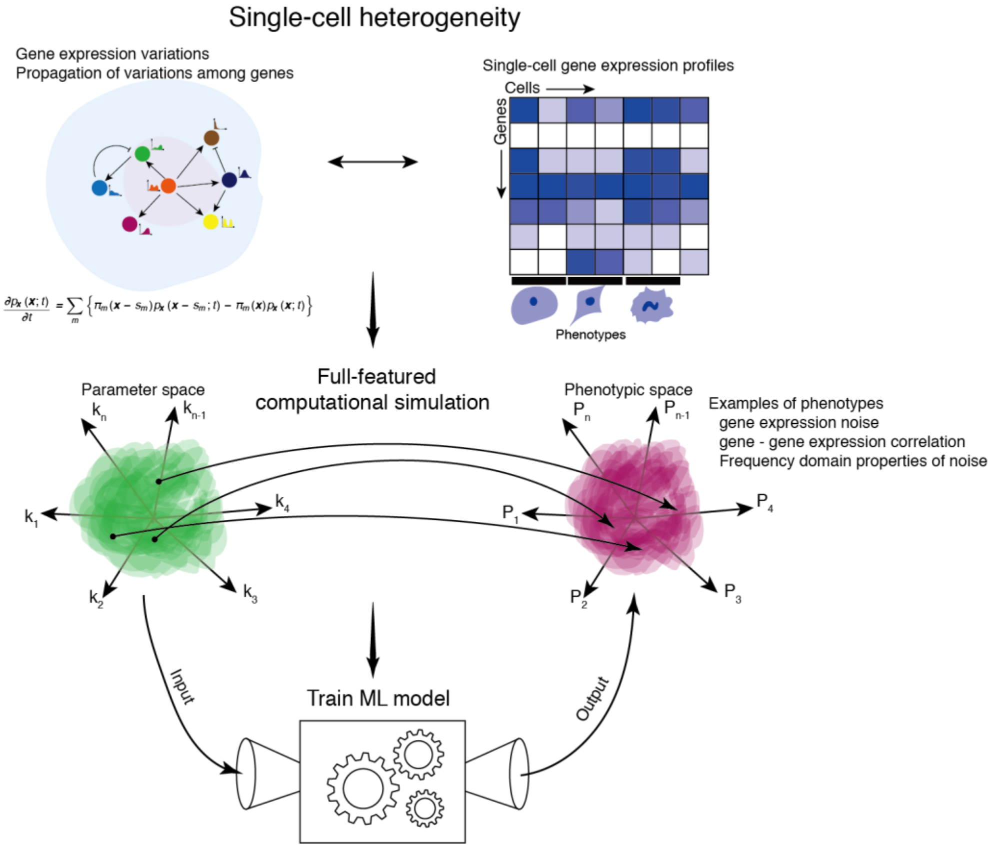

Figure A.1 Motivation and conceptual framework. Cell-to-cell gene expression heterogeneity is prevalent and can propagate from gene to gene across the gene regulatory network, giving rise to patterns of expression heterogeneity in the cell population that are potentially associated with cellular phenotypes. Given a biological network, our framework samples parameter combinations, conducts stochastic dynamical simulations to generate time series data sets from the network, builds machine learning (ML) models that connect parameter and phenotypic spaces, such as linking parameter values to cell-to-cell gene expression variations and gene-gene correlations across single cells. The ML models can be thought of as phenomenological solutions of the equations governing the stochastic dynamics of the network. They enable much faster computation of quantitative phenotypes from parameter combinations than using full-blown simulations and a better understanding of how the system's phenotypes are shaped by the parameters.

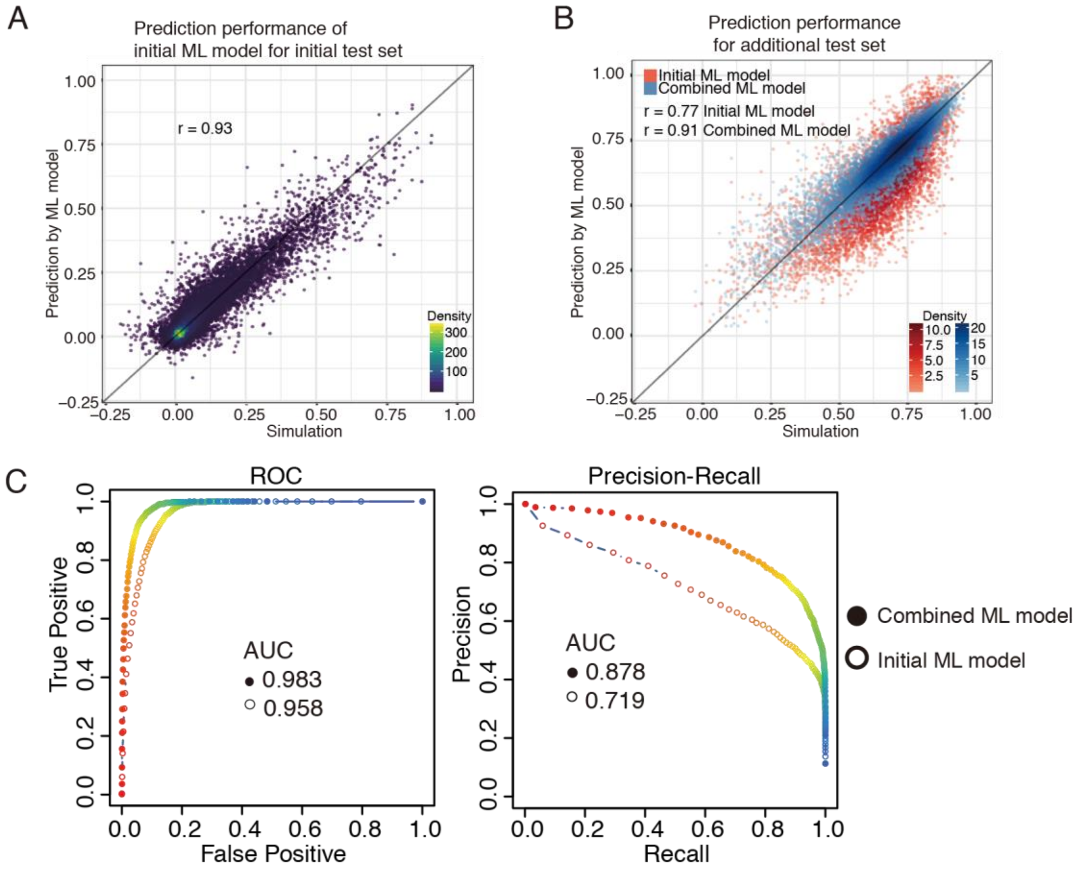

Figure A.2 ML model performance for a two-gene network. **(A)** Scatter plot showing the predicted (y) vs. the simulated (x) phenotypic values. The RF regression model trained on the initial training set was used to predict the phenotypic value for the initial test set. **(B)** Same as (A) but showing the prediction performance of the RF regression models trained on the initial training set (red) and the combined training set (blue) in predicting the additional test set (enriching for parameter combinations with high $Corr(m_X, m_Y)$). **(C)** Prediction performance of the RF classification models ($Corr(m_X, m_Y) > 0.7$ vs. < 0.7) evaluated using the combined test set, as indicated by the receiver operating characteristic (ROC) and precision-recall curves. Hollow circles correspond to data from the RF model trained using the initial training set, while solid circles are data from the RF model trained using the combined training set.

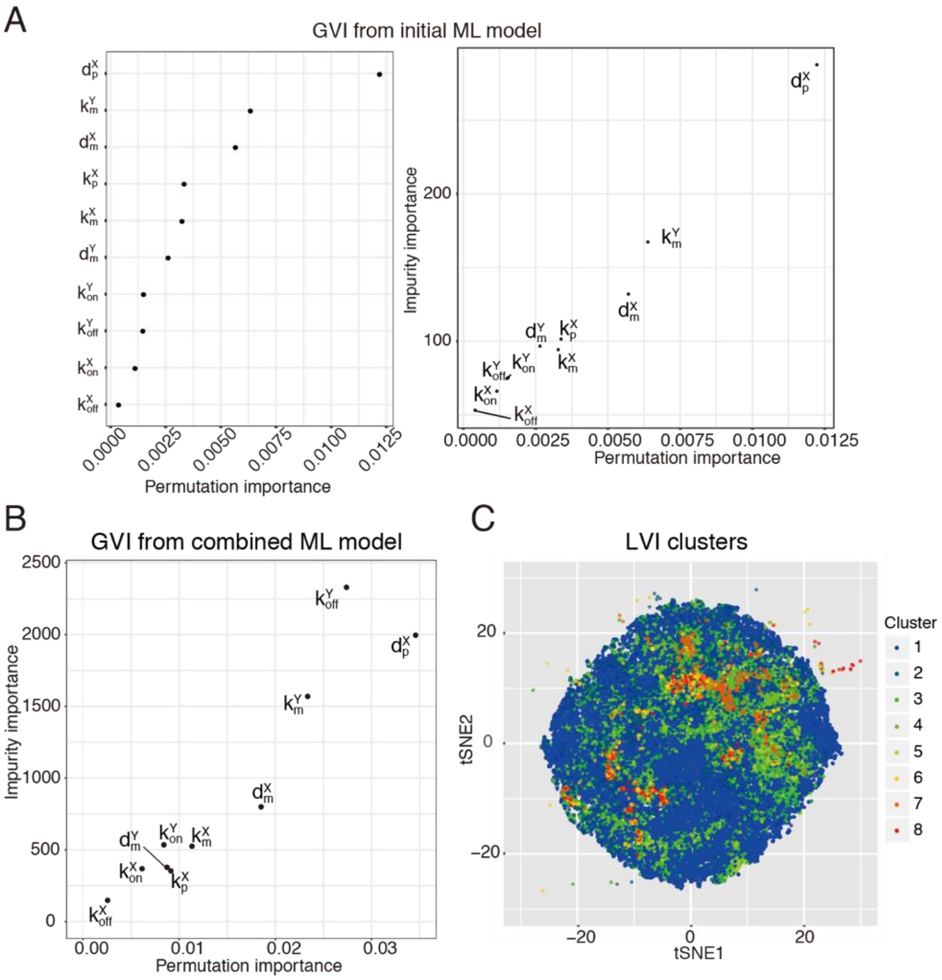

Figure A.3 Variable importance of ML models in a two-gene network. **(A)** (Left) Permutation GVI for the RF regression model trained on the initial training set. (Right) Impurity (y axis) vs. permutation (x axis) GVIs for the RF regression model trained on the initial training set are shown together in a scatter plot. **(B)** Impurity (y axis) vs. permutation (x axis) GVIs for the RF regression model trained on the combined training set are shown together in a scatter plot. **(C)** tSNE plot of all (initial and additional) parameter combinations colored by the cluster ID defined in Figure 3.5 D.

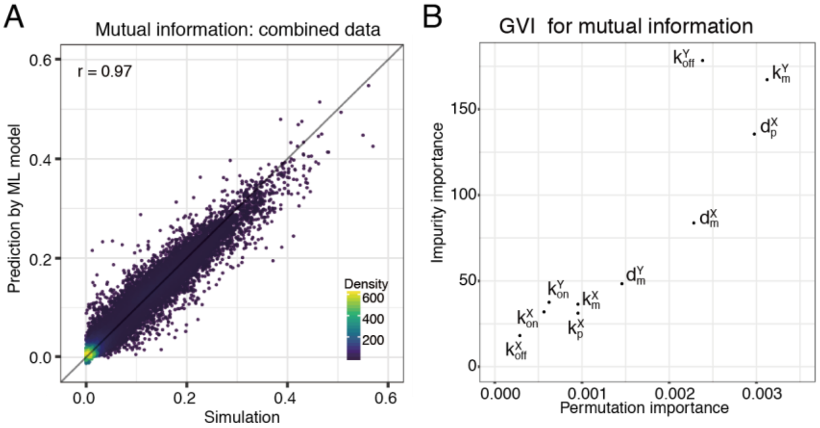

Figure A.4 MAPPA analysis on mutual information. **(A)** Scatter plot of predicted vs. simulated mutual information to illustrate the prediction performance of the RF regression model for mutual information ($\mathrm{r} = 0.97$); note that the RF model was trained using the combined training data; each point corresponds to a parameter combination.**(B)** Impurity (y axis) vs. permutation (x axis) GVIs for the RF regression model predicting mutual information trained on the combined training set are shown together in a scatter plot.

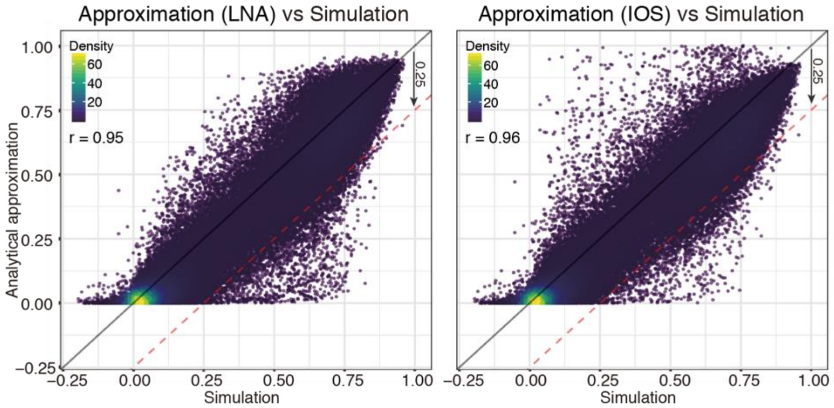

Figure A.5 Comparison between MAPPA and analytical approximation schemes. Scatter plot of $Corr(m_X, m_Y)$ computed from analytical approximation (y axis) versus that from the stochastic simulation in the entire dataset (both “initial” and “additional” – see Figure 3.5A). Analytical approximations are from LNA (left) and IOS (right).

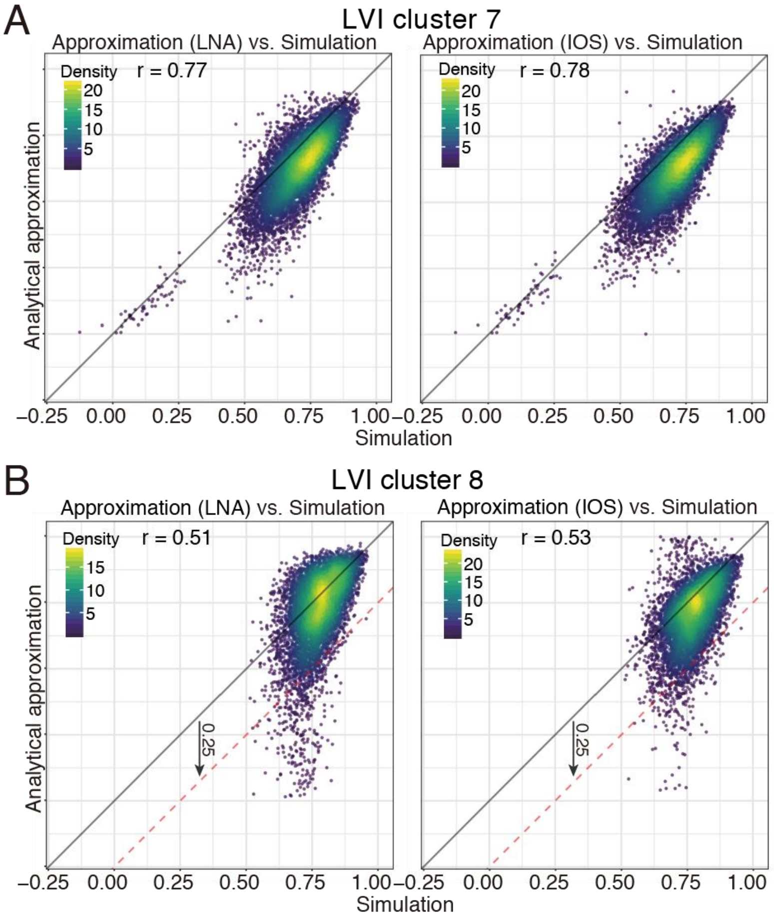

Figure A.6 Comparison between MAPPA and analytical approximation schemes over LVI clusters 7 and 8. **(A)-(B)** Scatter plots showing $Corr(m_X, m_Y)$ of analytical approximation (LNA) vs. simulation (left) and analytical approximation (IOS) vs. simulation (right) in LVI clusters (A) 7 and (B) 8.

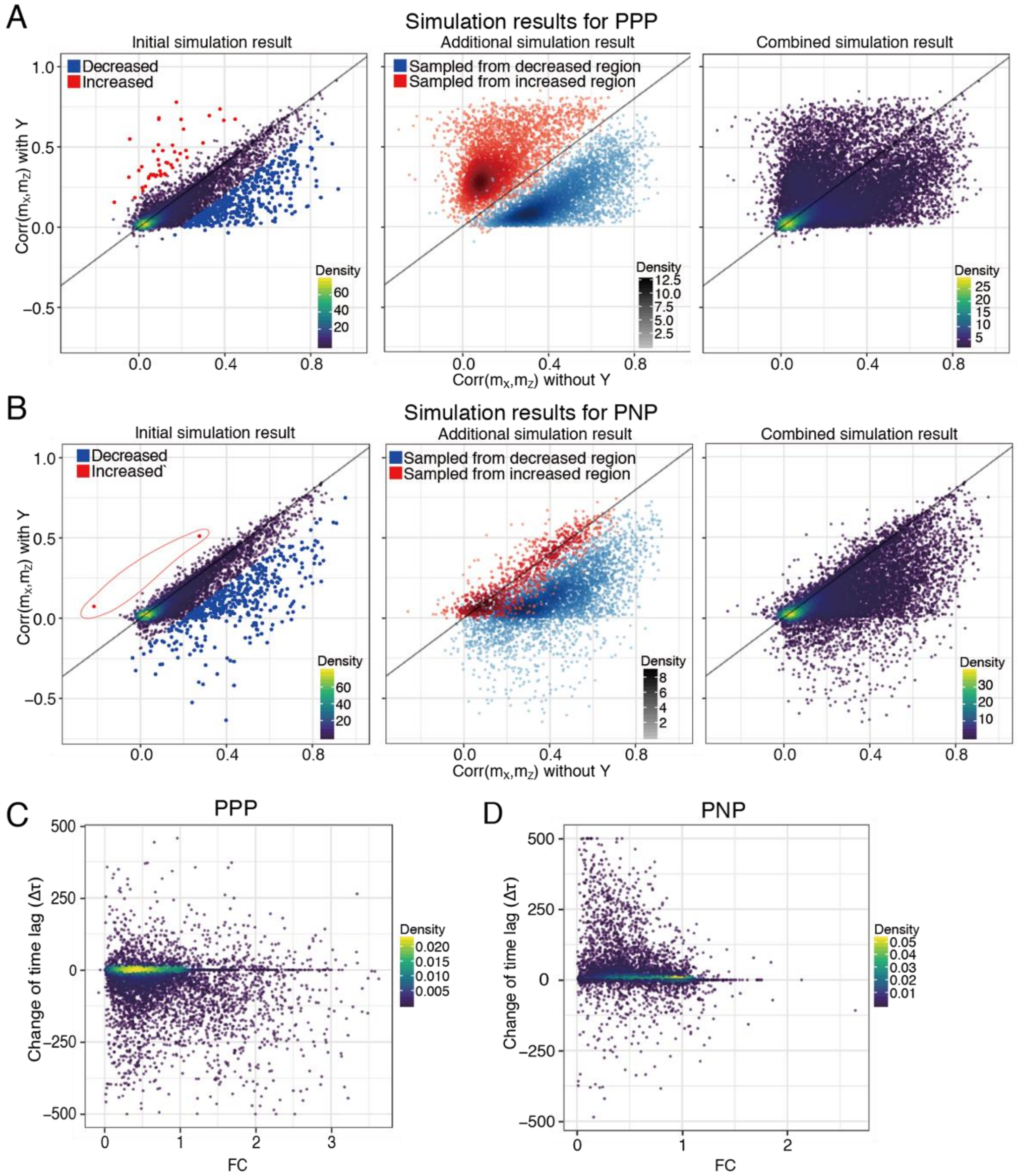

Figure A.7 Simulation results for three-gene feedforward networks. **(A)-(B)** Simulation results for (A) PPP and (B) PNP circuit types. (Left) Scatter plot showing the simulation results with (y axis) and without (x axis) the feedforward component (mediated by Y) for different parameter combinations (using the initial samples). Those with a difference in $Corr(m_X, m_Y)$ of greater than 0.2 are labeled with red (increased with Y) or blue (decreased with Y). (Center) Simulation results for the additional parameter combinations. The red (blue) dots correspond to parameter combinations sampled around those that resulted in the red (blue) dots in the left panel. (Right) The same but showing both the initial and additional parameter combinations. **(C)-(D)** Differences in the lag time (y) for achieving peak cross-correlations between the circuits with and without Y for (C) PPP and (D) PNP. PPP tends to lengthen time lags ($\Delta\tau < 0$) while PNP tends to shorten time lags ($\Delta\tau > 0$). For PNP, only parameter combinations with positive $Corr(m_X, m_Z)$ with Y were included for proper comparison between PPP and PNP.

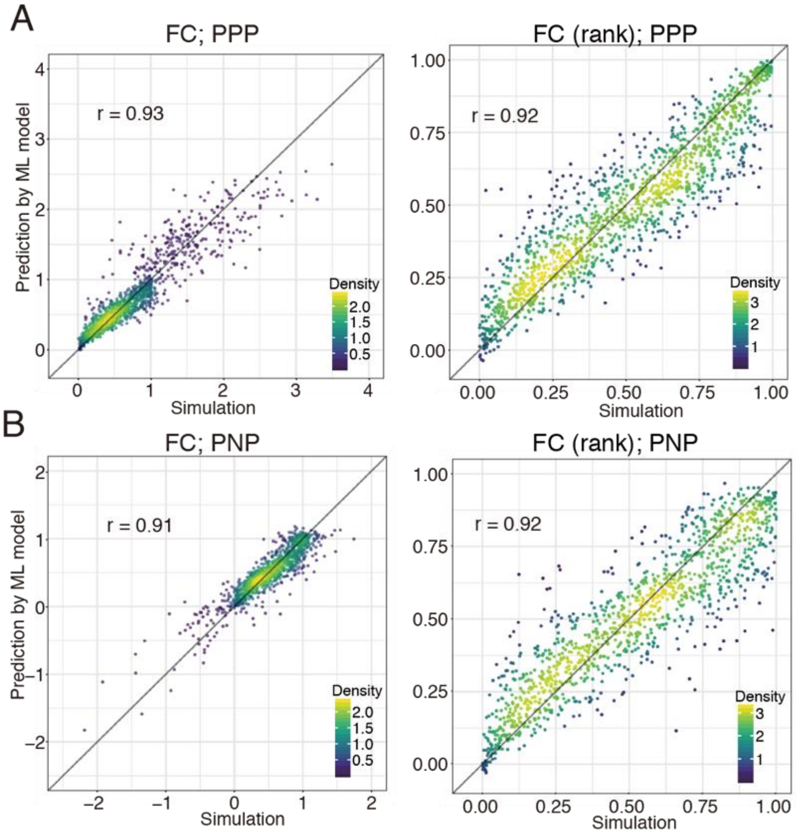

Figure A.8 ML model performance for three-gene feedforward networks. **(A)-(B)** The prediction performance of the RF regression model for FC (left) and FC (rank) (right) trained using the combined training sets for (A) PPP (FC: $r = 0.93$, FC (rank): $r = 0.92$) and (B) PNP (FC: $r = 0.91$, FC (rank): $r = 0.92$).

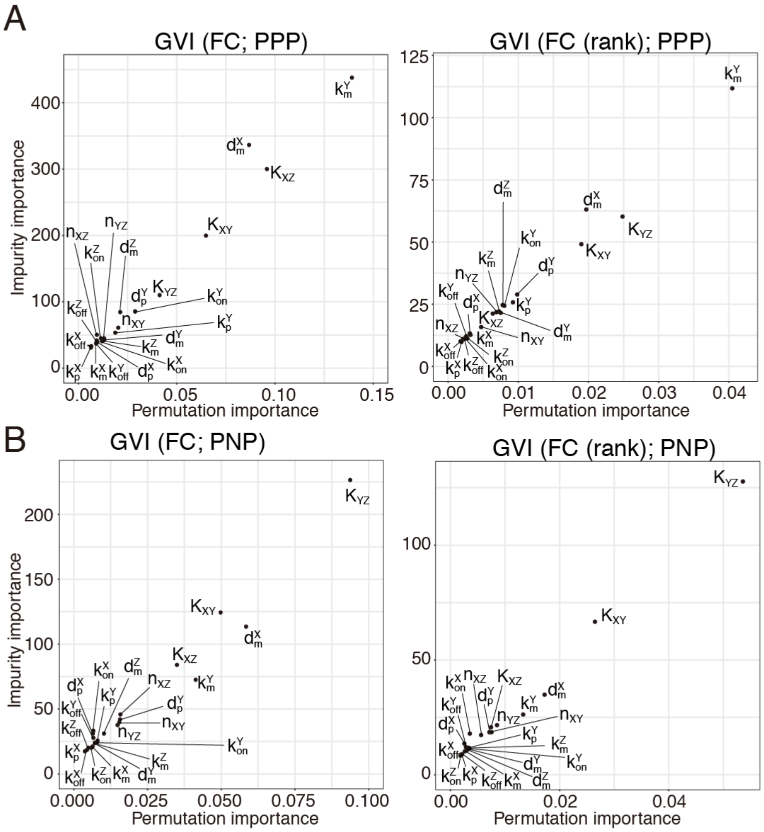

Figure A.9 Impurity and permutation GVI of FC and FC (rank) in three-gene networks. **(A)-(B)** Impurity and permutation GVIs are shown together for (A) PPP and (B) PNP. Left panels are for FC, and right panels are for FC (rank). Ranks for highly important parameters are largely consistent between the impurity and permutation importance measures.

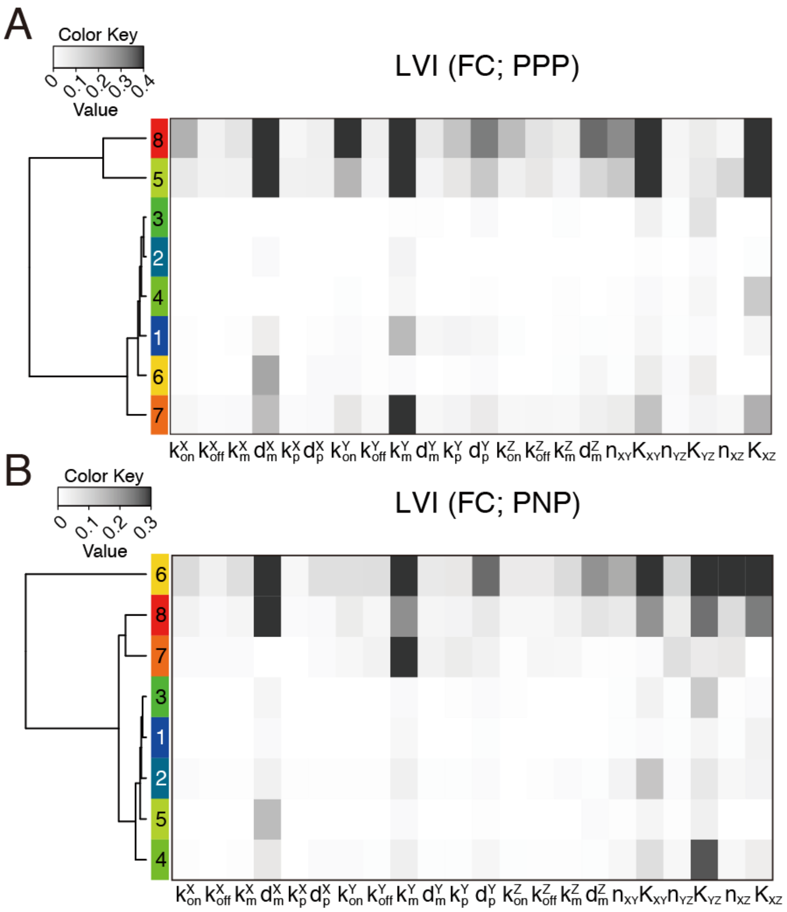

Figure A.10 Local variable importance generated by ML models for FC. **(A)-(B)** The LVI (from the ML model for FC) of the parameter combinations were clustered and the average values of each cluster is shown for (A) PPP and (B) PNP. The cluster number is shown in the color bar (section A.8).

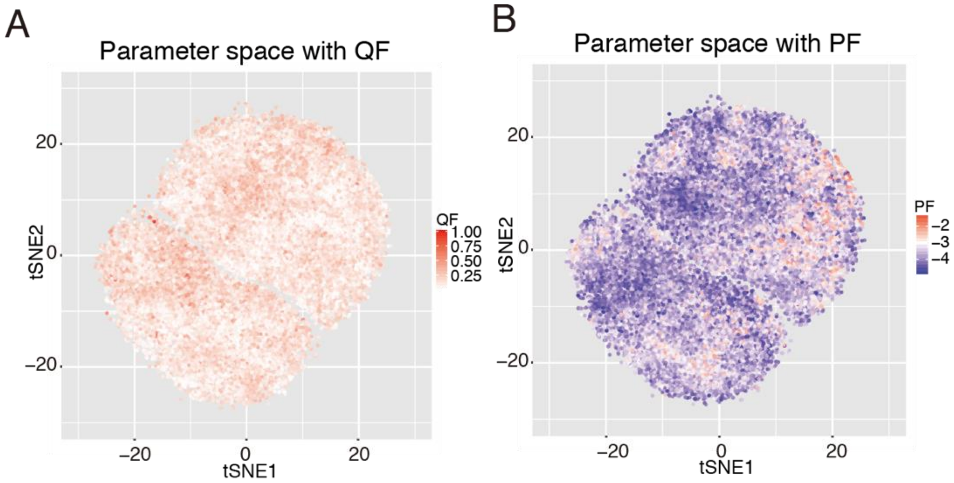

Figure A.11 Distribution of phenotypes in the parameter space. **(A)** tSNE plot of the initial parameter combinations colored by QF. **(B)** tSNE plot of the initial parameter combinations colored by PF. See A.14 for additional details on the logged unit of PF.

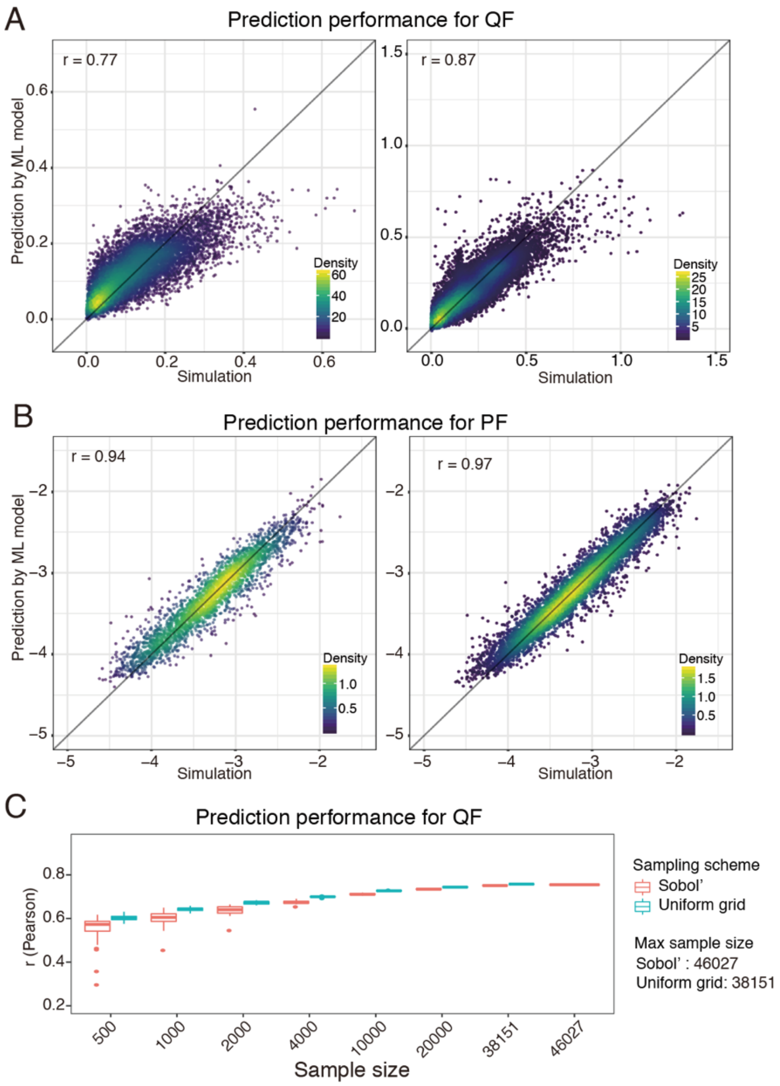

Figure A.12 Prediction performance of ML models for oscillation phenotypes. **(A)** Scatter plot of predicted vs. simulated QF to illustrate the prediction performance of the RF regression model for QF for initial (left) and combined (right) data sets. The color scale denotes the distribution density reflecting the relative abundance of data points. **(B)** Scatter plot of predicted vs. simulated PF to illustrate the prediction performance of the RF regression model for PF for initial (left) and combined (right) data sets. **(C)** Comparison of prediction performance on a test data set for different training sample sizes between uniform grid and Sobol’ sampling schemes. The test data set was prepared by pooling 4500 parameter combinations from both uniform grid and Sobol’ schemes and not used for ML model training.

A.16 Parameter ranges and grids defined for parameter sampling sampling

Grids	k_{on}^{X}	k_{off}^{X}	k_{m}^{X}	d_{m}^{X}	k_{p}^{X}	d_{p}^{X}	k_{on}^{Y}	k_{off}^{Y}	k_{m}^{Y}	d_{m}^{Y}	k_{p}^{Y}	d_{p}^{Y}	n_{XY}	K_{XY}
Grid 1	0.04	0.01	0.1	0.004	0.1	0.0005	0.04	0.01	0.1	0.004	0.001	0.0001	1	133.3333
Grid 2	0.08	0.0644	0.278	0.0101	0.278	0.00142	0.08	0.0644	0.32	0.0101	0.001	0.0001		
Grid 3	0.12	0.119	0.774	0.0253	0.774	0.00403	0.12	0.119	1.02	0.0253	0.001	0.0001		
Grid 4	0.16	0.173	2.15	0.0635	2.15	0.0114	0.16	0.173	3.27	0.0635	0.001	0.0001		
Grid 5	0.2	0.228	5.99	0.16	5.99	0.0325	0.2	0.228	10.5	0.16	0.001	0.0001		
Grid 6	0.24	0.282	16.7	0.401	16.7	0.0923	0.24	0.282	33.5	0.401	0.001	0.0001		
Grid 7	0.28	0.337	46.4	1.01	46.4	0.262	0.28	0.337	107	1.01	0.001	0.0001		
Grid 8	0.32	0.391	129	2.53	129	0.744	0.32	0.391	342	2.53	0.001	0.0001		
Grid 9	0.36	0.446	359	6.37	359	2.11	0.36	0.446	1090	6.37	0.001	0.0001		
Grid 10	0.4	0.5	1000	16	1000	6	0.4	0.5	3500	16	0.001	0.0001		

Table A.2 Parameter grid for the two-gene network. (Related to Figure 3.3; uniform grid sampling). The feasible range of individual parameters were divided into 10 equally sized bins (except n_{XY} and K_{XY}). Uniform grid sampling was used to sample parameter combinations (section A.3). The unit of K_{XY} is the copy number (Table A.1; section A.2.2). Since the gene X is considered to encode for a transcription factor regulating gene Y, k_m^X and k_p^X were restricted to not exceed 1000 (Table A.1; section A.2.2).

Range	k_{on}^{X}	k_{off}^{X}	k_{m}^{X}	d_{m}^{X}	k_{p}^{X}	d_{p}^{X}	k_{on}^{Y}	k_{off}^{Y}	k_{m}^{Y}	d_{m}^{Y}	k_{p}^{Y}	d_{p}^{Y}	k_{on}^{Z}	k_{off}^{Z}	k_{m}^{Z}	d_{m}^{Z}	k_{p}^{Z}	d_{p}^{Z}	n_{XY}	K_{XY}	n_{YZ}	K_{YZ}	n_{XZ}	K_{XZ}
Min	0.04	0.01	0.1	0.004	0.1	0.0005	0.04	0.01	0.1	0.004	0.1	0.0005	0.04	0.01	0.1	0.004	0.1	0.0005	1	0.2	1	0.2	1	0.2
Max	0.4	0.5	1000	16	1000	6	0.4	0.5	1000	16	1000	6	0.4	0.5	1000	16	1000	6	5	5	5	5	5	5

Table A.3 Parameter range for the three-gene feedforward network. (Related to Figure 3.13; Sobol sampling). Sobol sampling was used to sample the parameter combinations (section A.3). The unit of the Ks (K_{XY}, K_{YX}, and K_{XZ}) is the relative ratio to the mean protein copy number (Table A.1; section A.2.2). Since all genes encode transcription factors, k_m and k_p of all genes were restricted to not exceed 1000 (Table A.1; section A.2.2).

Grids	k_{on}^{X}	k_{off}^{X}	k_{m}^{X}	d_{m}^{X}	k_{p}^{X}	d_{p}^{X}	k_{on}^{Y}	k_{off}^{Y}	k_{m}^{Y}	d_{m}^{Y}	k_{p}^{Y}	d_{p}^{Y}	n_{XY}	K_{XY}	n_{YX}	K_{YX}
Grid 1	0.04	0.01	0.1	0.004	0.1	0.0005	0.04	0.01	0.1	0.004	0.1	0.0005	1	30	1	30
Grid 2	0.08	0.0644	0.278	0.0101	0.278	0.00142	0.08	0.0644	0.32	0.0101	0.278	0.00142	5	100	5	100
Grid 3	0.12	0.119	0.774	0.0253	0.774	0.00403	0.12	0.119	1.02	0.0253	0.774	0.00403		300		300
Grid 4	0.16	0.173	2.15	0.0635	2.15	0.0114	0.16	0.173	3.27	0.0635	2.15	0.0114		1000		1000
Grid 5	0.2	0.228	5.99	0.16	5.99	0.0325	0.2	0.228	10.5	0.16	5.99	0.0325		3000		3000
Grid 6	0.24	0.282	16.7	0.401	16.7	0.0923	0.24	0.282	33.5	0.401	16.7	0.0923				
Grid 7	0.28	0.337	46.4	1.01	46.4	0.262	0.28	0.337	107	1.01	46.4	0.262				
Grid 8	0.32	0.391	129	2.53	129	0.744	0.32	0.391	342	2.53	129	0.744				
Grid 9	0.36	0.446	359	6.37	359	2.11	0.36	0.446	1090	6.37	359	2.11				
Grid 10	0.4	0.5	1000	16	1000	6	0.4	0.5	3500	16	1000	6				

Table A.4 Parameter grid for the two-gene negative feedback network. (Related to Figure 3.18; uniform grid sampling). The feasible range of parameters were divided into grids with varying numbers of bins. Uniform grid sampling was used to sample parameter combinations (section A.3). The unit of K_{XY} and K_{YX} is the copy number (Table A.1; section A.2.2). Since both genes X and Y encode transcription factors, k_{m}^{X}, k_{p}^{X}, and k_{p}^{Y} were restricted to not exceed 1000 (Table A.1; section A.2.2).

Appendix B: Supporting information for Chapter 4

B.1 <u>Description of a multiscale T cell activation model</u>

We describe the detailed model of the T cell activation occurring through the interactions between three cell types: conventional CD4+ T cells (Tconvs), regulatory T cells (Tregs), and dendritic cells (DCs) (Figure 4.1). The variables and parameters of the model can be found in Table 4.1 and B.1. This model was implemented and simulated with the MATLAB, and the MATLAB codes are available on Github (https://github.com/pkm304/multiscale_t_cell_activation).

B.1.1 TCR signaling (DC:TC1)

This component consists of kinetic proofreading of antigen recognition and the effective signaling strength that regulates downstream pathways, including the production of IL-2 and IL-2Rα (François et al., 2013; Voisinne et al., 2015). To make the model description self-contained, we layout the detailed derivation from (François et al., 2013).

B.1.1.1 Kinetic proofreading

B.1.1.1.1 Reactions

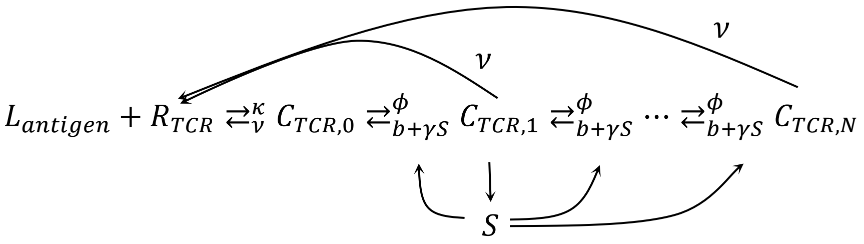

$$L_{antigen} + R_{TCR} \underset{\nu}{\overset{\kappa}{\rightleftarrows}} C_{TCR,0} \underset{b+\gamma S}{\overset{\phi}{\rightleftarrows}} C_{TCR,1} \underset{b+\gamma S}{\overset{\phi}{\rightleftarrows}} \cdots \underset{b+\gamma S}{\overset{\phi}{\rightleftarrows}} C_{TCR,N} \qquad (B.1)$$

B.1.1.1.2 Equations

Corresponding equations are as bellow:

$$\frac{dS_{SHP1}}{dt} = \alpha C_{TCR,1}\left(S_{SHP1,T} - S_{SHP1}\right) - \beta S_{SHP1}, \tag{B.2}$$

$$\begin{aligned}\frac{dC_{TCR,0}}{dt} = \kappa\left(L_{antigen} - \sum_{i=0}^{N} C_{TCR,i}\right)\left(R_{TCR} - \sum_{i=0}^{N} C_{TCR,i}\right)\\ +(b+\gamma S_{SHP1})C_{TCR,1} - (\phi+\nu)C_{TCR,0},\end{aligned} \tag{B.3}$$

$$\begin{aligned}\frac{dC_{TCR,j}}{dt} = \phi C_{TCR,j-1} + (b+\gamma S_{SHP1})C_{TCR,j+1}\\ -(\phi+b+\gamma S_{SHP1}+\nu)C_{TCR,j},\end{aligned} \tag{B.4}$$

$$\frac{dC_{TCR,N}}{dt} = \phi C_{TCR,N-1} - (b+\gamma S_{SHP1}+\nu)C_{TCR,N}, \tag{B.5}$$

where j runs from 1 to N-1.

At steady states, the summation of equations for $C_{TCR,j}$ above leads to:

$$\kappa\left(L_{antigen} - \sum_{i=0}^{N} C_{TCR,i}\right)\left(R_{TCR} - \sum_{i=0}^{N} C_{TCR,i}\right) = \nu \sum_{i=0}^{N} C_{TCR,i}\,. \tag{B.6}$$

Assuming $\sum_{i=0}^{N} C_{TCR,i} \ll R_{TCR}$, we obtain

$$\kappa L_{antigen} R_{TCR} = (\kappa R + \nu)\nu \sum_{i=0}^{N} C_{TCR,i}\,, \tag{B.7}$$

$$\nu \sum_{i=0}^{N} C_{TCR,i} = L_{antigen}\frac{\kappa R_{TCR}}{\nu + \kappa R}. \tag{B.8}$$

Other equations become

$$S_{SHP1} = S_{SHP1,T}\frac{C_{TCR,1}}{C_{TCR,1} + C_{TCR,*}}, \text{where } C_{TCR,*} = \frac{\beta}{\alpha}, \tag{B.9}$$

$$0 = L_{antigen}\frac{\kappa R_{TCR}}{\nu + \kappa R} + (b + S_{SHP1})C_{TCR,1} - (\phi + \nu)C_{TCR,0}, \tag{B.10}$$

$$0 = \phi C_{j-1} + (b + S_{SHP1})C_{TCR,j+1} - (\phi + b + S_{SHP1} + \nu)C_{TCR,j}, \tag{B.11}$$

$$0 = \phi C_{TCR,N-1} - (b + S_{SHP1} + \nu)C_{TCR,N}. \tag{B.12}$$

To solve for $C_j{}'s$, we first obtain solutions of

$$0 = \phi + (b + S_{SHP-1})r^2 - (\phi + b + S_{SHP1} + \nu)r = f(r) \tag{B.13}$$

as

$$r_{\pm} = \frac{\phi + b + S_{SHP1} + \nu \pm \sqrt{(\phi + b + S_{SHP1} + \nu)^2 - 4\phi(b + S_{SHP1})}}{2(b + S_{SHP1})}. \tag{B.14}$$

Finally, $C_{TCR,j}$ can be expressed as

$$C_{TCR,j} = a_+ r_+^j + a_- r_-^j. \tag{B.15}$$

Since $f(1) = -\nu < 0 < \phi = f(0)$, it is always the case that $r_+ > 1 > r_- > 0$. To obtain a_+ and a_-, we manipulate the following two equations,

$$\begin{aligned} 0 &= L_{antigen}\frac{\kappa R_{TCR}\nu}{\nu + \kappa R_{TCR}} + a_+\big((b + S_{SHP1})r_+ - \phi - \nu\big) \\ &\quad + a_-\big((b + S_{SHP1})r_- - \phi - \nu\big) \\ &= L_{antigen}\frac{\kappa R_{TCR}\nu}{\nu + \kappa R_{TCR}} + \frac{a_+\nu}{r_+ - 1} + \frac{a_-\nu}{r_- - 1} \end{aligned} \tag{B.16}$$

$$\sum_{i=0}^{N} C_{TCR,i} = \frac{\kappa R_{TCR} L_{antigen}}{\nu + \kappa R_{TCR}} = \frac{a_+(r_+^{N+1} - 1)}{r_+ - 1} + \frac{a_-(r_-^{N+1} - 1)}{r_- - 1} \tag{B.17}$$

Finally, we obtain

$$a_+ = -a_-\left(\frac{r_-}{r_+}\right)^{N+1}\frac{r_+ - 1}{r_- - 1}, \tag{B.18}$$

$$a_- = (1 - r_-)\frac{\kappa R_{TCR} L_{antigen}}{\nu + \kappa R_{TCR}}\left(1 - \left(\frac{r_-}{r_+}\right)^{N+1}\right)^{-1}, \tag{B.19}$$

$$a_+ = (r_+ - 1)\frac{\kappa R_{TCR} L_{antigen}}{\nu + \kappa R_{TCR}}\left(\frac{r_-}{r_+}\right)^{N+1}\left(1 - \left(\frac{r_-}{r_+}\right)^{N+1}\right)^{-1}. \tag{B.20}$$

Other variables at steady states can be obtained as,

$$\begin{aligned} C_{TCR,N} &= a_+ r_+^N + a_- r_-^N = a_- r_-^N\left(1 - \frac{r_-(r_+ - 1)}{r_+(r_- - 1)}\right) \\ &= \frac{\kappa R_{TCR} L_{antigen}}{\nu + \kappa R_{TCR}}\left(1 - \left(\frac{r_-}{r_+}\right)\right) r^N \left(1 - \left(\frac{r_-}{r_+}\right)^{N+1}\right)^{-1}, \end{aligned} \tag{B.21}$$

$$C_{TCR,1} = a_+ r_+ + a_- r_- = a_- \left(r_- - \left(\frac{r_-}{r_+}\right)^{N+1} \frac{r_+ - 1}{r_- - 1} \right)$$

$$= \frac{\kappa R_{TCR} L_{antigen}}{\nu + \kappa R_{TCR}} r_-(1 - r_-) \left(1 + \frac{(r_-/r_+)^{N+1}(r_+ - 1)}{r_- - r_-^2} \right) \left(1 - \left(\frac{r_-}{r_+}\right)^{N+1} \right)^{-1}. \quad (\mathrm{B.22})$$

For large N, $(r_-/r_+)^{N+1} = \epsilon \to 0$. Thus,

$$a_- = (1 - r_-) \frac{\kappa R_{TCR} L_{antigen}}{\nu + \kappa R_{TCR}} + O(\epsilon), \quad (\mathrm{B.23})$$

$$C_{TCR,0} \approx a_- + O(\epsilon), \quad (\mathrm{B.24})$$

$$C_{TCR,1} \approx a_- r_- + O(\epsilon) = \frac{\kappa R_{TCR} L_{antigen}}{\nu + \kappa R_{TCR}} r_-(1 - r_-) + O(\epsilon), \quad (\mathrm{B.25})$$

$$C_{TCR,N} \approx \frac{\kappa R_{TCR} L_{antigen}}{\nu + \kappa R_{TCR}} \left(1 - \left(\frac{r_-}{r_+}\right) \right) r_-^N + O(\epsilon). \quad (\mathrm{B.26})$$

Once S_{SHP1} is determined using $S_{SHP1} = S_{SHP1,T} \frac{C_{TCR,1}}{C_{TCR,1} + C_{TCR,1}^*}$, other variables follow from it.

B.1.2 Costimulatory signaling and inhibition by CTLA4 (DC:TC2 and TR:DC1)

This component describes binding kinetics of CD80/86, CD28, and CTLA4 and the trans-endocytosis of CD80/86 by CTLA4 (Collins et al., 2002; Jansson et al., 2005; Khailaie et al., 2018; Larsen et al., 2005; van der Merwe et al., 1997; Qureshi et al., 2011; Sugár et al., 2017)

B.1.2.1 CD28-CD80/86 binding kinetics

B.1.2.1.1 Reactions for both Tconvs and Tregs

$$L_{CD80|CD86} + R_{CD28} \underset{k_{costim}^{off}}{\overset{k_{costim}^{on}}{\rightleftarrows}} C_{costim}, \quad (\mathrm{B.27})$$

$$L_{CD80|CD86} + R_{CTLA4} \underset{k_{CTLA4}^{off}}{\overset{k_{CTLA4}^{on}}{\rightleftarrows}} C_{CTLA4}, \quad (\mathrm{B.28})$$

$$C_{CTLA4} \xrightarrow{k_{CTLA4}^{endo}} \emptyset. \tag{B.29}$$

We assumed the expression level of CD28 in the plasma membrane of Tconvs remains fixed. The cycling of CTLA4 is maintained at steady states for Tregs. Also, once the complexes of CTLA4 and CD80/86 are internalized, the complexes are instantly degraded.

B.1.2.1.2 Equations

B.1.2.1.2.1 Tconvs

We assume that the Tconv:DC engagement ceases before the considerable accumulation of CTLA4 by the Tconv. Thus, $R_{CTLA4} = 0$ for the whole time.

$$\frac{dC_{costim}}{dt} = k_{costim}^{on}\left(\frac{L_{CD80|CD86}}{S_{DC}} - C_{costim}\right)\left(\frac{R_{CD28}}{S_T} - C_{costim}\right) - k_{costim}^{off} \cdot C_{costim}. \tag{B.30}$$

At steady states,

$$C_{costim} = \frac{1}{2}\left(R_{CD28}/S_T + L_{CD80|CD86}/S_{DC} + k_{costim}^{off}/k_{costim}^{on} - \sqrt{\left(R_{CD28}/S_T + L_{CD80|CD86}/S_{DC} + k_{costim}^{off}/k_{costim}^{on}\right)^2 - 4R_{CD28}/S_T \cdot L_{CD80|CD86}/S_{DC}}\right). \tag{B.31}$$

C_{costim} was assumed to be the determinant of immune synapse formation. If either C_{costim} falls below a threshold (set to 5 in the simulation) or the simulation time passes 48 hours (whichever happens first), the Tconv stops engaging with the DC and receiving signals of TCR and costimulation.

B.1.2.1.2.2 Tregs

We assumed that Tregs maintain a constant CTLA4 level in their cell membranes. This assumption slightly underestimates the actual value during active negative feedback regulation, given our data that IL-2 signaling increases CTLA4 expression by Tregs.

$$\frac{dC_{costim}}{dt} = k_{costim}^{on}\left(\frac{L_{CD80|CD86}}{S_{DC}} - C_{costim} - C_{CTLA4}\right)\left(\frac{R_{CD28}}{S_T} - C_{costim}\right) - k_{costim}^{off}C_{costim}, \tag{B.32}$$

$$\frac{dC_{CTLA4}}{dt} = k_{CTLA4}^{on}\left(\frac{L_{CD80|CD86}}{S_{DC}} - C_{costim} - C_{CTLA4}\right)\left(\frac{R_{CTLA4}}{S_T} - C_{CTLA4}\right) - k_{CTLA4}^{off}C_{CTLA4} - k_{CTLA4}^{endo}C_{CTLA4}. \tag{B.33}$$

At steady states, given k_{costim}^{on}, k_{costim}^{off}, k_{CTLA4}^{on}, and $k_{CTLA4}^{off} \gg k_{CTLA4}^{endo}$,

$$k_{costim}^{on}\left(\frac{L_{CD80|CD86}}{S_{DC}} - C_{costim} - C_{CTLA4}\right)\left(\frac{R_{CD28}}{S_T} - C_{costim}\right) - k_{costim}^{off}C_{costim} = 0, \tag{B.34}$$

$$k_{CTLA4}^{on}\left(\frac{L_{CD80|CD86}}{S_{DC}} - C_{costim} - C_{CTLA4}\right)\left(\frac{R_{CTLA4}}{S_T} - C_{CTLA4}\right) - k_{CTLA4}^{off}C_{CTLA4} = 0, \tag{B.35}$$

which can be solved numerically for C_{costim} and C_{CTLA4}.

B.1.2.2 Detailed description of trans-endocytosis of CD80/86 by Tregs

We further implemented the regulation of the trans-endocytosis efficiency by costimulation with the assumption that costimulation strength upregulates the trans-endocytosis efficiency. This assumption was based on the fact that CD28 signaling increases the adhesion of T cells to DCs and, therefore, is likely to increase the efficiency of CTLA-4-mediated trans-endocytosis (Thauland et al., 2014).

$$\begin{aligned}\frac{dL_{CD80|CD86}}{dt} &= -k_{CTLA4,eff}^{endo} \cdot C_{CTLA4,tot} \\ &= -k_{CTLA4}^{endo}\left(f_{cont\_low} + \left(f_{cont\_high} - f_{cont\_low}\right) \cdot \left(1 + \frac{K_{CD28,tr\rightarrow Umin}}{C_{costim,tr}}\right)^{-1}\right) \\ &\quad \times V_{neighbor} \cdot n_{tr} \cdot S_{DC:TR} \cdot C_{CTLA4},\end{aligned} \tag{B.36}$$

where $k_{CTLA4,eff}^{endo}$ is the effective rate of endocytosis of CTLA4 and $C_{CTLA4,tot}$ is the total number of the CD80|CD86:CTLA4 complexes in the immune synapses formed by Tregs and a DC.

B.1.3 Competition for IL-2 between a Tconv and Tregs (TC:I1, TC:I2, and TR:I1)

In this component, we describe the dynamics of IL2Ra production, IL-2 production, secretion, and diffusion, and IL-2-IL-2R binding and endocytosis.

B.1.3.1 IL2 receptor production and IL-2-IL2 receptor binding dynamics

We follow the descriptions by: (Busse et al., 2010; Feinerman et al., 2010; Tkach et al., 2014; Voisinne et al., 2015)

B.1.3.1.1 Reactions

$$\emptyset \xrightarrow{transcription} mR_{IL2R\alpha}, \tag{B.37}$$

$$mR_{IL2R\alpha} \xrightarrow{k_{mIL2R\alpha}^{deg}} \emptyset, \tag{B.38}$$

$$mR_{IL2R\alpha} \xrightarrow{translation} mR_{IL2R\alpha} + R_{IL2R\alpha}, \tag{B.39}$$

$$R_{IL2R\alpha} \xrightarrow{k_{IL2R\alpha}^{deg}} \emptyset, \tag{B.40}$$

$$R_{IL2R\alpha} + R_{IL2R\beta\gamma} \underset{k_{IL2\alpha;\beta\gamma}^{off}}{\overset{k_{IL2\alpha;\beta\gamma}^{on}}{\rightleftarrows}} R_{IL2R}, \tag{B.41}$$

$$R_{IL2R} + I_{IL2} \underset{k_{IL2R}^{off}}{\overset{k_{IL2R}^{on}}{\rightleftarrows}} C_{IL2R}, \tag{B.42}$$

$$C_{IL2R} \xrightarrow{k_{C_{IL2R}}^{endo}} \emptyset. \tag{B.43}$$

B.1.3.1.2 Equations

$$\begin{aligned}\frac{dmR_{IL2R\alpha}}{dt} = {} & k_{mIL2R\alpha}^{transcription(basal)} + k_{mIL2R\alpha}^{transcription(TCR,costim)} P_{TCR,costim\to IL2R\alpha}^{on} \\ & + k_{mIL2R\alpha}^{transcription(pSTAT5)} P_{JAK\to pSTAT5}^{on} - k_{mIL2\alpha}^{deg} mR_{IL2R\alpha},\end{aligned} \tag{B.44}$$

where

$$P^{on}_{TCR,costim\to IL2R\alpha} = \left(1 + \left(\begin{matrix}\left(\dfrac{C_N}{K_{TCR\to IL2R\alpha}}\right)^{n_{TCR\to IL2R\alpha}} \\ + \left(\dfrac{C_{costim}}{K_{costim\to IL2R\alpha}}\right)^{n_{costim\to IL2R\alpha}}\end{matrix}\right)^{-1}\right)^{-1}, \quad (B.45)$$

$$P^{on}_{JAK\to pSTAT5} = \frac{1}{1 + \left(\dfrac{K_{JAK\to pSTAT5}}{S_{JAK}}\right)^{n_{JAK\to pSTAT5}}}\left(1 - P^{on}_{TCR\to IL2R\alpha}\right), \quad (B.46)$$

$$S_{JAK} = \frac{R_{IL2\alpha}}{R_{IL2\alpha} + R_{IL2\alpha,0}} \cdot \frac{I_{IL2}}{I_{IL2} + K_{IL2\to JAK}(R_{IL2\alpha})}, \quad (B.47)$$

$$K_{IL2\to JAK}(R_{IL2\alpha}) = K^{high}_{IL2\to JAK}\frac{R_{IL2\alpha}}{R_{IL2\alpha} + R_{IL2\alpha,0}} + K^{low}_{IL2\to JAK}\frac{R_{IL2\alpha,0}}{R_{IL2\alpha} + R_{IL2\alpha,0}}. \quad (B.48)$$

The rest of the differential equations are

$$\frac{dR_{IL2R\alpha}}{dt} = k^{translation}_{IL2R\alpha}\, mR_{IL2R\alpha} - k^{deg}_{IL2R\alpha} R_{IL2R\alpha}, \quad (B.49)$$

$$\frac{dR_{IL2R}}{dt} = k^{on}_{IL2\alpha;\beta\gamma}(R_{IL2R\alpha} - R_{IL2R})(R_{IL2R\beta\gamma} - R_{IL2R}) - k^{off}_{IL2\alpha;\beta\gamma} R_{IL2R}, \quad (B.50)$$

$$\frac{dC_{IL2R}}{dt} = k^{on}_{IL2R}(R_{IL2R} - C_{IL2R})I - k^{off}_{IL2R} C_{IL2R} - k^{endo}_{C_{IL2R}} C_{IL2R}. \quad (B.51)$$

Thus, at steady states,

$$R_{IL2R} = \frac{1}{2}\Big(\big(R_{IL2R\alpha} + R_{IL2R\beta\gamma} + K_{IL2R\alpha:\beta\gamma,d}\big) - \sqrt{\big(R_{IL2R\alpha} + R_{IL2R\beta\gamma} + K_{IL2R\alpha:\beta\gamma,d}\big)^2 - 4R_{IL2R\alpha}R_{IL2R\beta\gamma}}\Big), \quad (B.52)$$

$$C_{IL2R} = \frac{I_{IL2}R_{IL2R}}{K_{C_{IL2R}} + I_{IL2}}, \quad (B.53)$$

$$\text{where } K_{C_{IL2R}} = \frac{k^{off}_{IL2R}}{k^{on}_{IL2R}} \approx 10pM. \quad (B.54)$$

B.1.3.2 IL2 production dynamics

We follow the descriptions by: (Tkach et al., 2014; Voisinne et al., 2015)

B.1.3.2.1 Reactions

$$\emptyset \xrightarrow{transcription} I_{mIL2}, \tag{B.55}$$

$$I_{mIL2} \xrightarrow{translation+secretion} I_{mIL2} + I_{IL2}. \tag{B.56}$$

B.1.3.2.2 Equations

$$\frac{dI_{mIL2}}{dt} = k_{mIL2}^{transcription(TCR,costim)} P_{TCR,costim\to IL2}^{on} - k_{mIL2}^{deg} I_{mIL2}, \tag{B.57}$$

where

$$P_{TCR,costim\to IL2}^{on} = \frac{1}{1+\left(\frac{K_{TCR\to IL2}}{C_N}\right)^{n_{TCR\to IL2}}} \times \frac{1}{1+\left(\frac{K_{costim\to IL2}}{C_{costim}}\right)^{n_{costim\to IL2}}} \cdot \left(1 - P_{pSTAT5\to IL2}^{on}\right) \tag{B.58}$$

for CD4 T cells (Lim et al., 2015).

The secretion rate of IL2 is

$$q_{IL2} = k_{IL2}^{translation} I_{mIL2}. \tag{B.59}$$

B.1.3.3 IL-2 secretion, diffusion, and consumption dynamics

We integrated models from (Busse et al., 2010; Oyler-Yaniv et al., 2017; Shvartsman et al., 2001; Thurley et al., 2015) into a partial differential equation (PDE). Ordinary differential equations (ODEs) in the previous subsections are linked to the model component introduced here.

B.1.3.3.1 Reactions

$$\emptyset \xrightarrow{q_{IL2}} I_{IL2}, \tag{B.60}$$

$$I_{IL2} \xrightarrow{k_{IL2,extr}^{deg}} \emptyset, \tag{B.61}$$

$$I_{IL2} + R_{IL2R,tc} \underset{k_{IL2R}^{off}}{\overset{k_{IL2R}^{on}}{\rightleftarrows}} C_{IL2R,tc}, \tag{B.62}$$

$$I_{IL2} + R_{IL2R,tr} \rightleftarrows_{k_{IL2R}^{off}}^{k_{IL2R}^{on}} C_{IL2R,tr}. \tag{B.63}$$

B.1.3.3.2 Equations

The concentration of IL-2 is modeled through a reaction-diffusion equation.

$$\frac{\partial I_{IL2}}{\partial t} = D_{IL2} \cdot \nabla^2 I_{IL2} - n_{tr} \cdot j_{IL2,tr}^{consum} - k_{IL2,extr}^{deg} \cdot I_{IL2}, \tag{B.64}$$

where

$$j_{IL2,tr}^{consum} = k_{IL2R}^{on} \cdot I_{IL2R} \cdot R_{IL2R,tr} - k_{IL2R}^{off} \cdot C_{IL2R,tr}, \tag{B.65}$$

$$(\text{assuming steady states}) = k_{C_{IL2R}}^{endo} \cdot C_{IL2R,tr} = k_{C_{IL2R}}^{endo} \cdot \frac{I_{IL2} \cdot R_{IL2R,tr}}{K_{C_{IL2R}} + I_{IL2}}. \tag{B.66}$$

Boundary conditions are

$$-4\pi\rho^2 \cdot D_{IL2} \left.\frac{\partial I_{IL2}}{\partial r}\right|_{r=\rho} = q_{IL2} - k_{IL2R}^{on} \cdot I_{IL2R} \cdot R_{IL2R,tc} + k_{IL2R}^{off} \cdot C_{IL2R,tc} \tag{B.67}$$

and

$$I(r = \infty, t) = 0. \tag{B.68}$$

We numerically solved this equation using the MATLAB for actual simulations.

B.1.3.3.3 Steady-state solution

We layout the analytical derivation of the steady-state solution based on (Oyler-Yaniv et al., 2017). Since the time scale of relaxation of IL-2 diffusion (~60s) is much shorter than that of IL-2 receptor dynamics (~several hours), we assume the density of IL-2, I_{IL2}, reaches steady states at any given moment (time intervals of few minutes) (Oyler-Yaniv et al., 2017). Thus, we only need to solve the following steady-state equation,

$$0 = D_{IL2} \cdot \nabla^2 I_{IL2} - n_{tr} \cdot j_{IL2,tr}^{consum} - k_{IL2,extr}^{deg} \cdot I_{IL2}. \tag{B.69}$$

With additional assumptions that $I_{IL2} \ll K_{C_{IL2R}} \approx 32\, pM$ and n_{tr} is constant throughout the spatial compartment, we obtain $j_{IL2,tr}^{consum} = \frac{k_{C_{IL2R}}^{endo} \cdot R_{IL2R,tr}}{K_{C_{IL2R}}} \cdot I_{IL2} =$

$k_{IL2R}^{consum} \cdot I_{IL2}$, where $k_{IL2R}^{consum} \equiv \frac{k_{C_{IL2R}}^{endo} \cdot R_{IL2R,tr}}{K_{C_{IL2R}}}$. Finally, we obtain an analytically tractable equation,

$$0 = \nabla^2 I_{IL2} - \frac{\delta}{D_{IL2}} I_{IL2}, \tag{B.70}$$

where $\delta \equiv n_{tr} \cdot k_{IL2R}^{consum} + k_{IL2,extr}^{deg}$. With a suitable change of variables such that $\tilde{r} \equiv \frac{r}{\lambda}$, where $\lambda = \sqrt{\frac{D_{IL2}}{\delta}} = \sqrt{\frac{D_{IL2}}{n_{tr} \cdot k_{IL2R}^{consum} + k_{IL2,extr}^{deg}}}$, we obtain

$$0 = \widetilde{\nabla}^2 I_{IL2} - I_{IL2}. \tag{B.71}$$

Assuming the spherical symmetry (i.e., the perfect spherical shape of T cell and isotropic IL2 secretion), we only need to solve the radial part of the equation,

$$\left(\frac{\partial^2}{\partial \tilde{r}^2} + \frac{2}{\tilde{r}} \frac{\partial}{\partial \tilde{r}}\right) I - I = 0. \tag{B.72}$$

With $I(\tilde{r}) = \frac{J(\tilde{r})}{\tilde{r}}$, we obtain

$$\frac{\partial^2 J(\tilde{r})}{\partial \tilde{r}^2} = J(\tilde{r}). \tag{B.73}$$

The general solution of this equation is

$$J(\tilde{r}) = A e^{\tilde{r}} + B e^{-\tilde{r}}, \tag{B.74}$$

or

$$I(\tilde{r}) = \frac{A e^{\tilde{r}}}{\tilde{r}} + \frac{B e^{-\tilde{r}}}{\tilde{r}} = \frac{A' e^{\frac{r}{\lambda}}}{r} + \frac{B' e^{-\frac{r}{\lambda}}}{r}. \tag{B.75}$$

Using the boundary condition, $I(r = \infty, t) = 0$, we determine $A' = 0$. From the other boundary condition,

$$-4\pi\rho^2 \cdot D_{IL2} \left.\frac{\partial I_{IL2}}{\partial r}\right|_{r=\rho} = q_{IL2} - k_{IL2R}^{on} \cdot I_{IL2R} \cdot R_{IL2R,tc} + k_{IL2R}^{off} \cdot C_{IL2R,tc}, \tag{B.76}$$

we can determine B' in terms of other parameters. By plugging $I(\tilde{r}) = \frac{B' \cdot e^{-r/\lambda}}{r}$ into the boundary condition at $r = \rho$, we obtain

$$-4\pi\rho^2 \cdot D_{IL2}\left(-\frac{B' e^{-\frac{\rho}{\lambda}}}{\rho^2} - \frac{B' e^{-\frac{\rho}{\lambda}}}{\lambda\rho}\right)$$
$$= q_{IL2} - k_{IL2R}^{on} \cdot R_{IL2R,tc}\frac{B' \cdot e^{-\frac{\rho}{\lambda}}}{\rho} + k_{IL2R}^{off} \cdot C_{IL2R,tc}. \tag{B.77}$$

By solving this for B', we obtain

$$B' = \frac{q_{IL2} + k_{IL2R}^{off} \cdot C_{IL2R,tc}}{4\pi D_{IL2}\left(1 + \frac{\rho}{\lambda}\right) + \frac{k_{IL2R}^{on} \cdot R_{IL2R,tc}}{\rho}} \exp\frac{\rho}{\lambda}. \tag{B.78}$$

Finally, the solution $I(r)$ is

$$I(r) = \frac{q_{IL2} + k_{IL2R}^{off} \cdot C_{IL2R,tc}}{4\pi D_{IL2}\left(1 + \frac{\rho}{\lambda}\right) + \frac{k_{IL2R}^{on} \cdot R_{IL2R,tc}}{\rho}} \frac{\exp\left(-\frac{r-\rho}{\lambda}\right)}{r}. \tag{B.79}$$

The concentration of IL-2 at $r = \rho$ is

$$I(r = \rho) = \frac{q_{IL2} + k_{IL2R}^{off} \cdot C_{IL2R,tc}}{4\pi D_{IL2} \cdot \rho\left(1 + \frac{\rho}{\lambda}\right) + \frac{k_{IL2R}^{on} \cdot R_{IL2R,tc}}{\rho}}. \tag{B.80}$$

B.1.4 Spatiotemporal dynamics of Tregs and their internal states described by coupled partial differential equations

In this component, we describe the spatial dynamics of Tregs and their internal states, resulting in coupled partial differential equations along with the equations in section

B.1.4.1 Treg movement

There are three possible mechanisms of the dynamical spatiotemporal regulation of Treg density: 1) chemoattraction or chemorepulsion due to cytokines or chemokines secreted by responding Tconvs or DCs (Chavanis, 2008; Rapp et al., 2019), 2) proliferation induced by IL-2 sensing (Amado et al., 2013), and 3) decrease of the cell motility upon the engagement with DCs (Thauland et al., 2014). All of these possibilities are taken into account as:

$$\begin{aligned}\frac{\partial n_{tr}}{\partial t} &= -\nabla\cdot\left(n_{tr}\cdot\chi_0\left(1-\frac{n_{tr}}{K_{cc}}\right)\cdot\nabla a\right)\\ &+\nabla\cdot\left(n_{tr}\cdot\nabla U\cdot\left(1-\frac{n_{tr}}{K_{cc}}\right)\right)+\nabla\cdot\left(D_{tr}\cdot\nabla n_{tr}\right)\\ &+k_{IL2\to treg}^{prolif}\frac{P_{JAK\to pSTAT5,tr}^{on}}{\left(K_{IL2\to treg}^{prolif}+P_{JAK\to pSTAT5,tr}^{on}\right)}\cdot n_{tr}\cdot\left(1-\frac{n_{tr}}{K_{cc}}\right),\end{aligned} \tag{B.81}$$

where U is the attractive potential describing the decrease of the Treg motility due to the engagement with DCs and regulated by costimulation and pSTAT5 levels of Tregs (Chinen et al., 2016; Thauland et al., 2014):

$$\begin{aligned}U(r) = -U_{min}&\left(1+\left(\frac{C_{costim,tr}}{K_{CD28,tr\to Umin}}+\frac{P_{JAK\to pSTAT5,tr}^{on}}{K_{pStat5,tr\to Umin}}\right)^{-1}\right)^{-1}\\ &\times\left(1-\frac{r^{n_U}}{r_{half}+\ r^{n_U}}\right),\end{aligned} \tag{B.82}$$

$\left(1-\frac{n_{tr}}{K_{cc}}\right)$ is the carrying capacity factor estimated based on the physical volume of Tregs. a is an arbitrary cytokine or chemokine inducing chemoattraction or chemorepulsion. D_{tr} is also assumed to be a function of r:

$$D_{tr}(r) = \begin{cases} D_{tr,high}-\left(D_{tr,high}-D_{tr,low}\right) \\ \times\left(1+\left(\frac{C_{costim,tr}}{K_{CD28,tr\to Umin}}+\frac{P_{JAK\to pSTAT5,tr}^{on}}{K_{pStat5,tr\to Umin}}\right)^{-1}\right)^{-1}, r<15\ um \\ D_{tr,high},\ \ r>15\ um \end{cases}\cdot \tag{B.83}$$

The boundary condition is

$$-n_{tr}\chi_0\left(1-\frac{n_{tr}}{K_{cc}}\right)\nabla a+n_{tr}\cdot\nabla U\cdot\left(1-\frac{n_{tr}}{K_{cc}}\right)+D_{tr}\nabla n_{tr}=0, \tag{B.84}$$

at $r = \rho$ and ∞. The more natural description instead of using the attractive potential seems to be the Feller boundary condition, so-called a sticky boundary condition, which can be pursued later (Bou-Rabee and Holmes-Cerfon, 2019; Leszczyński and Bartłomiejczyk, 2015; Peters and Barenbrug, 2002).

B.1.4.2 Time evolution of internal states of Tregs

The internal states of Tregs evolve upon receiving signals from secreted IL-2 or other sources such as costimulatory ligands or pMHCII of DCs. We developed a general mathematical description of the internal dynamics of an entity described as a frequency using PDEs. In general, the number density of a molecular species R in Tregs is written as $n_R = R \cdot n_{tr}$, where R is the number of a molecular species per cell. Then, the time evolution of n_R is

$$\frac{\partial n_R}{\partial t} = \frac{\partial R}{\partial t} \cdot n_{tr} + R \cdot \frac{\partial n_{tr}}{\partial t} = \left(f_{prod} + f_{deg}\right) \cdot n_{tr} + \frac{n_R}{n_{tr}} \cdot \frac{\partial n_{tr}}{\partial t}, \tag{B.85}$$

where f_{prod} and f_{deg} are the production and degradation rates of R, respectively. The suitable form for implementing in the pdepe function of the MATLAB software (see section B.1.6 for the MATLAB implementation) is

$$\begin{aligned} \frac{n_{tr}}{n_R} \cdot \frac{\partial n_R}{\partial t} &= \frac{{n_{tr}}^2}{n_R} \cdot \left(f_{prod} + f_{deg}\right) + \frac{\partial n_{tr}}{\partial t} \\ &= \nabla \cdot \left(n_{tr}\left(1 - \frac{n_{tr}}{K_{cc}}\right)(\nabla U - \chi_0 \cdot \nabla a) + D_{tr} \cdot \nabla n_{tr}\right) \\ &\quad + \frac{{n_{tr}}^2}{n_R} \cdot \left(f_{prod} + f_{deg}\right) \\ &\quad + k_{IL2\to treg}^{prolif} \frac{P_{JAK\to pSTAT5,tr}^{on}}{\left(K_{IL2\to treg}^{prolif} + P_{JAK\to pSTAT5,tr}^{on}\right)} \cdot n_{tr} \cdot \left(1 - \frac{n_{tr}}{K_{cc}}\right), \end{aligned} \tag{B.86}$$

where

$$c \equiv \frac{n_{tr}}{n_R}, \tag{B.87}$$

$$f \equiv n_{tr}\left(1-\frac{n_{tr}}{K_{cc}}\right)(\nabla U-\chi_0\cdot\nabla a)+D_{tr}\cdot\nabla n_{tr}, \tag{B.88}$$

$$\begin{aligned} s \equiv & \frac{{n_{tr}}^2}{n_R}\cdot\left(f_{prod}+f_{deg}\right) \\ & +k_{IL2\to treg}^{prolif}\frac{P_{JAK\to pSTAT5,tr}^{on}}{\left(K_{IL2\to treg}^{prolif}+P_{JAK\to pSTAT5,tr}^{on}\right)}\cdot n_{tr}\cdot\left(1-\frac{n_{tr}}{K_{cc}}\right). \end{aligned} \tag{B.89}$$

Specifically, we implemented dynamics of $mIL2R\alpha$ (mRNA of $IL2R\alpha$) and $IL2R\alpha$ as

$$\begin{aligned} \frac{\partial n_{mIL2R\alpha,tr}}{\partial t} &= \frac{\partial mR_{IL2R\alpha,tr}}{\partial t}\cdot n_{tr}+mR_{IL2R\alpha,tr}\cdot\frac{\partial n_{tr}}{\partial t} \\ &= \begin{pmatrix} k_{mIL2R\alpha,tr}^{transcription(basal)}+k_{mIL2R\alpha}^{transcription(pSTAT5)}\cdot P_{JAK\to pSTAT5,tr}^{on} \\ -k_{mIL2\alpha}^{deg}\cdot\dfrac{n_{mIL2R\alpha,tr}}{n_{tr}} \end{pmatrix}\cdot n_{tr} \\ &\quad +\frac{n_{mIL2R\alpha,tr}}{n_{tr}}\cdot\frac{\partial n_{tr}}{\partial t}, \end{aligned} \tag{B.90}$$

$$\begin{aligned} \frac{\partial n_{IL2R\alpha,tr}}{\partial t} &= \frac{\partial R_{IL2R\alpha,tr}}{\partial t}\cdot n_{tr}+R_{IL2R\alpha,tr}\cdot\frac{\partial n_{tr}}{\partial t} \\ &= \left(k_{IL2R\alpha}^{translation}\cdot\frac{n_{mIL2R\alpha,tr}}{n_{tr}}-k_{IL2R\alpha}^{deg}\cdot\frac{n_{IL2R\alpha,tr}}{n_{tr}}\right)\cdot n_{tr}+\frac{n_{IL2R,tr}}{n_{tr}}\cdot\frac{\partial n_{tr}}{\partial t}, \end{aligned} \tag{B.91}$$

where

$$P_{JAK\to pSTAT5,tr}^{on}(r)=\frac{1}{1+\left(\dfrac{K_{JAK\to pSTAT5}}{S_{JAK,tr}(r)}\right)^{n_{JAK\to pSTAT5}}}, \tag{B.92}$$

$$S_{JAK,tr}(r)=\frac{\dfrac{n_{R_{IL2\alpha}}}{n_{tr}}}{\dfrac{n_{R_{IL2\alpha}}}{n_{tr}}+R_{IL2\alpha,0}}\cdot\frac{I_{IL2}}{I_{IL2}+K_{IL2\to JAK}\cdot\left(\dfrac{n_{R_{IL2\alpha}}}{n_{tr}}\right)}, \tag{B.93}$$

$$K_{IL2\to JAK}\left(\frac{n_{R_{IL2\alpha}}}{n_{tr}}\right)=K_{IL2\to JAK}^{high}\frac{\dfrac{n_{R_{IL2\alpha}}}{n_{tr}}}{\dfrac{n_{R_{IL2\alpha}}}{n_{tr}}+R_{IL2\alpha,0}}+K_{IL2\to JAK}^{low}\frac{R_{IL2\alpha,0}}{\dfrac{n_{R_{IL2\alpha}}}{n_{tr}}+R_{IL2\alpha,0}}. \tag{B.94}$$

B.1.5 Signal integration from TCR, costimulation, and IL-2 and translation into the proliferation capacity

In a priming Tconv, the signaling strengths, $C_{TCR,N}$, C_{costim}, and S_{JAK} are integrated for functional outcomes.

B.1.5.1 Division destiny

One of the integrated functional outcomes is the division destiny, the number of divisions the responding Tconv undergoes (Marchingo et al., 2014). Myc has been suggested as a signal integrator, of which the dynamics determine the division destiny (Heinzel et al., 2017).

B.1.5.1.1 Reactions

$$\emptyset \xrightarrow{transcription} mR_{Myc}, \tag{B.95}$$

$$mR_{Myc} \xrightarrow{k_{mMyc}^{deg}} \emptyset, \tag{B.96}$$

$$mR_{Myc} \xrightarrow{translation} mR_{Myc}+R_{Myc}, \tag{B.97}$$

$$R_{Myc} \xrightarrow{k_{Myc}^{deg}} \emptyset. \tag{B.98}$$

B.1.5.1.2 Equations

$$\frac{dmR_{Myc}}{dt} = k_{mMyc}^{transcription(basal)} + k_{mMyc}^{transcription(all)} \cdot P_{TCR,costim,JAK\rightarrow PI3K}^{on} - k_{mMyc}^{deg} \cdot mR_{Myc}, \tag{B.99}$$

$$\frac{dR_{Myc}}{dt} = k_{Myc}^{translation} mR_{Myc} - k_{Myc}^{deg} R_{Myc}, \tag{B.100}$$

where

$$P^{on}_{TCR,costim,JAK\rightarrow PI3K} = \left(1 + \left(\begin{matrix}\left(\frac{C_N}{K_{TCR\rightarrow PI3K}}\right)^{n_{TCR\rightarrow PI3K}} + \left(\frac{C_{costim}}{K_{costim\rightarrow PI3K}}\right)^{n_{costim\rightarrow PI3K}} \\ + \left(\frac{S_{JAK}}{K_{JAK\rightarrow PI3K}}\right)^{n_{costim\rightarrow PI3K}}\end{matrix}\right)^{-1}\right)^{-1}. \qquad (B.101)$$

B.1.6 Implementation of PDEs using the pdepe function in the MATLAB software

The general formula of PDEs in the pdepe function can be described as

$$c\left(x,t,u,\frac{\partial u}{\partial x}\right) \cdot \frac{\partial u}{\partial t} = x^{-m}\frac{\partial}{\partial x}\left(x^m \cdot f(x,t,u,)\right) + s\left(x,t,u,\frac{\partial u}{\partial x}\right), \qquad (B.102)$$

with the general boundary condition

$$p(x,t,u) + q(x,t) \cdot f\left(x,t,u,\frac{\partial u}{\partial x}\right). \qquad (B.103)$$

m determines the dimensionality of the system; $m = 0$, 1, and 2 refer to 1-D linear, 2-D cylindrical, and 3-D spherical systems with angular symmetries, respectively.

B.2 MAPPA framework and simulation procedure

Most of the model parameters were obtained from existing previous literature (see Table 4.1 and B.1 for detailed descriptions and references of parameters). While parameters related to ligand-receptor binding kinetics could be obtained from the literature, parameters associated with Hill functions connecting upstream signals and downstream effects could not be determined since they are phenomenological descriptions and subject to cell-cell heterogeneities, even under shared environments. Initial conditions of model variables (such as the initial level of CD80/86 or initial density of Tregs) can be considered as parameters externally provided. However, these values also vary significantly during homeostatic conditions. Therefore, simulating the model under a few fixed parameter combinations cannot account for phenotypic variations of the T cell response, leading us to apply the MAPPA framework outlined below.

MAPPA is a computational framework that uses Random Forests to build quantitative maps between parameter space and phenotypic space for complicated models with analytical intractability _. This framework determines the contribution of individual parameters sampled throughout the plausible parameter space on a range of phenotypes, both at the global level (i.e., across all configurations in the parameter space), or local level (i.e., across specific configurations in the parameter space only). For our studies, the plausible parameter space was constructed using homeostatic parameter value ranges (see Table 4.1). We factored in the effects of inflammation on the costimulatory ligand level (CD80/86 on a DC), for which we considered two different ranges, 100,000-1,000,000 and 300,000-3,000,000 for homeostasis and inflammation, respectively. Within these parameter ranges, we sampled 20,000 parameter combinations using the Sobol' sampling scheme, which, when compared to a pseudorandom sampling scheme, ensures uniform coverage of high-dimensional space.

Simulations were conducted using the MATLAB software for each parameter combination. The simulation time was from 0 to 120 hours, reflecting the typical time scale of the T cell response. The units of variables were set to be either copy numbers for intracellular species or copy numbers per um^3 for extracellular species. The units of parameters were converted to those compatible with the units of variables. Matlab code is available on Github (https://github.com/pkm304/multiscale_t_cell_activation).

ODEs and PDEs were connected with boundary conditions at the interface of spatial compartments (Figure 4.1). By utilizing the separation of time scales between gene expression dynamics occurring over hours and spatial dynamics of cell movement and IL-2 diffusion reaching stationary states occurring over minutes, we were able to use the built-in ODE and PDE solvers (ode45 and pdepe, respectively) of the MATLAB, rather than creating a new simulation scheme. We decomposed each simulation of ODEs and PDEs into 5-minute intervals, which is the optimal separation of time scales. For each 5-minute interval, the initial boundary conditions were based on the simulation results from the previous time interval.

B.3 Effective size of the IL-2 niche per cell

We estimate the effective size of the IL-2 niche provided by an IL-2 secreting Tconv in homeostasis based on the model T cell zone and related quantities (Figure 4.15; Table B.1). $f_{pSTAT5+} = 0.1$ indicates that 10% of the volume of the T cell zone is affected by IL-2 secreting Tconv. From $N_{IL2+} = 792$, we derive the mean effective range l_D of the IL-2 niche for each IL2 secretor:

$$\frac{4}{3}\pi({l_D}^3 - {r_{tr}}^3) \cdot N_{IL2+} = V_{IL2+} \cdot N_{IL2+} = f_{pSTAT5+} \cdot V_{tot}, \tag{B.104}$$

where the volume of Tregs is excluded and V_{IL2+} is the effective volume of the IL-2 niche per IL-2 secreting cell. Finally, we obtain

$$l_D = \left(\frac{3}{4\pi} \cdot \frac{f_{pSTAT+} \cdot V_{tot}}{N_{IL2+}} - r_{tr}^3\right)^{\frac{1}{3}} = 9.79\mu m. \tag{B.105}$$

We can consider the quantities, $l_D = 9.79\mu m$ and $V_{IL2+} = 3406.8\mu m^3$, as a fundamental spatial unit of T-cell-T-cell interactions mediated by paracrine IL-2.

Table B.1 Quantities defined in the model T cell zone.

Notation	Description	Value
$\boldsymbol{V_{tot}}$	Volume of (model) T cell zone	2.7×10^{7} µm^{3}
$\boldsymbol{f_{IL2+}}$	Frequency of IL-2 secreting CD4^{+} T cells	0.01
$\boldsymbol{f_{pSTAT5+}}$	Frequency of pSTAT5^{+} Tregs	0.1
$\boldsymbol{n_{tr}}$	Number density of Tregs	0.0004 µm^{-3}
$\boldsymbol{N_{tr}}$	Number density of Tregs	10800 cells
$\boldsymbol{n_{tconv}}$	Number density of Tconvs	0.00293 µm^{-3}
$\boldsymbol{N_{tconv}}$	Number of Tconv	79200 cells
$\boldsymbol{N_{IL2+}}$	Number of IL-2 secreting Tconvs	792 cells
$\boldsymbol{n_{IL2+}}$	Number density of IL-2 secreting Tconvs	2.93×10^{-5} µm^{-3}
$\boldsymbol{r_{tc}}, \boldsymbol{r_{tr}}$	Radius of Tconv and Treg	5 µm

B.4 Probabilistic models of clonal expansion

B.4.1 Sequential encounter model

We employed the mathematical description of collisions between cells under the assumption that each self-activated T cells randomly moves around with the average speed, $v_{rand} = 5\mu m/min$ (Fricke et al., 2016). A self-activated T cell sweeps the space with a cross-section, $\sigma = \pi \cdot (r_{tc} + l_D)^2 = 706.86\,\mu m^2$. The volume the activated Tconv with this cross-section sweeps per minute is $V_{sweep} = \sigma \cdot v_{rand}$ (Figure 4.18). Then, we estimate the number of IL-2 secreting Tconv encounters within their IL-2 niches per unit time as $R_{enc} = n_{IL2+} \cdot \sigma \cdot v_{rand} = 0.104\,min^{-1} = 6.2\,h^{-1}$, where $n_{IL2+} = 2.93 \times 10^{-5}$. In homeostasis, each encounter lasts $\tau \approx 2\,min$ given the size of the IL2 niche per cell ($l_D \approx 10\mu m$) and the average speed of T cell movement, $v_{rand} = 5\mu m/min$. The average accumulated duration of encounters per hour is

$\tau_{cumul} \approx 12\ min$, which is around 20% of an hour. This duration is substantially below the duration that a self-activated T cell under Treg suppression needs for maintaining the proliferation signals and suppressing the apoptotic signals since, as we have seen (Figure 4.5), a self-activated T cell barely achieves a high level of IL2-Ra enough to sense IL-2.

By applying the Poisson process, we obtained the probability of having x encounters per hour given the average encounter rate, R_{enc} as

$$P_{hour}(x, R_{enc}) = \frac{{R_{enc}}^{x} \cdot e^{-R_{enc}}}{x!}\ . \tag{B.106}$$

To get more intuition, we compute the probability of equal to or more than 30 encounters per hour,

$$P_{hour}(x \geq 30, 6.2) = \sum_{x \geq 30} \frac{6.2^{x} \cdot e^{-6.2}}{x!} = 5.64 \times 10^{-12}, \tag{B.107}$$

which is an extremely low probability. To undergo a complete clonal expansion, self-activated T cells should get enough signals for five days or 120 hours (Heinzel et al., 2017). If we assume that the average number of encounters enough to maintain the activated T cell for a clonal expansion is $N_{enc.thresh}$, then the probability of clonal expansion can be obtained as

$$P_{clonal} = \{P_{hour}(x \geq N_{enc.thresh}, R_{enc})\}^{120}. \tag{B.108}$$

Assuming $N_{enc.thresh} = 15$, a condition of obtaining IL-2 signals around half of the whole duration,

$$P_{clonal} = \{P_{hour}(x \geq 15, 6.2)\}^{120} \approx 10^{-326}. \tag{B.109}$$

The average precursor number of self-activated T cells undergoing clonal expansion during five days in the model T cell zone is

$$N_{clonal} = N_{IL2+} \cdot P_{clonal} \approx 10^{-323}. \tag{B.110}$$

We interpret this as we expect a self-activated T cell in the model T cell zone would eventually escape and undergo clonal expansion if we wait for $\frac{5}{10^{-323}} \approx 10^{324}$ days $\approx 10^{321}$ years, which is essentially impossible within the scope of the age of the universe (13.7 billion years).

B.4.2 Cluster formation model

For a cluster of cells to go through clonal expansion, the formed cluster should sustain at least 10 hours, the duration of cell division (Heinzel et al., 2017). We assume that after 10 hours, the cluster can sustain the mutual signaling milieu to keep IL-2 availability with the increasing cluster size (Zenke et al., 2020). The probability of forming a cluster of $S_{cluster}$ cells within the unit volume, V_{IL2+}, of the per-cell average IL-2 niche persisting more than 10 hours can be decoupled as

$$P_{clonal}(S_{cluster}) = P_{formation}(S_{cluster}) \cdot P_{persist}(S_{cluster}), \qquad (\mathrm{B.111})$$

where $P_{formation}$: the probability of cluster formation and $P_{persist}$: the probability of 10-hour persistence of the cluster.

We derive $P_{formation}(S_{cluster})$ by applying the Poisson process (Richardson, 1946). With the expected number of IL-2 secreting Tconv in the unit volume, $\lambda_{IL2+} = n_{IL2+} \cdot V_{IL2+} = f_{pSTAT5+}$, we obtain

$$P_{formation}(S_{cluster}) = \frac{(\lambda_{IL2+})^{S_{cluster}} e^{-\lambda_{IL2+}}}{S_{cluster}!} = \frac{\left(f_{pSTAT5+}\right)^{S_{cluster}} e^{-f_{pSTAT5+}}}{S_{cluster}!}. \qquad (\mathrm{B.112})$$

The expected number of the clusters with $S_{cluster}$ cells in the model T cell zone is

$$\begin{aligned} N_{cluster}(S_{cluster}) &= \frac{V_{tot}}{V_{IL2+}} \cdot P_{formation}(S_{cluster}) = \frac{V_{tot}}{V_{IL2+}} \cdot \frac{(\lambda_{IL2+})^{S_{cluster}} e^{-\lambda_{IL2+}}}{S_{cluster}!} \\ &= N_{IL2+} \cdot \frac{\left(f_{pSTAT5+}\right)^{S_{cluster}-1} e^{(-f_{pSTAT5+})}}{S_{cluster}!}. \qquad (\mathrm{B.113}) \end{aligned}$$

where $\frac{V_{tot}}{V_{IL2+}}$ is the number of the unit volume in the model T cell zone. Interestingly, $P_{formation}(S_{cluster})$ and $N_{cluster}(S_{cluster})$ are expressed with the experimentally measurable quantities, $f_{pSTAT5+}$ and N_{IL2+}.

Derivation of the functional form of $P_{persist}(S_{cluster})$ requires information of the kinetics for T cell-T cell adhesions (Figure 4.21). From previous intravital imaging studies (Fricke et al., 2016; Matheu et al., 2015), we obtained important time scales. With the average speed of T cells, $v_{rand} = \frac{5\mu m}{min}$ and the average size of the IL-2 niche per cell, $l_D \approx 10\mu m$ the time scale τ_{on} for new self-activated T cells joining an already existing cluster is $\tau_{on} \approx \frac{10}{5} = 2\ min$ (Figure 4.21). With the mean contact duration between T cells, $\tau_{contact} = 1.5\ min$ (Matheu et al., 2015), the rate of disengagement of cells from a cluster can be estimated as $k_{off} \sim \frac{1}{1.5}\ min^{-1}$.

With this time scale information, we further derived the functional forms of k_{on} and k_{off}. For a preformed cluster with $S_{cluster}$ cells, the probability of an additional self-activated, IL-2 secreting Tconv encountering this cluster within the IL-2 niche is

$$P_{add} = \frac{V_{IL2+} \cdot S_{cluster}^{\frac{2}{3}}}{V_{tot}} = \frac{\frac{f_{pSTAT5+} \cdot V_{tot}}{N_{IL2+}} \cdot S_{cluster}^{\frac{2}{3}}}{V_{tot}}, \qquad (\mathrm{B}.114)$$

where the numerator describes the volume of IL-2 niche of the cluster. Note that we used $S_{cluster}^{\frac{2}{3}}$ rather than $S_{cluster}$ because cells in the periphery of the cluster contribute to the IL-2 niche of the cluster seen by incoming cells (Richardson, 1946). Assuming that this encounter happens within τ_{on} and there are N_{IL2+} self-activated, IL-2 secreting Tconvs, we obtain k_{on} as

$$k_{on} = P_{add} \cdot \frac{N_{IL2+}}{\tau_{on}} = \frac{f_{pSTAT5+} \cdot S_{cluster}^{\frac{2}{3}}}{\tau_{on}}. \qquad (\mathrm{B}.115)$$

For deriving k_{off}, we assume that, again, only the cells in the periphery of the clusters are subject to detachment. We further assumed that as the size of the cluster increases, the cells in the cluster adhere to each other more firmly, leading to decreased k_{off}. Finally, we obtained k_{off} as

$$k_{off} = \frac{k_{off.max}}{1 + \frac{S_{cluster}}{K_{cluster}}} \cdot S_{cluster}^{\frac{2}{3}}, \qquad (\mathrm{B}.116)$$

where $k_{off.max} = \frac{1}{1.5}\ min^{-1}$and $K_{cluster} \approx 10$.

With those estimated kinetic parameters, we now derive $P_{persist}(S_{cluster})$. We start from a dynamical equation describing the cluster size:

$$\begin{aligned} \frac{dS_{cluster}}{dt} = k_{on} - k_{off} &= \frac{f_{pSTAT5+} \cdot S_{cluster}^{\frac{2}{3}}}{\tau_{on}} - \frac{k_{off.max}}{1 + \frac{S_{cluster}}{K_{cluster}}} \cdot S_{cluster}^{\frac{2}{3}} \\ &= -\left(\frac{k_{off.max}}{1 + \frac{S_{cluster}}{K_{cluster}}} - \frac{f_{pSTAT5+}}{\tau_{on}} \right) \cdot S_{cluster}^{-\frac{1}{3}} \cdot S_{cluster} \\ &= -\delta(S_{cluster}) \cdot S_{cluster}, \end{aligned} \qquad (\mathrm{B}.117)$$

where we introduced the effective decay parameter,

$$\delta(S_{cluster}) \equiv \left(\frac{k_{off.max}}{1 + \frac{S_{cluster}}{K_{cluster}}} - \frac{f_{pSTAT5+}}{\tau_{on}} \right) \cdot S_{cluster}^{-\frac{1}{3}}. \qquad (\mathrm{B}.118)$$

Finally, the probability of 10-hour persistence of a cluster with $S_{cluster}$ cells can be estimated as,

$$P_{persist}(S_{cluster}) \approx \exp[-\delta(S_{cluster}) \cdot 10\ hours]. \qquad (\mathrm{B}.119)$$

Thus far, we have derived P_{clonal} as

$$P_{clonal}(S_{cluster}) = P_{formation}(S_{cluster}) \cdot P_{persist}(S_{cluster})$$
$$= \frac{(n_{IL2+} \cdot V_{IL2+})^{S_{cluster}} e^{-n_{IL2+} \cdot V_{IL2+}}}{S_{cluster}!}$$
$$\times \exp\left[-\left(\frac{k_{off.max}}{1 + \frac{S_{cluster}}{K_{cluster}}} - \frac{f_{pSTAT5+}}{\tau_{on}}\right) \cdot S_{cluster}{}^{-\frac{1}{3}} \cdot 10\ hours\right]. \qquad (B.120)$$

The proper interpretation of $P_{clonal}(S_{cluster})$ is the probability of formation and clonal expansion of a cluster of the size, $S_{cluster}$, in the unit volume, V_{IL2+}, the per-cell average size of IL-2 niche provided by a self-activated, IL-2 secreting Tconv. With this, we further derived the expression of the probability of formation and clonal expansion of clusters with $S_{cluster} \geq 5$ cells anywhere in the total volume, V_{tot}. The threshold size, five cells, was obtained from (Bosch et al., 2017). The total volume, V_{tot}, can be thought of being comprised of multiple V_{IL2+}. Then, the total number of the unit volume is $N_{unit} = \frac{V_{tot}}{V_{IL2+}} \approx 7920$. First, we obtained the probability of nonexistence of the cluster with the size ≥ 5 as

$$P_{null} = \prod_{S_{cluster} \geq 5} \binom{N_{unit}}{0} \cdot P_{clonal}(S_{cluster})^0 \cdot \left(1 - P_{clonal}(S_{cluster})\right)^{N_{unit}}$$
$$= \prod_{S_{cluster} \geq 5} \left(1 - P_{clonal}(S_{cluster}) \cdot \frac{N_{unit}}{N_{unit}}\right)^{N_{unit}}$$
$$\approx \prod_{S_{cluster} \geq 5} \exp\left(-N_{unit} \cdot P_{clonal}(S_{cluster})\right)$$
$$= \exp\left[-\sum_{S_{cluster} \geq 5} N_{unit} \cdot P_{clonal}(S_{cluster})\right], \qquad (B.121)$$

where the approximation with exponential function is valid given that $N_{unit} \cdot P_{clonal}(S_{cluster}) \ll 1$ and $N_{unit} \gg 1$. The probability of clonal expansion in anywhere of V_{tot} is

$$P_{clonal.tot} = 1 - P_{null} = 1 - \exp\left[- \sum_{S_{cluster} \geq 5} N_{unit} \cdot P_{clonal}(S_{cluster}) \right]. \quad (B.122)$$

$P_{clonal.tot}$ for varying the self-activated T cell frequencies are plotted for different $k_{off.max}$, $\frac{1}{1.5}$, $\frac{1}{2}$, and $\frac{1}{2.5}$, where lower $k_{off.max}$ indicates the condition that self-activated T cells achieve higher adhesive capacity, possibly due to inflammation (Figure 4.21B).

B.5 Cell population models of the peripheral Treg maintenance

We consider the population dynamics of Tregs at two different organizational levels, i.e., the intranodal level and organismal levels (Figure 4.22). Our goal is to show that the homeostatic frequencies of self-activated, IL-2 secreting Tconvs (1-2% of Tconvs) and pSTAT5$^+$ Tregs (10-15% of Tregs) are sufficient to maintain the physiologic peripheral Treg pool size based on the reasonable values of parameters and variables related to Treg population dynamics inferred from the existing literature and quantitative arguments.

Recently, at least two subtypes of Tregs, i.e., central Tregs (cTregs) and effector Tregs (eTregs) has been shown to exist with different phenotypes in terms of responsiveness to IL-2 and dwelling time in lymph nodes (Owen et al., 2018; Smigiel et al., 2014; Tong et al., 2019). cTregs show naïve phenotypes and rely on IL-2 for their survival and proliferation while eTregs are derived from cTregs and independent of IL2, yet dependent on the ICOS signaling from dendritic cells (Smigiel et al., 2014). The frequency ratio between these two subtypes in SLOs is roughly 1:1 despite significant variations across SLOs. Therefore, we only consider cTregs for modeling their maintenance in the periphery dependent on IL-2, which is roughly half of the total Treg population.

B.5.1 Intranodal Treg population dynamics

Again, we utilize the model T cell zone and related quantities (Figure 4.15; Table B.1) to describe the intranodal dynamics of the Treg population (Figure 4.22A). We can write the governing equation of the population dynamics of cTregs as

$$\frac{dn_{ctr}}{dt} = k_{entry} + k_{prolif} \cdot f_{pSTAT5+} \cdot n_{ctr} - k_{decay} \cdot \left(1 - f_{psTAT5+}\right) \cdot n_{ctr}, \quad (\mathrm{B}.123)$$

where k_{decay} includes exit, death, and conversion of cTregs. In homeostasis, the following relationship should hold,

$$0 = k_{entry} + k_{prolif} \cdot f_{pSTAT5+} \cdot n_{ctr} - k_{decay} \cdot \left(1 - f_{psTAT5+}\right) \cdot n_{ctr}, \qquad (\mathrm{B}.124)$$

where $n_{ctr} = 0.0002\mu m^{-3}$(half of the total Treg density) and $f_{pSTAT5+} = 0.15$ for cTregs. The experiment of blocking T cell entry by (Tong et al., 2019) allows us to infer the value of k_{entry}. The average dwelling time of cTregs was shown to be 10 hours after blocking entry (equivalent to $k_{entry} = 0$). Thus, we have

$$k_{prolif} \cdot f_{pSTAT5+} - k_{decay} \cdot \left(1 - f_{psTAT5+}\right) \approx -0.1h^{-1}. \qquad (\mathrm{B}.125)$$

To achieve the homeostatic cTreg density, $n_{ctr} = 0.0002\mu m^{-3}$,

$$\begin{aligned} k_{entry} &= -\left(k_{prolif} \cdot f_{pSTAT5+} - k_{decay} \cdot \left(1 - f_{psTAT5+}\right)\right) \cdot n_{ctr} \\ &= 0.00002\mu m^{-3} h^{-1}. \end{aligned} \qquad (\mathrm{B}.126)$$

Finally, if we can infer k_{prolif} from additional experimental data and the resultant value is reasonable, then the homeostatic IL-2 niche size is sufficient to maintain the physiologic size of the Treg population at least at the intranodal level. In Figure 3 of (Smigiel et al., 2014), two weeks of IL-2 blocking led to the decrease of the cTreg frequency from 22×10^4 to 7×10^4 in the spleen, leaving the frequency of eTreg unchanged. Since IL-2 blocking leads to $f_{pSTAT5+} \approx 0$ (Smigiel et al., 2014), we now have

$$\frac{dn_{ctr}}{dt} = k_{entry} - k_{decay} \cdot n_{ctr}, \tag{B.127}$$

where k_{entry} is now a function of time since the total Treg pool also decreases due to the lack of IL-2 signals. We assume that k_{entry} is directly proportional to the total peripheral Treg pool size and employ the total Treg population decay rate, $k_{decay,tot} = 0.00263\ h^{-1}$ (the mean half-life: 11 days or 264 hours) from (Vukmanovic-Stejic et al., 2006). Since $k_{decay} \gg k_{decay,tot}$, we may consider the system maintains quasi-steady states over the time scale of two weeks,

$$k_{entry}(t) - k_{decay} \cdot n_{ctr}(t) \approx 0. \tag{B.128}$$

Given that $k_{entry}(2\ weeks) = k_{entry} e^{-k_{decay,tot} \cdot 2\ weeks} = 8.27 \times 10^{-6}\ \mu m^{-3} h^{-1}$ and $n_{ctr}(2\ weeks) = 6.36 \times 10^{-5} \mu m^{-3}$, we can infer that $k_{decay} \approx 0.13 h^{-1}$, indicating that the mean dwelling time of cTregs without IL-2 signal is around 7.7 hours. Finally, we obtain k_{prolif} as

$$k_{prolif} \cdot f_{pSTAT5+} - k_{decay} \cdot \left(1 - f_{psTAT5+}\right) \approx -0.1 h^{-1} \tag{B.129}$$

$$\begin{aligned} k_{prolif} &\approx \frac{k_{decay} \cdot \left(1 - f_{psTAT5+}\right) - 0.1 h^{-1}}{f_{pSTAT5+}} \\ &\approx \frac{0.13 \cdot (1 - 0.15) - 0.1}{0.15} = 0.07\ h^{-1}, \end{aligned} \tag{B.130}$$

indicating the doubling time is $\frac{\ln(2)}{0.07} \cong 10\ hours$. This value is compatible with data from (Heinzel et al., 2017) that showed the duration of each division is about 10 hours, although this was derived from conventional T cells.

Experimental data showed that $f_{pSTAT5+}$ is variable across SLOs in the range of 0.05-0.15 (Liu et al., 2015) for all Tregs in SLOs. cTregs tend to have higher values of $f_{pSTAT5+}$ due to their preferential localization with IL-2 secreting Tconvs and migratory DCs via CCR7 (Smigiel et al., 2014). Furthermore, (Milanez-Almeida et al., 2015) showed that the frequency of Tregs with an activated phenotype (CD69^{+}) is around 20% of the all Tregs in SLOs, potentially due to memory of Tregs for IL-2 signal experience. Thus, we may assume the plausible range of $f_{pSTAT5+}$ for extreme cases to be between 0.07 and 0.20 depending on SLOs due to different self-antigen loads and the basal inflammation status. With this range of $f_{pSTAT5+}$, k_{prolif} can be estimated between 0.02 and 0.30 (doubling times spanning from 2.32 hours to 34.7 hours), which include the reasonable range, 0.035-0.07 (doubling time of 10-20 hours).

Taken together, the homeostatic condition with the frequency (1-2% of total CD4^{+} T cells) of self-reactive T cells secreting IL-2 and the frequency (10-15% of all Tregs) of pSTAT5^{+} Tregs meet the homeostatic maintenance of the Treg population size with reasonable parameter values inferred from existing experimental data at the intranodal level.

B.5.2 Organismal Treg population dynamics

Taking the value of k_{prolif} estimated above (to say $k_{prolif} \approx 0.07\ h^{-1}$), we will show that at the organismal level, homeostatic maintenance of cTregs is possible with the value of $f_{pSTAT5+}$ less than or comparable to the ones measured experimentally in SLOs (Figure 4.22B). The total Treg pool of the whole body (more precisely in the lymphatic system) is regulated with thymic output, peripheral proliferation/survival, and decay (death, exit, and conversion) giving

$$\frac{d\left(N_{cTreg}\right)}{dt} = k_{thy,Treg} + k_{prolif} \cdot f_{pSTAT5+,tot} \cdot N_{cTreg} \\ -k_{decay,tot} \cdot \left(1 - f_{pSTAT5+,tot}\right) \cdot N_{cTreg}, \quad \text{(B.131)}$$

where N_{cTreg}: the total number of cTreg in all SLOs, $k_{thy,Treg}$: the thymic output of Tregs, and $f_{pSTAT5,tot}$: the fraction of cTreg within the IL-2 niche at the organismal level. From (den Braber et al., 2012; Milanez-Almeida et al., 2015), we obtained the homeostatic values of parameters and variables as

$$N_{Treg} = 1.44 \times 10^{6}\ cells, \quad \text{(B.132)}$$

$$N_{cTreg} \approx 0.5 \times 1.44 \times 10^{6}\ cells = 7.2 \times 10^{5}\ cells, \quad \text{(B.133)}$$

$$k_{thy,Treg} = 13800\ cells\ d^{-1} = 575\ cells\ h^{-1}. \quad \text{(B.134)}$$

At steady states, we have

$$0 = k_{thy,Treg} + k_{prolif} \cdot f_{pSTAT5+} \cdot N_{cTreg} \\ -k_{decay,tot} \cdot \left(1 - f_{pSTAT5+}\right) \cdot N_{cTreg}, \quad \text{(B.135)}$$

which leads to

$$f_{pSTAT5+,tot} = \frac{k_{decay,tot} \cdot N_{cTreg} - k_{thy,Treg}}{\left(k_{prolif} + k_{decay,tot}\right) \cdot N_{cTreg}} = \frac{1894 - 575}{52300} = 0.025. \quad \text{(B.136)}$$

We can estimate $f_{pSTAT5+,tot}$ in a stricter manner by adding cTregs, not in SLOs but in other organs such as ones in peripheral blood circulation, thus not being able to obtain IL-2 signals. If we assume the number of those cTregs to be similar to that of SLOs, $N_{cTreg,add} = 7.2 \times 10^{5}\ cells$, then

$$f_{pSTAT5+,tot} = \frac{k_{decay,tot} \cdot \left(N_{cTreg} + N_{cTreg,add}\right) - k_{thy,Treg}}{\left(k_{prolif} + k_{decay,tot}\right) \cdot N_{cTreg}} \\ = \frac{3788 - 575}{52300} = 0.06. \quad \text{(B.137)}$$

This more stringent estimation of $f_{pSTAT5+,tot}$ is still comparable to or less than the values of $f_{pSTAT5+}$ measured from SLOs, indicating that IL-2 niche created by responding self-reactive T cells with the homeostatic frequency (1-2%) of Tconvs in SLOs is (more than) enough to maintain the physiologic peripheral cTreg population pool at the whole organismal level.

B.5.3 Treg regulation of the frequency of IL-2 secretion T cells

We derive the quantitative expression of the Tregs' negative regulation over the frequency of IL-2 secreting Tconvs in the model T cell zone (Figure 4.24). This requires quantities such as the predisposed number of potentially self-reactive Tconvs (f_{self}), the total number of distinct self-peptide sequences presented through MHC-II (P_{tot}), and the number of distinct peptide sequences presented in a particular lymph node (P_{LN}). Then, we can estimate the number of T cells that are potentially activated upon the cognate antigen encounter in the lymph node as

$$N_{self.LN} = N_{tconv} \cdot f_{self} \cdot \frac{P_{LN}}{P_{tot}}. \tag{B.138}$$

The number of IL-2 secreting Tconvs, $N_{IL2+}$is governed by

$$\frac{dN_{IL2+}}{dt} = k_{act} - \frac{1}{\tau_{sec.dur}}.N_{IL2+}, \tag{B.139}$$

where k_{act} is the rate of CD4$^+$ T cell activation (cells/hour) and $\tau_{sec.dur}$ is the duration of IL-2 secretion by activated CD4$^+$ T cells, which was the phenotype of interest (IL-2.sec.dur) in the MAPPA analysis (Figure 4.4, 4.5, and 4.6). At steady states, we have

$$N_{IL2+} = k_{act} \cdot \tau_{sec.dur}. \tag{B.140}$$

Further derivation of k_{act} is possible through the population-level dynamics of Tconvs in a lymph node. With the average dwelling time of CD4$^+$ T cells in a lymph node,

$\tau_{dwell} = 11$ hours, obtained from (Mandl et al., 2012), the homeostatic population size of CD4$^+$ T cells is determined by

$$0 = k_{entry.tc} - \frac{N_{tconv}}{\tau_{dwell}}, \tag{B.141}$$

where $k_{entry.tc}$ is the entry rate of Tconvs to an SLO (cells/hour). This expression can be rearranged as

$$k_{entry.tc} = \frac{N_{tconv}}{\tau_{dwell}}. \tag{B.142}$$

Based on this, we obtain the entry rate of self-reactive Tconvs that are potentially activated in the particular lymph node by self-antigens as

$$k_{entry.self.LN} = k_{entry.tc} \cdot f_{self} \cdot \frac{P_{LN}}{P_{tot}} = \frac{N_{tconv}}{\tau_{dwell}} \cdot f_{self} \cdot \frac{P_{LN}}{P_{tot}}. \tag{B.143}$$

By introducing an additional probability factor, f_{act} describing the probability of the SLO-specific self-reactive Tconvs being activated upon encounter with cognate antigen-bearing DCs, we obtain k_{act} as

$$k_{act} = k_{entry.self.LN} \cdot f_{act} = \frac{N_{tconv}}{\tau_{dwell}} \cdot f_{self} \cdot \frac{P_{LN}}{P_{tot}} \cdot f_{act}. \tag{B.144}$$

Finally, the steady-state N_{IL2+} can be written as

$$N_{IL2+} = k_{act} \cdot \tau_{sec.dur} = N_{tconv} \cdot f_{self} \cdot f_{act} \cdot \frac{P_{LN}}{P_{tot}} \cdot \frac{\tau_{sec.dur}}{\tau_{dwell}}. \tag{B.145}$$

The parameters that are dependent on the Treg density are f_{act}, P_{LN}, and $\tau_{sec.dur}$, and Treg regulation on these parameters are mediated via DCs. f_{self} can be estimated as $f_{self} = 0.04 - 0.1$ based on (Amado et al., 2013; Richards et al., 2015). Given that the precursor frequency of CD4$^+$ T cells that can recognize a particular self-peptide-MHC-II complex in mice is 0.1-10 per 10^6 cells (Jenkins and Moon, 2012), the number of unique peptide-MHC-II complexes in a mouse can be estimated as $P_{tot} = \frac{f_{self}}{1/1{,}000{,}000} =$

$40{,}000 - 100{,}000$. The number of unique self-peptide-MHC-II complexes per SLO can roughly be estimated as $P_{LN} = 1{,}000 - 10{,}000$ based on (Fugmann et al., 2017; Wan et al., 2020). Assuming $f_{act} = 1$, P_{LN} = 5,000, and $\tau_{sec.dur} = 20$, we estimate as $N_{IL2+} = 720$, which is near to the value, $N_{IL2+} = 792$ we defined above. We require further experimental data to constrain these parameters.

B.6 Supplementary Figures

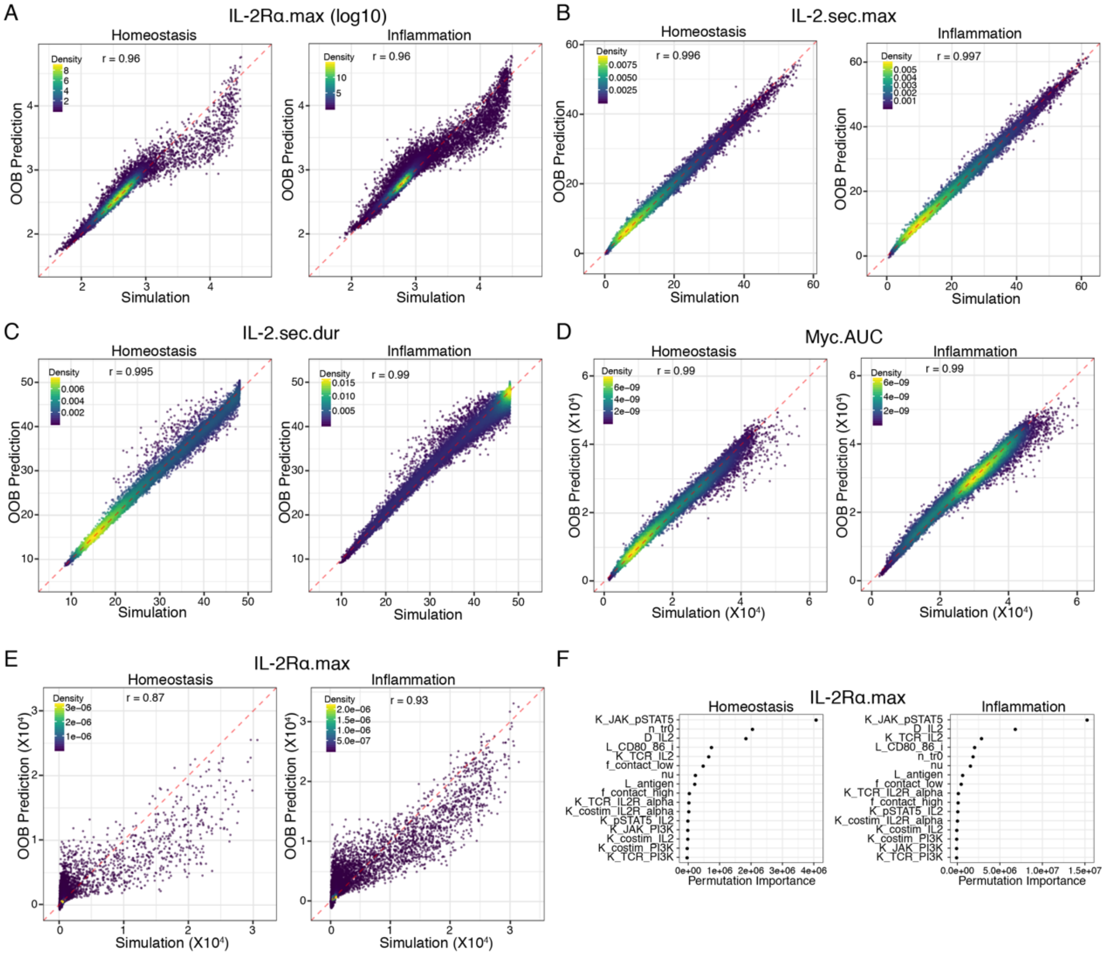

Figure B.1 Machine learning model performance for each activation phenotype for homeostasis and inflammation. **(A)-(D)** Scatter plots showing out-of-bag predictions from ML models vs. simulation results for (A) IL-2Ra.max (log10), (B) IL-2.sec.max, (C) IL-2.sec.dur, and (D) Myc.AUC. (**E)** ML model performance for IL-2Ra.max (in original scale) shown as a scatter plot between out-of-bag predictions from ML models vs. simulation results. OOB-out-of-bag. **(F)** Global variable importance determining IL-2Ra.max.

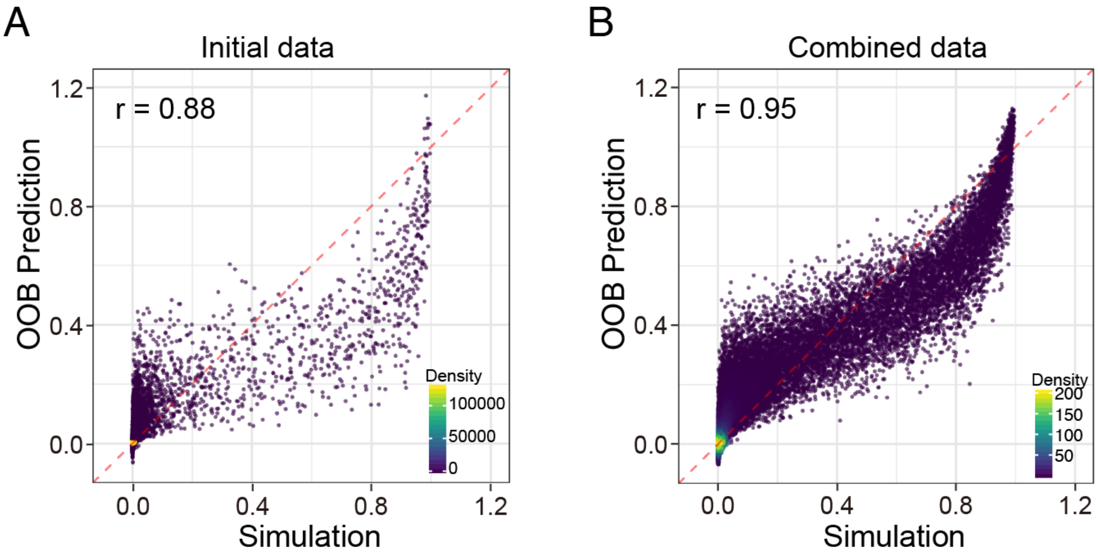

Figure B.2 Prediction performance of ML model for pSTAT5.max. **(A)-(B)** Scatter plots showing the concordance between the independently simulated pSTAT5.max (x-axis) and those predicted by a RF ML regression model (y-axis) using out-of-bag (OOB) data (i.e., data not used for training). Two RF ML models are shown: A is based on the initial simulations ("initial data") only while B is based on initial data plus additional simulations enriched for parameter configurations with large pSTAT5.max values ("combined data"), thus increasing prediction performance. Each r value represents the Pearson correlation coefficient between the predicted and simulated pSTAT5.max values. Each dot represents the pSTAT5.max for a specific parameter configuration.

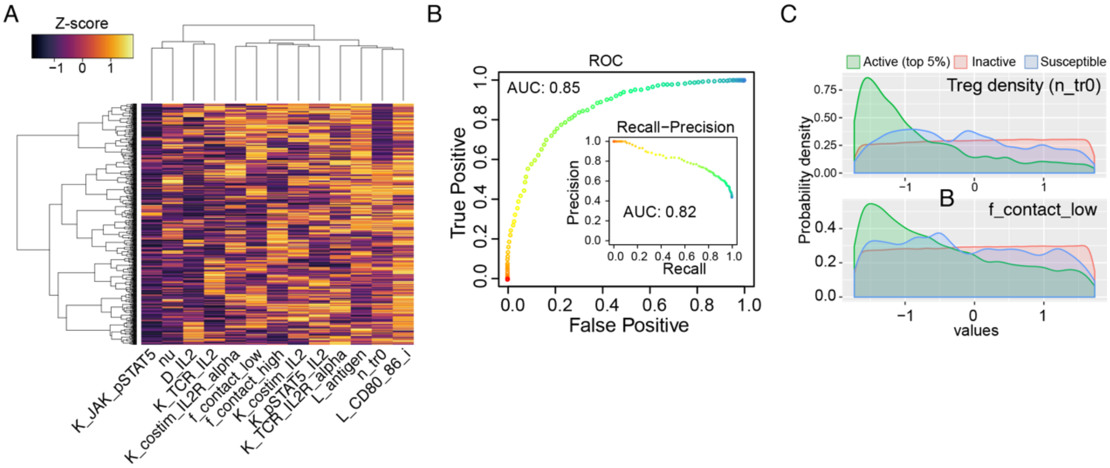

Figure B.3 Delineation of susceptible configurations. **(A)** Heatmap illustrating individual parameters (columns) and their standard scores (Z-score) within each susceptible configuration (rows). **(B)** Prediction performance of the RFML classification model comparing susceptible and active configurations. Performance was assessed using the receiver operator characteristic (ROC) and precision-recall curves; area under the curve (AUC) used as the quantitative metric. **(C)** Distributions of values for the top two parameters from Figure 4.14A, the Treg density (n_tr0) and the baseline contact efficiency (f_contact_low). Distributions are shown for active, inactive, and susceptible configurations. See Figure 4.14.

B.7 Parameters and variables used in the T cell activation model

Table B.2 Parameters and variables used in the T cell activation model

Name	Definition	MATLAB notation	Value	Unit	References	Etc.
$\boldsymbol{\kappa}$	pMHC-TCR on-rate	kappa	10^{-4}	s^{-1}	(Altan-Bonnet and Germain, 2005; François et al., 2013)	
$\boldsymbol{\nu}$	pMHC-TCR off-rate	nu	0.1~1	s^{-1}	(Altan-Bonnet and Germain, 2005; François et al., 2013)	0.2~0.4 for MAPPA
$\boldsymbol{N}$	Number of phosphorylation steps	N	5		(François et al., 2013)	
$\boldsymbol{\phi_{max}}$	Phosphorylation rate	phi_max	0.09	s^{-1}	(François et al., 2013)	
$\boldsymbol{b}$	Spontaneous dephosphorylation rate	b	0.04	s^{-1}	(François et al., 2013)	
$\boldsymbol{\gamma}$	Phosphatase efficiency	gamma	1.2×10^{-6}	s^{-1}	(François et al., 2013)	
$\boldsymbol{S_{SHP1,T}}$	Number of phosphatase (SHP-1) per cell	S_SHP1_t	60,000		(François et al., 2013	
$\boldsymbol{C^{*}_{TCR,1}}$	Half saturation level of for activation	C_TCR_1_star	500		(François et al., 2013)	
$\boldsymbol{k^{on}_{costim}}$	Association rate of CD80/86 and CD28	k_on_costim	0.77 ± 0.06	$\mu m^2 s^{-1}$	(Collins et al., 2002)	Converted to 2D rate following (Jansson and Davis, 2011)
$\boldsymbol{k^{off}_{costim}}$	dissociation rate of CD80/86 and CD28	k_off_costim	28 ± 2	s^{-1}	(Collins et al., 2002)	
$\boldsymbol{k^{on}_{CTAL4}}$	Association rate of CD80/86 and CTLA4	k_on_CTLA4	1.09	$\mu m^2 s^{-1}$	(Collins et al., 2002)	Converted to 2D rate following (Jansson and Davis, 2011)
$\boldsymbol{k^{off}_{CTLA4}}$	Dissociation rate of CD80/86 and CTLA4	k_off_CTLA4	5.1	s^{-1}	(Collins et al., 2002)	
$\boldsymbol{k^{endo}_{CTLA4}}$	Rate of CTLA4 endocytosis	k_endo_CTLA4	0.291	min^{-1}	(Khailaie et al., 2017)	
$\boldsymbol{k^{transcription(basal)}_{mIL2R\alpha}}$	Basal transcription rate of IL2Rα	k_transc_basal_mIL2R_alpha	$0.03 \times \boldsymbol{k^{deg}_{IL2\alpha}}$	h^{-1}	(Voisinne et al., 2015)	
$\boldsymbol{k^{transcription(TCR,costim)}_{mIL2R\alpha}}$	Transcription rate of IL2Rα downstream of TCR and costimulation	k_transc_TCR_costim_mIL2R_alpha	$10 \times \boldsymbol{k^{deg}_{IL2\alpha}}$	h^{-1}	(Voisinne et al., 2015)	

$\boldsymbol{k_{mIL2R\alpha}^{transcription(pSTAT5)}}$	Transcription rate of IL2Rα downstream of pSTAT5	k_transc_pSTAT5_mIL2R_alpha	$4 \times 10^2 \times \boldsymbol{k_{IL2\alpha}^{deg}}$	h^{-1}	(Voisinne et al., 2015)	
$\boldsymbol{K_{TCR \rightarrow IL2R\alpha}}$	Half saturation level of TCR activation for IL2Rα production	K_TCR_IL2R_alpha	0.2 0.3		(François et al., 2013) (Voisinne et al., 2015)	0.1~1for MAPPA
$\boldsymbol{n_{TCR \rightarrow IL2R\alpha}}$	Hill coefficient of TCR activation for IL2Rα production	n_TCR_IL2R_alpha	1		(Voisinne et al., 2015)	
$\boldsymbol{K_{costim \rightarrow IL2R\alpha}}$	Half saturation level of costimulation for IL2Rα production	K_costim_IL2R_alpha	10~100		This study	Varied for MAPPA
$\boldsymbol{n_{costim \rightarrow IL2R\alpha}}$	Hill coefficient of costimulation for IL2Rα production	n_costim_IL2R_alpha	1		This study	
$\boldsymbol{K_{JAK \rightarrow pSTAT5}}$	Half saturation level of JAK activation for IL2Rα production	K_JAK_pSTAT5	0.05		(Voisinne et al., 2015)	0.01~0.1 for MAPPA
$\boldsymbol{n_{JAK \rightarrow pSTAT5}}$	Hill coefficient of JAK activation for IL2Rα production	n_JAK_pSTAT5	2		(Busse et al., 2010; Feinerman et al., 2010; Voisinne et al., 2015)	For bistability of IL2Rα
$\boldsymbol{K_{IL2 \rightarrow JAK}^{high}}$	Half saturation level of IL2 for JAK activation (for high IL2Rα level)	K_IL2_JAK_high	1	pM	(Voisinne et al., 2015)	
$\boldsymbol{K_{IL2 \rightarrow JAK}^{low}}$	Half saturation level of IL2 for JAK activation (for low IL2Rα level)	K_IL2_JAK_low	50	pM	(Voisinne et al., 2015)	
$\boldsymbol{R_{IL2R\alpha,0}}$	Half saturation level of IL2Rα for JAK activation	R_IL2R_alpha_0	2×10^4		(Voisinne et al., 2015)	
$\boldsymbol{k_{mIL2\alpha}^{deg}}$	Degradation rate of IL2Rα mRNA	k_deg_mIL2R_alpha	0.2	h^{-1}	(Voisinne et al., 2015)	
$\boldsymbol{k_{IL2R\alpha}^{translation}}$	Translation rate of IL2Rα	k_transl_IL2R_alpha	$10^2 \times \boldsymbol{k_{mIL2\alpha}^{deg}}$	h^{-1}	(Voisinne et al., 2015)	
$\boldsymbol{k_{IL2R\alpha}^{deg}}$	Rate of IL2Rα endocytosis	k_deg_IL2R_alpha	$ln(2)/5$ 0.05	h^{-1}	(Duprez et al., 1988; Tkach et al., 2014) (Duprez and Dautry-Varsat, 1986; Voisinne et al., 2015)	Set to 0.05 in this study
$\boldsymbol{K_{IL2R\alpha:\beta\gamma,d}}$	$k_{IL2\alpha;\beta\gamma}^{off}/k_{IL2\alpha;\beta\gamma}^{on}$	K_IL2R_a_bg	2700		(Cotari et al., 2013)	
$\boldsymbol{k_{IL2\alpha;\beta\gamma}^{on}}$	Association rate of IL2Rα and IL2Rβγ		Not needed			
$\boldsymbol{k_{IL2\alpha;\beta\gamma}^{off}}$	Dissociation rate of IL2Rα-IL2Rβγ complexes		Not needed			
$\boldsymbol{k_{C_{IL2R}}^{endo}}$	Rate of endocytosis of IL2-IL2R complexes	k_endo_C_IL2R	$ln(2)/0.25$ 1.7	h^{-1}	(Duprez et al., 1988) (Busse et al., 2010)	Set to 2 in this study

$\boldsymbol{k_{IL2R}^{on}}$	Association rate of IL2 and IL2R	k_on_IL2R	1.1×10^{11}	$M^{-1}h^{-1}$	(Wang and Smith, 1987)	
$\boldsymbol{k_{IL2R}^{off}}$	Dissociation rate of IL2-IL2R complexes	k_off_IL2R	0.83	h^{-1}	(Wang and Smith, 1987)	
$\boldsymbol{K_{C_{IL2R},d}}$	Equilibrium dissociation constant ($\boldsymbol{k_{IL2R}^{off}/k_{IL2R}^{on}}$)	K_IL2_tr	1.0×10^{-11}	M	(Wang and Smith, 1987)	Used only for Tregs
$\boldsymbol{k_{mIL2}^{transcription(TCR)}}$	Transcription rate of IL2 downstream of TCR and costimulation	k_transc_TCR_ mIL2	162	h^{-1}	(Ferguson et al., 2001)	
$\boldsymbol{k_{mIL2}^{transcription(costim)}}$	Transcription rate of IL2 downstream of costimulation	k_transc_costim_mIL2				
$\boldsymbol{k_{mIL2}^{deg}}$	Degradation rate of IL-2 mRNA molecules	k_deg_mIL2	0.2	h^{-1}	(Shim et al., 2002)	
$\boldsymbol{k_{IL2}^{translation}}$	Translation rate of IL-2	k_transl_IL2	266	h^{-1}	(Ferguson et al., 2001; Voisinne et al., 2015)	
$\boldsymbol{k_{IL2}^{sec}}$	$\frac{k_{mIL2}^{transcription(TCR,costim)} k_{IL2}^{translation}}{k_{mIL2}^{deg}}$		60 7.5×3600 $1{,}200 \pm 500$	s^{-1} h^{-1} min^{-1}	(Voisinne et al., 2015) (Tkach et al., 2014) (Huang et al., 2013)	Dynamical variable in this study (q_{IL2})
$\boldsymbol{K_{TCR\rightarrow IL2}}$	Half saturation level of TCR activation for IL2 production	K_TCR_IL2	0.2 0.8		(François et al., 2013) (Voisinne et al., 2015)	0.1~1 for MAPPA
$\boldsymbol{n_{TCR\rightarrow IL2}}$	Hill coefficient of TCR activation for IL2 production	n_TCR_IL2	1		(Voisinne et al., 2015)	
$\boldsymbol{K_{costim\rightarrow IL2}}$	Half saturation level of costimulation for IL2 production	K_costim_IL2	10~100		This study	Varied for MAPPA
$\boldsymbol{n_{costim\rightarrow IL2}}$	Hill coefficient of costimulation for IL2 production	n_costim_IL2	1		This study	
$\boldsymbol{K_{pSTAT5\rightarrow IL2}}$	Half saturation level of pSTAT5 for IL2 production	K_pSTAT5_IL2	$1/3 \cdot 10^{5}$		(Tkach et al., 2014)	0.1~1 for MAPPA
$\boldsymbol{n_{pSTAT5\rightarrow IL2}}$	Hill coefficient of pSTAT5 for IL2 production	n_pSTAT5_IL2	1		This study	
$\boldsymbol{D_{IL2}}$	Diffusion constant of IL2	D_IL2	(aq) 100 (ext) 16 10 (T cell zone) 100	$\mu m^{2}s^{-1}$	(Weidemann et al., 2011) (Höfer et al., 2012) (Busse et al., 2010) (Ross and Pompano, 2018)	aq: aqueous buffer ext: extracellular matrix 10~100 for MAPPA
$\boldsymbol{k_{IL2,extr}^{deg}}$	Degradation rate of IL2 in the extracellular space of lymph nodes	k_deg	0.1	h^{-1}	(Busse et al., 2010)	
$\boldsymbol{k_{mMyc}^{transcription(basal)}}$	Basal transcription rate of Myc	k_transc_basal_mMyc	$0.03 \times \boldsymbol{k_{Myc}^{deg}}$	h^{-1}	(Voisinne et al., 2015)	

$\boldsymbol{k_{mMyc}^{transcription(TCR,costim,JAK))}}$	Transcription rate of Myc downstream of TCR, costimulation, and JAK	k_transc_PI3K_mMyc	$50 \times \boldsymbol{k_{Myc}^{deg}}$	h^{-1}	(Voisinne et al., 2015)	
$\boldsymbol{k_{mMyc}^{deg}}$	Degradation rate of Myc mRNA	k_deg_mMyc	0.2	h^{-1}	(Voisinne et al., 2015)	
$\boldsymbol{k_{Myc}^{translation}}$	Translation rate of Myc	k_transl_Myc	$20 \times \boldsymbol{k_{mIL2\alpha}^{deg}}$	h^{-1}	(Voisinne et al., 2015)	
$\boldsymbol{k_{Myc}^{deg}}$	Degradation rate of Myc	k_deg_Myc	0.099	h^{-1}	(Heinzel et al., 2017)	
$\boldsymbol{K_{TCR \rightarrow PI3K}}$	Half saturation level of TCR activation for PI3K activation	K_TCR_PI3K	0.2 0.3		(François et al., 2013) (Voisinne et al., 2015)	0.1~1 for MAPPA
$\boldsymbol{n_{TCR \rightarrow PI3K}}$	Hill coefficient of TCR activation for PI3K activation	n_TCR_PI3K	1		(Voisinne et al., 2015)	
$\boldsymbol{K_{Costim \rightarrow PI3K}}$	Half saturation level of costimulation for PI3K activation	K_costim_PI3K	10~100		This study	Varied for MAPPA
$\boldsymbol{n_{Costim \rightarrow PI3K}}$	Hill coefficient of costimulation for PI3K activation	n_costim_PI3K	1		This study	
$\boldsymbol{K_{JAK \rightarrow PI3K}}$	Half saturation level of JAK activation for PI3K production	K_JAK_PI3K	0.05		(Voisinne et al., 2015)	0.01~0. 1 for MAPPA
$\boldsymbol{n_{JAK \rightarrow PI3K}}$	Hill coefficient of JAK activation for PI3K activation	n_JAK_PI3K	1		(Voisinne et al., 2015)	
$\boldsymbol{\rho}$	Radius of a T cell		4~10	μm		Set to 5 in this study
$\boldsymbol{n_{tr}}$	Number density of regulatory T cells	n_tr, n_tr0	0.0001~0.001	μm^{-3}	This study	0.001: gastric lymph nodes
$\boldsymbol{S_{DC}}$	Surface area of dendritic cells	S_DC	1,800~2,400	μm^2	(Miller et al., 2004)	Set to in this study
$\boldsymbol{S_{DC:T}}$	Surface area of dendritic cell-T cell contacts	S_DC_TR	1~8 (avg)~70 12.6	μm^2	(Miller et al., 2004) (Jansson and Davis, 2011)	Set to in this study
$\boldsymbol{S_T}$	Surface area of T cells	S_T	314.16	μm^2		
$\boldsymbol{D_{tr}}$	Motility coefficient of Tregs	D_tr	0.83~1.76 0.17 (free Treg) 0.017 (Treg in contact with DC)	$\mu m^2 min^{-1}$ $\mu m^2 s^{-1}$	(Wu et al., 2015) This study	JURKAT T-cells 3D In vivo Tregs
$\boldsymbol{\chi_0}$	Chemotactic constant	chi_0	0~100		This study	Set to 0 in this study

$\boldsymbol{K_{cc}}$	Carrying capacity of Treg	K_cc	0.003	μm^{-3}	This study	
$\boldsymbol{k_{IL2\to treg}^{prolif}}$	Proliferation rate of Tregs induced by IL2	k_prolif_max	0.0385 1.07×10^{-5}	h^{-1} s^{-1}	This study	Doubling time: 18 hours
$\boldsymbol{K_{IL2\to treg}^{prolif}}$	Half maximum level of pSTAT5 for Treg proliferation	K_prolif_IL2	0.1		This study	
$\boldsymbol{U_{min}}$	Minimum attractive potential between DCs and Tregs	U_min	0.05		This study	To simulate adhesive force between DCs and Tregs
$\boldsymbol{n_U}$	Steepness of the potential	n_U	5		This study	
$\boldsymbol{r_{half}}$	Distance leading to half	r_half	15	μm	This study	
$\boldsymbol{K_{CD28,tr\to Umin}}$	Half saturation CD28 signaling strength for adhesion	K_CD28_tr_U_min	5		This study	
$\boldsymbol{K_{pSTAT5,tr\to Umin}}$	Half saturation pSTAT5 signaling strength for adhesion	K_pSTAT5_tr_U_min	0.1		This study	
$\boldsymbol{f_{cont\_low}}$ $\boldsymbol{f_{cont\_high}}$	Contact efficiency between Tregs and DCs	f_contact_low f_contact_high	0.1~0.4 1~2.5		This study	Varied for MAPPA
$\boldsymbol{V_{neighbor}}$	Volume of space encompassing the region where Tregs are in the engagement with DCs	V_neighbor	837.8	μm^3		$\frac{3}{4}\pi(15^2 - 5^2)$
$\boldsymbol{L_{antigen}}$	Number of peptide-MHC per cell	L_antigen	$1 \sim 10^5$		(Altan-Bonnet and Germain, 2005; François et al., 2013)	100~1000 for MAPPA
$\boldsymbol{R_{TCR}}$	Number of TCR per cell	R_TCR	30,000		(Altan-Bonnet and Germain, 2005; François et al., 2013)	
$\boldsymbol{C_{TCR,j}}$, $\boldsymbol{j = 0, \ldots, N}$		C_TCR_N			(François et al., 2013)	
$\boldsymbol{S_{SHP1}}$	Number of activated phosphatase (SHP-1) per cell	S_SHP_1			(François et al., 2013)	
$\boldsymbol{\phi}$	Phosphorylation rate	phi		s^{-1}	(François et al., 2013)	
$\boldsymbol{R_{CD28}}$	Number of CD28 molecules per cell	R_CD28	30,000		(Sugár et al., 2017)	Similar to TCR
$\boldsymbol{L_{CD80\|CD86}}$	Number of CD80/86 molecules per cell	L_CD80_86, L_CD80_86_i	CD86: 400,000 CD80/CD86: 300,000		(Qureshi et al., 2011) (Khailaie et al., 2017)	100,000~1,000,000 and 300,000~3,000,000 for MAPPA

$\boldsymbol{R_{CTLA4}}$	Number of CTLA-4 molecules on plasma membrane per cell	R_CTLA4	24500	(Khailaie et al., 2017)	
$\boldsymbol{C_{CTLA4}}$	Number of CD80/86-CTLA-4 complexes per cell	C_CTLA4			
$\boldsymbol{C_{costim}}$	Number of CD80/86-CD28 complexes per cell	C_costim			
$\boldsymbol{P^{on}_{TCR\rightarrow IL2R\alpha}}$	Activation function of TCR for IL2Rα production	P_on_TCR_IL2			
$\boldsymbol{P^{on}_{JAK\rightarrow pSTAT5}}$	Activation function of JAK for pSTAT5 signaling	P_on_JAK_pSTAT5			
$\boldsymbol{P^{on}_{costim\rightarrow IL2R\alpha}}$	Activation function of costimulation for IL2Rα production	P_on_costim_IL2R_alpha			
$\boldsymbol{P^{on}_{TCR\rightarrow IL2}}$	Activation function of TCR for IL2 production	P_on_TCR_IL2			
$\boldsymbol{P^{on}_{pSTAT5\rightarrow IL2}}$	Inhibition function of pSTAT5 for IL2 production	P_on_pSTAT5_IL2			
$\boldsymbol{P^{on}_{costim\rightarrow IL2}}$	Activation function of costimulation for IL2 production	P_on_costim_IL2			
$\boldsymbol{P^{on}_{TCR,costim,JAK\rightarrow PI3K}}$	Activation function of TCR, costimulation, and JAK for PI3K activation	P_on_signals_PI3K			
$\boldsymbol{S_{JAK}}$	Normalized level of activated JAK	S_JAK		(Voisinne et al., 2015)	
$\boldsymbol{mR_{IL2R\alpha}}$	Number of IL2Rα mRNA	mR_IL2R_alpha			
$\boldsymbol{R_{IL2R\alpha}}$	Number of IL2Rα molecules on plasma membrane per cell	R_IL2R_alpha	Tconv (basal): 3 Tconv (TCR): 1000 Tconv (IL2 max): 4×10^4 Treg (basal): 10^3 Treg (IL2 max): 4×10^4 Treg (constant): 10^4	(Voisinne et al., 2015) (Voisinne et al., 2015) (Voisinne et al., 2015) (Voisinne et al., 2015) (Voisinne et al., 2015) (Feinerman et al., 2010)	
$\boldsymbol{R_{IL2R\beta\gamma}}$	Number of IL2R$\beta\gamma$ molecules on plasma membrane per cell	R_IL2R_bg	Basal (w/o TCR	(Cotari et al., 2013) (Tkach et al., 2014)	w/o: without

			activation): 1000 Max (with TCR activation): 10000		
$\boldsymbol{R_{IL2R}}$	Number of IL2R molecules (IL2Rα-IL2Rβγ complexes) on plasma membrane per cell	R_IL2R			
$\boldsymbol{C_{IL2R}}$	Number of IL2-IL2R complexes on plasma membrane per cell	C_IL2R			
$\boldsymbol{I_{mIL2}}$	Number of IL2 mRNA per cell	mI_IL2			
$\boldsymbol{I_{IL2}}$	Concentration of IL2 in extracellular space in lymph node	I_IL2		μm^{-3} pM	
$\boldsymbol{q_{IL2}}$	Secretion rate of IL2 to extracellular space	q_IL2	~10	s^{-1}	$\boldsymbol{k_{IL2}^{translation} \cdot I_{mIL2}}$
$\boldsymbol{n_{tr}}$	Number density of Tregs in extracellular space surrounding a priming Tconv in lymph node	n_tr		μm^{-3}	
$\boldsymbol{mR_{Myc}}$	Number of Myc mRNA per cell	mMyc			
$\boldsymbol{R_{Myc}}$	Number of Myc protein per cell	Myc			

Bibliography

Akkaya, B., Oya, Y., Akkaya, M., Souz, J.A., Holstein, A.H., Kamenyeva, O., Kabat, J., Matsumura, R., Dorward, D.W., Glass, D.D., et al. (2019). Regulatory T cells mediate specific suppression by depleting peptide–MHC class II from dendritic cells. Nature Immunology *20*, 218.

Almeida, A.R.M., Zaragoza, B., and Freitas, A.A. (2006). Indexation as a Novel Mechanism of Lymphocyte Homeostasis: The Number of CD4+CD25+ Regulatory T Cells Is Indexed to the Number of IL-2-Producing Cells. The Journal of Immunology *177*, 192–200.

Alon, U. (2007). Network motifs: theory and experimental approaches. Nature Reviews Genetics *8*, 450–461.

Altan-Bonnet, G., and Germain, R.N. (2005). Modeling T Cell Antigen Discrimination Based on Feedback Control of Digital ERK Responses. PLOS Biology *3*, e356.

Altan-Bonnet, G., Mora, T., and Walczak, A.M. (2019). Quantitative Immunology for Physicists. ArXiv:1907.03891 [q-Bio].

Amado, I.F., Berges, J., Luther, R.J., Mailhé, M.-P., Garcia, S., Bandeira, A., Weaver, C., Liston, A., and Freitas, A.A. (2013). IL-2 coordinates IL-2–producing and regulatory T cell interplay. J Exp Med *210*, 2707–2720.

Angermann, B.R., Klauschen, F., Garcia, A.D., Prustel, T., Zhang, F., Germain, R.N., and Meier-Schellersheim, M. (2012). Computational modeling of cellular signaling processes embedded into dynamic spatial contexts. Nat Methods *9*, 283–289.

Arpino, J.A.J., Hancock, E.J., Anderson, J., Barahona, M., Stan, G.-B.V., Papachristodoulou, A., and Polizzi, K. (2013). Tuning the dials of Synthetic Biology. Microbiology *159*, 1236–1253.

Asada, T., and Yoshida, H. (2003). Coefficient criterion for four-dimensional Hopf bifurcations: a complete mathematical characterization and applications to economic dynamics. Chaos, Solitons & Fractals *18*, 525–536.

Babtie, A.C., and Stumpf, M.P.H. (2017). How to deal with parameters for whole-cell modelling. Journal of The Royal Society Interface *14*, 20170237.

Baptista, A.P., Gola, A., Huang, Y., Milanez-Almeida, P., Torabi-Parizi, P., Urban, J.F., Shapiro, V.S., Gerner, M.Y., and Germain, R.N. (2019). The Chemoattractant Receptor Ebi2 Drives Intranodal Naive CD4+ T Cell Peripheralization to Promote Effective Adaptive Immunity. Immunity *50*, 1188-1201.e6.

Baum, K., Politi, A.Z., Kofahl, B., Steuer, R., and Wolf, J. (2016). Feedback, Mass Conservation and Reaction Kinetics Impact the Robustness of Cellular Oscillations. PLoS Comput. Biol. *12*, e1005298.

Becskei, A., and Serrano, L. (2000). Engineering stability in gene networks by autoregulation. Nature *405*, 590–593.

Berman, G.J., Choi, D.M., Bialek, W., and Shaevitz, J.W. (2014). Mapping the stereotyped behaviour of freely moving fruit flies. Journal of The Royal Society Interface *11*, 20140672.

Bialek, W. (2018). Perspectives on theory at the interface of physics and biology. Rep. Prog. Phys. *81*, 012601.

Bohineust, A., Garcia, Z., Beuneu, H., Lemaître, F., and Bousso, P. (2018). Termination of T cell priming relies on a phase of unresponsiveness promoting disengagement from APCs and T cell division. Journal of Experimental Medicine *215*, 1481–1492.

Bosch, A.J.T., Bolinger, B., Keck, S., Stepanek, O., Ozga, A.J., Galati-Fournier, V., Stein, J.V., and Palmer, E. (2017). A minimum number of autoimmune T cells to induce autoimmunity? Cellular Immunology *316*, 21–31.

Bou-Rabee, N., and Holmes-Cerfon, M. (2019). Sticky Brownian Motion and its Numerical Solution. ArXiv:1906.06803 [Cond-Mat].

Brandman, O., and Meyer, T. (2008). Feedback Loops Shape Cellular Signals in Space and Time. Science *322*, 390–395.

Breiman, L. (1996). Bagging Predictors. Machine Learning *24*, 123–140.

Breiman, L. (2001). Random Forests. Machine Learning *45*, 5–32.

Brennecke, P., Reyes, A., Pinto, S., Rattay, K., Nguyen, M., Küchler, R., Huber, W., Kyewski, B., and Steinmetz, L.M. (2015). Single-cell transcriptome analysis reveals coordinated ectopic gene-expression patterns in medullary thymic epithelial cells. Nature Immunology *16*, 933–941.

Busse, D., de la Rosa, M., Hobiger, K., Thurley, K., Flossdorf, M., Scheffold, A., and Hofer, T. (2010). Competing feedback loops shape IL-2 signaling between helper and regulatory T lymphocytes in cellular microenvironments. Proceedings of the National Academy of Sciences *107*, 3058–3063.

Butler, T.C., Kardar, M., and Chakraborty, A.K. (2013). Quorum sensing allows T cells to discriminate between self and nonself. PNAS *110*, 11833–11838.

Cahalan, M.D., and Parker, I. (2005). Close encounters of the first and second kind: T–DC and T–B interactions in the lymph node. Seminars in Immunology *17*, 442–451.

Cao, Z., and Grima, R. (2018). Linear mapping approximation of gene regulatory networks with stochastic dynamics. Nat Commun *9*, 1–15.

Chavanis, P.-H. (2008). A stochastic Keller-Segel model of chemotaxis. ArXiv:0804.4425 [Cond-Mat].

Chinen, T., Kannan, A.K., Levine, A.G., Fan, X., Klein, U., Zheng, Y., Gasteiger, G., Feng, Y., Fontenot, J.D., and Rudensky, A.Y. (2016). An essential role for the IL-2 receptor in T_{reg} cell function. Nature Immunology *17*, 1322–1333.

Coder, B.D., Wang, H., Ruan, L., and Su, D.-M. (2015). Thymic Involution Perturbs Negative Selection Leading to Autoreactive T Cells That Induce Chronic Inflammation. J.I. *194*, 5825–5837.

Collins, A.V., Brodie, D.W., Gilbert, R.J.C., Iaboni, A., Manso-Sancho, R., Walse, B., Stuart, D.I., van der Merwe, P.A., and Davis, S.J. (2002). The Interaction Properties of Costimulatory Molecules Revisited. Immunity *17*, 201–210.

Cotari, J.W., Voisinne, G., Dar, O.E., Karabacak, V., and Altan-Bonnet, G. (2013). Cell-to-Cell Variability Analysis Dissects the Plasticity of Signaling of Common γ Chain Cytokines in T Cells. Sci. Signal. *6*, ra17–ra17.

Davis, M.M., and Bjorkman, P.J. (1988). T-cell antigen receptor genes and T-cell recognition. Nature *334*, 395–402.

den Braber, I., Mugwagwa, T., Vrisekoop, N., Westera, L., Mögling, R., Bregje de Boer, A., Willems, N., Schrijver, E.H.R., Spierenburg, G., Gaiser, K., et al. (2012). Maintenance of Peripheral Naive T Cells Is Sustained by Thymus Output in Mice but Not Humans. Immunity *36*, 288–297.

Desponds, J., Mayer, A., Mora, T., and Walczak, A.M. (2017). Population dynamics of immune repertoires. ArXiv:1703.00226 [q-Bio].

DiToro, D., Winstead, C.J., Pham, D., Witte, S., Andargachew, R., Singer, J.R., Wilson, C.G., Zindl, C.L., Luther, R.J., Silberger, D.J., et al. (2018). Differential IL-2 expression defines developmental fates of follicular versus nonfollicular helper T cells. Science *361*, eaao2933.

Dixit, P.D., Wagoner, J., Weistuch, C., Pressé, S., Ghosh, K., and Dill, K.A. (2018). Perspective: Maximum caliber is a general variational principle for dynamical systems. J. Chem. Phys. *148,* 010901.

Dolken, L., Ruzsics, Z., Radle, B., Friedel, C.C., Zimmer, R., Mages, J., Hoffmann, R., Dickinson, P., Forster, T., Ghazal, P., et al. (2008). High-resolution gene expression profiling for simultaneous kinetic parameter analysis of RNA synthesis and decay. RNA *14*, 1959–1972.

Duprez, V., and Dautry-Varsat, A. (1986). Receptor-mediated endocytosis of interleukin 2 in a human tumor T cell line. Degradation of interleukin 2 and evidence for the absence of recycling of interleukin receptors. J. Biol. Chem. *261*, 15450–15454.

Duprez, V., Cornet, V., and Dautry-Varsat, A. (1988). Down-regulation of high affinity interleukin 2 receptors in a human tumor T cell line. Interleukin 2 increases the rate of surface receptor decay. J. Biol. Chem. *263*, 12860–12865.

Eldar, A., and Elowitz, M.B. (2010). Functional roles for noise in genetic circuits. Nature *467*, 167–173.

Elf, J., and Ehrenberg, M. (2003). Fast Evaluation of Fluctuations in Biochemical Networks With the Linear Noise Approximation. Genome Res. *13*, 2475–2484.

Elowitz, M.B., Levine, A.J., Siggia, E.D., and Swain, P.S. (2002). Stochastic Gene Expression in a Single Cell. Science *297*, 1183–1186.

Esfahani, K., Elkrief, A., Calabrese, C., Lapointe, R., Hudson, M., Routy, B., Miller, W.H., and Calabrese, L. (2020). Moving towards personalized treatments of immune-related adverse events. Nature Reviews Clinical Oncology 1–12.

Estrada, J., Wong, F., DePace, A., and Gunawardena, J. (2016). Information Integration and Energy Expenditure in Gene Regulation. Cell *166*, 234–244.

Farh, K.K.-H., Marson, A., Zhu, J., Kleinewietfeld, M., Housley, W.J., Beik, S., Shoresh, N., Whitton, H., Ryan, R.J.H., Shishkin, A.A., et al. (2015). Genetic and epigenetic fine mapping of causal autoimmune disease variants. Nature *518*, 337–343.

Feinerman, O., Veiga, J., Dorfman, J.R., Germain, R.N., and Altan-Bonnet, G. (2008). Variability and Robustness in T Cell Activation from Regulated Heterogeneity in Protein Levels. Science *321*, 1081–1084.

Feinerman, O., Jentsch, G., Tkach, K.E., Coward, J.W., Hathorn, M.M., Sneddon, M.W., Emonet, T., Smith, K.A., and Altan-Bonnet, G. (2010). Single-cell quantification of IL-2 response by effector and regulatory T cells reveals critical plasticity in immune response. Molecular Systems Biology *6*, 437.

Ferguson, H.A., Kugel, J.F., and Goodrich, J.A. (2001). Kinetic and mechanistic analysis of the RNA polymerase II transcription reaction at the human interleukin-2 promoter. Journal of Molecular Biology *314*, 993–1006.

Filipczyk, A., Marr, C., Hastreiter, S., Feigelman, J., Schwarzfischer, M., Hoppe, P.S., Loeffler, D., Kokkaliaris, K.D., Endele, M., Schauberger, B., et al. (2015).

Network plasticity of pluripotency transcription factors in embryonic stem cells. Nature Cell Biology *17*, 1235–1246.

Filtz, T.M., Vogel, W.K., and Leid, M. (2014). Regulation of transcription factor activity by interconnected, post-translational modifications. Trends Pharmacol Sci *35*, 76–85.

Flajnik, M.F., and Kasahara, M. (2010). Origin and evolution of the adaptive immune system: genetic events and selective pressures. Nature Reviews Genetics *11*, 47–59.

Forger, D.B., and Peskin, C.S. (2005). Stochastic simulation of the mammalian circadian clock. Proceedings of the National Academy of Sciences *102*, 321–324.

François, P., Voisinne, G., Siggia, E.D., Altan-Bonnet, G., and Vergassola, M. (2013). Phenotypic model for early T-cell activation displaying sensitivity, specificity, and antagonism. PNAS *110*, E888–E897.

Fricke, G.M., Letendre, K.A., Moses, M.E., and Cannon, J.L. (2016). Persistence and Adaptation in Immunity: T Cells Balance the Extent and Thoroughness of Search. PLOS Computational Biology *12*, e1004818.

Fugmann, T., Sofron, A., Ritz, D., Bootz, F., and Neri, D. (2017). The MHC Class II Immunopeptidome of Lymph Nodes in Health and in Chemically Induced Colitis. The Journal of Immunology *198*, 1357–1364.

Fuhrmann, F., Lischke, T., Gross, F., Scheel, T., Bauer, L., Kalim, K.W., Radbruch, A., Herzel, H., Hutloff, A., and Baumgrass, R. (2016). Adequate immune response ensured by binary IL-2 and graded CD25 expression in a murine transfer model. ELife *5*.

Germain, R.N. (2001). The Art of the Probable: System Control in the Adaptive Immune System. Science *293*, 240–245.

Germain, R.N. (2012). Maintaining system homeostasis: the third law of Newtonian immunology. Nat Immunol *13*, 902–906.

Germain, R.N. (2018). Will Systems Biology Deliver Its Promise and Contribute to the Development of New or Improved Vaccines? What Really Constitutes the Study of “Systems Biology” and How Might Such an Approach Facilitate Vaccine Design. Cold Spring Harb Perspect Biol *10*, a033308.

Germain, R.N., Meier-Schellersheim, M., Nita-Lazar, A., and Fraser, I.D.C. (2011). Systems Biology in Immunology: A Computational Modeling Perspective. Annual Review of Immunology *29*, 527–585.

Gillespie, D.T. (2000). The chemical Langevin equation. The Journal of Chemical Physics *113*, 297–306.

Gillespie, D.T. (2007). Stochastic Simulation of Chemical Kinetics. Annual Review of Physical Chemistry *58*, 35–55.

Ginot, F., Theurkauff, I., Detcheverry, F., Ybert, C., and Cottin-Bizonne, C. (2018). Aggregation-fragmentation and individual dynamics of active clusters. Nature Communications *9*, 696.

Goentoro, L., Shoval, O., Kirschner, M., and Alon, U. (2009). The incoherent feedforward loop can provide fold-change detection in gene regulation. Mol Cell *36*, 894–899.

Gonze, D., and Abou-Jaoudé, W. (2013). The Goodwin Model: Behind the Hill Function. PLOS ONE *8*, e69573.

Grima, R., Thomas, P., and Straube, A.V. (2011). How accurate are the non-linear chemical Fokker-Planck and chemical Langevin equations? The Journal of Chemical Physics *135*, 084103.

Guisoni, N., Monteoliva, D., and Diambra, L. (2016). Promoters Architecture-Based Mechanism for Noise-Induced Oscillations in a Single-Gene Circuit. PLOS ONE *11*, e0151086.

Gunawardena, J. (2014). Models in biology: ‘accurate descriptions of our pathetic thinking.’ BMC Biology *12*, 29.

Gutenkunst, R.N., Waterfall, J.J., Casey, F.P., Brown, K.S., Myers, C.R., and Sethna, J.P. (2007). Universally Sloppy Parameter Sensitivities in Systems Biology Models. PLOS Computational Biology *3*, e189.

Hassler, T., Urmann, E., Teschner, S., Federle, C., Dileepan, T., Schober, K., Jenkins, M.K., Busch, D.H., Hinterberger, M., and Klein, L. (2019). Inventories of naive and tolerant mouse CD4 T cell repertoires reveal a hierarchy of deleted and diverted T cell receptors. Proc Natl Acad Sci USA *116*, 18537–18543.

Hayes, A.J., Rane, S., Scales, H.E., Meehan, G.R., Benson, R.A., Maroof, A., Schroeder, J., Tomura, M., Gozzard, N., Yates, A.J., et al. (2019). Spatiotemporal Modeling of the Key Migratory Events During the Initiation of Adaptive Immunity. Front. Immunol. *10*.

Heijst, J.W.J. van, Gerlach, C., Swart, E., Sie, D., Nunes-Alves, C., Kerkhoven, R.M., Arens, R., Correia-Neves, M., Schepers, K., and Schumacher, T.N.M. (2009). Recruitment of Antigen-Specific CD8+ T Cells in Response to Infection Is Markedly Efficient. Science *325*, 1265–1269.

Heinzel, S., Giang, T.B., Kan, A., Marchingo, J.M., Lye, B.K., Corcoran, L.M., and Hodgkin, P.D. (2017). A Myc-dependent division timer complements a cell-death timer to regulate T cell and B cell responses. Nature Immunology *18*, 96–103.

Hemmers, S., Schizas, M., Azizi, E., Dikiy, S., Zhong, Y., Feng, Y., Altan-Bonnet, G., and Rudensky, A.Y. (2019). IL-2 production by self-reactive CD4 thymocytes scales regulatory T cell generation in the thymus. J Exp Med *216*, 2466–2478.

Höfer, T., Krichevsky, O., and Altan-Bonnet, G. (2012). Competition for IL-2 between Regulatory and Effector T Cells to Chisel Immune Responses. Front. Immunol. *3*.

Holehouse, J., and Grima, R. (2019). Revisiting the Reduction of Stochastic Models of Genetic Feedback Loops with Fast Promoter Switching. Biophysical Journal *117*, 1311–1330.

Homma, T., and Saltelli, A. (1996). Importance measures in global sensitivity analysis of nonlinear models. Reliability Engineering & System Safety *52*, 1–17.

Hopfield, J.J. (1974). Kinetic Proofreading: A New Mechanism for Reducing Errors in Biosynthetic Processes Requiring High Specificity. PNAS *71*, 4135–4139.

Huang, J., Brameshuber, M., Zeng, X., Xie, J., Li, Q., Chien, Y., Valitutti, S., and Davis, M.M. (2013). A Single Peptide-Major Histocompatibility Complex Ligand Triggers Digital Cytokine Secretion in CD4+ T Cells. Immunity *39*, 846–857.

Jagiella, N., Rickert, D., Theis, F.J., and Hasenauer, J. (2017). Parallelization and High-Performance Computing Enables Automated Statistical Inference of Multi-scale Models. Cels *4*, 194-206.e9.

Jansson, A., and Davis, S.J. (2011). Quantitative analysis predicts the relative therapeutic efficacy of different forms of CTLA4Ig. Molecular Immunology *49*, 527–536.

Jansson, A., Barnes, E., Klenerman, P., Harlén, M., Sørensen, P., Davis, S.J., and Nilsson, P. (2005). A Theoretical Framework for Quantitative Analysis of the Molecular Basis of Costimulation. The Journal of Immunology *175*, 1575–1585.

Jenkins, M.K., and Moon, J.J. (2012). The Role of Naive T Cell Precursor Frequency and Recruitment in Dictating Immune Response Magnitude. The Journal of Immunology *188*, 4135–4140.

Jovanovic, M., Rooney, M.S., Mertins, P., Przybylski, D., Chevrier, N., Satija, R., Rodriguez, E.H., Fields, A.P., Schwartz, S., Raychowdhury, R., et al. (2015). Dynamic profiling of the protein life cycle in response to pathogens. Science *347*, 1259038–1259038.

Kampen, N.G.V. (2007). Stochastic Processes in Physics and Chemistry, Third Edition (Amsterdam ; Boston: North Holland).

Kazeroonian, A., Fröhlich, F., Raue, A., Theis, F.J., and Hasenauer, J. (2016). CERENA: ChEmical REaction Network Analyzer—A Toolbox for the Simulation and Analysis of Stochastic Chemical Kinetics. PLOS ONE *11*, e0146732.

Khailaie, S., Rowshanravan, B., Robert, P.A., Walker, L.S.K., Sansom, D.M., and Meyer-Hermann, M. (2017). Quantitative characterization of CTLA4 trafficking and turnover using a combined in vitro and in silico approach. BioRxiv 106898.

Khailaie, S., Rowshanravan, B., Robert, P.A., Waters, E., Halliday, N., Badillo Herrera, J.D., Walker, L.S.K., Sansom, D.M., and Meyer-Hermann, M. (2018). Characterization of CTLA4 Trafficking and Implications for Its Function. Biophysical Journal *115*, 1330–1343.

Killebrew, J.R., Perdue, N., Kwan, A., Thornton, A.M., Shevach, E.M., and Campbell, D.J. (2011). A Self-Reactive TCR Drives the Development of Foxp3 $^+$ Regulatory T Cells That Prevent Autoimmune Disease. J.I. *187*, 861–869.

Kim, J.M., Rasmussen, J.P., and Rudensky, A.Y. (2007). Regulatory T cells prevent catastrophic autoimmunity throughout the lifespan of mice. Nat Immunol *8*, 191–197.

Klein, L., Robey, E.A., and Hsieh, C.-S. (2019). Central CD4 + T cell tolerance: deletion versus regulatory T cell differentiation. Nat Rev Immunol *19*, 7–18.

Koeppl, H., Hafner, M., and Lu, J. (2013). Mapping behavioral specifications to model parameters in synthetic biology. BMC Bioinformatics *14*, S9.

Kohanim, Y.K., Tendler, A., Mayo, A., Friedman, N., and Alon, U. (2019). Endocrine autoimmune disease as a fragility of immune-surveillance against hypersecreting mutants. BioRxiv 845750.

Košmrlj, A., Chakraborty, A.K., Kardar, M., and Shakhnovich, E.I. (2009). Thymic Selection of T-Cell Receptors as an Extreme Value Problem. Phys. Rev. Lett. *103*, 068103.

Krovi, S.H., Kappler, J.W., Marrack, P., and Gapin, L. (2019). Inherent reactivity of unselected TCR repertoires to peptide-MHC molecules. Proc Natl Acad Sci USA *116*, 22252–22261.

Krueger, A., Ziętara, N., and Łyszkiewicz, M. (2017). T Cell Development by the Numbers. Trends in Immunology *38*, 128–139.

Krummel, M.F., Bartumeus, F., and Gérard, A. (2016). T cell migration, search strategies and mechanisms. Nat Rev Immunol *16*, 193–201.

Kuehn, H.S., Ouyang, W., Lo, B., Deenick, E.K., Niemela, J.E., Avery, D.T., Schickel, J.-N., Tran, D.Q., Stoddard, J., Zhang, Y., et al. (2014). Immune dysregulation in human subjects with heterozygous germline mutations in CTLA4. Science *345*, 1623–1627.

Kuznetsov, Y. (2004). Elements of Applied Bifurcation Theory (New York: Springer).

Kwiatkowski, D., Phillips, P., Schmidt, P., and Shin, Y. (1992). Testing the null hypothesis of stationarity against the alternative of a unit root: How sure are we that economic time series have a unit root? Journal of Econometrics *54*, 159–178.

Larsen, C.P., Pearson, T.C., Adams, A.B., Tso, P., Shirasugi, N., Strobert, E., Anderson, D., Cowan, S., Price, K., Naemura, J., et al. (2005). Rational development of LEA29Y (belatacept), a high-affinity variant of CTLA4-Ig with potent immunosuppressive properties. Am. J. Transplant. *5*, 443–453.

Lathrop, S.K., Santacruz, N.A., Pham, D., Luo, J., and Hsieh, C.-S. (2008). Antigen-specific peripheral shaping of the natural regulatory T cell population. J Exp Med *205*, 3105–3117.

Le Borgne, M., Ladi, E., Dzhagalov, I., Herzmark, P., Liao, Y.F., Chakraborty, A.K., and Robey, E.A. (2009). The impact of negative selection on thymocyte migration in the medulla. Nature Immunology *10*, 823–830.

Lee, M., Mandl, J.N., Germain, R.N., and Yates, A.J. (2012). The race for the prize: T-cell trafficking strategies for optimal surveillance. Blood *120*, 1432–1438.

Legoux, F.P., Lim, J.-B., Cauley, A.W., Dikiy, S., Ertelt, J., Mariani, T.J., Sparwasser, T., Way, S.S., and Moon, J.J. (2015). CD4+ T Cell Tolerance to Tissue-Restricted Self Antigens Is Mediated by Antigen-Specific Regulatory T Cells Rather Than Deletion. Immunity *43*, 896–908.

Leszczyński, H., and Bartłomiejczyk, A. (2015). Structured populations with diffusion and Feller conditions. Mathematical Biosciences and Engineering *13*.

Li, F., Long, T., Lu, Y., Ouyang, Q., and Tang, C. (2004). The yeast cell-cycle network is robustly designed. PNAS *101*, 4781–4786.

Li, G.-W., Burkhardt, D., Gross, C., and Weissman, J.S. (2014). Quantifying Absolute Protein Synthesis Rates Reveals Principles Underlying Allocation of Cellular Resources. Cell *157*, 624–635.

Li, H., Hou, Z., and Xin, H. (2005). Internal noise stochastic resonance for intracellular calcium oscillations in a cell system. Physical Review E *71*.

Liaw, A., and Wiener, M. (2002). Classification and regression by randomForest. R News *2*, 18–22.

Lim, H.-S., Cordoba, S.-P., Dushek, O., Goyette, J., Taylor, A., Rudd, C.E., and Merwe, P.A. van der (2015). Costimulation of IL-2 Production through CD28 Is Dependent on the Size of Its Ligand. The Journal of Immunology *195*, 5432–5439.

Lim, W.A., Lee, C.M., and Tang, C. (2013). Design Principles of Regulatory Networks: Searching for the Molecular Algorithms of the Cell. Mol Cell *49*, 202–212.

Liu, Z., Gerner, M.Y., Panhuys, N.V., Levine, A.G., Rudensky, A.Y., and Germain, R.N. (2015). Immune homeostasis enforced by co-localized effector and regulatory T cells. Nature *528*, 225–230.

Loyola R, D.G., Pedergnana, M., and Gimeno García, S. (2016). Smart sampling and incremental function learning for very large high dimensional data. Neural Networks *78*, 75–87.

Lythe, G., Callard, R.E., Hoare, R.L., and Molina-París, C. (2016). How many TCR clonotypes does a body maintain? Journal of Theoretical Biology *389*, 214–224.

Malhotra, D., Linehan, J.L., Dileepan, T., Lee, Y.J., Purtha, W.E., Lu, J.V., Nelson, R.W., Fife, B.T., Orr, H.T., Anderson, M.S., et al. (2016). Tolerance is established in polyclonal CD4 + T cells by distinct mechanisms, according to self-peptide expression patterns. Nature Immunology *17*, 187–195.

Mandl, J.N., Liou, R., Klauschen, F., Vrisekoop, N., Monteiro, J.P., Yates, A.J., Huang, A.Y., and Germain, R.N. (2012). Quantification of lymph node transit times reveals differences in antigen surveillance strategies of naïve CD4+ and CD8+ T cells. PNAS *109*, 18036–18041.

Mandl, J.N., Monteiro, J.P., Vrisekoop, N., and Germain, R.N. (2013). T Cell-Positive Selection Uses Self-Ligand Binding Strength to Optimize Repertoire Recognition of Foreign Antigens. Immunity *38*, 263–274.

Mangan, S., and Alon, U. (2003). Structure and function of the feed-forward loop network motif. PNAS *100*, 11980–11985.

Marchingo, J.M., Kan, A., Sutherland, R.M., Duffy, K.R., Wellard, C.J., Belz, G.T., Lew, A.M., Dowling, M.R., Heinzel, S., and Hodgkin, P.D. (2014). Antigen affinity, costimulation, and cytokine inputs sum linearly to amplify T cell expansion. Science *346*, 1123–1127.

Mariani, L., Schulz, E.G., Lexberg, M.H., Helmstetter, C., Radbruch, A., Löhning, M., and Höfer, T. (2010). Short-term memory in gene induction reveals the regulatory principle behind stochastic IL-4 expression. Molecular Systems Biology *6*.

Martins, A.J., Narayanan, M., Prüstel, T., Fixsen, B., Park, K., Gottschalk, R.A., Lu, Y., Andrews-Pfannkoch, C., Lau, W.W., Wendelsdorf, K.V., et al. (2017). Environment Tunes Propagation of Cell-to-Cell Variation in the Human Macrophage Gene Network. Cels *4*, 379-392.e12.

Matheu, M.P., Othy, S., Greenberg, M.L., Dong, T.X., Schuijs, M., Deswarte, K., Hammad, H., Lambrecht, B.N., Parker, I., and Cahalan, M.D. (2015). Imaging regulatory T cell dynamics and CTLA4-mediated suppression of T cell priming. Nature Communications *6*, 6219.

McInnes, L., Healy, J., and Melville, J. (2018). UMAP: Uniform Manifold Approximation and Projection for Dimension Reduction. ArXiv:1802.03426 [Cs, Stat].

McKane, A.J., Nagy, J.D., Newman, T.J., and Stefanini, M.O. (2007). Amplified Biochemical Oscillations in Cellular Systems. Journal of Statistical Physics *128*, 165–191.

Mckay, M.D., Beckman, R.J., and Conover, W.J. (2000). A Comparison of Three Methods for Selecting Values of Input Variables in the Analysis of Output from a Computer Code. Technometrics *42*, 55.

Meier-Schellersheim, M., Varma, R., and Angermann, B.R. (2019). Mechanistic Models of Cellular Signaling, Cytokine Crosstalk, and Cell-Cell Communication in Immunology. Front. Immunol. *10*, 2268.

Menares, E., Gálvez-Cancino, F., Cáceres-Morgado, P., Ghorani, E., López, E., Díaz, X., Saavedra-Almarza, J., Figueroa, D.A., Roa, E., Quezada, S.A., et al. (2019). Tissue-resident memory CD8 + T cells amplify anti-tumor immunity by triggering antigen spreading through dendritic cells. Nature Communications *10*, 4401.

Meredith, M., Zemmour, D., Mathis, D., and Benoist, C. (2015). Aire controls gene expression in the thymic epithelium with ordered stochasticity. Nature Immunology *16*, 942–949.

van der Merwe, P.A., Bodian, D.L., Daenke, S., Linsley, P., and Davis, S.J. (1997). CD80 (B7-1) Binds Both CD28 and CTLA-4 with a Low Affinity and Very Fast Kinetics. J Exp Med *185*, 393–404.

Milanez-Almeida, P., Meyer-Hermann, M., Toker, A., Khailaie, S., and Huehn, J. (2015). Foxp3 $^{+}$ regulatory T-cell homeostasis quantitatively differs in murine peripheral lymph nodes and spleen: Immunomodulation. Eur. J. Immunol. *45*, 153–166.

Milanez-Almeida, P., Meyer-Hermann, M., Toker, A., Khailaie, S., and Huehn, J. (2015). Foxp3+ regulatory T-cell homeostasis quantitatively differs in murine peripheral lymph nodes and spleen. European Journal of Immunology *45*, 153–166.

Miller, M.J., Hejazi, A.S., Wei, S.H., Cahalan, M.D., and Parker, I. (2004). T cell repertoire scanning is promoted by dynamic dendritic cell behavior and random T cell motility in the lymph node. PNAS *101*, 998–1003.

Milo, R., and Phillips, R. (2015). Cell Biology by the Numbers (New York, NY: Garland Science).

Milo, R., Shen-Orr, S., Itzkovitz, S., Kashtan, N., Chklovskii, D., and Alon, U. (2002). Network Motifs: Simple Building Blocks of Complex Networks. *298,* 5.

Mohammadi, P., Beerenwinkel, N., and Benenson, Y. (2017). Automated Design of Synthetic Cell Classifier Circuits Using a Two-Step Optimization Strategy. Cell Systems *4*, 207-218.e14.

Moon, J.J., Dash, P., Oguin, T.H., McClaren, J.L., Chu, H.H., Thomas, P.G., and Jenkins, M.K. (2011). Quantitative impact of thymic selection on Foxp3+ and Foxp3− subsets of self-peptide/MHC class II-specific CD4+ T cells. PNAS *108*, 14602–14607.

Murphy, K.M., and Weaver, C. (2016). Janeway's Immunobiology (New York, NY: W. W. Norton & Company).

Myers, D.R., Zikherman, J., and Roose, J.P. (2017). Tonic Signals: Why Do Lymphocytes Bother? Trends in Immunology *38*, 844–857.

Neph, S., Stergachis, A.B., Reynolds, A., Sandstrom, R., Borenstein, E., and Stamatoyannopoulos, J.A. (2012). Circuitry and Dynamics of Human Transcription Factor Regulatory Networks. Cell *150*, 1274–1286.

O'Gorman, W.E., Dooms, H., Thorne, S.H., Kuswanto, W.F., Simonds, E.F., Krutzik, P.O., Nolan, G.P., and Abbas, A.K. (2009). The Initial Phase of an Immune Response Functions to Activate Regulatory T Cells. The Journal of Immunology *183*, 332–339.

Owen, D.L., Mahmud, S.A., Vang, K.B., Kelly, R.M., Blazar, B.R., Smith, K.A., and Farrar, M.A. (2018). Identification of Cellular Sources of IL-2 Needed for Regulatory T Cell Development and Homeostasis. J.I. *200*, 3926–3933.

Oyler-Yaniv, A., Oyler-Yaniv, J., Whitlock, B.M., Liu, Z., Germain, R.N., Huse, M., Altan-Bonnet, G., and Krichevsky, O. (2017). A Tunable Diffusion-Consumption Mechanism of Cytokine Propagation Enables Plasticity in Cell-to-Cell Communication in the Immune System. Immunity *46*, 609–620.

Park, K., Prüstel, T., Lu, Y., and Tsang, J.S. (2019). Machine learning of stochastic gene network phenotypes. BioRxiv 825943.

Pathria, R.K., and Beale, P.D. (2011). Statistical Mechanics (Academic Press).

Paulsson, J. (2004). Summing up the noise in gene networks. Nature *427*, 415–418.

Peccoud, J., and Ycart, B. (1995). Markovian Modeling of Gene-Product Synthesis. Theoretical Population Biology *48*, 222–234.

Percival, D.B., and Walden, A.T. (1993). Spectral Analysis for Physical Applications (Cambridge University Press).

Peters, E.A.J.F., and Barenbrug, Th.M.A.O.M. (2002). Efficient Brownian dynamics simulation of particles near walls. II. Sticky walls. Physical Review E *66*.

Pett, J.P., Kondoff, M., Bordyugov, G., Kramer, A., and Herzel, H. (2018). Co-existing feedback loops generate tissue-specific circadian rhythms. Life Science Alliance *1*, e201800078.

Purves, D., Augustine, G.J., Fitzpatrick, D., Hall, W.C., LaMantia, A., Mooney, R.D., Platt, M.L., White,L.E. (2017). Neuroscience (New York: Sinauer Associates is an imprint of Oxford University Press).

Quigley, M.F., Greenaway, H.Y., Venturi, V., Lindsay, R., Quinn, K.M., Seder, R.A., Douek, D.C., Davenport, M.P., and Price, D.A. (2010). Convergent recombination shapes the clonotypic landscape of the naive T-cell repertoire. Proceedings of the National Academy of Sciences *107*, 19414–19419.

Qureshi, O.S., Zheng, Y., Nakamura, K., Attridge, K., Manzotti, C., Schmidt, E.M., Baker, J., Jeffery, L.E., Kaur, S., Briggs, Z., et al. (2011). Trans-Endocytosis of CD80 and CD86: A Molecular Basis for the Cell-Extrinsic Function of CTLA-4. Science *332*, 600–603.

Rabani, M., Levin, J.Z., Fan, L., Adiconis, X., Raychowdhury, R., Garber, M., Gnirke, A., Nusbaum, C., Hacohen, N., Friedman, N., et al. (2011). Metabolic labeling of RNA uncovers principles of RNA production and degradation dynamics in mammalian cells. Nature Biotechnology *29*, 436–442.

Raj, A., and van Oudenaarden, A. (2008). Stochastic gene expression and its consequences. Cell *135*, 216–226.

Raj, A., Peskin, C.S., Tranchina, D., Vargas, D.Y., and Tyagi, S. (2006). Stochastic mRNA Synthesis in Mammalian Cells. PLoS Biology *4*, e309.

Rapp, M., Wintergerst, M.W.M., Kunz, W.G., Vetter, V.K., Knott, M.M.L., Lisowski, D., Haubner, S., Moder, S., Thaler, R., Eiber, S., et al. (2019). CCL22 controls immunity by promoting regulatory T cell communication with dendritic cells in lymph nodes. Journal of Experimental Medicine jem.20170277.

Raynal, L., Marin, J.-M., Pudlo, P., Ribatet, M., Robert, C.P., and Estoup, A. (2017). ABC random forests for Bayesian parameter inference. PCI Evol Biol 100036.

Redmond, A.K., Macqueen, D.J., and Dooley, H. (2018). Phylotranscriptomics suggests the jawed vertebrate ancestor could generate diverse helper and regulatory T cell subsets. BMC Evolutionary Biology *18*, 169.

Richards, D.M., Ruggiero, E., Hofer, A.-C., Sefrin, J.P., Schmidt, M., Kalle, C. von, and Feuerer, M. (2015). The Contained Self-Reactive Peripheral T Cell Repertoire: Size, Diversity, and Cellular Composition. The Journal of Immunology *195*, 2067–2079.

Richardson, L.F. (1946). The Probability of Encounters between Gas Molecules. Proceedings of the Royal Society of London. Series A, Mathematical and Physical Sciences *186*, 422–431.

Rodriguez, J., Ren, G., Day, C.R., Zhao, K., Chow, C.C., and Larson, D.R. (2019). Intrinsic Dynamics of a Human Gene Reveal the Basis of Expression Heterogeneity. Cell *176*, 213-226.e18.

Rosenblum, M.D., Remedios, K.A., and Abbas, A.K. (2015). Mechanisms of human autoimmunity. J. Clin. Invest. *125*, 2228–2233.

Rosenzwajg, M., Lorenzon, R., Cacoub, P., Pham, H.P., Pitoiset, F., Soufi, K.E., RIbet, C., Bernard, C., Aractingi, S., Banneville, B., et al. (2019). Immunological and clinical effects of low-dose interleukin-2 across 11 autoimmune diseases in a single, open clinical trial. Annals of the Rheumatic Diseases *78*, 209–217.

Ross, A.E., and Pompano, R.R. (2018). Diffusion of cytokines in live lymph node tissue using microfluidic integrated optical imaging. Analytica Chimica Acta *1000*, 205–213.

Sabatos, C.A., Doh, J., Chakravarti, S., Friedman, R.S., Pandurangi, P.G., Tooley, A.J., and Krummel, M.F. (2008). A Synaptic Basis for Paracrine Interleukin-2 Signaling during Homotypic T Cell Interaction. Immunity *29*, 238–248.

Saltelli, A., Ratto, M., Andres, T., null, Cariboni, J., Gatelli, D., Saisana, M., and Tarantola, S. (2008). Global Sensitivity Analysis: The Primer (John Wiley & Sons).

Saltelli, A., Ratto, M., Tarantola, S., and Campolongo, F. (2012). Update 1 of: Sensitivity Analysis for Chemical Models. Chem. Rev. *112*, PR1–PR21.

Sawicka, M., Stritesky, G., Reynolds, J., Abourashchi, N., Lythe, G., Molina-Paris, C., and Hogquist, K. (2014). From pre-DP, post-DP, SP4, and SP8 Thymocyte Cell Counts to a Dynamical Model of Cortical and Medullary Selection. Front. Immunol. *5*.

Schnoerr, D., Sanguinetti, G., and Grima, R. (2017). Approximation and inference methods for stochastic biochemical kinetics—a tutorial review. J. Phys. A: Math. Theor. *50*, 093001.

Schubert, D., Bode, C., Kenefeck, R., Hou, T.Z., Wing, J.B., Kennedy, A., Bulashevska, A., Petersen, B.-S., Schäffer, A.A., Grüning, B.A., et al. (2014). Autosomal dominant immune dysregulation syndrome in humans with CTLA4 mutations. Nat. Med. *20*, 1410–1416.

Schwanhäusser, B., Busse, D., Li, N., Dittmar, G., Schuchhardt, J., Wolf, J., Chen, W., and Selbach, M. (2011). Global quantification of mammalian gene expression control. Nature *473*, 337–342.

Setoguchi, R., Hori, S., Takahashi, T., and Sakaguchi, S. (2005). Homeostatic maintenance of natural Foxp3+ CD25+ CD4+ regulatory T cells by interleukin (IL)-2 and induction of autoimmune disease by IL-2 neutralization. J Exp Med *201*, 723–735.

Shim, J., Lim, H., R.Yates, J., and Karin, M. (2002). Nuclear Export of NF90 Is Required for Interleukin-2 mRNA Stabilization. Molecular Cell *10*, 1331–1344.

Shoval, O., Sheftel, H., Shinar, G., Hart, Y., Ramote, O., Mayo, A., Dekel, E., Kavanagh, K., and Alon, U. (2012). Evolutionary Trade-Offs, Pareto Optimality, and the Geometry of Phenotype Space. Science *336*, 1157–1160.

Shvartsman, S.Y., Wiley, H.S., Deen, W.M., and Lauffenburger, D.A. (2001). Spatial Range of Autocrine Signaling: Modeling and Computational Analysis. Biophysical Journal *81*, 1854–1867.

Smigiel, K.S., Richards, E., Srivastava, S., Thomas, K.R., Dudda, J.C., Klonowski, K.D., and Campbell, D.J. (2014). CCR7 provides localized access to IL-2 and defines homeostatically distinct regulatory T cell subsets. Journal of Experimental Medicine *211*, 121–136.

Sobol', I.M. (1967). On the distribution of points in a cube and the approximate evaluation of integrals. USSR Computational Mathematics and Mathematical Physics *7*, 86–112.

Soderberg, K.A., Payne, G.W., Sato, A., Medzhitov, R., Segal, S.S., and Iwasaki, A. (2005). Innate control of adaptive immunity via remodeling of lymph node feed arteriole. PNAS *102*, 16315–16320.

Stoeger, T., Battich, N., and Pelkmans, L. (2016). Passive Noise Filtering by Cellular Compartmentalization. Cell *164*, 1151–1161.

Stolley, J.M., and Campbell, D.J. (2016). A 33D1 $^{+}$ Dendritic Cell/Autoreactive CD4 $^{+}$ T Cell Circuit Maintains IL-2–Dependent Regulatory T Cells in the Spleen. J.I. *197*, 2635–2645.

Strogatz, S.H. (2015). Nonlinear Dynamics and Chaos: With Applications to Physics, Biology, Chemistry, and Engineering, Second Edition (Boulder, CO: Westview Press).

Sugár, I.P., Das, J., Jayaprakash, C., and Sealfon, S.C. (2017). Multiscale Modeling of Complex Formation and CD80 Depletion during Immune Synapse Development. Biophysical Journal *112*, 997–1009.

Suter, D.M., Molina, N., Gatfield, D., Schneider, K., Schibler, U., and Naef, F. (2011). Mammalian genes are transcribed with widely different bursting kinetics. Science *332*, 472–474.

Tanay, A., and Regev, A. (2017). Scaling single-cell genomics from phenomenology to mechanism. Nature *541*, 331–338.

Textor, J., Henrickson, S.E., Mandl, J.N., Andrian, U.H. von, Westermann, J., Boer, R.J. de, and Beltman, J.B. (2014). Random Migration and Signal Integration Promote Rapid and Robust T Cell Recruitment. PLOS Computational Biology *10*, e1003752.

Thauland, T.J., Koguchi, Y., Dustin, M.L., and Parker, D.C. (2014). CD28–CD80 Interactions Control Regulatory T Cell Motility and Immunological Synapse Formation. The Journal of Immunology *193*, 5894–5903.

Theofilopoulos, A.N., Kono, D.H., and Baccala, R. (2017). The multiple pathways to autoimmunity. Nature Immunology *18*, 716–724.

Thomas, P., Popovi, N., and Grima, R. (2014). Phenotypic switching in gene regulatory networks. Proceedings of the National Academy of Sciences *111*, 6994–6999.

Thurley, K., Gerecht, D., Friedmann, E., and Höfer, T. (2015). Three-Dimensional Gradients of Cytokine Signaling between T Cells. PLOS Computational Biology *11*, e1004206.

Tkach, K.E., Barik, D., Voisinne, G., Malandro, N., Hathorn, M.M., Cotari, J.W., Vogel, R., Merghoub, T., Wolchok, J., Krichevsky, O., et al. (2014). T cells translate individual, quantal activation into collective, analog cytokine responses via time-integrated feedbacks. ELife Sciences *3*, e01944.

Tong, A.A., Forestell, B., Murphy, D.V., Nair, A., Allen, F., Myers, J., Klauschen, F., Shen, C., Gopal, A.A., Huang, A.Y., et al. (2019). Regulatory T cells differ from conventional CD4+ T cells in their recirculatory behavior and lymph node transit times. Immunology & Cell Biology *97*, 787–798.

Trinh, V.A., and Hagen, B. (2013). Ipilimumab for advanced melanoma: A pharmacologic perspective. J Oncol Pharm Pract *19*, 195–201.

Turner, S.J., Doherty, P.C., McCluskey, J., and Rossjohn, J. (2006). Structural determinants of T-cell receptor bias in immunity. Nat Rev Immunol *6*, 883–894.

Venturi, V., Price, D.A., Douek, D.C., and Davenport, M.P. (2008). The molecular basis for public T-cell responses? Nature Reviews Immunology *8*, 231–238.

Villa-Vialaneix, N., Follador, M., Ratto, M., and Leip, A. (2012). A comparison of eight metamodeling techniques for the simulation of N2O fluxes and N leaching from corn crops. Environmental Modelling & Software *34*, 51–66.

Voisinne, G., Nixon, B.G., Melbinger, A., Gasteiger, G., Vergassola, M., and Altan-Bonnet, G. (2015). T Cells Integrate Local and Global Cues to Discriminate between Structurally Similar Antigens. Cell Reports *11*, 1208–1219.

Vukmanovic-Stejic, M., Zhang, Y., Cook, J.E., Fletcher, J.M., McQuaid, A., Masters, J.E., Rustin, M.H.A., Taams, L.S., Beverley, P.C.L., Macallan, D.C., et al. (2006). Human CD4$^+$ CD25^{hi} Foxp3$^+$ regulatory T cells are derived by rapid turnover of memory populations in vivo. J Clin Invest *116*, 2423–2433.

Wadhams, G.H., and Armitage, J.P. (2004). Making sense of it all: bacterial chemotaxis. Nat Rev Mol Cell Biol *5*, 1024–1037.

Wan, X., Vomund, A.N., Peterson, O.J., Chervonsky, A.V., Lichti, C.F., and Unanue, E.R. (2020). The MHC-II peptidome of pancreatic islets identifies key features of autoimmune peptides. Nature Immunology *21*, 455–463.

Wang, H.M., and Smith, K.A. (1987). The interleukin 2 receptor. Functional consequences of its bimolecular structure. Journal of Experimental Medicine *166*, 1055–1069.

Waysbort, N., Russ, D., Chain, B.M., and Friedman, N. (2013). Coupled IL-2–Dependent Extracellular Feedbacks Govern Two Distinct Consecutive Phases of CD4 T Cell Activation. J.I. *191*, 5822–5830.

Webre, D.J., Wolanin, P.M., and Stock, J.B. (2003). Bacterial chemotaxis. Current Biology *13*, R47–R49.

Weidemann, T., Worch, R., Kurgonaite, K., Hintersteiner, M., Bökel, C., and Schwille, P. (2011). Single Cell Analysis of Ligand Binding and Complex Formation of Interleukin-4 Receptor Subunits. Biophysical Journal *101*, 2360–2369.

Weiss, J.N. (1997). The Hill equation revisited: uses and misuses. The FASEB Journal *11*, 835–841.

Wheeler, K.M., Samy, E.T., and Tung, K.S.K. (2009). Cutting Edge: Normal Regional Lymph Node Enrichment of Antigen-Specific Regulatory T Cells with Autoimmune Disease-Suppressive Capacity. The Journal of Immunology *183*, 7635–7638.

White, J.A., Rubinstein, J.T., and Kay, A.R. (2000). Channel noise in neurons. Trends in Neurosciences *23*, 131–137.

Woller, A., Gonze, D., and Erneux, T. (2014). The Goodwin model revisited: Hopf bifurcation, limit-cycle, and periodic entrainment. Physical Biology *11*, 045002.

Wong, H.S., and Germain, R.N. (2018). Robust control of the adaptive immune system. Seminars in Immunology *36*, 17–27.

Wong, H.S., Park, K., Gola, A., Baptista, A.P., Miller, C.H., Deep, D., Lou, M., Boyd, L.F., Rudensky, A.Y., Savage, P.A., Altan-Bonnet, G., et al. A local regulatory T cell-mediated feedback process maintains immunological homeostasis by pruning self-activated T cells. Submitted to Cell.

Wu, P.-H., Giri, A., and Wirtz, D. (2015). Statistical analysis of cell migration in 3D using the anisotropic persistent random walk model. Nat Protoc *10*, 517–527.

Yates, A.J. (2014). Theories and Quantification of Thymic Selection. Front Immunol *5*.

Yi, J., Jung, J., Hong, S.-W., Lee, J.Y., Han, D., Kim, K.S., Sprent, J., and Surh, C.D. (2018). Unregulated antigen-presenting cell activation by T cells breaks self tolerance. PNAS 201818624.

Yu, W., Jiang, N., Ebert, P.J.R., Kidd, B.A., Müller, S., Lund, P.J., Juang, J., Adachi, K., Tse, T., Birnbaum, M.E., et al. (2015). Clonal Deletion Prunes but Does Not Eliminate Self-Specific αβ CD8+ T Lymphocytes. Immunity *42*, 929–941.

Zenke, S., Palm, M.M., Braun, J., Gavrilov, A., Meiser, P., Böttcher, J.P., Beyersdorf, N., Ehl, S., Gerard, A., Lämmermann, T., et al. (2020). Quorum Regulation via Nested Antagonistic Feedback Circuits Mediated by the Receptors CD28 and CTLA-4 Confers Robustness to T Cell Population Dynamics. Immunity *52*, 313-327.e7.

Zhang, G., and Lu, Y. (2012). Bias-corrected random forests in regression. Journal of Applied Statistics *39*, 151–160.

Zhang, Z., Gothe, F., Pennamen, P., James, J.R., McDonald, D., Mata, C.P., Modis, Y., Alazami, A.M., Acres, M., Haller, W., et al. (2019). Human interleukin-2 receptor β mutations associated with defects in immunity and peripheral tolerance. J. Exp. Med. *216*, 1311–1327.

Zhang, Z., Legoux, F.P., Vaughan, S.W., and Moon, J.J. (2020). Opposing peripheral fates of tissue-restricted self antigen-specific conventional and regulatory CD4+ T cells. European Journal of Immunology *50*, 63–72.